UNIVERSITY OF CATANIA

DEPARTMENT OF ELECTRICAL ELECTRONIC AND COMPUTER ENGINEERING

DOCTOR OF PHILOSOPHY IN SYSTEMS, ENERGY, COMPUTER AND TELECOMMUNICATIONS ENGINEERING XXXV CYCLE
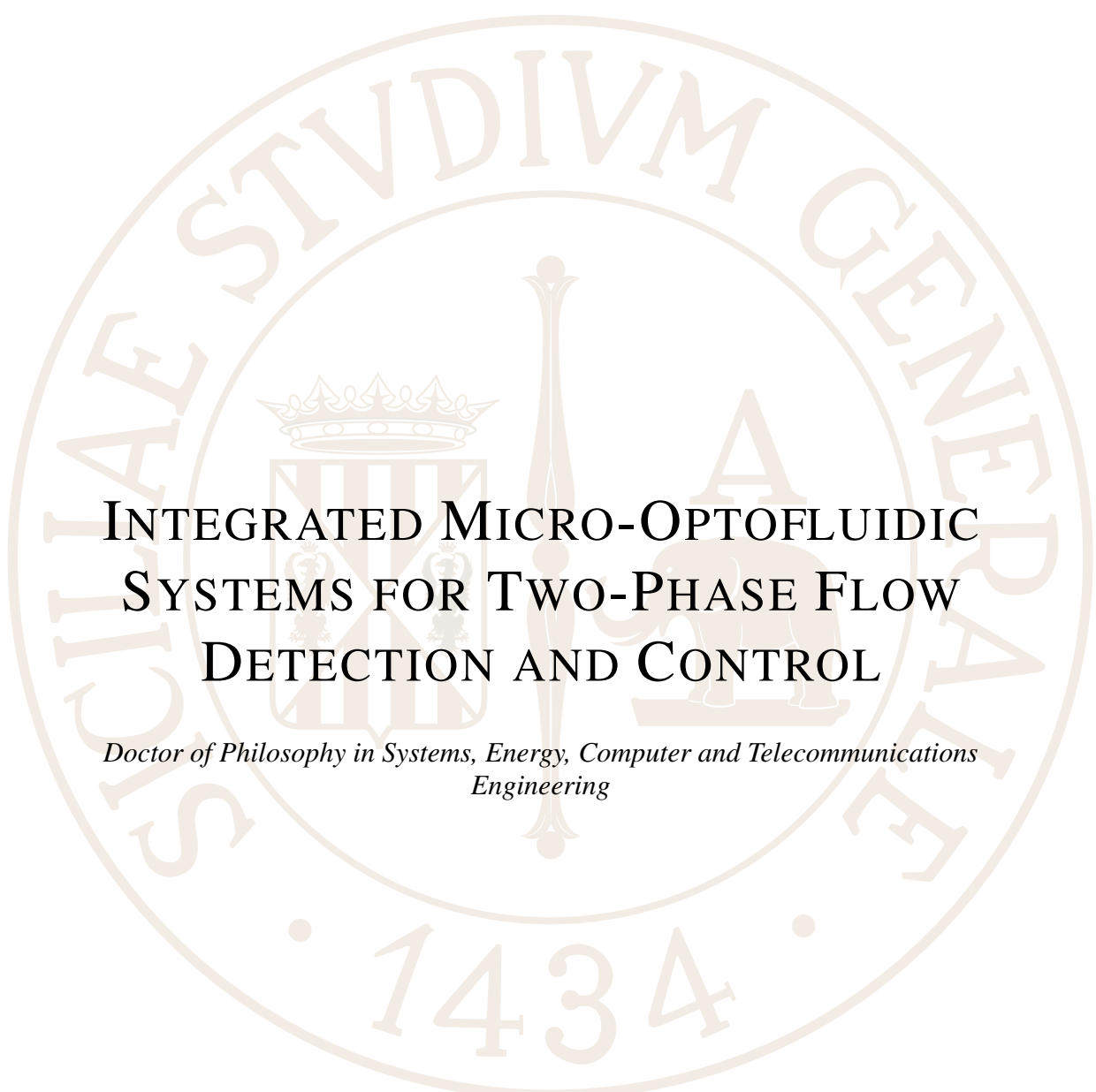
PHD THESIS

Integrated Micro-Optofluidic Systems for Two-Phase Flow Detection and Control

---

Author
Giovanna STELLA

Supervisor
Prof.ssa Maide BUCOLO
PhD Coordinator
Prof. Paolo ARENA

ACADEMIC YEAR 2021/2022

Giovanna STELLA

INTEGRATED MICRO-OPTOFLUIDIC SYSTEMS FOR TWO-PHASE FLOW DETECTION AND CONTROL

Doctor of Philosophy in Systems, Energy, Computer and Telecommunications Engineering

UNIVERSITY OF CATANIA

October 2022

Contents

List of Figures

List of Tables

UNIVERSITY OF CATANIA

Department of Electrical Electronic and Computer Engineering

Doctor of Philosophy in Systems, Energy, Computer and Telecommunications
Engineering XXXV Cycle

**Integrated Micro-Optofluidic Systems for Two-Phase Flow Detection and
Control**

by Giovanna STELLA

ABSTRACT

Microfluidics is the science of controlling and manipulating fluids that are geo-
metrically constricted into networks of small channels on the order of micrometers.
The objective of the research was double. From one side, to design and fabricate us-
ing low-cost technologies, micro-optofluidic (MoF) devices, capable to replicate and
miniaturize standard equipment used for biological and chemical analysis on sam-
ples. On the other side, to define methods and implement platforms for the real-time
detection and control of two-phase microfluidic processes suitable for the integration
with the MoF devices for a system-on-chip realization.

The two-phase microfluidic processes were obtained by flowing two immiscible flu-
ids in a slug regime or suspended particles/cells into a fluid within a micro-channel,
and optical techniques were used to monitor, detect and control the behavior of these
processes in an area inside the micro-channel. The optical technologies have been
chosen to be noninvasive, offering the advantages of real-time data acquisition and
being versatile for micro-optical components miniaturization.

Initially, technological aspects for the design and fabrication of MoF devices were
addressed by proposing four different designs of MoF devices and using two 3D-
printing-based fabrication techniques. Then, these MoF devices were used to define
methodologies and implement real-time platforms for the detection and control of
two-phase flow in micro-channels. These aspects were faced in Part I and Part II of
this thesis considering slug flows and particle suspensions, respectively.

The devices realized and the methodologies developed were used to realize two in-
tegrated systems, one for the real-time control of the slug flow and the other for the
real-time detection of the micro-particle velocity.

Different wide experimental campaigns were carried out to characterize the MoF
devices realized, to validate the methodologies developed, and to test the platforms
implemented and the integrated systems realized.

Introduction

The manipulation of small amounts of fluids and micrometer particles in suspension within microfluidic devices for the analysis of biological and chemical processes on low-cost, portable chips, such as System-on-a-Chips [1], [2] is a topic of great relevance in the development of cutting-edge biotechnology [3].

In this thesis, of particular interest are two-phase microfluidic processes, which can be obtained by two immiscible fluids or suspended particles/cells into a fluid within micro-channels with diameters in the order of micrometers [4]. Particularly, the immiscible fluids were investigated in the slug regime: a sequence interlaced between two fluids. The fluid suspensions were obtained with both biological fluids (cells of different nature and in different concentrations) and synthetic particles.

Depending on the experimental conditions under which they operate (physical, chemical, electrical and optical properties of both the phases and the devices) and the geometry designed for the micro-channel (straight, curvilinear, with converging or diverging paths and with chambers), the interaction of the two phases or the behavior of the suspended particles/cells can vary considerably along the channel, generating complex nonlinear behaviors [5]. Indeed these processes fall into the class of nonlinear systems with two inputs and infinite dimensions. In the experimental campaigns carried on in this thesis project, the input is the hydrodynamic strength of the fluids (flow rate or pressure) at the micro-channel inlets, while outputs are information investigated in an area of interest inside the micro-channel monitored optically.

It is therefore essential, to ensure high accuracy and especially repeatability of the processes, to have low-cost, non-invasive, and easy-to-use flow management and monitoring technologies, as well as flexible and accurate modeling methodologies for the realization of appropriate and robust control schemes.

The objective of the research was double. From one side, to design and fabricate using low-cost technologies, micro-optofluidic (MoF) devices, capable to replicate and miniaturize standard equipment used for biological and chemical analysis on samples. On the other side, to define methods and implement platforms for the real-time detection and control of two-phase microfluidic processes suitable for the integration with the MoF devices for a system-on-chip realization.

The optical technologies have been chosen for the process detection being non-invasive [6]. They offer the advantages of real-time data acquisition both by (photodiode or power meter) and images (camera) and are versatile for micro-optical components miniaturization [7]–[9].

In the first chapter of this thesis, the design and fabrication of four MoF devices were presented and characterized. These MoF devices integrate microfluidic components and micro-optical components. For their realization, to reduce and simplify the development cost, two approaches based on the 3D printing were investigated using two materials polydimethylsiloxane (PDMS) and HTL-resin.

An ad-hoc master-slave protocol was established to realize the PDMS MoF device, being not possible its direct use by 3D printers. In all the designs proposed the model of the standard T-junction is integrated with micro-optical components: from the fiber insertions (for the light direct access and detection in an area of interest) as in the slug detector and the slug switch, to the micro-waveguide and micro-mirror as in the slug velocity detector. A MoF chamber was, then, designed specifically for the investigation of particle/cell suspensions. Different working principles based on the light reflection and absorption were considered in the MoF device models.

These MoF devices were used to develop systems, methodologies, and platforms for the detection and control of the two-phase flow in micro-channels, as discussed in Part I and Part II of this thesis considering slug flows and particle suspensions, respectively.

- In **Part I**, being the slug flow an interlaced sequence of two fluids, two pieces of information were investigated: the frequency of the slug passage in a micro-channel area of investigation and their mean velocity. Initially. a comparison in the slug frequency detection by the slug flow detector and slug switch detector was considered. This led to highlighting the pros and cons of the two fabrications approach (based on HTL-resin and PDMS) and two working principles (based on the absorbance vs total internal reflection).

  Subsequently, thanks to a specific experimental set-up including simultaneously the acquisition of two photodiodes and a camera, an advanced data analysis procedure based was developed and implemented in a real-time Platform. Both information on the frequency and the velocity of the slug passage were detected in real-time during the experimental campaign. The MoF slug velocity detector was designed to miniaturize the experimental set-up, having information on both the frequency and the velocity of the slug passage.

  Using the MoF slug velocity detector and the methodology developed for the data analysis, an active control for the slug frequency passage was implemented and integrated in a micro-controller-based platform set-up. A Model Predictive Control (MPC) strategy was applied. The hydrodynamic strengths of the two fluids at the micro-channel inlets were set by a data-driven model used for the MPC definition and simultaneously the data were acquired and analyzed to evaluate the current slug frequency value. A real-time wide experimental campaign was carried out to confirm the robustness of the approach and its suitability for a system-on-chip integration.

  Finally, an example of passive control, based on chemical treatment of the micro-channels surface was presented.

- In **Part II**, the attention was focused on an optical data analysis strategy, a MoF device design correlated to a proper optical model to detect particle concentrations, and the establishment of a set-up suitable for the system-on-chip integration.

  The Digital Particle Image Velocimetry (DPIV) method was studied to be applied for the investigation of micro-particle velocities in micro-channel. The DPIV algorithm is based on movie data processing that are time consuming and require a complex equipment set-up. Starting from this consideration, an

ad-hoc procedure DPIV-based was implemented both to optimize its performance based on the experimental context and to extract the average of microparticle velocities. This latter was then compared with the information extracted by the optical signal (photodiode acquisition) for evaluating the suitability of this approach for system-on-chip development.

These methods were applied in a wide experimental campaign for the hydrodynamic study of unsteady biological flows and to investigate a specific particle suspensions regime, called inertial focusing.

Then, the MoF chamber was designed and realized. The device consists of a chamber specifically designed to study cell populations and optical fiber insertions to enlighten the process and acquire optical information. The MoF chamber was tested in different experimental contexts and its performance was compared with those of the MoF T-junction devices.

Chapter 1

Micro-Optofluidic devices

1.1 3D printing-based manufacturing

Lab-on-a-chip has gained significant attention starting from the 1990s [10]. In these devices a micrometric channel allows small volumes of fluids to be tested. Lab-on-a-chip devices can perform many operations usually needed in conventional biochemistry laboratories, from sample preparation to reaction, detection, and other procedures [11]. Moreover, their use is widely spreading thanks to advantages in terms of low-cost in manufacturing, power consumption saving, reduced time of analysis and mostly a small fluid expenditure for biological, chemistry, and medical applications [3], [12]–[15].

Within this context, lab-on-chip devices are used to detect and control two-phase flows into micro-channel, both in biomedical fields and chemical processes [2], [3], [14], [15]. The term two-phase flow refers to two immiscible fluids, which can be gas-liquid, immiscible liquid-liquid, or liquid and micro-particles, one dispersed in the other, and circulating into the same micro-system [6], [16]. Among the methods present in literature to detect two-phase flows, the optical one is advantageous in running an ample range of measurements and being minimally invasive [6].

In the past, microfluidic devices were produced by means of deposition, micro-fabrication photo-lithography and etching processes. The materials used were silicon, quartz and glass [17]–[22].

However, many disadvantages were experienced with these approaches as high raw materials costs, time-consuming and expensive processes needing clean rooms and limited channel geometries. To overcome all these limits, polymers were introduced since they are cheaper than glass or silicon [23], suitable for mass production and bio-compatible. Furthermore, polymers display good gas permeability, which is fundamental for biochemistry applications, together with satisfying optical transparency, which is essential in microfluidics to implement optical detection methods for observing and extracting information from biological or chemical samples [24]–[29].

Among all the polymer types tested in the past decade, Polydimethyl-Siloxane (PDMS) has emerged as the preferred choice [30]. PDMS can be easily molded by casting to

create micro and nano-structures with a fabrication process called soft-lithography
[31]. PDMS has relevant good properties, like non-toxicity, low-temperature curing,
transparency down to 280 nm which enable the use for optical detection, good gas
permeability and chemically inertness. However, some important limitations can be
evidenced in its use. Firstly, once the PDMS device is fabricated it is possible that
the micro-channels walls will undergo surface deformation due to the exposure to
non-polar organic solvents. These variations are caused by the swelling phenom-
ena. Second, being the PDMS quite chemical inert, in the manufacture of devices
it does not allow permanent bounding with itself and it is not easy to permanently
attach molecules or polymers of a different nature to its surface [10], [32]. This lim-
its the possibility to assemble complex structures because of poor adhesive bonding.
Nonetheless, recent advances to deliberately modify the surface properties of PDMS
are presented in [33] and different strategies to bond PDMS with various rigid and
flexible substrate materials are presented in [34]. Third, PDMS softness and ther-
mal expansion make it difficult to obtain high dimensional accuracy [31]. From the
processing point of view, even if the soft-lithography is a low-cost process, it takes
a long time to produce a device, since it requires several processing steps for the
manufacturing: fabrication of the master mold, PDMS liquid polymer mixing prepa-
ration, casting procedure, PDMS curing, and demolding [35].

The standard master-slave micro-fabrication methods, such as soft-lithography and
photo-lithography, traditionally used to fabricate lab-on-chip [31], [36] are expen-
sive and time-consuming [37] and in particular suffer from limited availability of
compatible biological materials [38].

The possibility to print a micro-device in one step with PDMS is still under investiga-
tion [39], on this purpose an ad-hoc master-slave fabrication protocol PDMS-based
3D printing was implemented in [7], [8]. However, the master-slave protocol needs
more steps for manufacturing and offers several advantages, including the need for
simple equipment, the use of low-cost materials and the absence of a strictly con-
trolled environment.

The second 3D printing approach proposed is the vat polymerization technique named
PµSL, patented by the company Boston Micro Fabrication (BMF, www.bmf3d.com)
using the photocurable HTL resin. The *PµSL* shows several advantages: short turn-
around time, down-to-micron precision and complex shape printing. The HTL resin-
based 3D printing technique allows the realization of a device in one piece (with no
assembly between parts) by using a one-step manufacturing procedure [10], [28],
[40]. The proposed method is an alternative to the stereo lithography technology,
which is recently used to fabricate organ-on-chip for their compatibility with bioma-
terials [41], [42].

These two innovative 3D printing approaches, the master-slave protocol PDMS-
based and the projection micro stereolithography (*PµSL*) HTL resin-based open the
way to new fabrication strategies in lab-on-a-chip and organ-on-a-chip devices real-
ization. In the following section, the used materials (PDMS and HTL resin), the pro-
posed novel approaches based on 3D printing technologies and the micro-optofluidic
devices realized will be presented in detail.

1.1.1 Materials

In the master-slave protocol PDMS-based, the master for PDMS casting is printed
using two materials: VeroWhitePlus RGD835 and FullCure705. RGD835 was pur-
chased from OVERMACH S.p.A. (Parma, Italy) and it is a proprietary blend of

acrylate monomers and photo activators. FullCure705 was purchased from OVER-MACH S.p.A. (Parma, Italy) and, as for RGD835, it is a proprietary blend of acrylate monomers and photo activators. FullCure705 is a breakaway support that is removed by water jetting once the printing process is accomplished. The breakaway support is not part of the final system and is only needed to print not supported cavities.

The master is 3D-printed on a 3D printer Stratasys Objet260 Connex1 (Stratasys, Los Angeles, CA, USA) and it is used as a mold to cast devices. For casting micro-optofluidic devices the SYLGARDTM 184 Silicone Elastomer kit, composed of a Polymethyl Siloxane (PDMS) elastomer and a suitable curing agent, was purchased from Farnell Italia S.R.L. (Sylgard 184 elastomer kit, Dow Corning, 148 Midland, Michigan, USA). The master-slave protocol PDMS-based for device manufacturing is detailed in the following section.

In the projection micro stereolithography ($P\mu SL$), the material used is the HTL Resin. It is a high-performance, rigid and heat-resistant yellow resin proprietary developed by Boston Micro Fabrication (BMF, Maynard, Massachusetts). HTL was used to manufacture devices printing on the microArch S140 ultra-high resolution (10μm) 3D printer (BMF, Maynard, Massachusetts). This resin grade was selected because of its temperature stability and mechanical properties making it suitable for autoclave sterilization. The resin has, according to its technical data sheet (TDS), a heat distortion temperature (HDT) equal to $140.7°C$ (0.45MPa) and a Glass Transition Temperature (Tg) of $172°C$. This last parameter is the temperature at which the amorphous regions experience the transition from a rigid state to a more flexible state making the temperature at the border of the solid state into a rubbery state [43]. Therefore, the resin is suitable for repeated autoclave cycles making the devices suitable for multiple reuses.

1.1.2 Master-slave protocol PDMS-based

The micro-optical components and the micro-optofluidic devices can be realized in PDMS by using the master-slave protocol. The phases of this fabrication process are summarized in Fig. 1.1.

The first step is to design the master molds systems with a 3D drawing and modeling software, such as Solidworks (Dassault Systèmes) or Inventor (Autodesk). After obtaining the Computer-Aided Design (CADs) files, they can be printed by using a 3D printer. In order to obtain better manufacturing results in resolution and surface quality an inkjet printer was used.

Generally, the master is obtained by overlaying thin layers of photo-sensible resin, and at each layer, the printer lights up the resin with UV rays in order to reticulate it. In the end, it could happen that, microscopically, the master is not perfectly reticulated and this could compromise the reticulation of the PDMS device in the master-slave procedure. In the beginning, a chemical treatment, proposed in [7], was used to overcome this issue. It was possible to improve the protocol by changing the chemical treatment with a UV treatment of 1 hour at 35 °C in an ad-hoc UV exposition chamber controlled in temperature. The neon tubes used for the UV treatment (Philips UV-A TL-8W G5) have a wavelength of 300 nm and can deform the master in the case of uncontrolled exposure and consequently the PDMS device. A system for temperature control inside the chamber was implemented by a micro-controller (with an Arduino system) and a temperature sensor. Once created the master mold system, the next step is to generate the PDMS system.

The composite PDMS is obtained from the mixture of silicone elastomer base and curing agent (Sylgard 184 elastomer kit, Dow Corning). These are mixed together
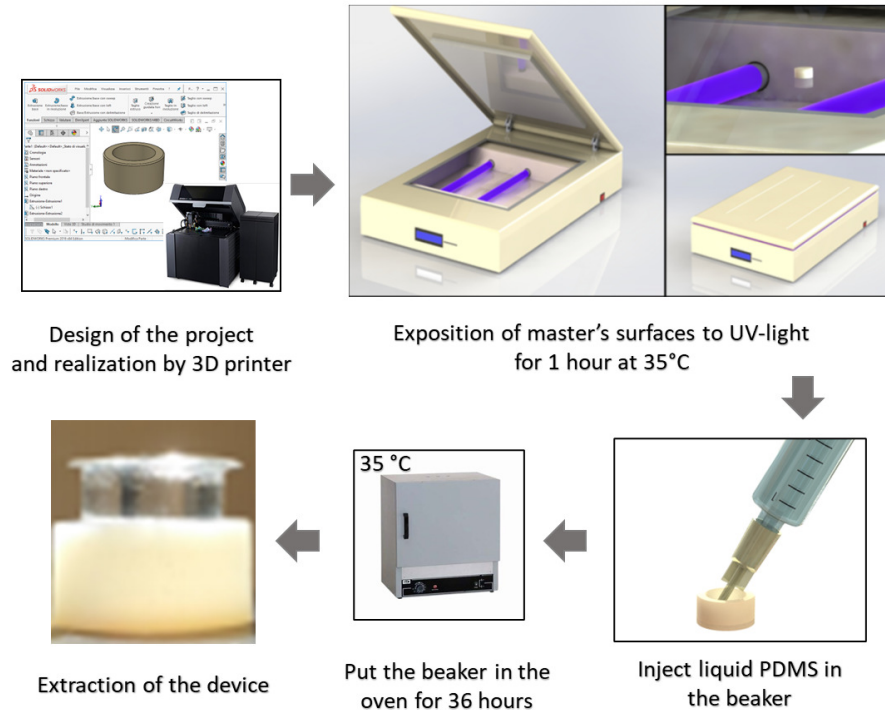
FIGURE 1.1: The phases of the master-slave protocol PDMS-based presented for the 3D printing fabrication of devices. The CAD of the mold is printed and UV-treated to guarantee the proper reticulation of the PDMS device.

according to the proportion (10 : 1) for the device layer (micro-systems) and to the proportion of (5 : 1) for the bulk cover layer. After the mixing phase, in the compound, some bubbles are appearing, and before starting with the next phase they are removed by using a degassing procedure performed by a vacuum bell. After the degassing, the PDMS is poured into the master and placed in an oven at $35°C$ for 36 hours or alternately left at room temperature for 48 hours.

Finally, the PDMS systems are peeled from their master molds. For assembling the device, the PDMS device layer and the bulk cover layer are bounded by a reversible bound procedure.

1.1.3 Projection Micro Stereolithography HTL resin-based

The micro-optical components and the micro-optofluidic devices can be realized in HTL resin by using the Projection Micro Stereolithography technique, which allows for ultra-high resolution, accuracy, and precision.

PμSTL is a hybrid technique combining the benefits of SLA (Stereolithography) and DLP (Digital Light Processing) 3D printing techniques. Basically, micro-sized parts are printed in the top-down direction, as it happens in the SLA; but the resin is cured as done in DLP, i.e. by using a digital projection screen rather than a small spot laser. The working principle of the projection micro stereolithography HTL resin-based technique is shown in Fig. 1.2.

Like other 3D printing processes, the PμSL begins with a Computer-Aided Design (CAD) file. This file is then sliced into a series of 2D images called digital masks that show or hide specific areas of a layer. Each layer has a mask, and each layer is added until the entire 3DP structure is complete. To fabricate individual layers, slicing data is sent to the 3D printing system. The BMF printers platform features
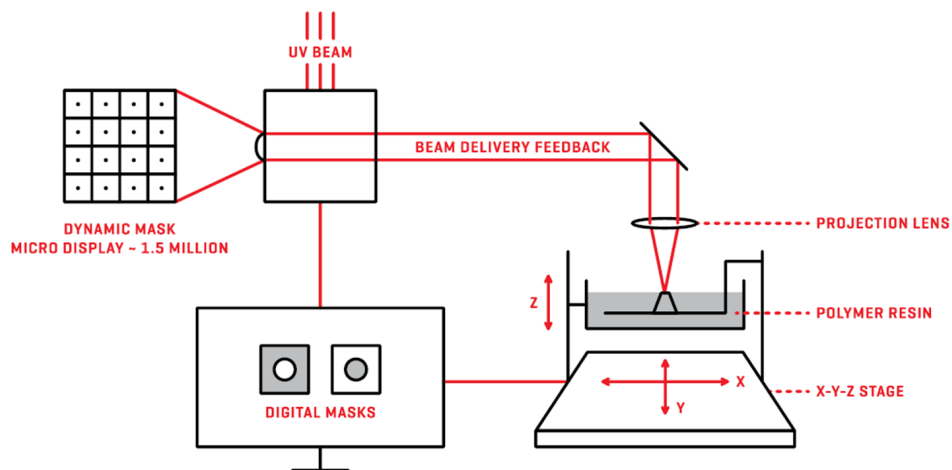
FIGURE 1.2: Working principle of the projection micro stereolithography HTL resin-based technique presented for the fabrication of 3D printing devices.

a digital light processing chip (DLP), a projection lens, motion control stages, and a reservoir for the UV-curable resin.

Within a BMF 3D printing system, UV light is projected onto a DLP chip according to the layer's mask pattern. By controlling the projection lens, PμSL technology can achieve resolutions of several micrometers or hundreds of nanometers. UV-curable materials include plastic resins that are rigid, tough, high-temperature resistant, biocompatible, flexible, or transparent. In addition to engineering and biomedical plastics, PμSL technology supports the use of hydrogels and composite resins that contain ceramic or metal particles.

This 3D printing approach allows printing directly the entire micro-optofluidic devices or micro-optical components in a single step reducing the manufacturing time.

1.2 T-junction micro-optofluidic slug detector

1.2.1 Working principle and design

The T-junction micro-optofluidic slug detector exploits the phenomenon of light absorption for two-phase flow detection of immiscible fluids. Assuming that two fluids with quite different refraction indices flow in a micro-channel and an incident laser beam interferes with them in a specific test section of the micro-channel, it is possible to obtain a different light transmission based on which fluid is interfering with the laser beam at that moment.

A schematic of the working principle is shown in Fig. 1.3 (a), while the CAD design of the micro-optofluidic system is presented in Fig. 1.3 (b). To practically exploit this physical principle, the geometry of the micro-optofluidic device has been appropriately determined, also thanks to the help of appropriate simulations reported in previous studies [8]. Briefly, the device has two inlets, necessary for the inlet of the two fluids characterizing the two-phase fluid to be studied, which are connected to the two micro-channels that, forming a T-junction, guarantee the formation of the slug flow. At a sufficient distance from the T-junction for the two-phase flow stabilization, with orthogonal orientation to the main microfluidic channel, the micro-channels for the optical fiber's insertion have been designed.

The device presented in the paper [8] includes the integration of a micro-optical waveguide. In this thesis, to take more advantage of the absorption detection capability, the micro-optical waveguide has been replaced with direct lighting and acquisition in the area of interest with fiber insertion.

Thanks to optical fiber insertion, the laser light is conveyed to a specific section of the investigated micro-channel. The light travels through the sample and is detected by a second optical fiber aligned at the opposite side of the micro-channel. The optical signal acquired is then correlated to the flow inside the micro-channel. The design of this device is independent of the fluids' selection and their refraction indices.

(a)   (b)
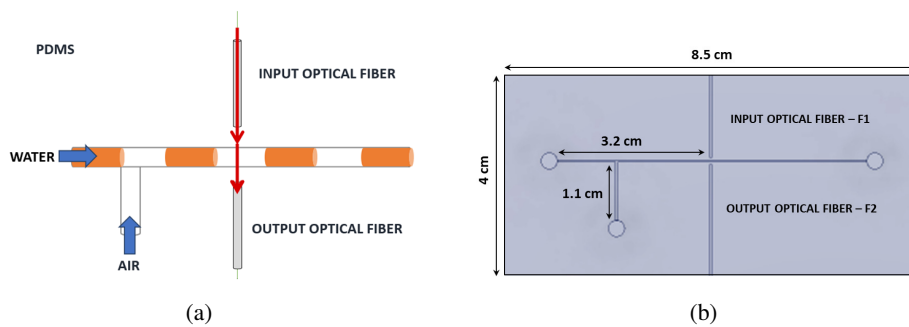
FIGURE 1.3: (a) Working principle of the T-junction micro-optofluidic slug detector based on the absorbance phenomenon; (b) CAD representation and measurements in a frontal perspective: the microfluidic T-junction channel and the optical fibers insertions with a squared section and a diameter of 400 μm.

1.2.2 Device realization PDMS-based

The T-junction micro-optofluidic slug detector was realized in PDMS by using a master-slave protocol, which has already been explained in detail in the paper [8] and in the Section 9.1.

The fabrication process for the realization of the micro-optofluidic device is summarized in Fig. 1.4.
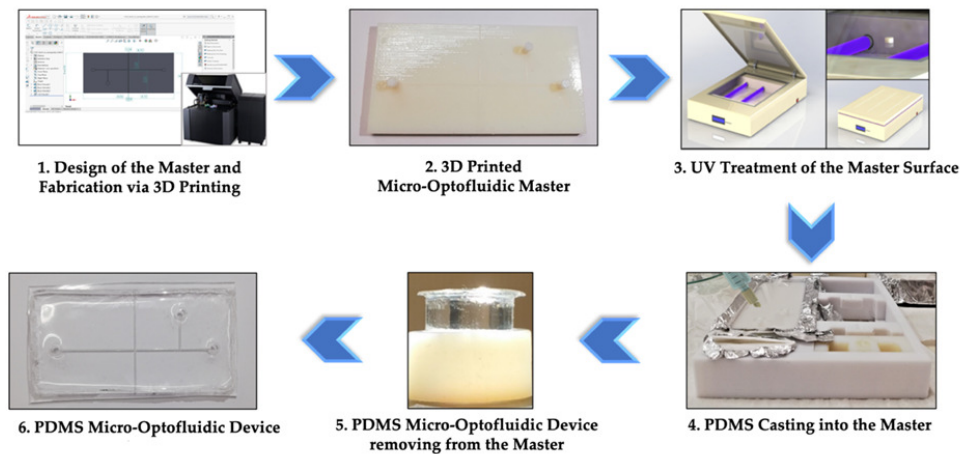
FIGURE 1.4: Master-slave protocol PDMS-based to fabricate the T-junction micro-optofluidic slug detector.

The fabrication process starts with the design of the micro-optofluidic system, shown in Fig. 1.3. The Computer-Aided-Design (*CAD*) was established based on a trade-off among the results of ray-tracing simulations, the material (PDMS) and the fabrication technology (*3D printing*). All the details are reported in [8]. The master-slave mold is printed by using an ink-jet printer model Objet260 Connex1, Stratasys (Rheinmnster, Germany).

The material used for the mold was the VeroWhitePlus, while the FullCure705 (OVERMACH S.p.A., Parma, Italy) was used as support. In previous work [7], a chemical treatment was adopted, and further improvement was reached thanks to UV-based illumination. In the following phase, the silicone and the curing agent of PDMS (Sylgard 184 elastomer kit, Dow Corning) are mixed together according to the proportion $(10:1)$ for the device layer and to the proportion of $(5:1)$ for the bulk cover layer. After the degassing, the PDMS is poured into the two masters and leave them for 48h at room temperature.

Finally, the two micro-systems were peeled from their masters and bounded by a reversible bound procedure. In this way, the final device can be obtained.

1.2.3 Device realization HTL resin-based

The T-junction micro-optofluidic slug detector was also realized in HTL resin by using the Projection micro stereolithography (PμSTL) technique, which allows for ultra-high resolution, accuracy, and precision. In addition, being designed and printed as a single piece avoids fluid leakage phenomena or adhesive bonding issues. The fabrication process for the realization of the micro-optofluidic device is summarized in Fig. 1.5.

The micro-optofluidic device was designed using Autodesk Fusion 360 first and then, the STL file was transferred to the 3D printer for the build step. The microArch® S140 ultra-high resolution (10 μm) 3D printer was used for the printing. The two devices manufactured by the two processing approaches have the same design in terms of micro-channel dimensions, optical section location, inlet and outlet channels dimension, and T-junction geometry. As shown in Fig. 1.6, all these features characterize the two devices, although some changes have been made to the device made in HTL resin, in terms of inlets and outlet positioning, compared to
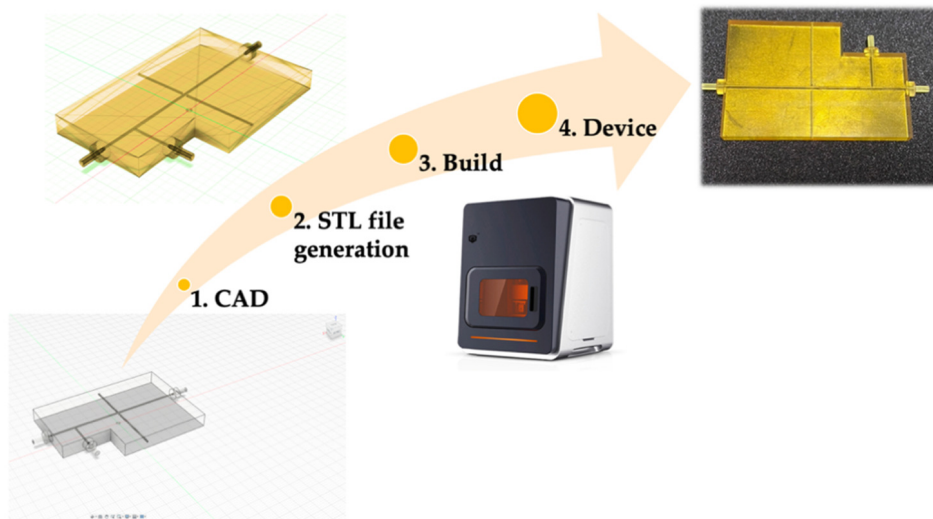
FIGURE 1.5: PμSTL HTL resin-based to fabricate the T-junction micro-optofluidic slug detector.

(a) (b)
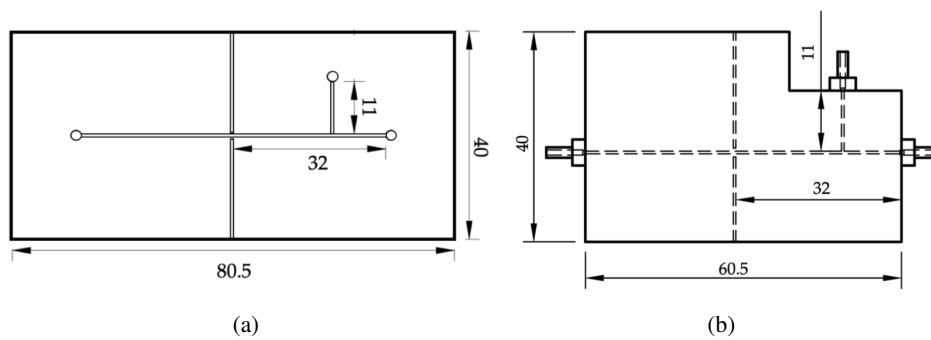
FIGURE 1.6: Comparison of CAD geometries with a top view between the T-junction micro-optofluidic slug detector (a) for PDMS-based and (b) HTL resin-based technology. Sizes are expressed in mm.

the device made in PDMS. This choice allowed to improve flow stabilization because of the absence of abrupt direction changes. In fact, even if the inlets and outlet channel's dimensions remained unchanged, these are orthogonal to the microfluidic channel in the PDMS device and, instead, are coaxial and aligned with the main microfluidic channel in HTL resin-Device.

The latter design choice for the PDMS device is forced by the manufacturing approach that, being based on resin's casting, makes it impractical to realize coaxial inlets and outlets.

1.3 T-junction micro-optofluidic slug switch

1.3.1 Working principle and design

The T-junction micro-optofluidic slug switch, described in detail in [7], exploits the phenomenon of total internal reflection. The operative principle is the following: assuming that two fluids with quite different refractive indices flow in a microfluidic channel and an incident laser beam interferes with them in a test section, we can obtain a selective light reflection and transmission based on which fluid is interfering with the laser at that moment. This is possible in specific geometric conditions established in relation to the fluids and material refractive indices. The polymer selected to realize the device is the PDMS, for its optical properties (refractive index $\eta_{PDMS} = 1.41$) and fast prototyping [44].

The fluids used to generate the two-phase flow were the air and deionized (DI) water which have the refractive indices $n_{air} = 1$ and $n_{water} = 1.33$, respectively. In Fig. 1.7 (a), a cartoon of the mentioned working principle is shown: the reflection condition at the air passage along with the transmission condition at the water passage.

Snell's law allows the computation of the limit angles for the total reflection at the interfaces PDMS-AIR ($\theta_{L1} = \angle45.17$) and PDMS-WATER ($\theta_{L2} = \angle70.6$).

Considering a micro-channel test section and positioning a laser beam with an inclination angle (α) in relation to a micro-channel perpendicular in the range $\theta_{L1} < \alpha < \theta_{L2}$, the light will be reflected at the air passage and transmitted at the water passage based on their refractive indices. The reflection angle is the same as the incident angle α, while for the transmission angle, the light passage through two subsequent interfaces has to be considered: the PDMS-WATER and the WATER-PDMS.

The CAD design of the micro-optofluidic system is presented in Fig. 1.7 (b) and was set based on the characteristic of air and water.
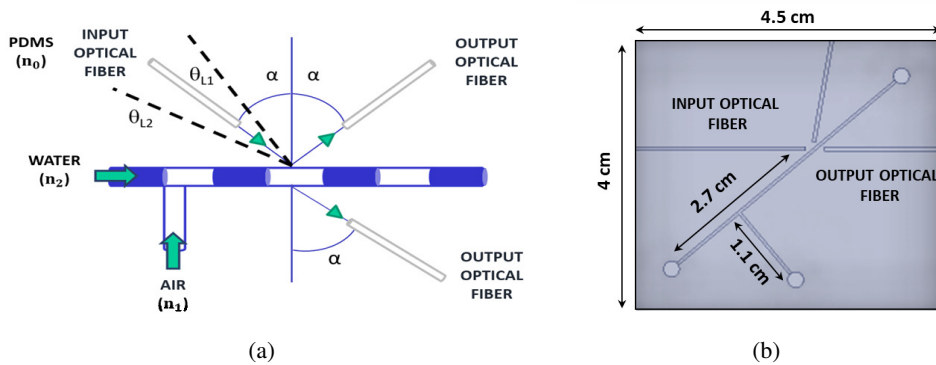
FIGURE 1.7: (a) Working principle of the T-junction micro-optofluidic slug switch based on the total internal reflection phenomenon; (b) CAD representation and measurements in a frontal perspective: the microfluidic T-junction and the optical fibers insertions with a squared section and a diameter of 400 μm.

1.3.2 Device realization PDMS-based

The T-junction micro-optofluidic slug switch was realized in PDMS by using a master-slave protocol, which has already been explained in detail in the paper [7]. The fabrication process for the realization of the micro-optofluidic device is summarized in Fig. 1.8. The developed protocol consists of four steps: the CAD design of the master, the master realization by the 3D printer (the mold), the surface treatment of the master and finally the PDMS chip realization (the slave).
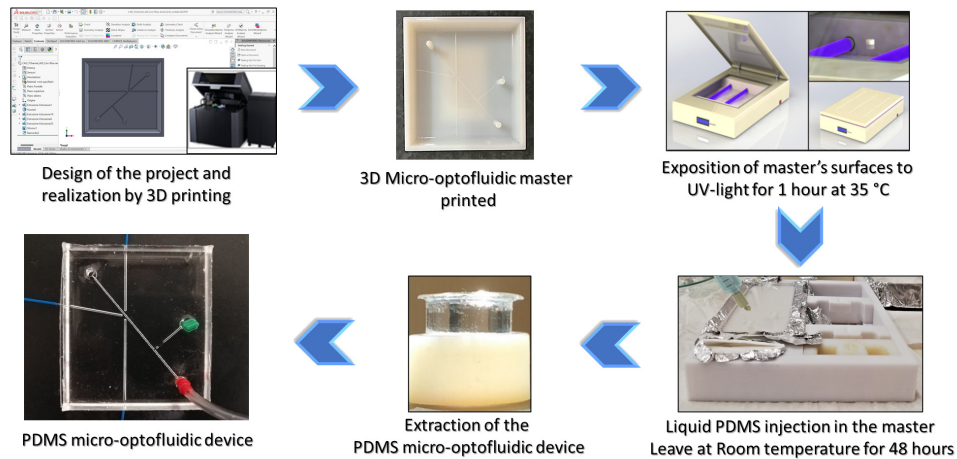
FIGURE 1.8: Master-slave protocol PDMS-based to fabricate the T-junction micro-optofluidic slug switch.

The CAD of the master was designed in Solidworks and sent to the 3D printer (Object 30). It has a resolution of 49 μm in the work plane and, of 28 μm along the z-axis, that is the direction along which the print head of the printer moves. The accuracy is around 0.1 mm with slight variations depending on the geometry, the size, the orientation, the material and the post-processing method. Two polymers are used by the printer: the Whiteplus 835 (inspired by ABS) is the main polymer and the FullCure 705 is the support polymer.

In the second step, thanks to the UV-based illumination, it was improved the affinity surface to ensure an easy peeling of the PDMS slave from the mold.

The two components of PDMS (Sylgard 184 elastomer kit, Dow Corning), the silicone and the curing agent were mixed according to the proportion (10:1) for the device layer and with a proportion of (5:1) for the bulk cover layer. After the degassing, the PDMS was poured into the master and left for 48 h at room temperature. Finally, the PDMS device was peeled from the master and assembled with a 0.5 mm thick bulk by a reversible bound procedure.

1.4 T-junction micro-optofluidic slug velocity detector

1.4.1 Working principle and design

The T-junction micro-optofluidic slug velocity detector presents the same working principle as the T-junction micro-optofluidic slug detector, but mainly exploits the phenomenon performed by an integrated micro-optical component able to split the light into two paths.

The micro-optical component, named micro-splitter (μSPT), was realized by including a micro-mirror (μMR) in-between two micro-waveguides (μWGs) of length L with a squared section of 1 *mm* side as shown in Fig. 1.9 (a).

To bend the light beam coming from the input source, the working principle is as follows: an input optical fiber guides the light, coming from a light source, through a first waveguide (μWG1) towards a micro-mirror (μMR). The light, after being angled by the latter, is guided to the output optical fiber by a second waveguide (μWG2).

The micro-mirror geometry consists of two angled surfaces M1 and M2, respectively tilted of the angles $\{\beta; \gamma\}$ with respect to the light input section, as shown in Fig. 1.9 (b). The optimal values of $\{\beta = 57.35°; \gamma = 26°\}$ were identified by ray-tracing simulations (TracePro by Lambda Research Corporation) as shown in Fig. 1.9 (c).

(a)   (b)   (c)
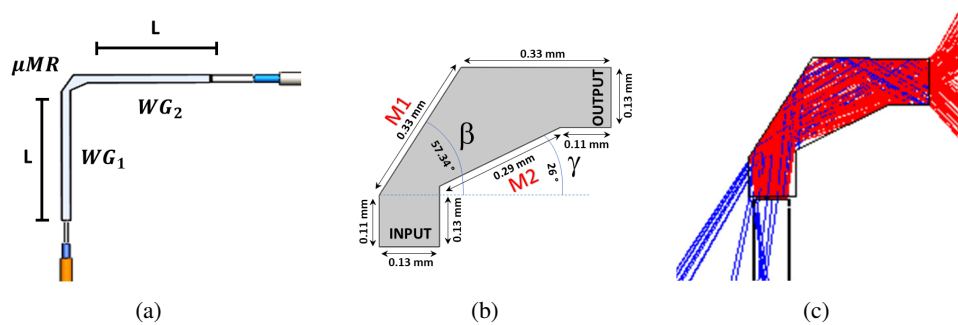
FIGURE 1.9: (a) Design of the micro-splitter (μSPT): a micro-mirror (μMR) in-between two micro-waveguides (μWGs) of length L. (b) CAD representation and measurements in a frontal perspective of the μMR. (c) Optimal values of $\{\beta; \gamma\}$ identified by ray tracing simulations.

The μSPT design leads to the minimization of the rays' dispersion and coveys the beam along the micro-optical device path toward the output light section.
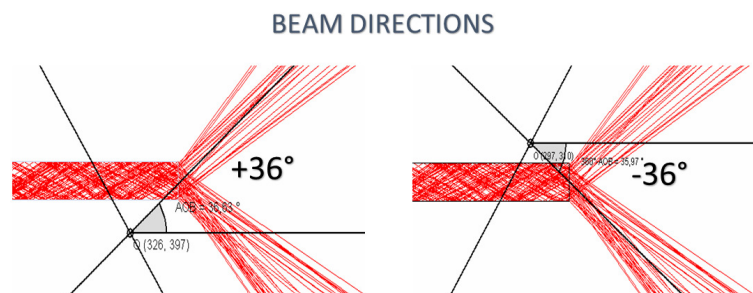
FIGURE 1.10: The two paths of the light beam after being bent by the μMR. An angle of about 36° was identified with respect to the main direction of the light.

(a)   (b)
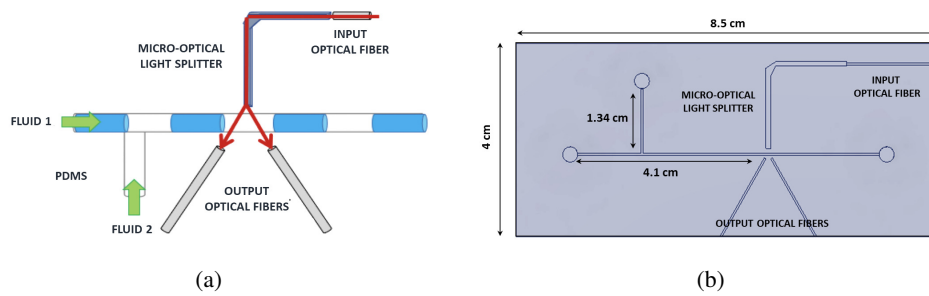
FIGURE 1.11: (a) Working principle of the T-junction micro-optofluidic slug velocity detector; (b) CAD representation and measurements in a frontal perspective: the microfluidic T-junction and the optical fibers insertions having a diameter of 400 μm.

It is worth noticing that in the μSPT, after the light was bent by the μMR, two light paths are obtained, more is the distance from the output surface more this effect becomes evident, see Fig. 1.9 (c). Analyzing the principal directions of the two light beams, an angle of about $36°$ respect to the output section of the μMR was identified (see Fig. 1.10).

In micro-optofluidics, it is important to confine and transport the light as close as possible to the sample, by guiding it into a small volume of the microfluidic channel and acquiring the emitted/transmitted radiation. To realize a low-cost portable device a micro-optofluidic device was designed to be compact, integrating the micro-optic component (the μSPT) and the microfluidic component (the T-junction microchannel). The device includes three optical fiber insertions and an allocation area for the micro-optical component. Through the input optical fiber insertion, the source light is conveyed to the μSPT and then reaches the area of the micro-channel investigated. The light, splitted in two paths thanks to the geometrical features of the μSPT, travels to the sample and it is detected by two optical fibers aligned at the opposite side of the micro-channel.

Thanks to the two output optical detection points, it is possible to develop a suitable methodology for the real-time detection of slugs' velocity. The orientation of the output optical fiber insertions was evaluated by ray-tracing simulations using the TracePro software (Lambda Research Corporation) and it will be discussed in the next section.

In the device design some constraints were considered:

- The μSPT diameter was set to 1 mm due to the 3D printing limitation;

- The distance between the μSPT and the micro-channel was set to 1 mm and the distance of the micro-channel respect the two output optical fibers insertions to 0.5 mm to ensure a safety manufacturing and avoid fluid leakage.

- The diameter of the output optical fiber was set equal to the micro-channel width of 400 μm to maximize the acquisition.

A schematic of the working principle is shown in Fig. 1.11 (a), while the CAD design of the micro-optofluidic system is presented in Fig. 1.11 (b).
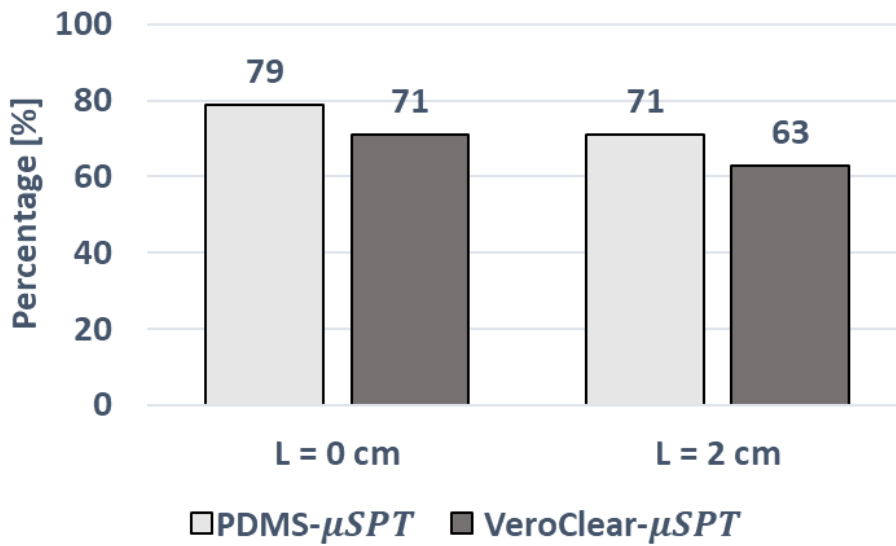
FIGURE 1.12: Histogram of the percentage of rays, obtained by ray-tracing simulations, reaching the output fiber surfaces for two different lengths $L = \{0; 2\}$ *cm* for the PDMS-μSPT and the VeroClear-μSPT.

1.4.2 Ray-tracing simulations

After designing the micro-optical component and the micro-device, their performances were studied by means of ray-tracing simulations in TracePro (Lambda, Research Corporation). This procedure allows for verification of the path of the rays inside the micro-optical components and devices, charting the spatial distribution of the incident rays in the surfaces of interest and conducting a comparative study between different configurations. The ray-tracing simulations were divided into two phases. In the first phase of simulation, the performance of the μSPT design was evaluated.

The selected materials for the μSPT were the polydimethylsiloxane (PDMS) and the VeroClear, materials with the advantages being bio-compatibility, optical transparency and suitability for low-cost rapid prototyping technologies, refractive indices $n_1 = 1.41$ and $n_3 = 1.53$, respectively.

In the simulation, the μSPT was assumed to be surrounded by air ($n_0 = 1$). As the refractive index of the chosen materials is greater than that of the surrounding material, the light transmitted from a source is able to travel within the micro-optical component thanks to the phenomenon of total internal reflection. The laser source was assumed to have a power of 0.1 mW and able to emit 100 rays. The diameter of the input and output optical fibers were set to 400 μm and 1 mm, respectively, and the distance between them and the μSPT was ideally set to zero. The results obtained by the ray-tracing simulations are reported in the histogram of Fig. 1.12, where the percentage of rays reaching the output optical fiber surface for two different lengths $L = \{0; 2\}$ *cm* are compared for the PDMS-μSPT and the VeroClear-μSPT. In all the cases the 60% of the rays reaches the output fiber surface, with an increase of 8% for L = 0 cm, and the performance of the two materials are almost equivalent with a variation of 8%.

The second phase of the simulation consists in evaluating the performance of the T-junction micro-optofluidic slug velocity detector with the μSPT integrated. The

material selected for the device was the PDMS, the main used material for the realization of devices in microfluidics.

In the case in which both the device and the μSPT are designed in PDMS, in order to permit the light transmitted from a source to travel within the micro-optical component thanks to the phenomenon of total internal reflection, the μSPT was designed to be shield by gold (refractive index $nAu = 0.47$) and placed in the allocation area of the micro-system, as done with the micro-optofluidic device presented in [8].
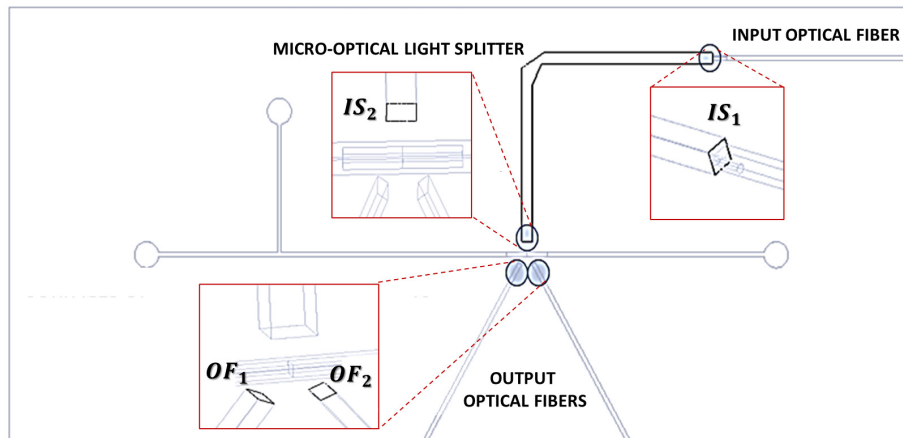
(a)
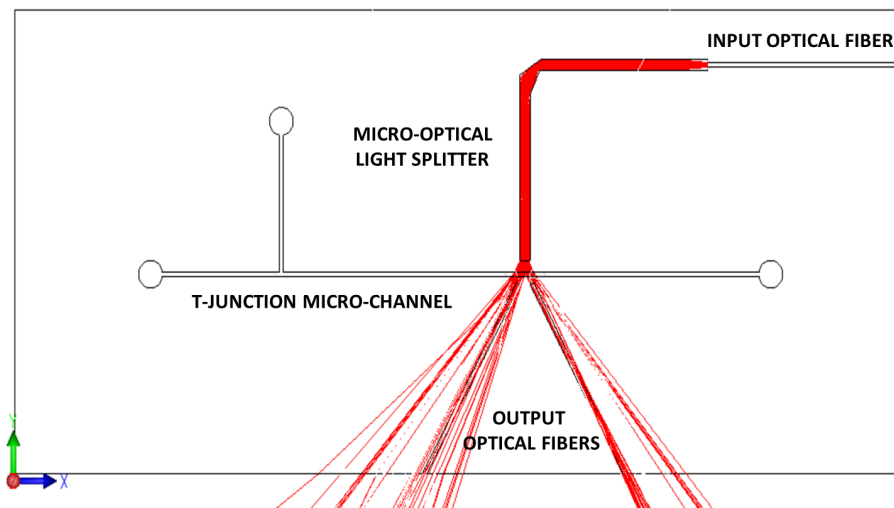
(b)

FIGURE 1.13: (a) Selection of the surfaces of interest investigated during the ray-tracing simulations; (b) the ray-tracing results obtained in simulations when the micro-channel was filled by water.

The aim is to realize a slug velocity detector and to do that two immiscible fluids, air and water, have been simulated to evaluate the emitted/transmitted light radiation inside the micro-channel and the absorbance/transmission properties of the investigated fluids.

The spatial distribution of the rays incident in four surfaces of interest (see Fig. 1.13) were investigated: the input and the output surfaces of the μSPT (IS_1 and IS_2) and

the surfaces of the two output optical fiber insertions (OF_1 and OF_2). In simulations, the used light source had 100 rays with a power of 1 mW.

The results obtained in simulations are shown in Fig. 1.14.

The percentage of incident rays evaluated at the input and the output of the μSPT is 100%, this means that in simulation the micro-optical component can transmit completely the light source inserted in the input. In the output fibers insertions surfaces, it is evident a reduction in the number of rays detected.

The μSPT has a diameter of 1 mm and the fiber insertions at the output have a diameter of 400 μm, equal to the micro-channel, in order to acquire only the light absorbed or transmitted by the fluids inside it. However, this primarily leads to a loss of 60 % of incident rays.

A further loss is due to the distance between the μSPT and the output optical fibers insertions, which are approximately 1.4 mm apart, and the rest of the loss is due to the absorption or transmission of the rays within the investigated fluids inside the micro-channel and the material with which the device was designed.

Despite this, the device manages to acquire at two acquisition points and to distinguish the two investigated fluids within the device. It can be seen that in the presence of air, the percentage of reading rays is lower than the percentage of rays in the presence of water.

The micro-optofluidic device was also designed and simulated by integrating the VeroClear-μSPT (refractive index $n_{VC} = 1.53$). Being the refractive index of the μSPT greater than that of the surrounding material, the PDMS device, the light transmitted from the source is able to travel within the micro-optical component without applying any layer on the μSPT as done with the PDMS-μSPT.

Similar results to the micro-optofluidic device with the PDMS-μSPT integrated were obtained.

1.4.3 Device realization PDMS-based

After having designed and investigated in simulation the T-junction micro-optofluidic slug velocity detector with the μSPT integrated, it is possible to move on to its realization, which consists of three phases.

The first phase includes the fabrication of the μSPT. Based on the materials investigated, two low-cost technologies were taken into account. The realization of the PDMS-μSPT was done using a master-slave approach based on the 3D printing technique, implemented by the authors, already presented in [7]–[9]. Then the PDMS-μSPT was gold-sputtered up to a thickness of 20 nm using an Emitech K-550 sputter coater (Ashford Kent, UK). The VeroClear-muSPT was directly 3D-printed by using an inkjet printer model Object260 Connex1, Stratasys. The same printer used for the printing of the master-slave mold is used for the realization of the PDMS-μSPT. The formulation of the resin, named VeroClear RGD810, was developed for PolyJet 3D printing by Stratasys and it is proprietary.

However, the safety data sheet (SDS) reports it is made of a complex mixture of photo activators and acrylate monomers. Once the building procedure was accomplished, in order to obtain a smoother surface, it was soaked in a 1% solution of sodium hydroxide, as suggested by Stratasys post-printing process guide.

The second phase includes the fabrication of the T-junction micro-optofluidic slug velocity detector in PDMS by using the same master-slave approach based on the 3D printing technique used for the realization of the PDMS-μSPT. The fabrication process of the μSPT and the device are summarized in Fig. 1.8.

The third phase includes the integration of the μSPT in the allocation area of the

(a)

(b)

(c)

(d)

(e)

(f)
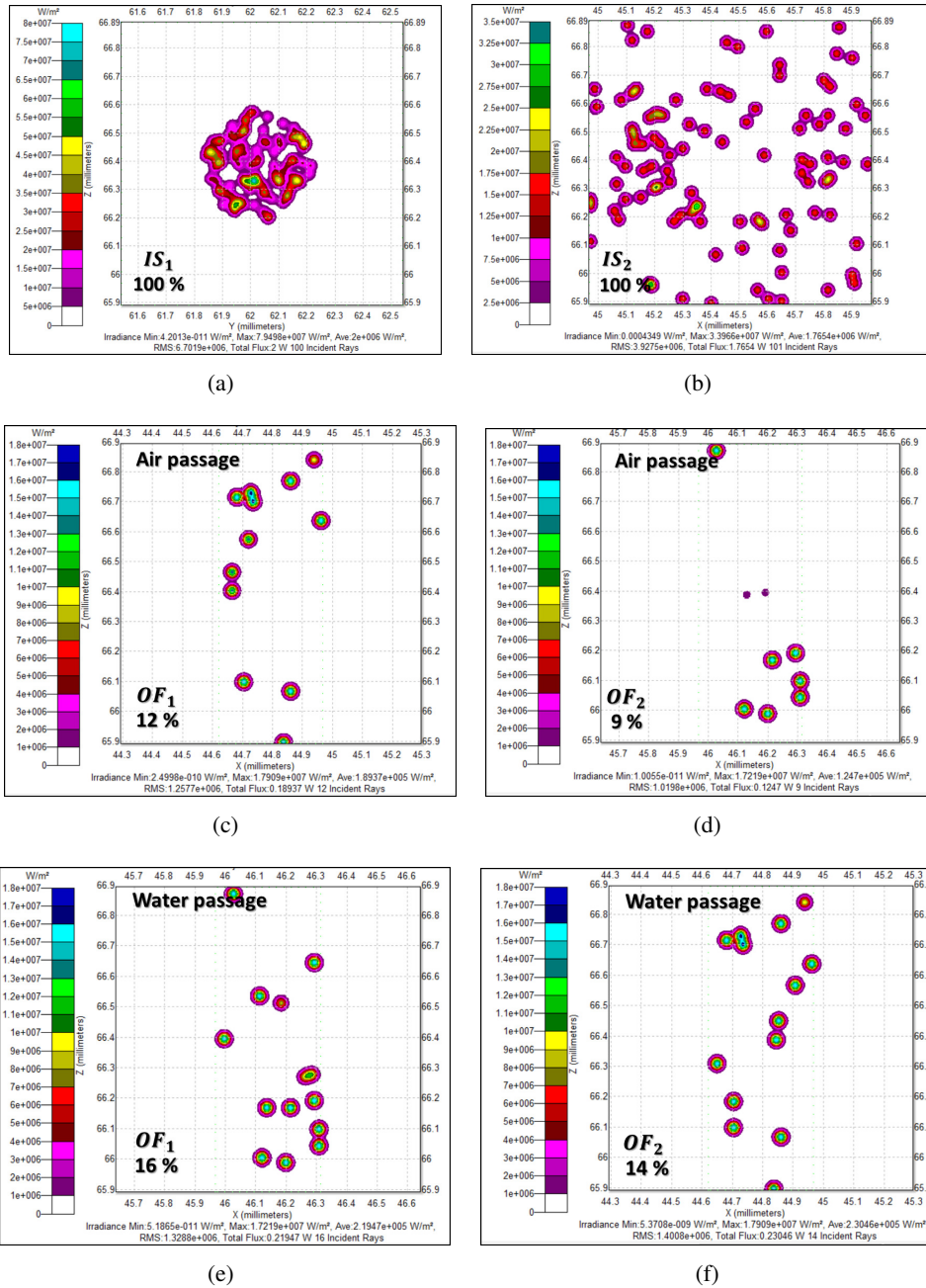
FIGURE 1.14: Radiance maps for the spatial (2D) distribution and the percentage of light rays at the test sections: (a) at the input surface IS_2 of the μSPT, (b) at the output surface IS_2 of the μSPT, (c)-(d) at the two output optical fibers insertions surfaces $\{OF_1$ and $OF_2\}$ when in the micro-channels there is the air passage and (e)-(f) the water passage.
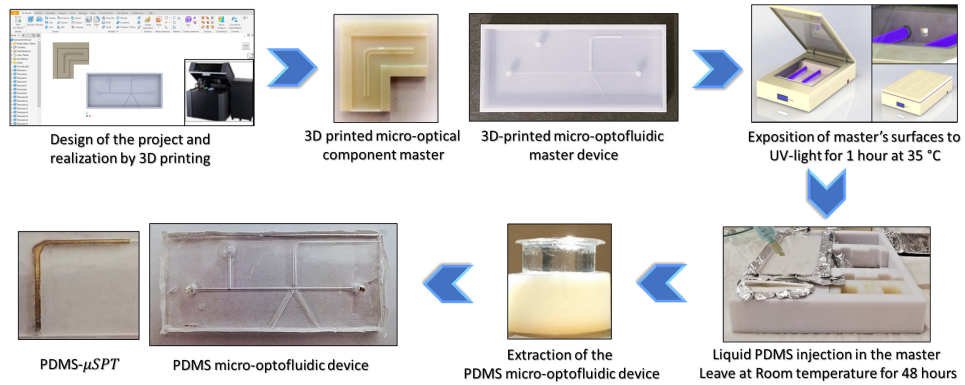
FIGURE 1.15: Master-slave protocol PDMS-based to fabricate the T-junction micro-optofluidic slug velocity detector and the PDMS-μSPT.
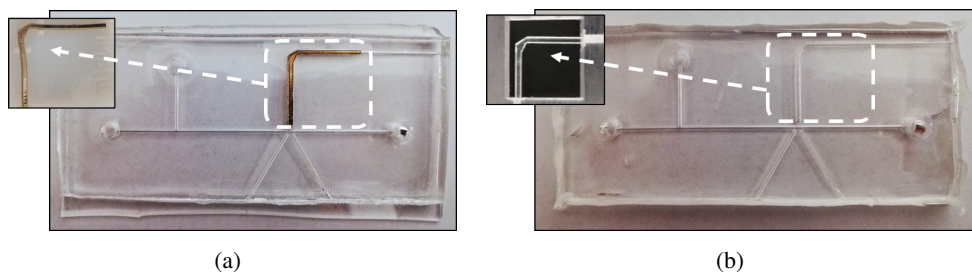
FIGURE 1.16: The complete PDMS T-junction micro-optofluidic slug velocity detector with the allocation area integrating (a) the gold-spattered PDMS-μSPT and (b) the VeroClear-μSPT.

T-junction micro-optofluidic slug velocity detector. Two devices were obtained: the first one including the gold-spattered PDMS-μSPT (see Fig. 1.16 (a)) and the second one the VeroClear-μSPT (see Fig. 1.16 (b)).

1.5 Micro-optofluidic chamber

1.5.1 Working principle and design

The micro-optofluidic chamber exploits the phenomenon of light absorption for the single-phase flow of fluids or the two-phase flow of immiscible fluids.

The aim of the design is the characterization of fluids of various natures and solutions at several concentrations within a chamber at the center of a microfluidic channel with one inlet and one outlet.

In the micro-optofluidic device designed, there is one input optical fiber insertion for the actuation system and two output optical fiber insertions for the detection systems. The operating principle is as follows: through the incoming fiber insertion, a light beam produced by a light source passes through the chamber, filled with the solution under investigation, and the outgoing beams are captured by the outgoing fibers insertions and sent to the detection systems, respectively. The intensity of the outgoing light beams will be lower than that of the incoming light beams due to the absorption of the fluid. In this way, it is possible to characterize the nature of the fluids under examination.

A schematic of the working principle is shown in Fig. 1.17 (a), while the final CAD design of the micro-optofluidic system is presented in Fig. 1.17 (b).

Before reaching the final design shown in Fig. 1.17 (b), several adjustments were made to the chamber dimensions, the size of the input optical fiber insertion and the distance between it and the chamber.

The different geometrical characteristics can affect the performance of the device, and to practically exploit the physical principle, several ray-tracing simulations were performed, which will be presented in the following section.

(a)   (b)
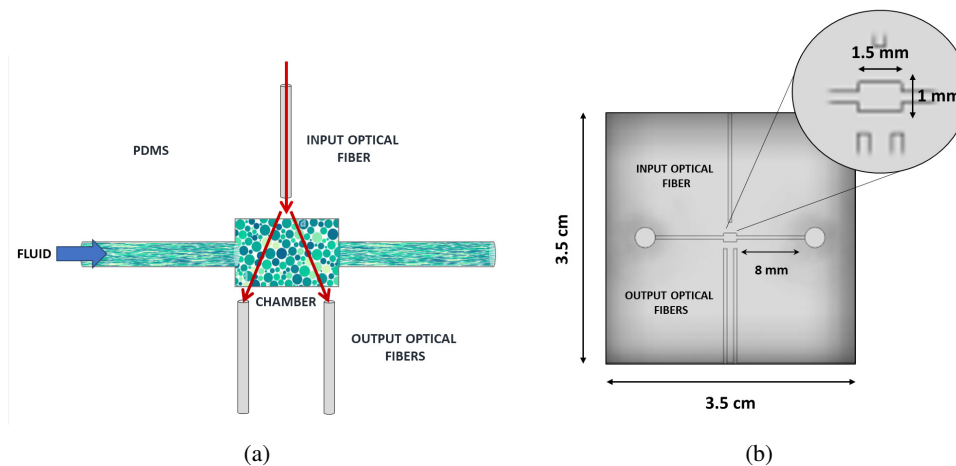
FIGURE 1.17: (a) Working principle of the T-junction micro-optofluidic chamber; (b) CAD representation and measurements in a frontal perspective: the microfluidic chamber with a dimension of 1.5 *mm x* 1 *mm x* 400 *μm*, and the microfluidic channel and fibers insertions with a squared section and a diameter of 400 *μm*.

Ray-Tracing simulations

Three CADs models of the micro-optofluidic chamber device were designed using Autodesk Inventor based on the dimension of the chamber, the diameter of the input
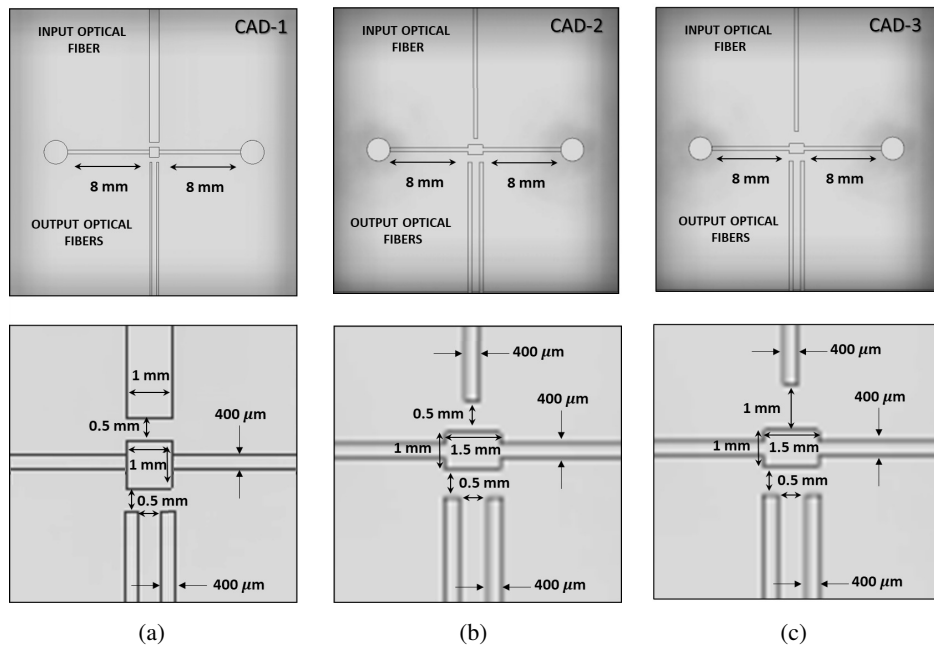
FIGURE 1.18: CADs representation and measurements in a frontal perspective: the microfluidic chamber and fibers insertions for (a) *CAD-1*, (b) *CAD-2* and (c) *CAD-3*.
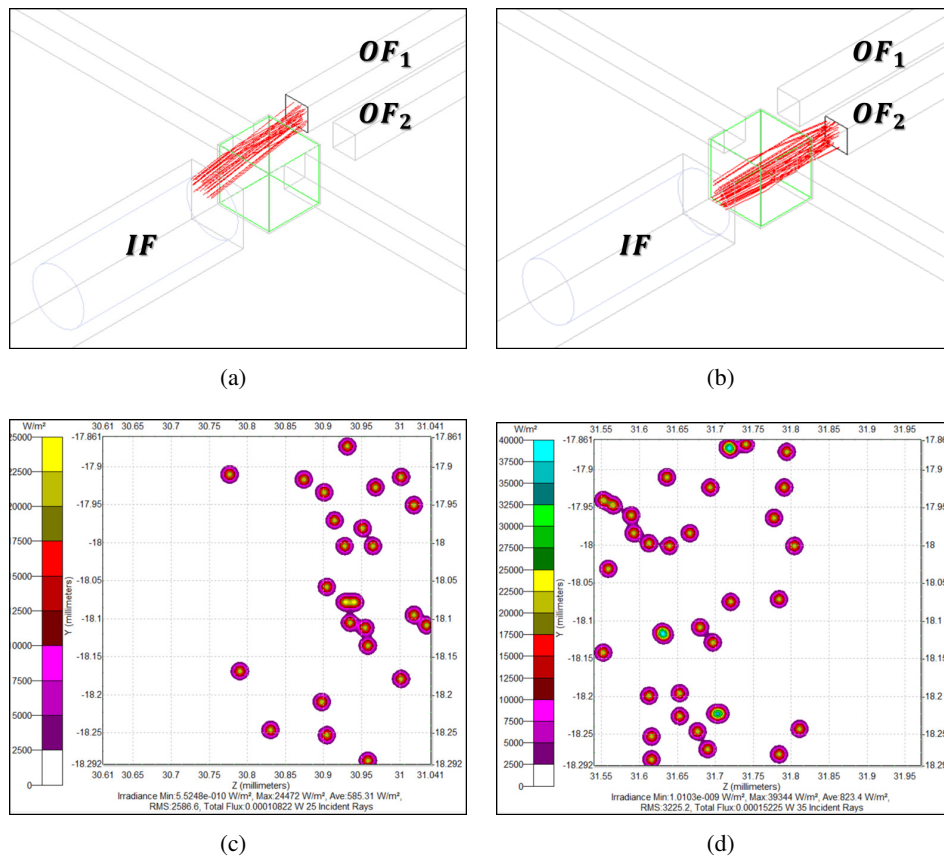
FIGURE 1.19: The ray-tracing results obtained in simulations for *CAD-1* when the channel was filled by water: (a)-(b) plots of the rays paths; (c)-(d) radiance maps for the spatial (2D) distribution and the percentage of light rays at the test sections.

(a)   (b)

(c)   (d)
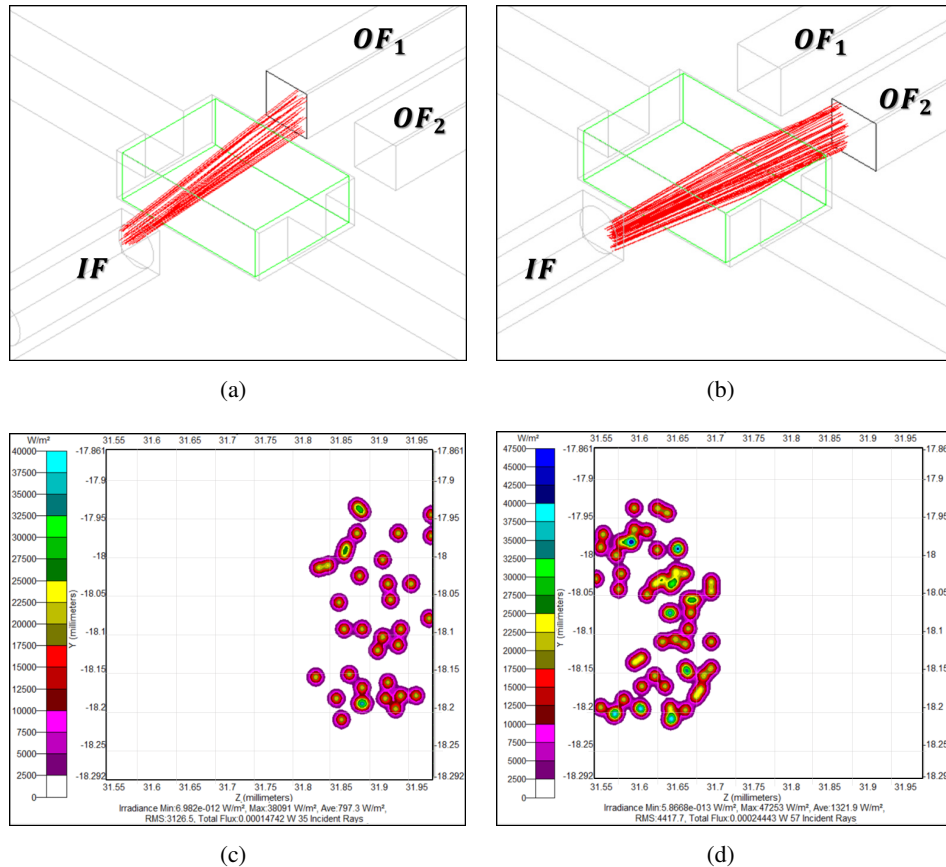
FIGURE 1.20: The ray-tracing results obtained in simulations for *CAD-2* when the channel was filled by water: (a)-(b) plots of the rays paths; (c)-(d) radiance maps for the spatial (2D) distribution of light rays at the test sections.

optical fiber insertion and the distance between this last one and the chamber. All the other dimensions such as the dimension of the micro-channel, the diameter of the output optical fibers insertions and the distance between them and the chamber were maintained constant in the three CADs models.

In Fig. 1.18 the CADs representation and the zooms of the measurements of interest are shown. In *CAD-1* the chamber dimension is 1 *mm* x 1 *mm* x 1 *mm*, the diameter of the input optical fiber insertion is 1 *mm* and the distance between this last one and the chamber is 0.5 *mm*. In *CAD-2* the chamber dimensions were changed in 1 *mm* x 1.5 *mm* x 0.4 *mm*, the diameter of the input optical fiber reduced at 0.4 *mm* and the distance between this last one and the chamber was maintained at 0.5 *mm*. Finally, in *CAD-3* the chamber dimensions were maintained at 1 *mm* x 1.5 *mm* x 0.4 *mm*, the diameter of the input optical fiber at 0.4 *mm* and the distance between this last one and the chamber was increased at 1 *mm* to improve the geometrical performance of the device.

The performance of the device models was evaluated by ray-tracing simulations using the TracePro software (Lambda Research Corporation). The light source, placed at the input optical fiber insertion *IF*, used during the simulations had a light beam of 200 rays and a power of 1 *mW* and it was assumed that the chamber was filled with water.

In Fig. 1.19 (a)-(b) the ray-tracing results obtained in simulations for *CAD-1*, when the light beam is captured from the output optical fiber on the left OF_1 and the light

(a)

(b)

(c)

(d)
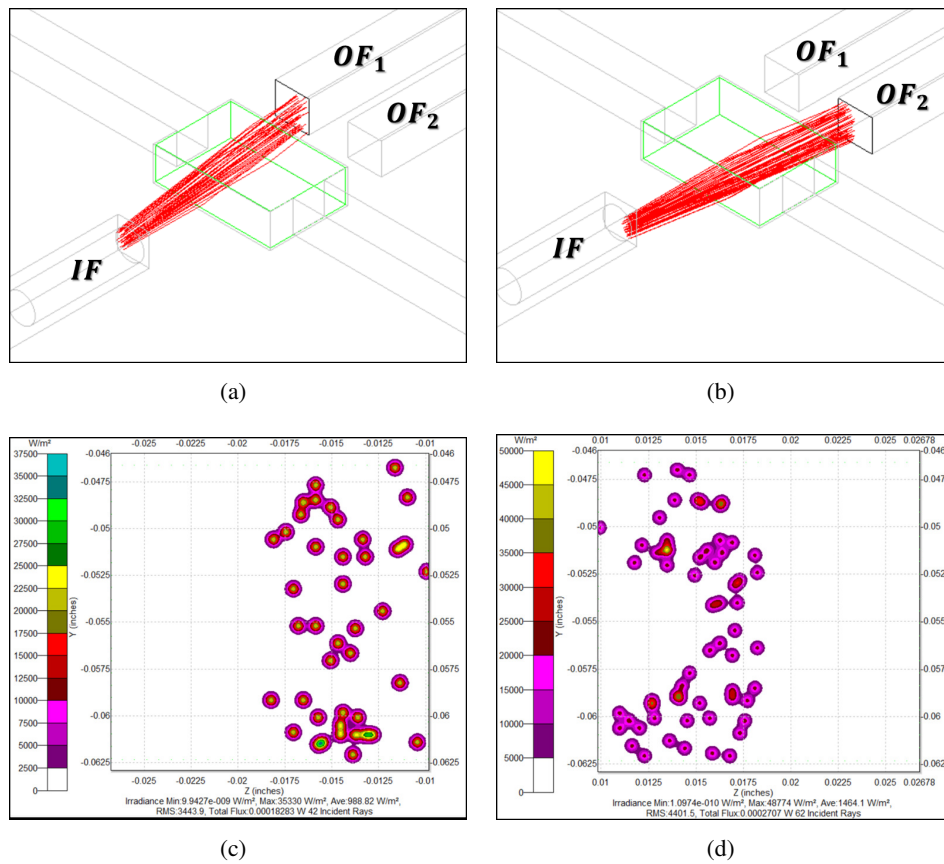
FIGURE 1.21: The ray-tracing results obtained in simulations for *CAD-3* when the channel was filled by water: (a)-(b) plots of the rays paths; (c)-(d) radiance maps for the spatial (2D) distribution of light rays at the test sections.
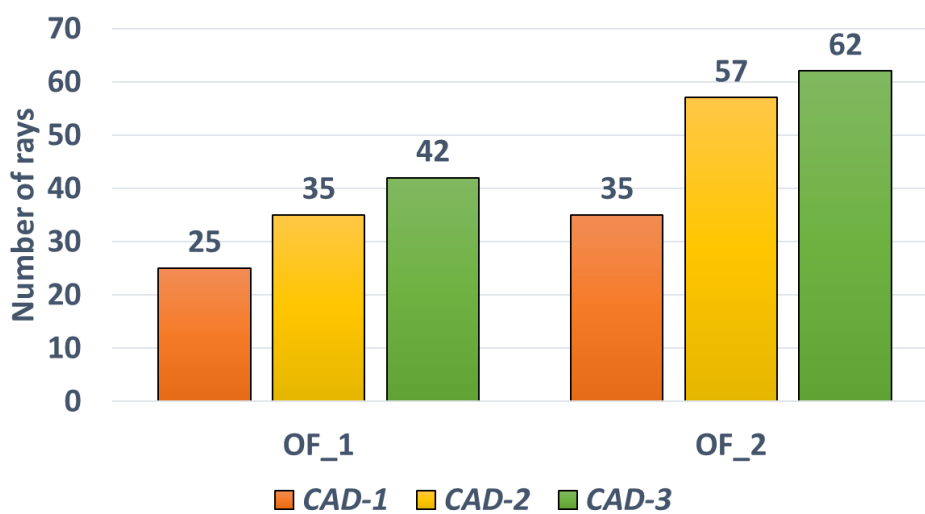
FIGURE 1.22: Comparison of the performance considering the device CADs: *CAD-1*, *CAD-2* and *CAD-3*. The bar plot reports the number of rays incidence on the surfaces of interest at the water passage.

beam captured from the output optical fiber on the right OF_2 are plotted. Additionally, in Fig. 1.19 (c)-(d) the spatial (2D) distributions of the rays at the test sections are shown.

In Fig. 1.20 and Fig. 1.21 the ray-tracing results and the spatial (2D) rays distributions for *CAD-2* and *CAD-3* are reported. By changing the chamber dimensions and the diameter of the input optical fiber insertion from *CAD-1* to *CAD-2*, a slight increase in the number of rays that hits the test sections is evident.

To obtain better performance another change was done in the CAD, increasing the distance between the input optical fiber and the chamber by passing from *CAD-2* to *CAD-3*.

The results showed in Fig. 1.20 and Fig. 1.21, show that a better-improved performance is obtained because the number of incident rays in *CAD-3* is greater than those obtained in *CAD-2*. In addition, the rays are better distributed in the output optical fibers surfaces.

It is evident in all the models that the incident rays are concentrated in the area between the two output optical fibers, but the distance between them cannot be further reduced because this is the minimum distance that can be reached by the 3D printer, so this minimum distance can be assumed as a constructive constraint. The comparison of the CADs' performance is reported in Fig. 1.22. The bar plot is related to the number of rays incidental to the surfaces of interest: the left output optical fiber OF_1 and the right output optical fiber OF_2 during the water passage. The color codes the considered CAD. An increase in performance was evinced by reducing the diameter of the input optical fiber and increasing the distance between this last one and the chamber.

The study carried out was useful to determine the geometric characteristics of the final device presented in 1.17.

1.5.2 Device realization PDMS-based

The micro-optofluidic chamber was realized in PDMS by using a master–slave approach based on the use of inkjet 3D printing techniques. The fabrication process for the realization of the micro-optofluidic device is summarized in Fig. 1.23.
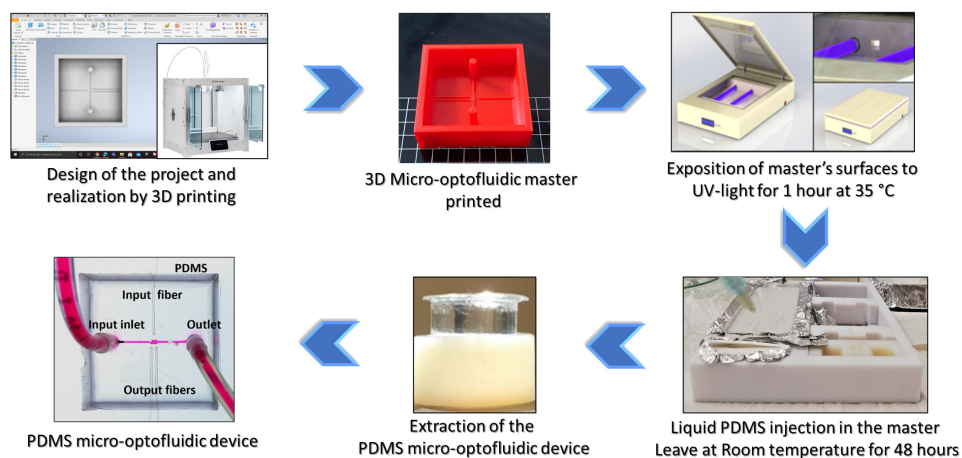
FIGURE 1.23: Master-slave protocol PDMS-based to fabricate the T-junction micro-optofluidic chamber.

After designing the CAD device in Autodesk Inventor, the STL file was generated and processed by using the open-source slicing software Ultimaker Cura to create the G-code. Then, the master was 3D printed by using the FDM 3D printing Ultimaker S5. The print core used, being compatible both with the 3D printing used and the model material selected, was the AA 0.25. Indeed, it is capable of creating very high-quality prints with very minute details, which was essential to realize the micro-channel and the fibers insertions having a size equal to 400 μm. While the print core used for the support materials was AA 0.40.

The master was printed by using the filament Ultimaker PLA – M0751 Red having a diameter equal to 2.85 mm. The filament Ultimaker White, also with a diameter of 2.85 mm, was used as support material. It was selected because it is easy and fast to remove, and it allows to obtain good surface quality for the model once it is removed. Thus, no additional surface post-treatments were required.

Before starting the PDMS casting phase, an important step needs to be performed. To avoid any type of reticulation of the resin in contact with the PDMS, an UV treatment was performed on the master surfaces.

Then, the silicone and the curing agent of PDMS were mixed according to the (10:1) proportion for the device layer and to the (5:1) proportion for the bulk cover layer. After degassing, the PDMS was poured into the master and left for 48 h at room temperature. In the end, the PDMS devices were peeled from the master and the device bound with a 0.5 mm thick bulk by a reversible bonding procedure.

Part I

SYSTEMS AND DEVICES FOR SLUG FLOWS DETECTION AND CONTROL

Chapter 2

T-junction micro-optofluidic slug detector

In this chapter, a portable micro-optofluidic device, the T-junction micro-optofluidic slug detector, presented in Chapter 1.2, was manufactured by using two different 3D printing techniques, the first one is the master–slave approach using the poly-dimethylsiloxane (PDMS) presented in Chapter 1.1.2, while the second one is the Projection Micro Stereolithography (PμSL) technique using the photocurable HTL resin presented in Chapter 1.1.3. Thanks to the proposed fabrication approaches, it is possible to reduce the fabrication costs and maintain a satisfactory building resolution. The proposed novel approaches based on 3D printing technologies and the used materials (PDMS and HTL resin) overcome all these weaknesses to manufacture micro-devices.

The two micro-optofluidic devices, having the same geometry integrating both micro-optical and microfluidic components, have been designed for slug flow detection in micro-channel. The slug process, formed by water and air, inside the micro-channel was monitored optically to evaluate its stability and the fluid interaction with the used materials. The obtained optical signal was correlated to the slug passage and analyzed for flow tracking.

A wide experimental campaign was done in different operative conditions. The information related to the slug passage, extracted from the signals, was considered to characterize the process within the HTL resin device. The stability of the process was investigated by using a replicated general factorial design. This can also identify which is the experimental operative condition for the optimal use of the micro-device. Once the optimal operative condition was selected, a detailed comparison between the slug process detected inside the HTL resin device and the PDMS device was carried out to evaluate the pros and cons of using different materials and fabrication techniques. The two materials used for the devices' manufacturing, i.e. PDMS and the HTL resin, respectively, were then analyzed in terms of their surface's roughness and water angle contact to fully understand the hydrodynamic differences detected within the two micro-channels.

2.1 Methods for devices surface characterization

Two surface characterization techniques were used: Atomic Force Microscopy (AFM, NTEGRA, NT-MDT, Zelenograd, Russia) to characterize the surface's roughness [45] and static water angle to measure hydrophilicity.

The AFM test was run in semi-contact mode, with a rate equal to 0.5 Hz, and by using a tip ETALON series (NT-MDT, Zelenograd, Russia) characterized by a resonant frequency of 140 ± 10 % kHz. The software used to measure the surface roughness in AFM figure is Image Analysis of Nova Px. In the AFM analysis, a 5x5 μm^2 area was investigated. For each analysis, three parameters were evaluated, which are the roughness distribution in the square surface (RMS), average roughness (RA), and the peak-to-peak parameter. All the surfaces characterized were obtained from the processing methods reported above without any further treatment.

Static water contact angles (Θ) measurements were run to evaluate the surface hydrophilicity of the two materials used. A Lite Optical Tensiometer TL100 with an accuracy of $\pm 3°$, at room temperature and in air atmosphere was used for the experiments. The test was carried out as follows: first, 5 μl of Milli-Q water drop, having a resistivity equal to 18.2 $M\Omega$ at $25°C$, was deposited on the device's surface with a calibrated micro-syringe; next, measurements of Θ were made on both sides of the two-dimensional projection of the droplet. Five different sets of measurements have been performed on different surface portions of every sample to obtain statistically reliable results.

In order to assess the optical properties of the two materials investigated for the realization of the micro-optofluidic devices, a transmission analysis was carried out using a spectrometer (USB2000, Ocean Optics, Dunedin, Florida). The Ocean Optics Transmission Probe (T200-RT-VIS-NIR, Ocean Optics, Dunedin, Florida) is connected to a halogen light source (LS-1, Ocean Optics, Dunedin, Florida) and to the spectrometer. The probe has two fibers with a diameter of about 200 μm, one illuminates the sample and the other one allows the operation of reading. The transmission is the percentage of energy passing through a system relative to the amount that passes through a reference. In the analysis, the reference sample of Polytetrafluoroethylene (PTFE) was considered in order to calibrate the instrument at a transmission value of 100 %. After the operation of calibration, the measurements were taken from the two materials.

2.1.1 PDMS and HTL resin surface analysis

For many applications in microfluidic technology, the behavior at the solid-liquid interface is of prime importance. For example, changes in the fluid wetting ability may affect the exchanged momentum of the fluid with the solid surface at the atomic scale, resulting in a velocity slip at the solid wall. Thus, considering that water is the main flowing fluid, it is important to measure the solid surfaces' behavior.

To be more specific, hydrophilic surfaces are more attractive toward water since, being they bear electric charges or polar groups, water molecules interact favorably with them. Instead, hydrophobic surfaces are water unattractive because, being non-polar, they cause water molecules to lack hydrogen bonding partners [46], [47].

Moreover, the flow characteristics in micro-channels may be different from the classical theory for macro-channels. Many experimental and numerical results demonstrated that the friction factor is much higher in micro-channels than in macro-ones [48]. In this context, the surface roughness is of fundamental importance for the understanding of these deviations, since by reducing the channel dimensions, the
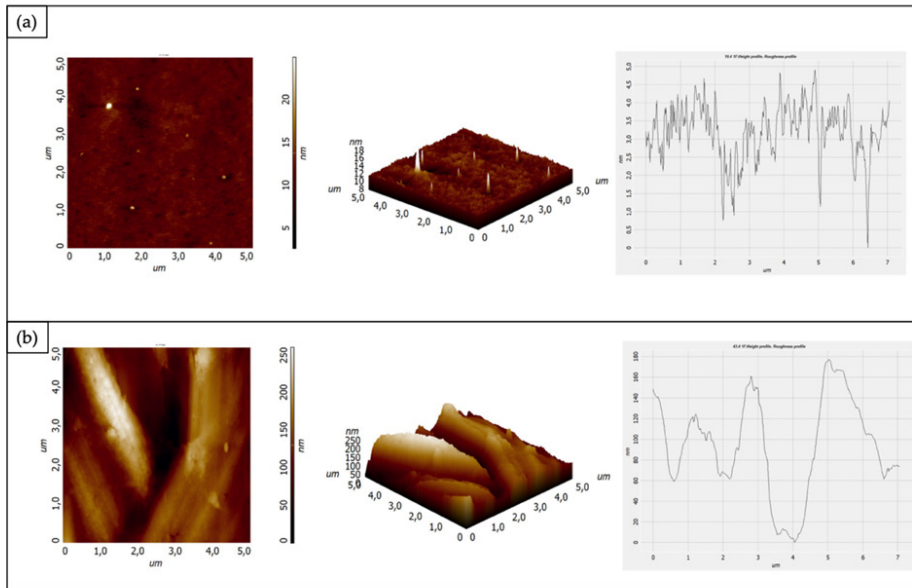
FIGURE 2.1: Roughness measurements of (a) PDMS and (b) HTL resin surface.

Material investigated	RMS [*nm*]	RA [*nm*]	Peak to peak [*nm*]
PDMS	1.097	0.763	35.158
HTL resin	47.056	37.324	259.121

TABLE 2.1: AFM analysis results for PDMS and HTL photocurable resin.

roughness importance increases. For all these reasons, both the static water contact angle and surface roughness must be evaluated to gain a complete understanding of the hydrodynamic nature of the two-phase fluid into the micro-channels of the two studied devices.

The surface roughness of the PDMS and HTL resin was evaluated using Atomic Force Microscopy (AFM). In AFM, the probe tip is fixed to a cantilever beam. The probe interacts with the surface and the resulting force deflects the beam in a repulsive manner, as described by Hooke's Law. In the same manner that spring changes dimensions under the influence of forces, the attractive and repulsive forces between atoms of the probe and the surface can also be monitored when brought extremely close to each other.

Hence, the net forces acting on the probe tip deflect the cantilever, and the tip displacement is proportional to the force between the surface and the tip. As the probe tip is scanned across the surface, a laser beam reflects off the cantilever. By monitoring the net (x, y, and z) deflection of the cantilever, a three-dimensional image of the surface is constructed [49]. The obtained results from AFM analysis are shown in Fig. 2.1 (a) for the PDMS and in Fig. 2.1 for the HTL resin.

The surface roughness of the HTL resin is higher than the PDMS ones (Table 2.1), in fact, both the RMS and the RA parameters evaluated for the HTL resin are 97% higher than the PDMS ones.

Moreover, according to the results, while for the HTL resin a thick web of filaments was spotted on the surface, the PDMS one appeared strongly flatter. While for PDMS the analysis revealed the presence of some scattered nanometric bubbles which can

Material investigated	CA [°]
PDMS	111.84
HTL resin	64.36

TABLE 2.2: Contact angle measurement results for PDMS and HTL photocurable resin.

originate from entrapped air or residual solvent.

The PDMS surface roughness analyzed with the AFM is the surface in contact with the 3D-printed mold. In literature, the PDMS surface roughness values obtained for many 3D-printed microfluidic devices are of the order of about ~ 2 μm [50], [51]. A UV gel smoothing technique allowed a change in the surface roughness from 70 nm to 3 nm [52].

In this work, a UV treatment was applied to the 3D master achieving a PDMS surface roughness of 1 nm. The relative roughness of the microfluidic channels can be measured as the ratio between the RA parameter and the side of the channel (this being a square section). This parameter can be used to evaluate the flow stability in the micro-channel.

For the studied surfaces the relative roughness was equal to 0.0001% and 0.0002% for PDMS and HTL resin, respectively. In other papers, relative roughness values of the order of magnitude of the micrometer were reported showing, for the devices, an increase of 8-38% for the fiction factors over the classical theory [53], [54]. Therefore, the values measured here let to conclude that there will be no instability of the flow inside the channel, i.e. flow slowdown or inhibition, for the manufactured devices. These measurements showed that both the manufacturing techniques used can guarantee a stable flow inside the micro-channel.

The water angle contact measurements are shown in Table 2.2. The contact angle for the PDMS was equal to 111.84°, while the HTL resin presented a value of 64.36°.

The micro-optofluidic devices have been tested by using an aqueous two-phase system. In some previous studies high water angle contacts showed advantageous results because when the aqueous droplets encounter a wall, they bounce off instead of sticking [55]. In other studies, low water contact angles resulted in some flow complications due to the adhesion of water droplets to the wall [56], [57]. In order to unveil issues with flow advancement and process stability within the channel, the slug flow detection for the two micro-optofluidic devices was studied as reported in the following sections.
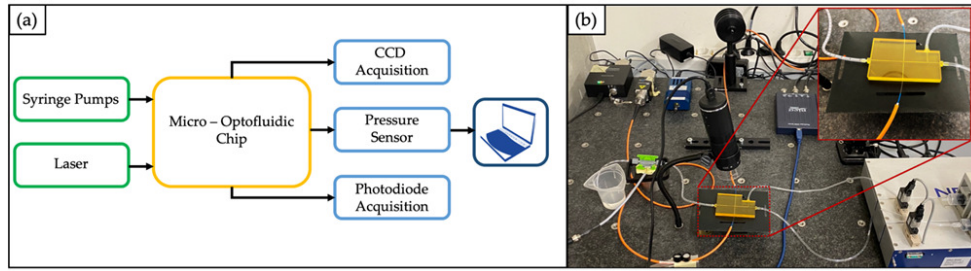
FIGURE 2.2: Experimental set-up: (a) block scheme; (b) real picture with the micro-optofluidic slug detector HTL-resin based.

2.2 Experimental set-up

The slug flow through the micro-optofluidic devices has been obtained by simultaneously pumping deionized water and air through the two inlets and the T-junction geometry. In fact, the two inlets have been connected to two different syringe pumps (neMESYS low-pressure module, Cetoni GmbH, Korbussen, Germany), which have been filled with de-ionized water and air, respectively. The constant flow rate has been varied at three levels: $\{0.1, 0.2, 0.3\} ml/min$.

A laser system (NovaPro 660-125, RGB Lasersystems, Kelheim, Germany) with an emission wavelength equal to 600 nm and an output power ranging between 1 mW and 5 mW has been used as the light source aimed at detecting two-phase flows.

Finally, to test the designed micro-optofluidic devices three different measurement systems have been considered:

- a photodiode (PDA100A, Thorlabs, Newton, NJ, USA) with a gain range between 30 *dB* and 40 *dB*, measuring the light intensity variation, connected to a PC oscilloscope (Picoscope 2204A, Pico Technology, Cambridgeshire, UK) with a sampling frequency of 1.5 *kHz*;

- a digital USB microscope placed above the optical acquisition section, that allowed the interactions between the main microfluidic channel and the light transmission to be monitored;

- a pressure sensor (SLF3S-1300F, Sensirion, Stäfa, Switzerland), having a sampling frequency equal to 200 *Hz*, monitoring the stability of the upstream fluid flow rate externally to the channel.

A block scheme and a real picture of the experimental set-up used with both the devices for the slug flow detection are shown, respectively, in Fig. 2.2 (a) and Fig. 2.2 (b).

2.3 Signals acquisition and processing

The acquired signals by the photodiode are a square wave. This behavior is justified by the different refractive index that characterizes the two fluids generating the tested two-phase flow: the refractive indices for the air and the water are respectively equal to $n_{Air} = 1$ and $n_{Water} = 1.3$.

Under these conditions, the higher level of the square wave signal corresponds to the water slug, while the lower level corresponds to the air slug. Each transition from the high to the low level of the square wave is characterized by the presence of signal
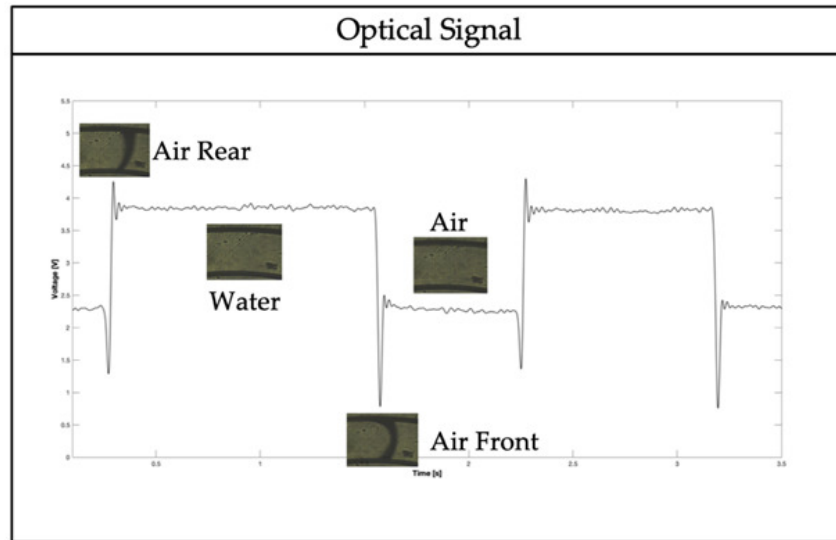
FIGURE 2.3: Optical acquired signal interpretation by acquired CCD video frames.

peaks depending on the transitory phase between the two fluid fronts. The signal detected by the photodiode is shown in Fig. 2.3.

The optical signals need signal smoothing. The signal post-processing was carried out using a Matlab (MathWorks) routine. After the acquisition phase, a low-pass filter with a 40 Hz cut-off frequency has been applied to saturate the signals, thus eliminating high-frequency components. Then, a smoothing procedure has been run to generate perfect square wave signals. By overlying the square wave to the saturated signals, it has been possible to identify the time frames corresponding to the air detection (T_a), and the time frames corresponding to the water detection (T_w) by the device.

In addition, to evaluate the mean period associated with a complete air-water slug passage the optical signal has been analyzed in the frequency domain. In fact, by obtaining the frequency spectrum, at first, it was possible to determine the frequency peak (f_{ph}), and then it was possible to determine the mean period T_{ph} by calculating the reciprocal of this parameter.

2.4 Results and discussion

2.4.1 Set-up optimization for the slug flow stability in the HTL resin Device

To optimize the slug flow detection set-up for the micro-optofluidic slug detector HTL resin-based a replicated general factorial design was carried out.

Two design factors (independent variables) have been considered for the test procedure: the laser input power (factor A) and the fluid flow rate (factor B). While factor A was varied at two levels (a = 2), factor B was varied at three levels (b = 3). The a = 2 levels correspond to 1mW and 5mW, respectively. The b = 3 levels correspond to $\{0.1, 0.2, 0.3\} ml/min$. The number of replications has been set equal to n = 3, for a total of $N = abn = 18$ experimental runs. The experimental plan is summarized in Table 2.3.
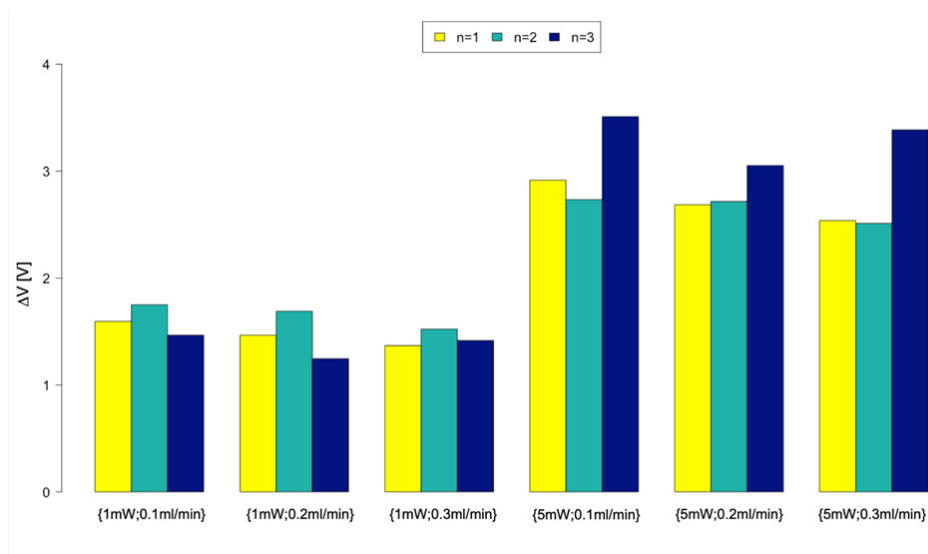
FIGURE 2.4: Bar plot showing the voltage difference (ΔV), for each investigated scenario and replication. Bar errors have not been added because they were strongly narrower than the bars' height.
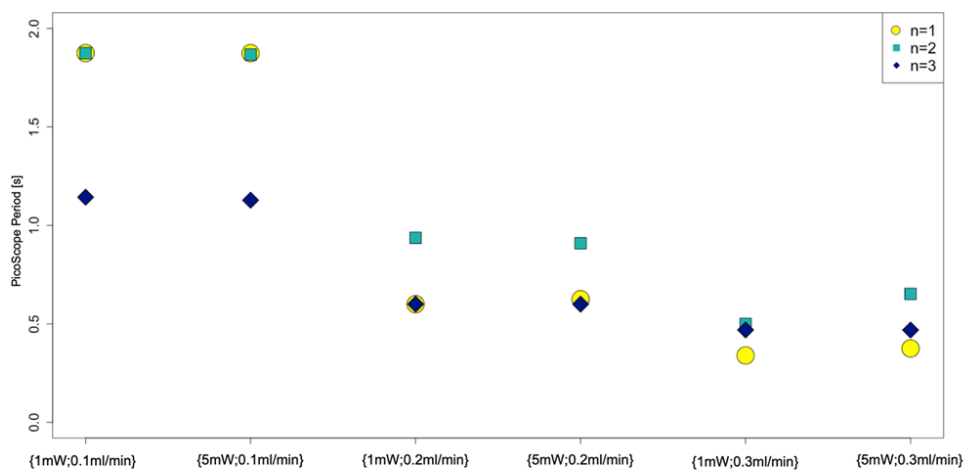
FIGURE 2.5: Trend related to the mean period (T_{ph}) associated with a complete air-water slug passage for each investigated scenario and replication. n = 1, 2, 3 refer to the three-run replications.

Factor	Symbol	Unit	Low level (−1)	Center level (0)	High level (+1)
Laser input power	A	$[mW]$	1	-	5
Flow rate	B	$[ml/min]$	0.1	0.2	0.3

TABLE 2.3: Experimental plan: factors and levels.

Next, the following responses (dependent variables) have been considered for the experimental plan:

- the voltage difference (ΔV), defined as the difference between the grand averages of the observations measured at the high and the low level of the square wave optical signal, respectively. The calculation of the voltage difference (ΔV) is as follows. By starting from the optical signal acquisition for a period of 15 s, the signal is post–processed as previously described. Next, in each acquired and post–processed optical signal the sequence of high-level values in the wave square is collected in time order, thus getting a single sample of $V_h(i)$ observations, for $i = 1, \ldots, N_h$. The same procedure is performed for the low levels of the square wave, thus obtaining a single sample of $V_l(i)$ observations, for $i = 1, \ldots, N_l$. Here $N_h \in (2, 5 \cdot 0^3, 10^4)$ and $N_l \in (2, 5 \cdot 10^3, 10^4)$. Next, the corresponding sample mean values ($\bar{X}_h$ and $\bar{X}_l$) and sample standard deviations (s_h and s_l) are evaluated for each sample $V_h(i)$ and $V_l(i)$, respectively. Having both $V_h(i)$ and $V_l(i)$ a very large number of observations, both their sample means ($\bar{V}_h$ and $\bar{V}_l$) are approximately normally distributed random variables with estimated parameters:

$$\begin{cases} \bar{V}_h \sim N\left(\bar{X}_h, \frac{s_h^2}{N_h}\right) \\ \bar{V}_l \sim N\left(\bar{X}_l, \frac{s_l^2}{N_l}\right) \end{cases} \tag{2.1}$$

Starting from this assumption, the response ΔV is a normal random variable having distribution:

$$\Delta V = \bar{V}_h - \bar{V}_l \sim N\left(\bar{X}_h - \bar{X}_l, \frac{s_h^2}{N_h} + \frac{s_l^2}{N_l}\right) \tag{2.2}$$

- The second investigated response is the mean period (T_{ph}) associated to a complete air-water slug passage, obtained as the reciprocal of the frequency peak gained from the amplitude spectrum of the acquired optical signal:

$$T_{ph} = \frac{1}{f_{ph}} = <T_w> + <T_a> \tag{2.3}$$

In particular, the first response ΔV is considered to show that the optical part of the device is really able to discriminate between the two fluids that make up the slug flow. While the second response T_{ph} is taken into account to evaluate if real hydrodynamic stability is achieved in the micro-channel.

Once the response observations have been calculated, an Analysis of Variance (ANOVA) study has been performed to investigate the statistical significance of each factor and its interaction. The observations regarding the first response, for all the investigated scenarios and all the run replications, are summarized in Table 2.4. While the ANOVA table for the ΔV response and a bar plot comparing the various cases are shown in Table 2.5 and Fig. 2.4, respectively.

Flow rate	[*ml/min*]	**0.1**	**0.2**	**0.3**
Input	1	(1.59, 1.75, 1.47)	(1.47, 1.69, 1.25)	(1.37, 1.52, 1.42)
Power				
[mW]	5	(2.92, 2.73, 3.51)	(2.69, 2.72, 3.05)	(2.54, 2.51, 3.39)

TABLE 2.4: Observations ΔV [V] for the investigated scenarios in the micro-optofluidic slug detector HTL resin-based. Factors: Input Power (P) and Flow Rate (FR). P = $\{1,5\}mW$; FR = $\{0.1, 0.2, 0.3\}ml/min$.

	Sum of squares	**df**	**Mean square**	**F value**	**p-value**
Model	8.854417	2	4.427208	60.70683	<0.0001
A-*input power*	8.72826	1	8.72826	119.6838	<0.0001
B-*flow rate*	0.126157	1	0.126157	1.729892	0.2082
Residual	1.093915	15	0.072928		
Lack of fit	0.035664	3	0.011888	0.134802	0.9374
Pure error	1.058252	12	0.088188		
Cor total	9.948332	17			
R-squared	0.8900				
Adj R-squared	0.8754				

TABLE 2.5: ANOVA table for the response voltage difference (ΔV).

From the ANOVA study shown in Table 2.5, the laser input power (factor A) is the only influential factor (p-value < 0.001) on voltage difference. Both the R-squared and the adjusted R-squared have high values ($R^2 = 0.89$, $R^2_{adj} = 0.87$), thus most of the variability in the observations is explained by the laser input power. From the model adequacy checking on the residuals, no anomalies were identified. A deeper investigation of the obtained results show that by increasing the input power of the laser, the gap existing between the averages at the high and low levels of the square wave optical signal almost doubles. This results in a higher discrimination power of the micro-optofluidic slug detector HTL resin-based between air and water.

However, increasing the input power leads to a slightly higher dispersion in the observations. When the laser power is at a low level, the discrimination power is still sufficient. Therefore, it is convenient to design a higher laser input power for all those scenarios where the difference between the refractive indices of the two investigated fluids is narrow.

The observations obtained for the mean period (T_{ph}) are summarized in Table 2.6 and shown in Fig. 2.5. The results of the ANOVA study are shown in Table 2.7.

The flow rate (factor B) is the only statistically influencing factor on the mean period, as shown in the ANOVA study (Table 2.7). Although the parameter laser input power (factor A) is clearly not influential ($p-value > 0.001$) on the mean period, it has been considered in the study to account for the possibility that at higher power

Flow rate	[*ml/min*]	**0.1**	**0.2**	**0.3**
Input	1	(1.88, 1.87, 1.14)	(0.60, 0.94, 0.60)	(0.37, 0.50, 0.47)
Power				
[mW]	5	(1.87, 1.87, 1.13)	(0.63, 0.91, 0.60)	(0.37, 0.65, 0.47)

TABLE 2.6: T_{ph} observations for the investigated scenarios in the micro-optofluidic slug detector HTL resin-based. Factors: Input Power (P) and Flow Rate (FR). P = $\{1,5\}mW$; FR = $\{0.1, 0.2, 0.3\}ml/min$.

	Sum of squares	df	Mean square	F value	p-value
Model	4.001519	2	2.00076	21.92583	<0.0001
A-*input power*	0.000931	1	0.000931	0.010199	0.9209
B-*flow rate*	4.000589	1	4.000589	43.84147	<0.0001
Residual	1.368769	15	0.091251		
Lack of fit	0.458317	3	0.152772	2.013578	0.1658
Pure error	0.910452	12	0.075871		
Cor total	5.370288	17			
R-squared	0.7451				
Adj R-squared	0.7111				

TABLE 2.7: ANOVA table for the response mean period (T_{ph}).

values, the fluid would be heated more, with a consequent lower viscosity value and a higher fluid velocity. No anomalies have been found from the model adequacy checking on the residuals. Both the R-squared and the adjusted R-squared have quite high values ($R^2 = 0.75$, $R^2_{adj} = 0.71$).

The flow stability is significantly improved at higher values of the flow rate, thus suggesting designing a flow rate equal to 0.3 ml/min. Summarizing the results obtained from the two responses, it is reasonably legitimate to assume that a good test configuration for the micro–optofluidic slug detector HTL resin-based should consider (P, FR) = (5 mW, 0.3 ml/min).

The optical signals and the corresponding amplitude spectrums related to the optimal operative condition are shown in Fig. 2.6 and 2.7 for both the investigated devices. Looking at them, it is possible to discriminate each fluid of the two–phase flow. Even though the discrimination between air and water is always possible, not always the maximum and minimum levels of the square wave optical signals are at the same level by repeating the signal acquisition under the same conditions.

This phenomenon can be attributed to centering problems between the two optical fibers (input and output) since, once inserted in the appropriate device's slots, a little mechanical backlash occurs. Nevertheless, what matters most is that, by focusing on the first investigated response (i.e. voltage difference ΔV), it was spotted reasonable repeatability at the same process condition for all the replications run.

2.4.2 Comparative analysis between PDMS and HTL resin devices

Once the optimal operative condition was identified for the micro-optofluidic slug detector HTL resin-based, a comparison was carried out with the micro-optofluidic slug detector PDMS-based. The aim is to identify the most performing device and the one affected by the lower repeatability error. The comparison between the two devices was carried out for all the investigated responses.

The chosen test set-up for the comparison was (P, FR) = (5 mW, 0.3 ml/min). This decision is justified by the fact that setting the flow rate equal to 0.3 ml/min showed to be the best operative condition for improving the flow stability while choosing the laser power equal to 5 mW allowed to have the highest discrimination between air and water levels.

The results relating to the voltage difference (ΔV) are summarized in Tab. 2.8 and in Fig. 2.8. The ΔV parameter is always higher for the micro-optofluidic slug detector PDMS-based, labeled as *PDMS device*, having an average value equal to 7.94 V, compared to the micro-optofluidic slug detector HTL resin-based, labeled as *HTL resin device*, which has a mean value equal to 2.81 V.
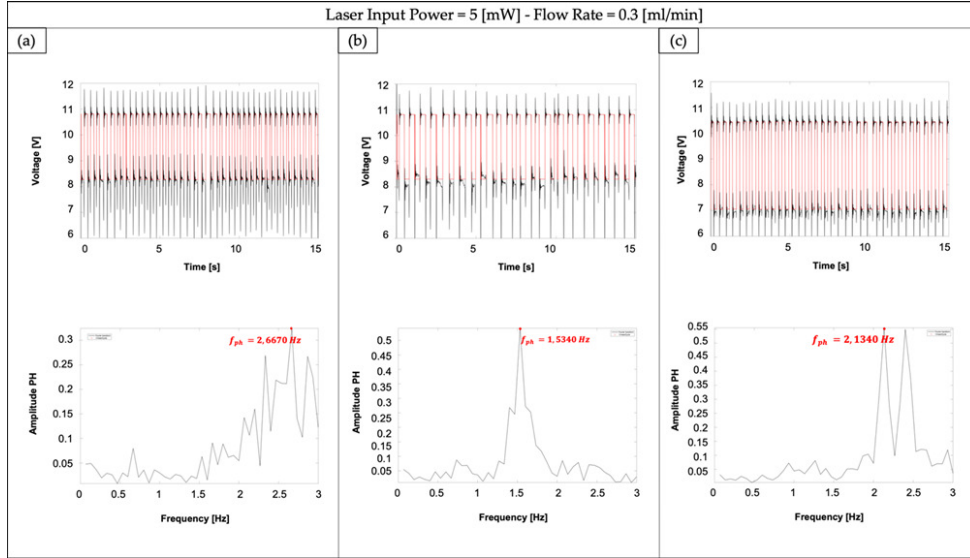
FIGURE 2.6: Optical signals for the micro-optofluidic slug detector HTL resin-based in the time domain (upper row) with (P, FR) = (5 mW, 0.3 ml/min) and optical signals (lower row) in the frequency domain with (P, FR) = (5 mW, 0.3 ml/min) for each replication: (a) n = 1, (b) n = 2 and (c) n = 3. The three identified peaks are necessary to evaluate the mean period (T_{ph}) associated with a complete air-water slug passage.
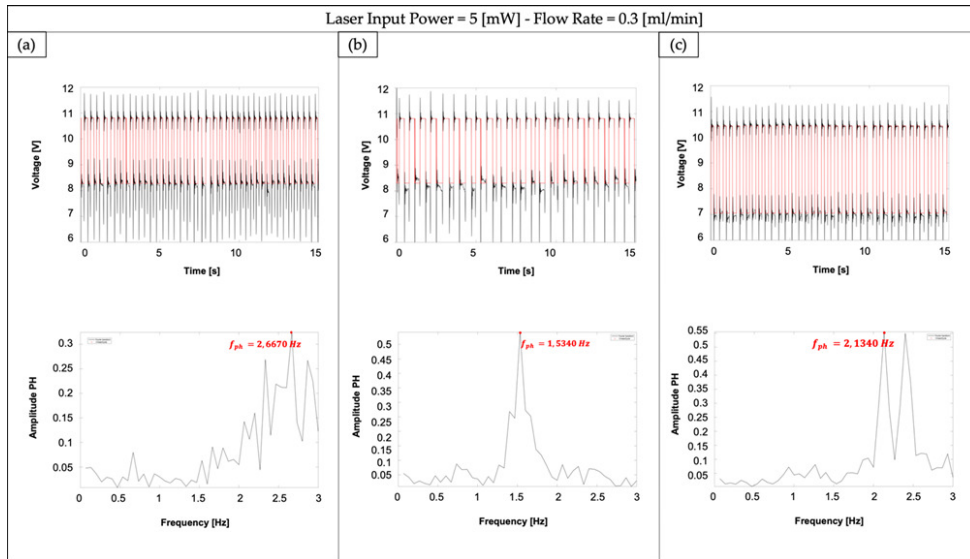
FIGURE 2.7: Optical signals for the micro-optofluidic slug detector PDMS-based in the time domain (upper row) with (P, FR) = (5 mW, 0.3 ml/min) and optical signals (lower row) in the frequency domain with (P, FR) = (5 mW, 0.3 ml/min) for each replication: (a) n = 1, (b) n = 2 and (c) n = 3. The three identified peaks are necessary to evaluate the mean period (T_{ph}) associated with a complete air-water slug passage.

			n = 1	n = 2	n = 3
ID	**Flow rate**	**Input power**	ΔV	ΔV	ΔV
[-]	**[ml/min]**	**[mW]**	$[V]$	$[V]$	$[V]$
PDMS device	0.3	5	7.80	6.29	9.73
HTL resin device	0.3	5	2.54	2.51	3.39

TABLE 2.8: A comparison between the PDMS device and the HTL resin device regarding the voltage difference (ΔV).
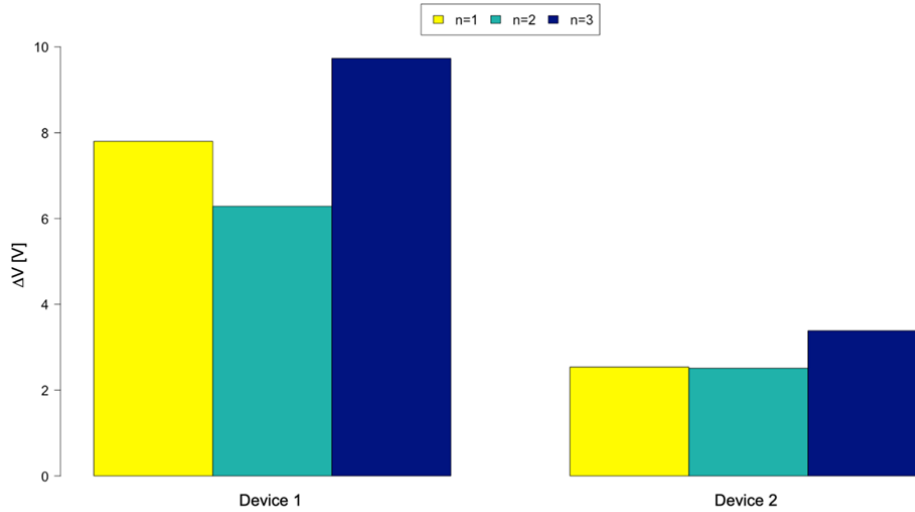
FIGURE 2.8: Bar plot comparing the PDMS device and the HTL resin device with respect to the first investigated response, i.e. the Voltage Difference (ΔV), for each replication. Bar errors have not been added because they were strongly narrower than the bars' height.

This result means that PDMS device better discriminates the two investigated fluids, since the gap between the high and the low level of the square wave optical signal is larger. This result is justifiable by the fact that the PDMS is fully transparent, while the HTL resin is not, as shown in Fig. 2.9. In order to assess the optical properties of the two materials investigated, a transmission analysis was carried out using a spectrometer (USB2000, Ocean Optics, Dunedin, Florida).

Considering a reference sample with 100% of transmission, a value of 126% was obtained for the PDMS and 17% for the HTL resin. This result states a difference in transparency between the two materials and it can be also seen in Fig. 2.9 where the fibers' insertions and the channel are clearly visible in the PDMS device in contrast to the HTL resin device. However, the dispersion of observations collected by using the HTL resin device ($\sigma = 0.50$) is much smaller than the PDMS device ($\sigma = 1.72$). This result can be explained by considering that, while the HTL resin device is manufactured with a high stiffness resin having Young's Modulus value equal to 1.32 MPa, the PDMS device is made of a flexible material which is characterized by a Young's Modulus of 3.9 MPa. Thus, the use of the PDMS device can lead to difficulties in centering the two optical fibers with a greater probability. Because, as soon as the optical fibers are inserted into the predisposed area (having a length of about 23 mm), they tend to flex the device in an easier way for PDMS material than HTL resin. For this reason, the alignment can lead to difficulties in centering the two optical fibers resulting in higher variations in the measurements obtained.

Once again, consistent with what has been said so far, the same reasoning can be made for the second investigated response, i.e. the mean period T_{ph}. In fact, accordingly, to the results summarized in Tab. 2.9 and shown in Fig. 2.10, the observed data for the PDMS device present a higher dispersion than the HTL resin device. Thus, the HTL resin device shows greater flow stability than the PDMS device. Even though the PDMS surface properties related to the angle of contact measurements should have allowed for a faster slug flow than the HTL resin device, being the PDMS surface hydrophobic and the HTL resin one hydrophilic, an opposite trend was shown by the experimental results obtained for the mean period T_{ph}.
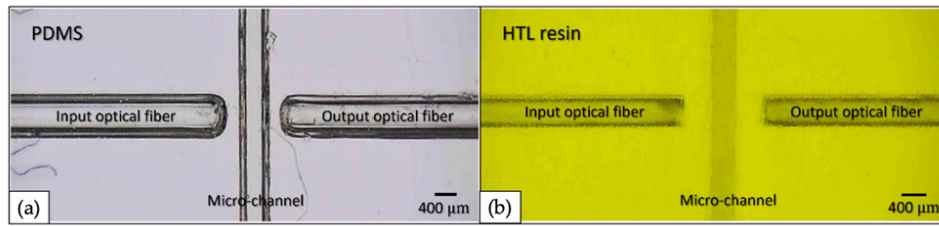
FIGURE 2.9: The images of (a) the PDMS device and (b) the HTL resin device showing the area, including the micro-channel and the inserted and aligned optical fibers, dedicated for the monitoring of the slug flow process.
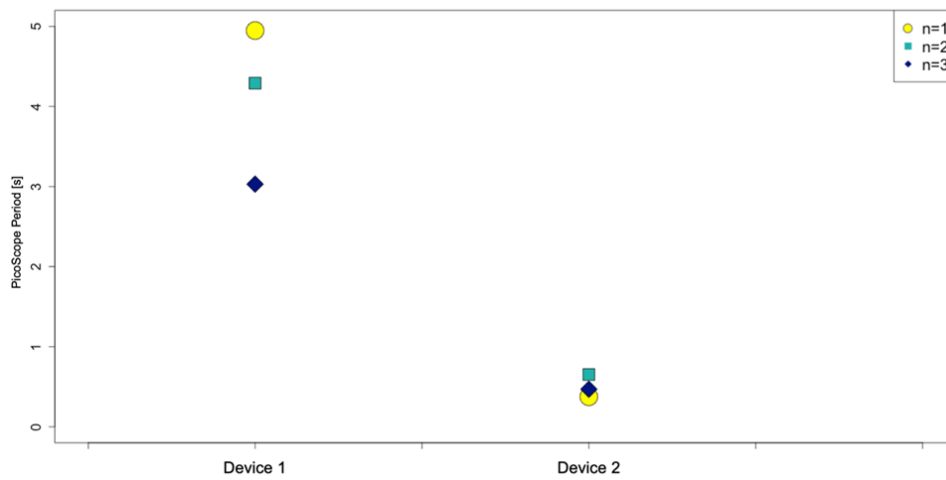
FIGURE 2.10: Comparison of the trend related to the mean period (T_{ph}) associated with a complete air-water slug passage between the PDMS device and the HTL resin device.

			n = 1	n = 2	n = 3	
ID	**Flow rate**	**Input power**	T_{ph}	T_{ph}	T_{ph}	**Mean**
[-]	**[ml/min]**	**[mW]**	$[s]$	$[s]$	$[s]$	$[s]$
PDMS device	0.3	5	4.95	4.29	3.03	4.09
HTL resin device	0.3	5	0.37	0.65	0.47	0.50

TABLE 2.9: A comparison between the PDMS device and the HTL resin device regarding the mean period associated with a complete air–water slug passage (T_{ph}).

Technologies	Fabrication process	Steps of the manufacturing process
PDMS-based 3D printing 3D printing	Master-slave approach	6
HTL resin-based 3D printing	Direct printing	2

TABLE 2.10: A comparison between the PDMS device and the HTL resin device in terms of main properties.

Contact angle	Relative roughness	Young's Modulus	Elongation at break	Trasparency
[°]	[%]	[MPa]	[%]	[%]
111.84	0.0001	1.32	100	126
65.36	0.0002	3.90	3	17

TABLE 2.11: A comparison between the PDMS device and the HTL resin device in terms of main properties.

Indeed, the mean period value for the HTL resin device is approximately equal to 12% the value for the PDMS device.

Although the results relating to this last comparison may appear contradictory with what has been said previously regarding the chemical nature of the surfaces identified, since the flow is slower in the PDMS device than in the HTL resin device, a further important aspect must be considered. The design of the macro-to-micro interface, that is the inlets connecting the micro-optofluidic device to the fluids loading tubes, implemented in the two analyzed devices is different. In fact, while the vertical (top-loading) inlet approach was used for the PDMS device (see Fig. 1.6 (a)), the parallel (in-line) ones were used for the HTL resin device (see Fig. 1.6 (b)). According to a previous study run for a similar flow velocity range [58], the design decision for the HTL resin device made it possible to obtain a maximum speed in the center of the channel and along itself. Instead, the approach used for the inlets in the PDMS device was able to obtain a maximum flow speed only in correspondence with the macro-to-micro interface, which adequately justifies the obtained results.

In conclusion, a comparison between the main properties for each of the two analyzed devices is summarized in Table 2.10 and Table 2.11.

Chapter 3

Slug detector and switch: devices in comparison

A slug flow consists of two immiscible fluids, one dispersed in the other, that are circulating in the same micro-system (for instance gas-liquid, immiscible liquid-liquid or liquid and micro-particles) [4], [59].

Nowadays, the study of slug flows in micro-channels has an important role in micronano technology, enabling the design of lab-on-chip devices in the bio-medical field as well as the study of chemical processes [2], [3].

In literature, different methods have been adopted to detect and control slug flows in micro-channels; in particular, the optical and sensor approaches offer the advantages of a wide range of measurement options being minimally invasive [6].

Optical signals were used to characterize the flow nonlinearity [5], [16] and some parameters have been introduced to classify and identify the slug flow inside the micro-channel [60], [61].

In this context, it is an open issue to switch from the equipment used to perform the standard optical sensing procedures to their miniaturization into a single low-cost portable device [62], [63].

In this chapter, the performance of two micro-optofluidic systems, the T-junction micro-optofluidic slug detector and the T-junction micro-optofluidic switch, proposed in [7], [8] and presented in the chapters 1.2 and 1.3 of this thesis, was compared. They were realized in PDMS using a master-slave approach based on the 3D printing technique. These devices were designed to be compact, integrating the micro-optic and micro-fluidic components, for the detection of slug flow.

To test the capability of the devices the optical signals acquired in a specific test section of the micro-channel were compared and to validate the optical information, a flow meter was placed at the outlet of the devices. The main characteristic of these devices is to be easily adopted in different experimental conditions and embedded in portable devices for real-time applications.

(a)   (b)
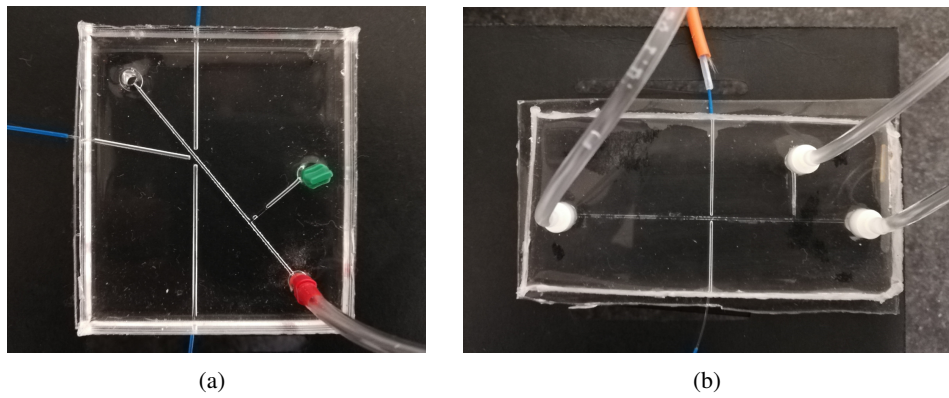
FIGURE 3.1: (a) The micro-optofluidic switch and (b) the micro-optofluidic slug detector with a T-junction micro-channel and the optical fiber insertions.
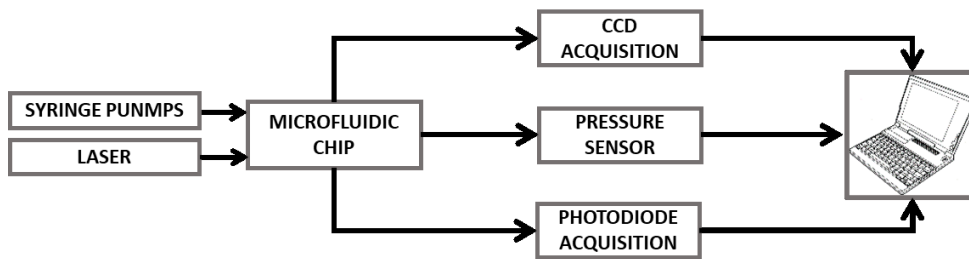
FIGURE 3.2: Block scheme of the experimental set-up.
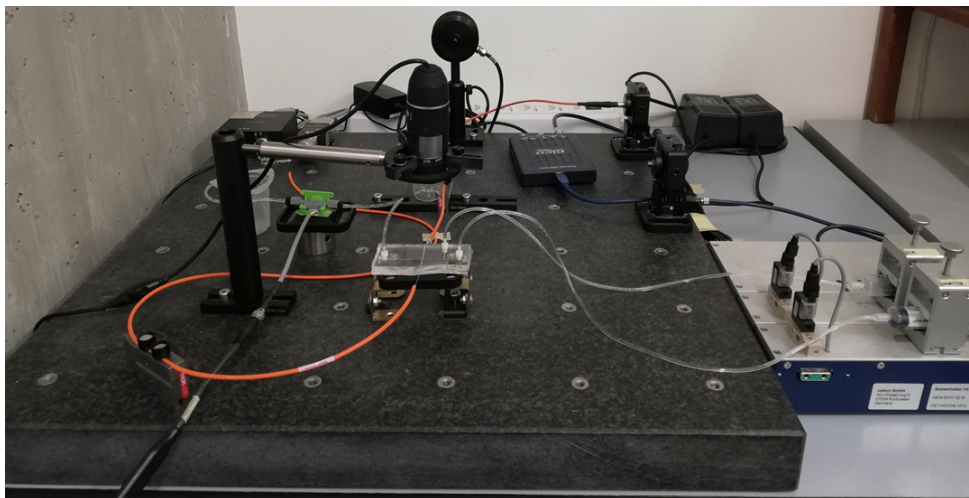
FIGURE 3.3: The experimental set-up used for the slug flow detection.

3.1 Experimental set-up

A continuous slug flow was generated by pumping de-ionized water and air at the T-junction of the micro-optofluidic systems realized shown in Fig. 3.1.

The block scheme and the experimental set-up for the slug flow detection of the micro-optofluidic systems are shown in Fig. 3.2 and in Fig. 3.3.

Two syringe pumps (neMESYS low-pressure module, Cetoni GmbH, Korbussen, Germany) were connected to the two channel inlets and a constant flow rate of 0.1 ml/min was imposed. The input light source was a laser system (NovaPro 660-125, RGB Lasersystems, Kelheim, Germany), that generates a light beam with a wavelength of 600 nm and an output power of 1 mW. As displayed in the block scheme of Fig. 3.2, it was implemented as a simultaneous acquisition. The light intensity variation was acquired by means of a photodiode with a gain of 40 dB (PDA100A, Thorlabs, Newton, NJ, USA) and the signal received was acquired by a PC oscilloscope (Picoscope 2204A, Pico Technology, Cambridgeshire, UK), with a sampling frequency of 1.5 KHz. For a visual inspection of the process a digital USB microscope, placed above the device, was used.

To validate the optical information by the two PDMS micro-optofluidic devices, a flow meter (SLF3S-1300F, Sensirion, Stäfa, Switzerland), with a sampling frequency of 200 Hz, was placed at the outlet of the devices, which was connected with the flow meter through a Tygon tube with an inner diameter of 1.3 mm.

(a) (b)

FIGURE 3.4: Optical and flow meter signals acquired in the micro-optofluidic slug detector correlated with the slug passage. (a) In the optical signal, two levels of luminosity are distinguished. The top level reveals the water presence and the low level the air. The two peaks are for the air slug front and rear. (b) In the flow meter signal, two levels of flow rate are distinguished. The top level reveals the water presence and the low level the air presence, as well. The negative peak is the air slug front and the positive peak is the air slug rear. The signal levels are associated with the video frames acquired simultaneously.

3.2 Optical and flow meter signal interpretation

The optical monitoring system placed in the test section of the devices measures the passage of the slug flow. The variation in the luminosity during the slug passage is due to the difference between the refraction index of the device material ($N_{PDMS} = 1.41$), air ($N_{air} = 1$), and water ($N_{water} = 1.3$).

Thanks to this phenomenon, it is possible to identify clearly the air and water passages in the optical signal that ranges on two levels. The top level reveals the water presence, the low level the air passage, and the two peaks the air slug front and rear. As an example, in Fig. 3.4 (a), it is shown the optical signal and the related video frames acquired during a slug passage in the test section of the micro-channel of the micro-optofluidic slug detector.

The flow monitoring system placed at the outlet of the device measures the water flow rate, i.e. the velocity of the fluid.

Thanks to this system, the optical information was validated by the flow meter signal, which identifies the air and water passages on two levels.

The top level reveals the water presence, the low level the air passage, a negative peak reveals the air slug front and a positive peak the air slug rear.

In Fig. 3.4 (b), it is shown the signal acquired at the outlet of the micro-optofluidic slug detector by using a flow meter.

(a)　　　　　　　　　　　　(b)
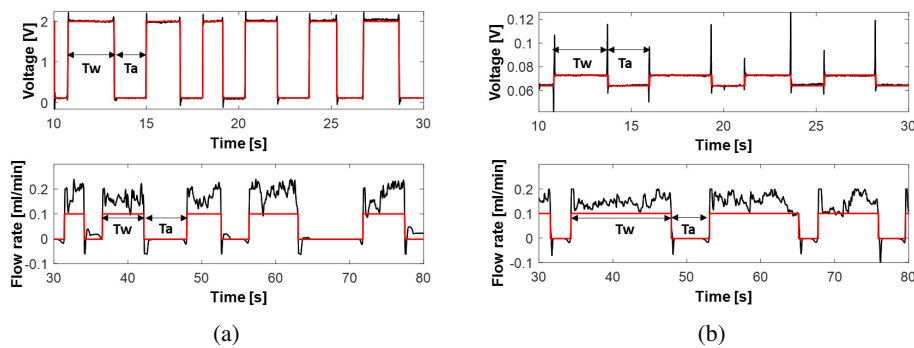
FIGURE 3.5: Optical and flow meter acquisition (black line) in (a) the micro-optofluidic switch and (b) the micro-optofluidic slug detector. The square wave (red line) overlapped with the signal, which ranges between two values, marks the passage period of water (*Tw*) and air slug (*Ta*).

(a)　　　　　　　　　　　　(b)
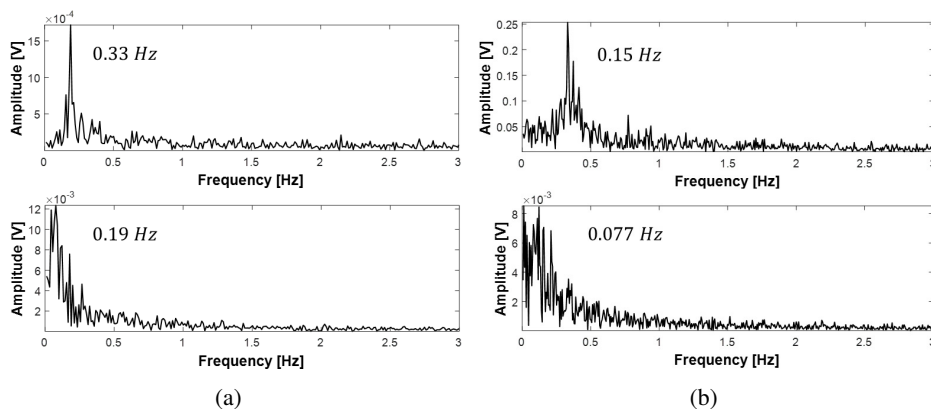
FIGURE 3.6: The spectrum of optical and flow meter signal acquired in (a) the micro-optofluidic switch and (b) the micro-optofluidic slug detector.

3.3 Results and discussion

3.3.1 Comparison of slug frequency measurements

After the simultaneous acquisition of the signals through the set-up shown in Fig. 3.2, a signal processing phase was implemented.

A low-pass filter with a 40 Hz cut-off frequency was applied and a signal smoothing procedure was performed. In the post-processing phase, through the creation of a square wave overlapped with the signals, it was possible to identify the passage period of water (Tw) and air slug (Ta) by using both optical and flow meter acquisition. Fig. 3.5 (a) and Fig.3.5 (b) show the optical signal acquired in the micro-optofluidic switch and in the micro-optofluidic slug detector after the post-processing phase. The square wave in the optical signal of the micro-optofluidic switch ranges between the high voltage level of 2 V, related to the water passage, and a low voltage level of 0.114 V, related to the air passage. For the micro-optofluidic slug detector, the square wave in the optical signal ranges between the high voltage level of 0.073 V, related to the water passage, and a low voltage level of 0.063 V, related to the air passage.

Fig. 3.5 (b) and Fig. 3.5 (b) show the flow meter signal acquired at the outlet of the micro-optofluidic switch and the micro-optofluidic slug detector after the post-processing phase in order to validate the optical signal acquired in the test section of the devices.

For both devices, the flow meter signal ranges between the high level of water flow rate of 0.1 ml/min and 0 ml/min related to the air flow rate. Even if the flow rate of air is 0.1 ml/min, it is set to zero. The first notable difference between the two devices is the level of the acquired optical signal.

Computing the spectra of the optical and flow meter signals acquired in both devices, it was possible to evidence the frequency peak (f) related to the inter-distance of slug passage. The spectra related to the optical and flow meter signal of the micro-optofluidic switch are shown in Fig. 3.6 (a) and of the micro-optofluidic slug detector are shown in 3.6 (b).

The periods related to the slug passage are reported in Fig. 3.7. $TD = <Tw> + <Ta>$ is the sum of the mean period of water and air slug detected in 1 min of acquisition; $TF = 1/f$ is the inverse of the frequency peak obtained from spectra. Looking at these results, the slug passage, detected by the flow meter-based set-up, lasts twice than the slug passage detected by the photodiode-based set-up. This is due to the change of geometry and lengths along the path. There is a decrease in the velocity during the passage from the micro-channel of the devices and the tube that links the output of the device with the flow meter. For this reason, the slug passage in the flow meter signal lasts more.

The second difference is due to the simultaneous monitoring systems adopted. It is really evident looking at the optical signal in time that the slug passage lasts less than the slug passage detected in the flow meter signal. This is due to the change of geometry and lengths along the path. In the adopted experimental campaign, the micro-channels of both devices have a square surface and a diameter of 400 μm. The tubes used to connect the output of the devices and the flow meter sensor have circular surfaces and an inner diameter of 1.3 mm.

Due to the continuity equation, $A_{ch}v_{ch} = A_t v_t$, where $A_{ch} = 400\,\mu m$, $v_{ch} = 0.0104 m/s$, $A_t = 1.33 mm$ and $v_t = 0.0013\,m/s$, there is a decrease of the velocity during the passage from the micro-channel of the devices and the tube that links the output of the device with the sensor. For this reason, the slug passage in the flow meter signal lasts
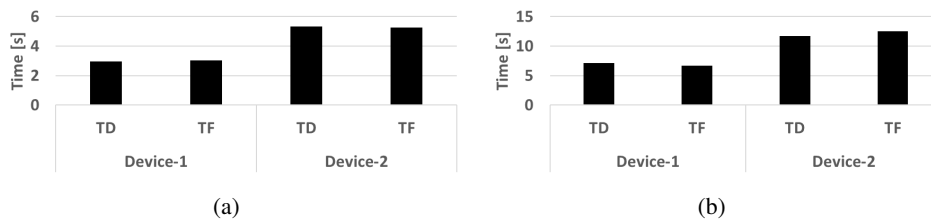
FIGURE 3.7: Mean period of slug flow detected (a) by photodiode-based set-up and (b) by flow meter-based set-up.

more.

Both the optical and the flow systems allow us to detect the slug flow, with some differences due to the change in path geometry. Therefore, it is clear from these results the importance of integrating the optical and fluidic parts within the microfluidic devices for better real-time detection of two-phase flows.

Chapter 4

Opto-mechanical system for slug velocity detection

Nowadays, the hydrodynamics of slug flows in micro-channels [59] play an important role in the micro-nano technology, enabling the design of lab-on-chip devices in the bio-medical field as well as in chemical processes [2], [3]. In this context, an open issue is that of developing low-cost detection systems, models, and control strategies easily adaptable in different operative conditions, able to guarantee the processes' reproducibility and reliability, and suitable for on-chip applications [1], [64].

The results presented in the literature are strictly related to specific experimental conditions, so far from a well-established framework that can drive flow control.

Recently, some case studies using System-on-a-Chip (SoC) predictive control strategies have been presented in literature [1], [65]. The SoC offers a high control level and modularity, but its functionalities are strongly dependent on the integrated control logic and the knowledge of the process model. In this complex scenario, in which the properties of the fluids, the input flow conditions, the channel geometry and the material surface properties can strongly affect the flow dynamics, the need to develop detection systems, models, and control strategies completely independent of any constraints related to the experimental conditions represents the bottleneck for widespread diffusion that SoC uses in microfluidic applications.

In slug flows, two immiscible fluids, one dispersed in the other, are circulating in the same micro-system (for instance gas-liquid, immiscible liquid-liquid, or liquid and micro-particles) [4], [59]. In general, their behavior is very complex: interfaces that adopt elaborate forms and classification of regimes can sometimes lead to inextricable phase diagrams, where many regimes are mixed up, identified as bubble, slug, or plug, annular, churn, and wispy annular.

Several approaches are available for detection and control in micro-channels [66], but, among them all, the optical methods have offered the advantages of a wide

range of non-invasive measurement options [67]. The most common optical investigation of microfluidic flows happens by continuous monitoring using a fast Charge-Coupled detector (fast-CCD camera), or a Particle Image Velocimetry (PIV) system [68], [69]. Both allow for obtaining detailed and precise flow information with the drawbacks of costly and bulky equipment. The challenge nowadays is to have methodologies based on low-cost technologies easily embedded in a portable device for real-time applications. In this context, data-driven approaches based on monitoring optical signals [67] can represent a good alternative since they are non-invasive, offer easy integration of optical sensors with the microfluidic chips [70], [71], and, in future development, the possibility of being even embedded in a chip [7].

In the micro-optofluidic device presented in [7], the advantage of the integration of micro-optical and microfluidic components in one device is proved by taking the advantage of advanced signal analysis methodology to process the optical information and controlling the flow.

Advantages can also be envisaged for SoC applications due to the simplicity of managing optical signals, as it is proved by a wide literature on flow classification in micro-channels [72], [73]. Advanced signals analysis methodologies have been developed to characterize the flow nonlinearity [5], for data-driven process identification [60], [74] and to define parameters for slug flow classification [61] to be used in the development of online control strategy [75]. Starting from the results presented in [61] where the frequency analysis of signals, acquired by a low-cost monitoring set-up, was used to classify the air and water dominance inside the micro-channel, in this thesis chapter, the attention was focused on the development of a methodology suitable for detection of the slug velocity in micro-channels. Additionally, the developed methodology was, in a second step, implemented to realize a platform, easy to be integrated into a SoC, for real-time slug flow velocity detection.

In the experiments carried out, the slug flow was generated by the interaction of two immiscible fluids {air and water} in two serpentine micro-channels of diameter {320 μm and 640 μm}. The serpentine geometry, enhancing the unpredictability of the flow, guarantees the robustness of the methodologies and the platform presented. The optical-based approach based on the acquisition and processing of optical signals has been extended to a more general framework.

Two methods have been considered: the dual-slit methodology based on the cross-correlation analysis to compute the slug velocity [76] and the spectral analysis to compute the slug frequency [61]. An experimental campaign was carried out by setting nine different flow operative conditions at the inlets. Thanks to the methods used, in each experiment, it was possible to distinguish the water and air slugs' velocity and the water and air slugs' frequency. The two parameters were also correlated.

The results obtained were used to implement a platform for the real-time detection of the slug velocity. Two experiments were carried out monitoring the slug flow in different operative conditions and the platform performance was successfully validated.

4.1 Experimental set-up

A continuous slug flow was generated by pumping de-ionized water and air at the Y-junction of serpentine micro-channels in a Cyclic Olefin Copolymer (COC) with a square section and positioned horizontally. Two syringe pumps (neMESYS low-pressure module, Cetoni GmbH, Korbussen, Germany) were connected to the two
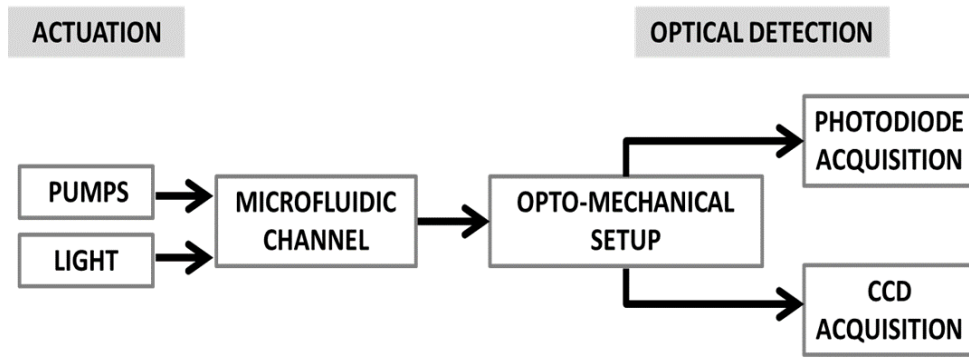
(a)
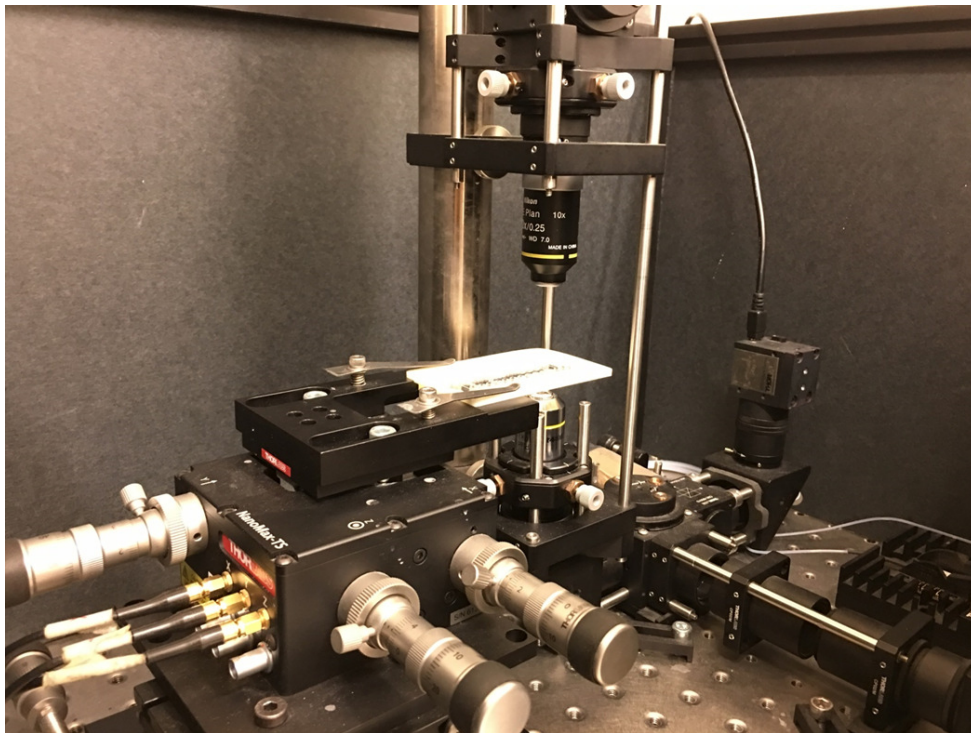
(b)

FIGURE 4.1: (a) The flowchart of the experimental set-up; (b) a picture of the opto-mechanical experimental set-up.

channel inlets. The flow chart and a picture of the complete experimental set-up are shown in Fig. 4.1 (a)-(b).

The process was monitored in a micro-channel area by the simultaneous acquisition of the light intensity variation using a couple of photodiodes (SM05PD1A, Thorlabs, Newton, NJ, USA), with a sampling rate of $2\,kHz$, placed at a distance of $10\,mm$ from each other and a CCD camera (DCU224, Thorlabs, Newton, NJ, USA) with a frame rate of $25\,frame/s$. The CCD video was used to have a visual inspection of the process. A frame sequence of the slug passage acquired by the CCD is in Fig. 4.1 (d). A detailed description of the optical set-up and the signals pre-processing is given in [61].

The serpentine micro-channels used in this chapter are shown in Fig. 4.2 (a)-(b), where the two rectangles are placed in the investigation areas. The micro-channel in Fig. 4.2 (a) has a diameter of $320\,\mu m$ and a length of $50\,mm$ (labeled as $G-320$), and

the micro-channel in Fig. 4.2 (b) has a diameter of 640 μm and a length of 121 mm (labeled as $G-640$). The geometry $G-320$ was used in the experiments carried out to establish an optical signals processing methodology for the computation of slug velocity and slug frequency. Both geometries were considered for the validation of real-time velocity detection by the ad hoc platform implemented.

In Fig. 4.2 (c), an example of the trends of the signals acquired by a couple of photodiodes $\{ph1, ph2\}$ in $G-320$ is shown. As discussed widely in [61], these optical signals are correlated with air/water slugs passage as follows: the top level represents the presence of water in the channel, while the lower level the presence of air in the channel. The two lowest peaks reveal the slugs' fronts and rears. Indeed, during the slugs passage, the intensity of the light decreases suddenly due to the difference between the refraction index of COC ($N_{COC} = 1.5$) and air ($N_{air} = 1$), so the air slug contour becomes darker than the inside of the slug and the chip wall. This effect is less evident during the water passage since the water refraction index ($N_{water} = 1.3$) is closer to the one of the COC. Thanks to this phenomenon, it is possible to clearly distinguish the air and water slugs passage in the signals.
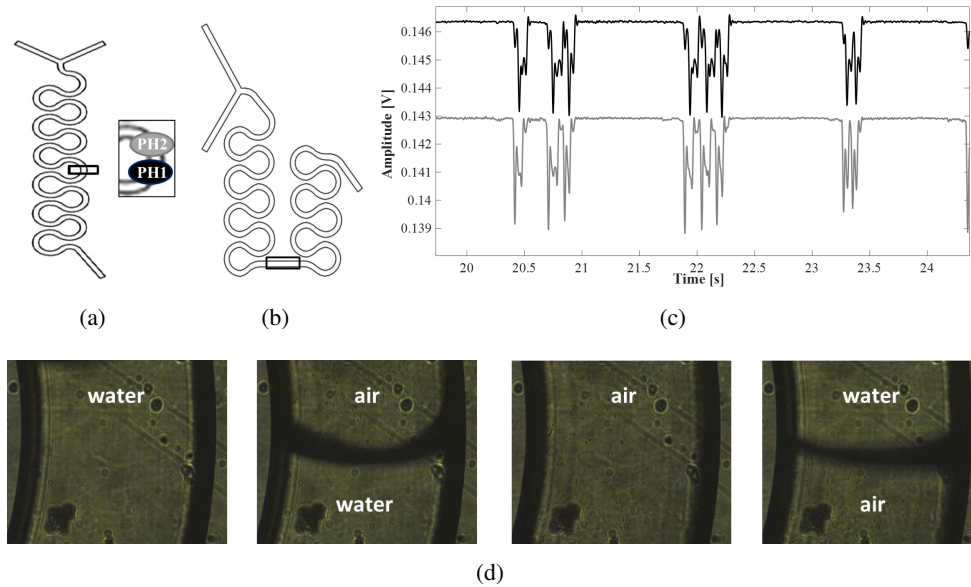
FIGURE 4.2: (a) The geometry of the serpentine channel of 320 μm (labeled as $G-320$); (b) the geometry of the serpentine channel of 640 μm (labeled as $G-640$); (c) an example of the trends of the signals acquired by the two photodiodes $\{ph1, ph2\}$ in $G-320$ in the experiment with an input flow rate $F = 0.3$ ml/min. The two rectangles in $G-320$ and $G-640$ point out the investigation areas where the two photodiodes are placed; (d) a frame sequence related to the slug passage acquired by the CCD.

4.2 Experimental campaigns

Nine experiments were carried out by feeding equal flow rates of water (F_w) and air (F_a) to the two inlets of the micro-channel $G-320$ as in the set $F \in \{0.1, 0.2, 0.3, 0.4, 0.5, 0.6, 0.7, 0.8, 0.9\}$ ml/min. The Air Fraction (AF) was respectively $AF = 0.5$. The process was monitored in a position after three bends from the Y-junction; see the insert in Fig. 4.2 (a). Data were acquired for 20 s, but the first and last 5 s of the acquisition were excluded from the analysis.

Three well-known dimensionless parameters widely used in fluid dynamics to establish some basic flow characteristics were computed: the Reynolds number, the Capillary number, and the Dean number [4]. The Reynolds number information is about the transition between the laminar and turbulent flow.

The boundary value is debatable, but generally, in microfluidics, it is assumed to be $Re = 1$. To enhance the process nonlinearity and be able to evaluate the robustness of the methodology proposed in our experiments, its value was in the range [1, 13]. The Capillary number on the order 10^{-3}, as it is in the experiments presented, assures the slugs' formation. Finally, the curve in the serpentine geometry can determine a re-circulation in the flow in the cross-section. The presence of these phenomena can be evaluated by a Dean number greater than 1, in the experiments ranges in [0.5, 6].

These parameters give an indication of some characteristics of the flow taken into account: the fluids properties, the micro-channel geometry, and input flow rates. Being the process highly nonlinear, it is not sufficient for its dynamical characterization and can not be used for process control. This underlines the need for data-driven approaches that can monitor and identify the process state in real-time.

To establish the velocity of the slug flow in the micro-channel, the data were analyzed in the time domain by using the dual-slit methodology, presented in [76]. Then, the slug frequency, corresponding to slug passage duration in time, was instigated by spectral analysis using the approach presented in [61].

4.3 Methods for slug velocity computation

4.3.1 Dual-slit methodology

In order to evaluate the slug velocity, the cross-correlation between optical signals acquired by $\{ph1, ph2\}$ was computed for each experiment.

A peak detected in the cross-correlation is representative of the time delay of the two signals and can be correlated with the time needed by the slug to move from one investigation point $\{ph2\}$ to another one $\{ph1\}$.

Knowing the distance between photodiodes, it is possible to compute the slug velocity using the following formula:

$$v = \frac{d_s}{n \cdot T_s} \tag{4.1}$$

where d_s is the distance between photodiodes scaled based on the magnification ($d_s = 1\ mm$), n is the delay in samples between the two signals, T_s is the sampling period (0.5 ms), and so $n \cdot T_s$ is the detectable delay in time [s].

In Fig. 4.3 (a), the cross-correlation function in a time window of 0.1 s is reported (equivalent to $200 samples$) for the experiment with $F = 0.3\ ml/min$. Two peaks can be detected, one at 2 ms (4 $samples$), and another one at 20 ms (40 $samples$). Based on the signal trend shown in Fig. 4.2 (c), the first peak can be related to the faster sequence of air slugs that anticipates and follows the passage of a long water slug. The second peak can be related to the passage of long water slugs itself.

Detecting different velocities is expectable given the process's nonlinearity. Based on the values of these delays, the two velocity values obtained are $\{0.5\ m/s,\ 0.05\ m/s\}$ that refer to the velocity of water and air slugs, respectively.

To validate the results, a sequence of obtained frames related to a slug passage was analyzed by the Digital Particle Image Velocimetry (DPIV) approach, used previously to detect the red blood cell velocity in micro-channels in [77]. The mean velocity detected at the slug front and rear was respectively $\{0.034\ m/s, 0.015\ m/s\}$.

4.3.2 Spectral analysis

The spectral analysis of optical signals for the flow characterization and classification in micro-channels was presented in [61] and used in [75] for the real-time slug flow control in a feed-forward configuration. The slug frequency is associated with the duration of slugs' passage.

It was implemented by computing the spectrum of the optical signal $\{ph2\}$. Then, the spectrum profile was approximated with a multi-mode Gaussian model and the dominant frequencies were detected. In both previous works [61], [75], the attention was focused on the single-mode Gaussian model and in the highest peak.

In this work, the two highest peaks were considered in order to investigate the behavior of the water and air slugs. As for the cross-correlation function, the two dominant frequencies were associated with the presence of long water slugs and short air slugs. In Fig. 4.3 (b), the spectrum of the optical signal $\{ph2\}$ for the experiment $F = 0.3\ ml/min$ is shown. The two peaks detected are at frequency $f = 1.33\ Hz$ and $f = 10.67\ Hz$. The highest one can be associated with the passage of long water slugs $T = 0.75\ s$, while the other one with the passage of short air slugs $T = 0.093\ s$ which refer to the frequency of water and air slugs, respectively.

(a)   (b)

(c)
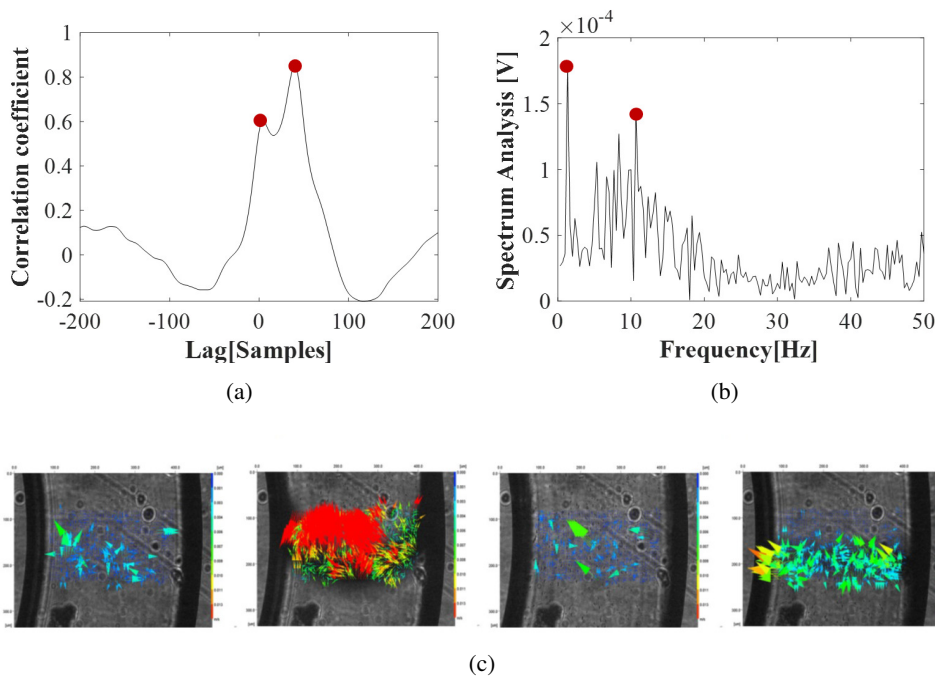
FIGURE 4.3: Optical signals processing of $\{ph1, ph2\}$ in $G - 320$ for the experiment with an input flow rate $F = 0.3\ ml/min$. (a) An example of the cross-correlation function for the computation of the slug velocity; (b) an example of the spectrum of the signal $\{ph2\}$ for the computation of the slug frequency. In both plots, the two higher peaks are highlighted with red dots; (c) a sequence of frames related to a slug passage analyzed by Digital Particle Image Velocimetry (DPIV).
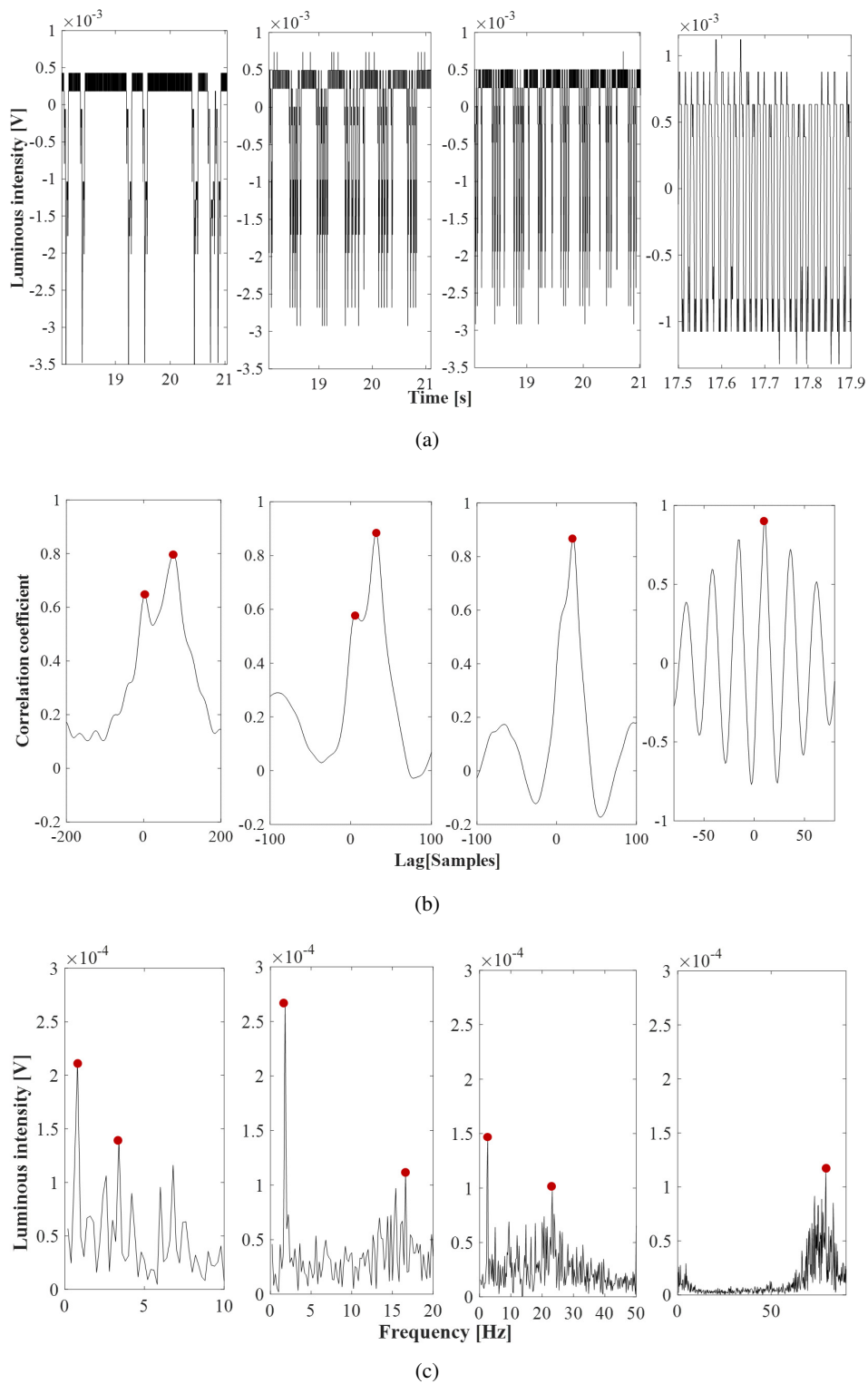
FIGURE 4.4: Dynamics of the slug flow in the experiments $F \in \{0.2, 0.4, 0.6, 0.9\}$ ml/min. (a) The trends of the raw optical signals acquired vary in the input flow rate. The change of the flow patterns from long water slugs is evidently interlaced by short air slugs one after another ($F = 0.2 \, ml/min$), to longer water slugs ($F = 0.4 - 0.6 \, ml/min$) followed by a train of smaller air/water passages and finally, a train of smaller water/air slugs ($F = 0.9 \, ml/min$); (b) the cross-correlation between the signals acquired through the two photodiodes, and in red dots the peaks detected; (c) the spectra of the optical signal $\{ph2\}$, and in red dot the peaks detected.

4.4 Results and discussion

4.4.1 Slug frequency and velocity measurements

Both methods were used to analyze the optical signals acquired in all the nine experiments $F \in \{0.1, 0.2, 0.3, 0.4, 0.5, 0.6, 0.7, 0.8\}$ *ml/min*. The signals of the two photodiodes $\{ph1, ph2\}$ were used to compute the slug velocity by the dual-slit methodology, whereas in the case of the spectral analysis only the information of one photodiode $\{ph2\}$ was used. Finally, the results obtained by the two approaches were mathematically correlated.

To evidence the signal dynamics in different experimental conditions, in Fig. 4.4 (a), the trends of the raw optical signals for the experiments $F \in \{0.2, 0.4, 0.6, 0.9\}$ *ml/min* are shown. A time window of 2 *s* was used for $F \in \{0.2, 0.4, 0.6\}$ *ml/min* and 0.5 *s* for the experiment $F = 0.9$ *ml/min*.

The process nonlinearity does not allow for having a periodic slugs passage; nevertheless, a changing pattern of the slug flows can be clearly distinguished at the increase of the input flow rate, as follows:

- $\{F = 0.1 - 0.2 \; ml/min\}$ long water slugs are interlaced with short air slugs, almost one after another;

- $\{F = 0.3 - 0.8 \; ml/min\}$ long water slugs are followed by a train of short air slugs in sequence;

- $\{F = 0.9 \; ml/min\}$ a fast train of short air/water slugs.

In the experiments $F \in \{0.1, \ldots, 0.8\}$ characterized by the passage of long water slugs, a slower dynamic is observed than the one obtained for $F = 0.9$ where an oscillatory-like trend is recognizable.

In Fig. 4.4 (b), the cross-correlation functions obtained for the four experiments $F \in \{0.2, 0.4, 0.6, 0.9\}$ *ml/min* are shown. A time window of 0.1 *s* (200 *samples*) was used for $F = 0.2$ *ml/min* and of 0.05 *s* (100 *samples*) for the other three experiments $F \in \{0.4, 0.6, 0.9\}$ *ml/min*. At the increase of the input flow rate, the convergence of the two peaks in one and a reduction of the time delay can be noticed, with air and water slugs having the same velocity. For the experiment $F = 0.9$ *ml/min*, an oscillatory trend in the cross-correlation function is evident and a sharp peak at 10 *samples* (5 *ms*) that stands for a velocity of 0.2 *m/s*.

The cross-correlation function was computed for all the nine experiments, but two peaks were detected only in the first five $F \in \{0.1, 0.2, 0.3, 0.4, 0.5\}$ *ml/min*. The method does not seem to be able to differentiate the water and air velocities in the experiments $F \in \{0.6, 0.7, 0.8\}$ *ml/min*, even though we can notice a difference in the flow patterns of Fig. 4.3 (a). Consequently, it was not possible to have an evaluation of the air velocity only in these conditions. The convergence of the slug flow towards a uniform velocity distribution, having the same water and air slugs' velocity, is obtained for $F = 0.9$ *ml/min*.

In Fig. 4.5 (a), the values of water velocity obtained by the highest peak were plotted versus the input flow rate: the blue dots are for $F \in \{0.1, 0.2, 0.3, 0.4, 0.5\}$ *ml/min* and the red dots for $F \in \{0.6, 0.7, 0.8, 0.9\}$ *ml/min*. In Fig. 4.5 (b) for $F \in \{0.1, 0.2, 0.3, 0.4, 0.5\}$ *ml/min*, the values of air velocity, obtained by the second peak, were reported. Both graphs were mathematically interpolated. It is worth noticing the parabolic increase in the water slug's velocity and the linear decrease in the air slug's velocity.

By the analysis of the slug pattern (Fig. 4.4 (a)), the velocity and the frequency
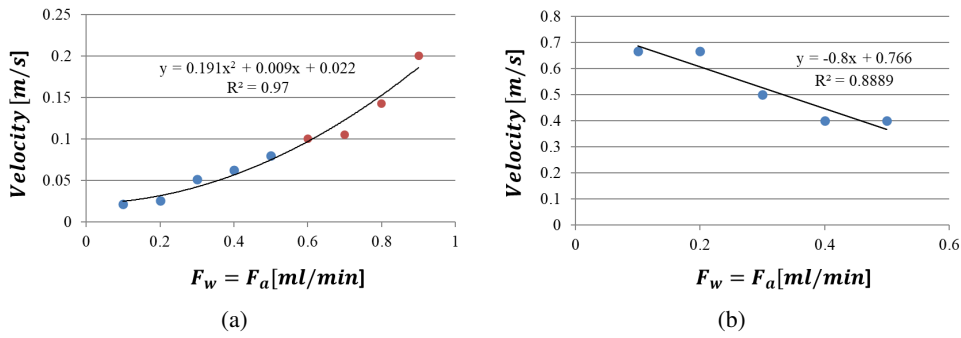
FIGURE 4.5: The cross-correlation function was computed for all nine experiments. (a) The values of water velocity obtained by the highest peak were plotted versus the input flow rate: the blue dot are for $F \in \{0.1, 0.2, 0.3, 0.4, 0.5\}$ ml/min and the red dots for $F \in \{0.6, 0.7, 0.8, 0.9\}$ ml/min; (b) the values of air velocity, obtained by the second peak for $F \in \{0.1, 0.2, 0.3, 0.4, 0.5\}$ ml/min.

of the air and water slugs are expected to be different from each other because of the slower dynamics and the convergence to the same value for $\{F = 0.9\ ml/min\}$. From this perspective, the analysis in the spectral domain seems more robust.

In Fig. 4.4 (c), the spectra of the optical signals for the experiments $F \in \{0.2, 0.4, 0.6, 0.9\}$ ml/min are shown. As expected, at the increase of the input flow rate, the convergence of the two peaks in one and an increase of the frequency of the slugs passage can be noticed, with the air and water slugs assuming the same duration. Coherently with the flow pattern of Fig. 4.3 (a), one sharp peak is obtained in the experiment $F = 0.9\ ml/min$ at $79.2\ Hz$ that stands for an average duration of the slug passage of $0.012\ s$.

The values of slug frequency were computed for all nine experiments and in Fig. 4.6 the values of the two peaks identified in the spectra are plotted versus the input flow rates $F \in \{0.1, 0.2, 0.3, 0.4, 0.5, 0.6, 0.7, 0.8\}$ ml/min. The water frequency is reported in Fig. 4.6 (a), and the air frequency is reported in Fig. 4.6 (b). In this case, by the mathematical interpolation at the increase of the input flow rate, the water slug frequency increases linearly in the range $[0.5,\ 3.5]$ Hz, whereas the air slug frequency has a parabolic trend $[1,\ 48]$ Hz. Therefore, a water slug passage can last from $[0.3,\ 2]$ s and an air slug passage $[0.02,\ 1]$ s. The convergence of the two dynamics for $F = 0.9\ ml/min$ is obtained when the high frequency becomes dominant having the water-air train flow pattern.

Finally, the results of the analysis in the frequency and time domain were graphically correlated. The spectral analysis shows two peaks for all eight experiments $F \in \{0.1, 0.2, 0.3, 0.4, 0.5, 0.6, 0.7, 0.8\}$ ml/min before reaching the convergence for $F = 0.9\ ml/min$. The cross-correlation function has two peaks for five experiments $F \in \{0.1, 0.2, 0.3, 0.4, 0.5\}$ ml/min.

In Fig. 4.7, the water velocity was plotted versus the water frequency for $F \in \{0.1, 0.2, 0.3, 0.4, 0.5\}$ ml/min (reported as blue dots) and versus the air frequency for $F \in \{0.6, 0.7, 0.8, 0.9\}$ ml/min (reported as red dots). The points were linearly interpolated, maintaining the distinction between the input flow ranges.

The nonlinearity of the process and its tendency to move from one flow pattern regime to another is underlined by a difference in the two linear interpolations. Additionally, these mathematical relations address the possibility to obtain the dominant velocity of the slug flow through the analysis of one signal in the frequency domain, thus reducing the complexity of the optical set-up and the data analysis.

(a)   (b)
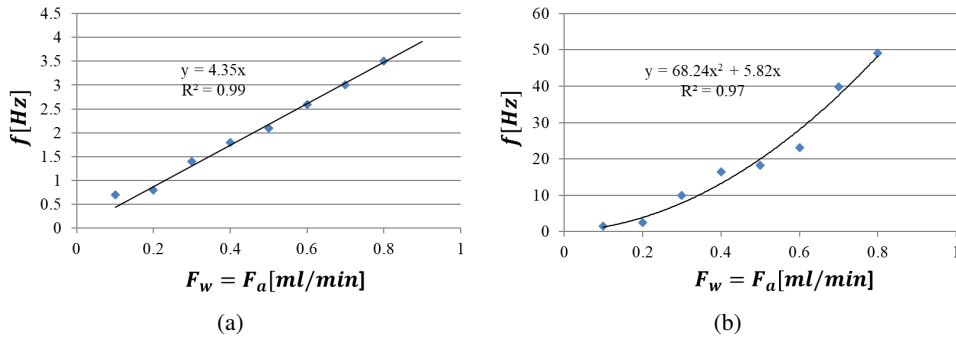
FIGURE 4.6: The values of slug frequency computed by the two peaks identified in the spectra versus the input flow rates for the eight experiments $F \in \{0.1, 0.2, 0.3, 0.4, 0.5, 0.6, 0.7, 0.8\}$ ml/min. (a) Water frequency; (b) air frequency.
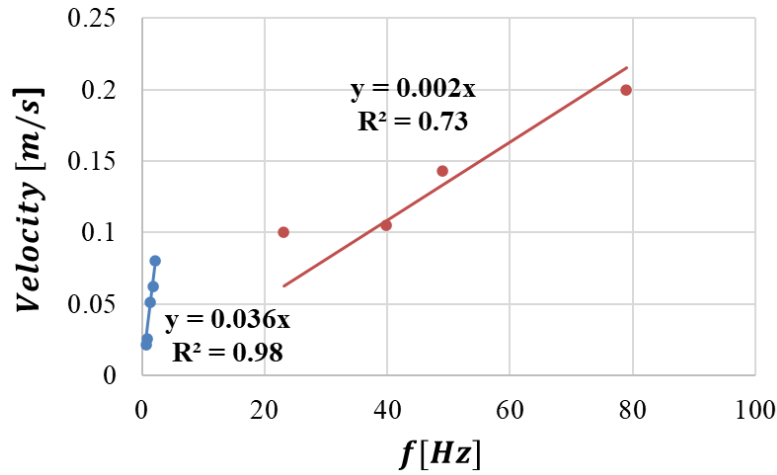
FIGURE 4.7: The water velocity plotted versus the water frequency for $F \in \{0.1, 0.2, 0.3, 0.4, 0.5\}$ ml/min (blue dots) and versus the air frequency for $F \in \{0.6, 0.7, 0.8, 0.9\}$ ml/min (red dots).

4.5 Theoretical aspects of nonlinear dynamics in slug flow

In [5], the potential of time series-based analysis as a powerful tool for studying the complex dynamics of two-phase microfluidic flows is shown.

Theoretically, the evolution of two-phase flow is classically descrived using the one-formulation of the Navier-Stokes equation:

$$\frac{\delta v}{\delta t} + v \cdot \Delta v = \frac{-1}{\rho}\Delta P + g + \frac{1}{\rho}\Delta[\mu(\Delta v + v \cdot \Delta v)] - \frac{\sigma}{\rho}(\Delta \cdot n)n\delta_I, \ \Delta v = 0 \qquad (4.2)$$

where v, P, ρ and μ are respectively the local velocity, pressure, density and dynamical viscosity of the flow, g denotes the gravity and σ is the surface tension. δ_I is the surface delta function, which is zero outside the interface and n is the unit normal vector, which is directed toward the continuous phase.

An important dimensionless parameter is the Reynolds number defined as:

$$Re = \frac{Lv}{\upsilon} \qquad (4.3)$$

where L and v are respectively the characteristic length of the micro-channel and the fluid velocity, while υ is the kinematic viscosity.

In general, Re expresses the ratio between the viscous ($\Delta^2 v$) and the inertial term (($v \cdot \Delta)v$) of the Navier-Stokes equation, so it represents an indicator of flow nonlinearity [78].

Connected to the Reynolds number, the Dean number for micro-flow in curvilinear channel is defined as:

$$De = Re\sqrt{\frac{R}{Rc}} \qquad (4.4)$$

where R is the width of the micro-channel and Rc its mean curvature radius.

For a sufficiently large Dean number ($De >> 1$), a pair of vortices forms in the cross-section, carrying flow from the inside to the outside of the bend across the center and back around the edges.

On the other hand, considering the role of the input flows in the two-phase flow generation, another two dimensionless numbers needs to be considered: the Capillary number (Ca) and the Air Fraction (AF). In this context, the two-phase flow under consideration consists of air and de-ionized water, so both parameters are evaluated as follows:

$$Ca = \frac{\mu(v_{air} + v_{water}) \cdot 0.5}{\sigma} \qquad (4.5)$$

$$AF = \frac{V_{air}}{V_{air} + V_{water}} \qquad (4.6)$$

where μ is the dynamic viscosity of water, v is the average flow velocity, σ is the surface tension between air and water and V indicates the volumetric flow rate. In particular, being the microfluidic process largely dominated by the interfacial effects, Ca enhances the relative importance of viscous to surface tension force meanwhile the AF highlights the fraction of the sample flow that is flushed in the micro-channel. In particular, in [5], the same experimental set-up is presented as in this chapter, and with regard to the experimental campaigns carried out in [5], the condition in which fluid flow rates are less than 1 ml/min is also presented in this chapter.

Non linear time series analysis was used to quantify the flow patterns and the slug dynamics in terms of the Largest Lyapunov exponent (LE)[79] and d_{inf} [80].

Lyapunov exponents are fully representative of the sensitivity to initial conditions (stretching phase) of a given nonlinear dynamical system, being positive for chaotic behaviour [81]. It is often sufficient to establish the existence of at least one positive Lyapunov exponent to define chaotic dynamics [82]. Therefore, the maximum Lyapunov exponent quantifies the degree of nonlinearity of the dynamical system, while d_{inf} is sensitive to both the stretching and folding mechanism, thus it is not only a complementary measure to the maximum Lyapunov exponent, but also a robust parameter for noise-corrupted time series. d_{inf} is defined as the non-null fixed point of the following equation [80]:

$$d(i+1) \approx \Lambda d(i) - \Gamma d^2(i) \qquad (4.7)$$

where Λ and Γ represent respectively e^λ (λ is the largest Lyapunov exponent) and the coefficient of the second-order correction term related to the folding effect. The largest Lyapunov exponent is estimated through the finite size Lyapunov exponent method [79]:

$$\lambda(\delta, \Delta) = \left\langle \frac{1}{T(\delta, \Delta)} \right\rangle ln\left(\frac{\delta}{\Delta}\right) \qquad (4.8)$$

where <> indicates the mean value, δ the initial error and Δ the tolerance, while T is the predictability time.

The Largest Lyapunov exponent and the d_{inf} can be considered respect to two characteristic parameters of the two-phase microfluidic processes as the Capillary Number (Ca) and Air Fraction AF.

The presented results in [5] simplify the classification of the slug flow dynamics: fixing a couple (Ca, AF) the resulting flow nonlinearity can be derived. In conclusion, the results in [5] show the capability of the proposed set of parameters (Lyapunov exponent and d_{inf}) to quantify the nonlinearity of the microfluidic process and its sensitivity to input flow variations.

4.6   Platform for real-time slug velocity detection

After the assessment of the methodology to compute the slug velocity through the analysis of optical signals, a LabVIEW Platform was implemented for real-time slug flow monitoring.

In Fig. 4.8, a flow chart of the system is reported. A module provided by Cetoni (neMESYS SDK software) was integrated into the Platform to drive the syringe pumps. Then, the signals, acquired in cycles based on an established time window, are visualized, pre-processed and processed by using the dual-slit methodology. The velocity values obtained per cycle, for both the air and water slugs, are collected in a chart, showing the trend of the velocity versus cycle. Two experiments were carried out using the micro-channels $G - 320$ and $G - 640$ as described in 4.1 and reported in Fig. 4.2 (a)-(b).

In Fig. 4.9, the GUI of the Platform is presented. It is possible to distinguish two
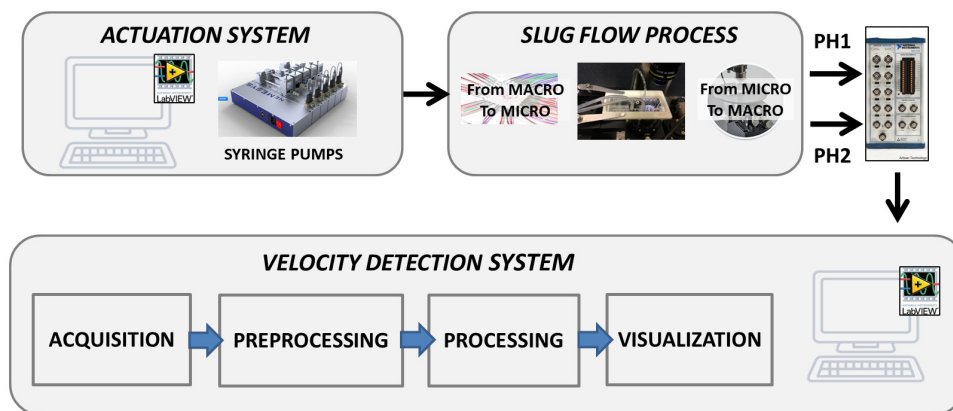
FIGURE 4.8: The flowchart of the platform to compute the slug velocity by the analysis of optical signals with the main functional blocks for the data: acquisition, preprocessing, processing, and visualization. The block that manages the pump-computer connection is also pointed out.

areas: the left area, used for inputting the experiment parameters, and the right area, used for the process data visualization.

- In the blank text boxes at the top of the left area, the user can set the parameters of the experiment: the distance between the photodiodes, the sampling frequency of the acquisition board (in Hz), and the time window length to be analyzed cyclically (in *samples*). By the text box in grey, labeled *Cycle Number*, the number of analysis cycles performed is visualized to inform the user
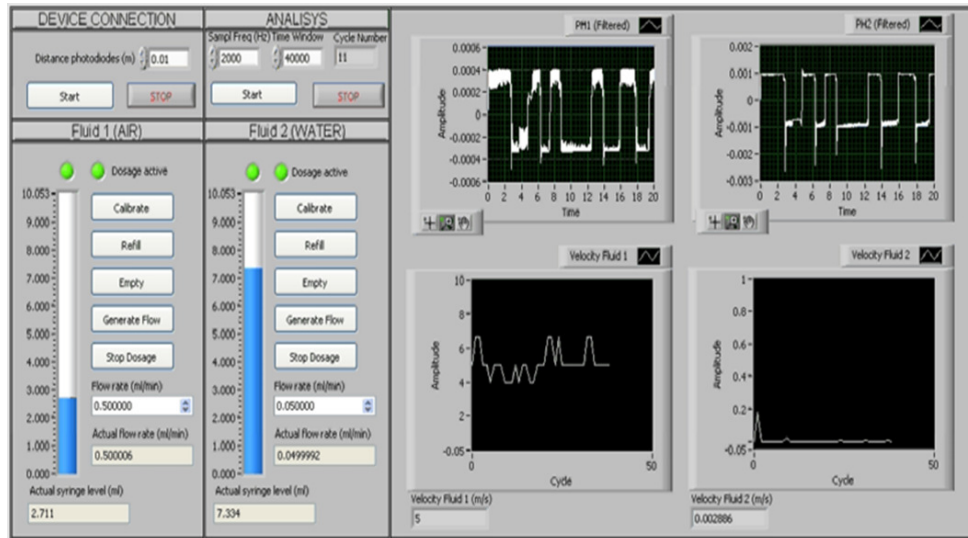
FIGURE 4.9: The GUI of the Platform. Two areas are distinguishable: the left area is used for user inputting and the right area is for data visualization.

about the number of points collected in the velocity chart and the time horizon monitored. At the bottom of the left area, it is possible to manage the two syringe pumps, set the desired values of the input flow rates (in *ml/min*), and check the actual values.

- At the top of the right area, the signals acquired by the two pre-processed photodiodes are plotted in real-time per cycle of 20 *s*. At the bottom, the charts that collect the water and air velocity are updated cycle-by-cycle. The values obtained for the ongoing cycle are also reported in the text box.

The implemented algorithm includes five blocks, described in detail below.

- The first block establishes the communication computer pumps and manages the pumps through some basic procedures such as calibration, refilling, emptying, and start-and-stop of the flow emission. In the GUI of the platform, these block functions are activated by buttons (see Fig. 4.9). The *Start* button in the **DEVICE CONNECTION** section establishes the communication with the pumps, while, in the two **FLUID** sections, we find the buttons to *Calibrate*, *Refill*, *Empty*, *Generate Flow*, and *Stop Dosage* as described previously. There are also two indicators that give feedback regarding the status of the pumps: the first led indicates that the pump is connected and the second one that the dosage is active. The velocity monitoring starts by pressing the *Start* button in the **ANALYSIS** section.

- The second block carries on the two signals acquisition at the established sample frequency and time-window length that subsequently splits them up into two data vectors to be analyzed separately (*Split Signals*).

- The third block (*Filtering*), related to the pre-processing, includes the procedures for the mean removal, a notch filter (at 50 Hz) and a low pass filter. In particular, two first-order Butterworth IIR filters with $\{fc = 30\ Hz$ and $fc = 48\ Hz\}$ have been used respectively for *Ph1* and *Ph2*. The system also provides a function for saving raw and filtered signals.

- The fourth block computes the cross-correlation between the filtered input signals (*Cross-Correlation*). Then, the *Peak Detector* function finds the delay in samples(n) related to the two peaks in the cross-correlation and computes the velocities of the two fluids by Equation 4.1. The system also provides a function for saving those values.

- Finally, the fifth block is for the visualization (*waveform graph*).

4.6.1 Slug velocity monitoring in a 320 μm micro-channel

The real-time flow information in the serpentine micro-channel $G - 320$ was monitored and analyzed by using a sampling frequency of 2 *Khz* and in a time window of 20 *s*. One inlet of the micro-channel was continuously fed with a water flow rate equal to 0.05 *ml/min*. The air flow rate at the second inlet was varied during the experiment in the set $\{0.1, 0.3, 0.5\}$ *ml/min*, maintaining each value for 13 cycles, and thus was around 260 *s*.

Differently from the experiments discussed in 4.4, the process was slowed down by decreasing the input flow rate of the water and by setting up an unbalanced configuration of the input flow rate water-air in order to guarantee more stability in the flow velocity [61].

Fig. 4.10 (a) shows the trend of the air (above) and water (below) slugs velocity during the entire duration of the experiment. The red vertical dotted lines separate the three-time intervals in which the air input flow rate was maintained unaltered. The horizontal arrows report the velocity average per interval. As can be noticed, the air and water slugs' velocity was the same, while one peak was identified in the cross-correlation function.

Fig. 4.11 (a) shows the trend of a signal $\{ph2\}$ in the condition air input flow rate 0.5 *ml/min* and the cross-correlation function obtained. Using very low input flow rates, no great difference is detected in the velocity values in time, but the flow velocity stability increases at the increase of the difference between the two input flow rates, as expected by previous studies [61].

The process nonlinearity leads to the variation of the velocity of 0.1 *m/s* which is significant considering that the total increase of the velocity is in the range $[0.3, 0.5]$ *m/s*. This phenomenon is particularly evident in the first two input flow rate conditions; then, a stabilization in the process is reached.

4.6.2 Slug velocity monitoring in a 640 μm micro-channel

The real-time flow information in the serpentine micro-channel $G - 640$ was monitored and analyzed by using a sampling frequency of 2 *Khz* and in a time window of 10 *s*.

The input flow rate of air and water at the two inlets of the micro-channel was set equal and varied during the experiment in the set $\{0.3, 0.5, 0.7\}$ *ml/min*, maintaining each value for 10 cycles (around 100 *s*).

A greater diameter leads to a faster transient time, giving the possibility to reach the flow steady condition. Fig. 4.10 (b) shows the trend of the air (above) and water (below) slugs velocity during the entire duration of the experiment. The red vertical dotted lines separate the three-time intervals considered in which the two input flow rates were unchanged. The horizontal arrows report the velocity average per interval. As can be noticed, the air and water slugs' velocities are different.

Fig. 4.11 (b) shows the trend of a signal $\{ph2\}$ in the condition input flow rate
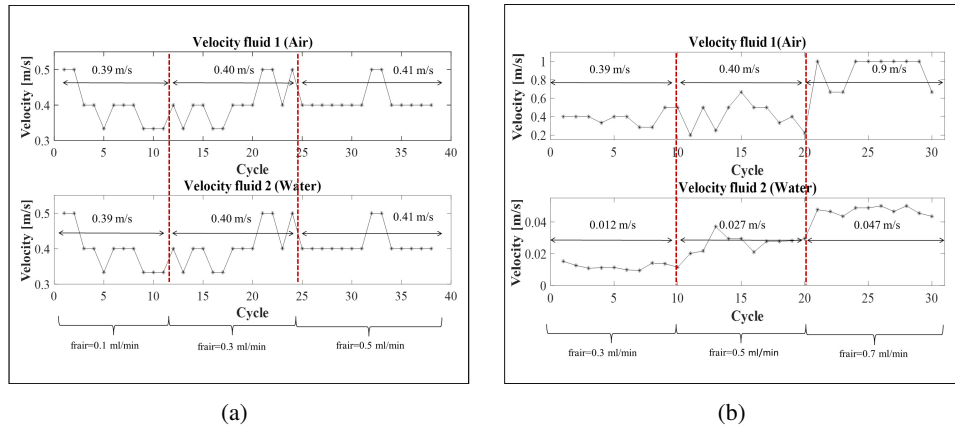
FIGURE 4.10: Velocity trends of the water and air fluids computed in real-time (a) in the serpentine micro-channel $G-320$ and (b) in the serpentine micro-channel $G-640$.
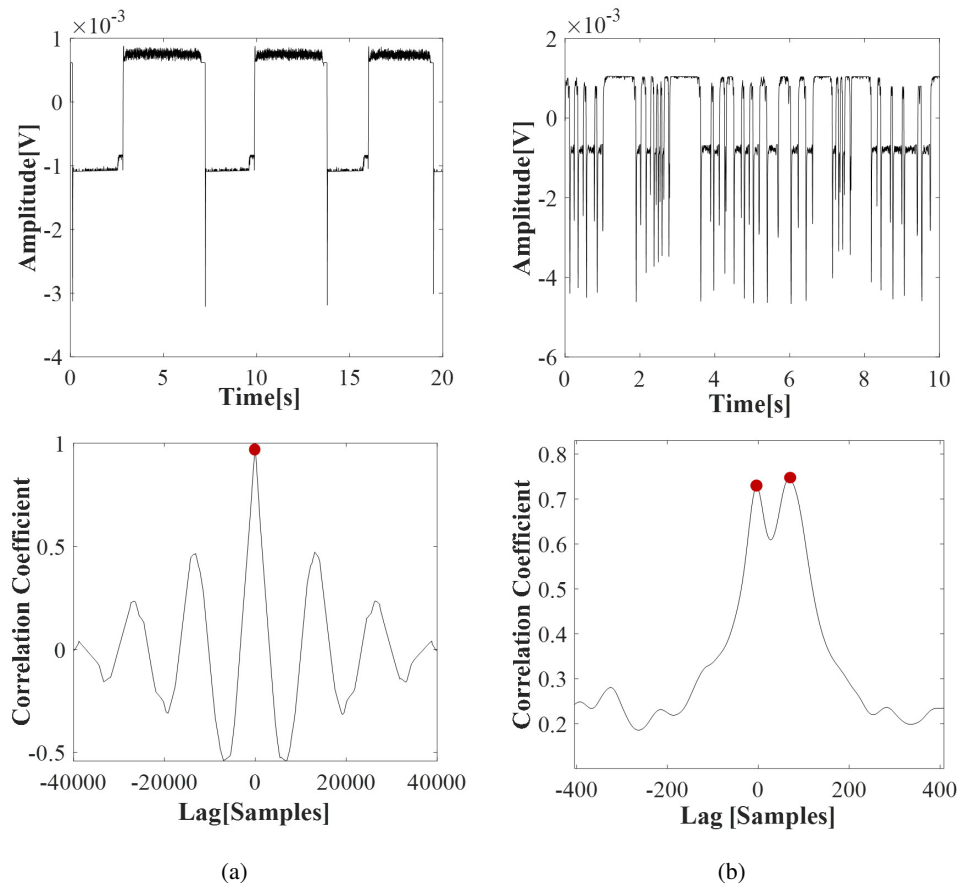
FIGURE 4.11: The trends of a signal $\{ph2\}$ and the cross-correlation functions: (a) in the serpentine micro-channel $G-320$ and (b) in the serpentine micro-channel $G-640$.

0.5 ml/min and the two peaks in the cross-correlation function. The trends of both air and water slugs' velocity increase throughout the entire experiment. On the other hand, the transient phase is not detectable in the first input condition $\{0.3\}$ ml/min, which is clearly visible in $\{0.5, 0.7\}$ ml/min.

In this experiment, it is important to notice that the process nonlinearity affects the air slug and water slug velocity differently. The air slug velocity increases in the

range $[0.2, 1.0]$ m/s; thus, in this case, variations of 0.1 m/s have a minor impact on the velocity detection.

As far as the water slug velocity is concerned, they are in the range $[0.01, 0.05]$ m/s, but, in this case, the variations detected are very small compared to the air slug velocity. The smoothness in the trend increases underlines the fact that the water flow is less affected by the process nonlinearity than the air flow.

Chapter 5

T-junction micro-optofluidic slug velocity detector

5.1 Micro-splitter characterization

In Section 1.4 of Chapter 1, it was presented the design and the realization of a micro-optical component able to guide and split the light into two paths. The micro-optical component, named micro-splitter (μSPT) was realized in two different materials, in Poly-dimethyl-siloxane (PDMS) and in VeroClear. Based on the materials used, two low-cost technologies were taken into account.

The PDMS-μSPT was manufactured by using a master-slave approach based on the 3D printing technique. For the characterization of this micro-component, a support structure was realized in a way that it was surrounded by air. It was 3D-printed having 4-pegs designed to touch as little as possible the PDMS-μSPT to minimize the rays dispersion (see Fig. 5.1 (a)). For the alignment of the input and output fibers with the PDMS-μSPT, two PDMS frames have been used to surround the holder with two slots for the fibers insertions, the same approach used in [9]. In Fig. 5.1 (a) at the center it is shown the mounting scheme and on the right a photo of the complete micro-optical characterization system (μOCS). The same approach was used for the realization of the μOCS for the VeroClear-μSPT.

The VeroClear-μSPT and the μOCS were directly 3D-printed by using an inkjet printer (Object260 Connexl, Stratasys). In Fig. 5.1 (b) the steps in the realization of theμOCS for the VeroClear-μSPT are reported, in particular on the left the bottom and top cover parts for the alignment of the fiber insertions, in the center, it is inserted the VeroClear-μSPT and on the right the complete μOCS.

5.1.1 Experimental set-up

The flowchart and the pictures of the experimental set-up, used for the PDMS-μSPT and VeroClear-μSPT characterization, are shown in Figs. 5.2 (a),(b) and (c).

The input light source is a laser system (RGB NovaPro Laser 660-125), that generates a light beam with a wavelength of 660 nm and a maximum output power
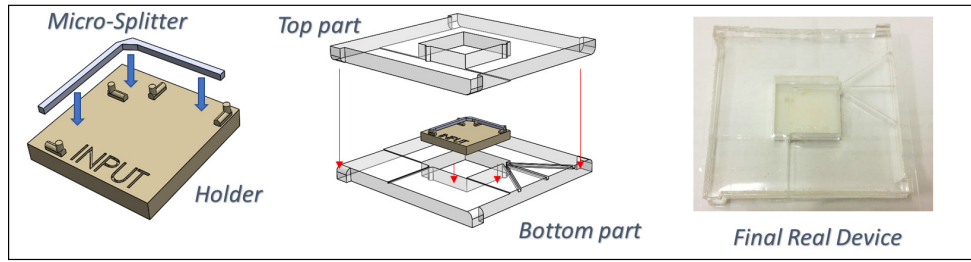
(a)
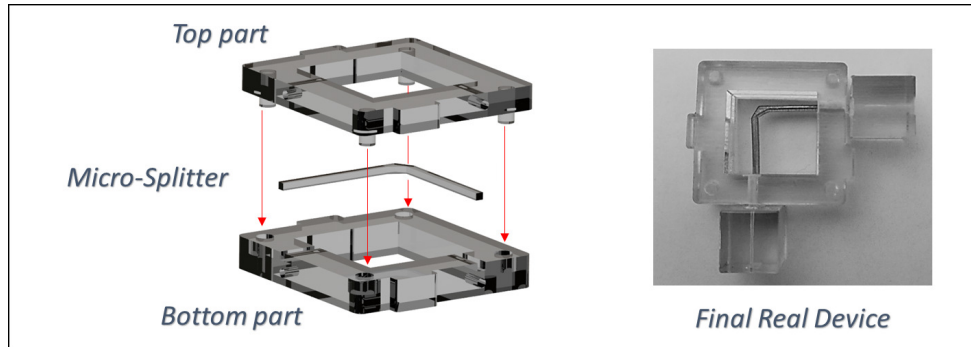
(b)

FIGURE 5.1: Steps in the realization of the PDMS and the VeroClear micro-optical characterization systems for (a) the PDMS-μSPT and (b) the VeroClear-μSPT. On the left, the holder designed to support the micro-optical component and the scheme of the holder with the top and bottom layers used for the alignment of the fibers; on the right, the photo of the complete micro-optical characterization systems.

of 125 mW. The output acquisition system consists of a photodiode with a gain of 0 dB (PDA100A, Thorlabs, Newton, NJ, USA) connected with a digital oscilloscope (Siglent SDS1102X) for the PDMS-μSPT and a PC oscilloscope (Picoscope 2204A, Pico Technology). The input and output of the μSPT are coupled by multi-mode optical fibers with core diameters $\{910 \pm 30; 365 \pm 14\} \mu m$ and $NA = 0.22$.

5.1.2 Experimental results

As introduced, in Section 1.4 of Chapter 1, the μSPT design was used both to guide and split the light rays. That suggests considering for the experimental set-up two different configurations of the output fiber alignment, as shown in Fig. 5.3 and described below.

- C1: one fiber insertion for an optical fiber is lined up with the output μSPT, as in a standard configuration with $d = 0.1$ mm (see Fig. 5.3 (a));

- C2: two fiber insertions for the optical fibers are arranged tilted of 36°, on the opposite side with respect to the main horizontal line of the output μSPT with $d = 0.5$ mm (see Fig. 5.3 (b)).

In Fig. 5.4 (a)-(b) the pictures of the PDMS-μSPT and the VeroClear-μSPT in the conditions of no-light passage and during the light-passage were shown.
Before proceeding with μSPT characterization, a calibration of the laser-photodiode system was performed. The input power laser was directly connected with the photodiode, using optical fibers of 910 μm and 400 μm, and varying the values of input
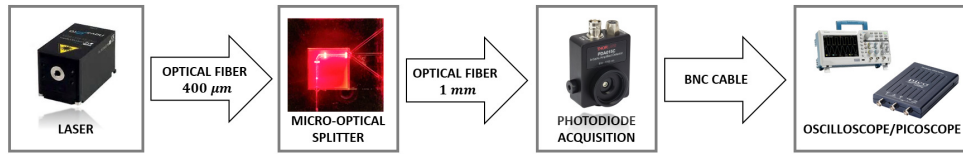
(a)
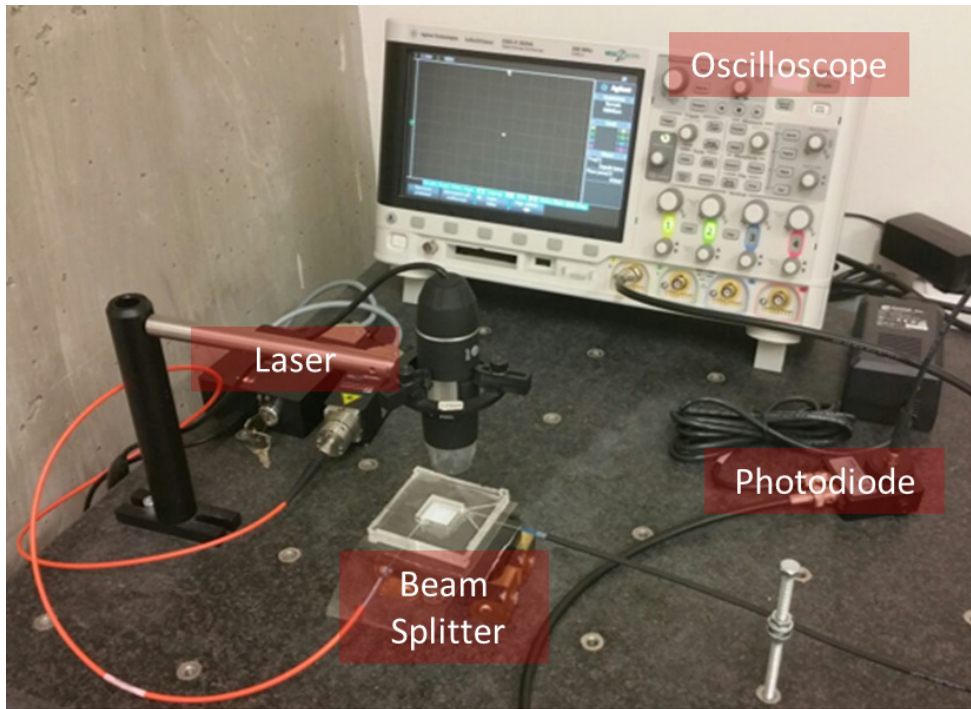
(b)
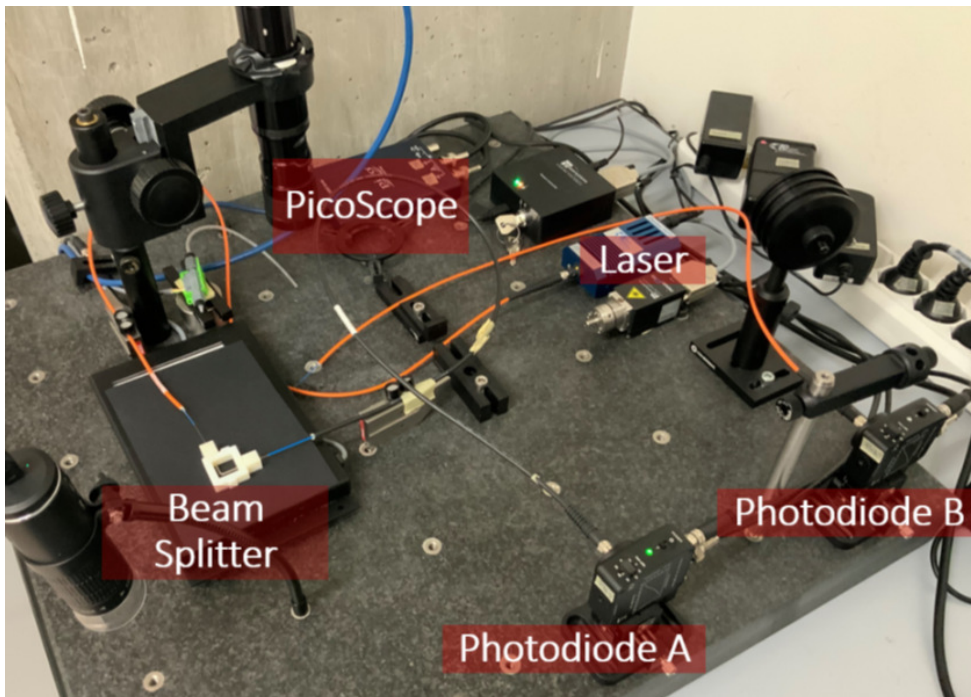
(c)

FIGURE 5.2: (a) The flow chart and the picture of the experimental set-up used for the micro-optical characterization of (b) the PDMS-μSPT and (c) the Vero-μSPT.

(a)   (b)
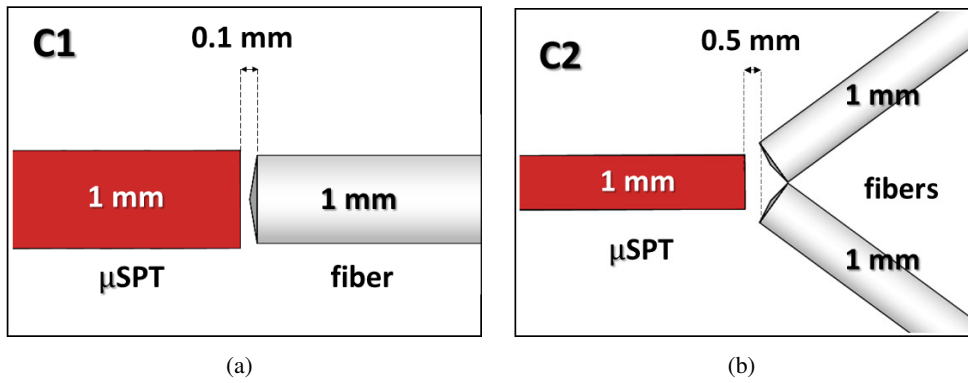
FIGURE 5.3: Two optical fiber arrangements of the μSPT with the d value were used. (a) One optical fiber is placed horizontally with respect to the waveguide (C1), (b) Two optical fibers are tilted, in opposite directions, of $36°$ respect to the waveguide (C2).

(a)

(b)
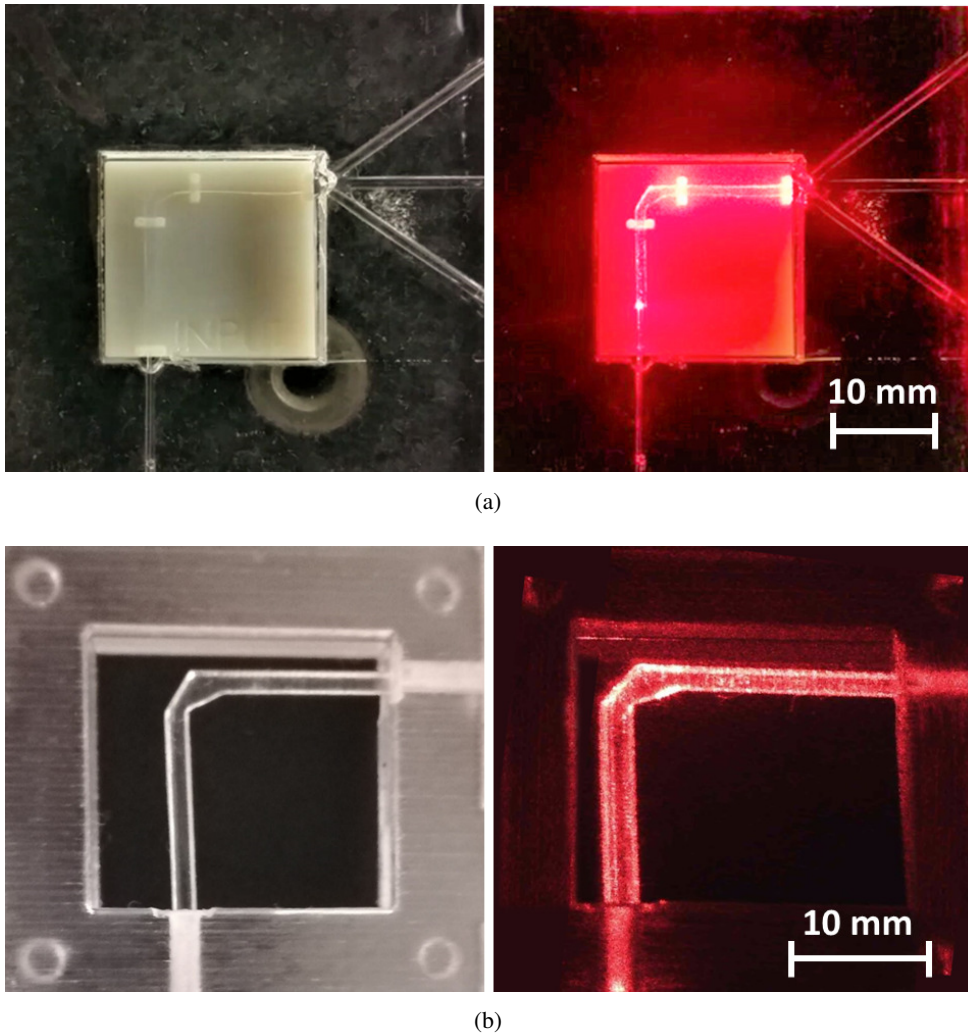
FIGURE 5.4: The pictures of the μSPT in the conditions of no-light passage and during the light-passage for (a) the PDMS-μSPT and (b) the VeroClear-μSPT.
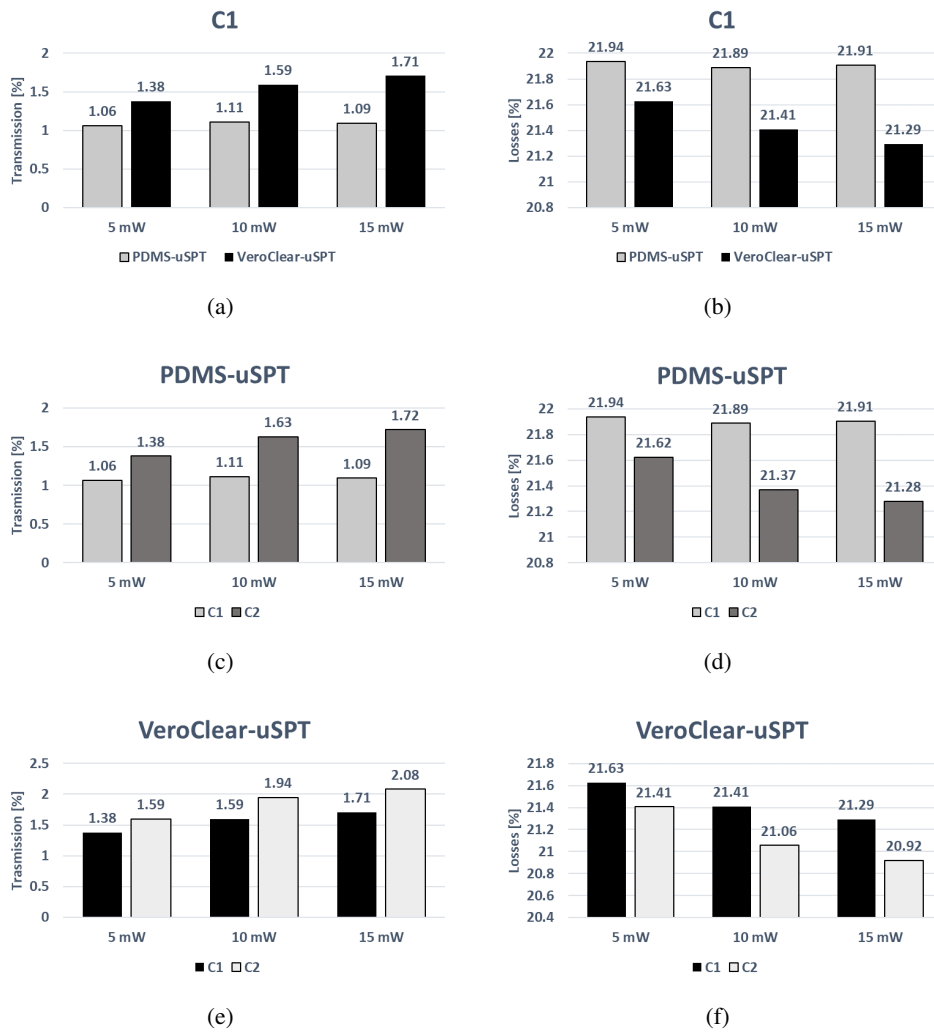
FIGURE 5.5: The Histograms of (a) transmission and (b) losses for the PDMS-μSPT and the VeroClear-μSPT in the arrangements C1 and the comparison for (c)-(e) the transmission and (d)-(f) losses in the arrangement $\{C1, C2\}$ with the PDMS-μSPT and the VeroClear-μSPT. The laser power at the input was varied in the set $\{5, 10, 15\} \, mW$.

power laser in the set $\{5, 10, 15\} \, mW$, the output values of voltage were reading from the photodiode.

After obtaining the input power-voltage calibration curve, the characterization of the micro-optical components was carried out. The laser coupled with a 400 μm optical fiber was placed at the input to the μSPT, varying its input power in the set $\{5, 10, 15\} \, mW$. At the output, the voltage values were acquired by means of the 1 mm optical fiber coupled with a photodiode. The distance d between the input-output fibers and the μSPT was set to 100 μm for the PDMS-μSPT and the VeroClear-μSPT in the first configuation (C1) and to 500 μm in the second configuration (C2). In order to understand the capability of the μSPTs to transmit light, the values of transmission were evaluated as the ratio between the output voltage reading and the input voltages reading obtained during the calibration phase. Taking into account the losses due to the coupled fibers with the μSPT in the input and the output of about 77%, obtained in [9], it was possible to calculate the losses in the μSPTs.

The histograms in Fig. 5.5 (a)-(b) report the values of transmission and losses in percentage for the experimental conditions C1 varying the laser power in the set

$\{5,10,15\}$ *mW* for the two materials investigated. It is evident that the PDMS-μSPT and the VeroClear-μSPT have the same value of transmission of about 1% and a losses percentage of 21.8%.

The histograms in Fig. 5.5 (c)-(d) report the values of transmission and losses in percentage for the experimental conditions $\{C1, C2\}$ varying the laser power in the set $\{5,10,15\}$ *mW* for the PDMS-μSPT and in Fig. 5.5 (e)-(f) for the VeroClear-μSPT. Despite the increase of the gap d the transmission globally detected is greater in configuration C2 with losses around 21.4% for both the μSPTs. Regarding the μSPT, looking at Fig. 5.4 (a), it is possible to localize the losses areas, the brighter spots of the picture, where the holder is in contact with the PDMS-μSPT. That confirms the possibility to split the information in two directions or using this set-up to maximize the acquisition.

Despite the fact that the VeroClear-μSPT is completely surrounded by air, with the exception of the input and output sections, with an air gap of $d = 100$-500 μm, the greatest losses occur in the input section.

However, from the results obtained, the VeroClear-μSPT appears to transmit more light than the PDMS-μSPT. Based on that results, it is possible to confirm the potential of the μSPT, in the cases investigated, the losses are not due to its design, but to the gap at the insertions and the surrounding material. The latter limitation, evident in the PDMS-μSPT, can be overcome by shielding this micro-optical component with other materials having a different refraction index to guarantee uniformity in the light path. The results presented are a proof of concept about the potential of creating micro-optical paths inside a micro-embedded device, an example can be found in a micro-optofluidic application discussed in [8] and at Section 1.4 of Chapter 1 where the micro-optical component just presented is integrated into a micro-optofluidic device. Its characterization is presented in the following section.

5.2 Slug velocity detector characterization

In this section, two embedded micro-optofluidic devices integrating the micro-optical components discussed in the section above, designed and realized in Section 1.4 of Chapter 1, were characterized to detect the slug frequency and the slug velocity considering a slug flow within the micro-channels.

The two embedded micro-optofluidic devices are a PDMS micro-optofluidic slug velocity detector integrating a VeroClear-μSPT, labeled as *Device-1* and a PDMS micro-optofluidic slug velocity detector integrating a gold PDMS-μSPT, labeled as *Device-2*.

To establish the velocity of the slug flow in the micro-channel, the data were analyzed in the time domain by using the dual-slit methodology, presented in [76] and in Section 4.3.1 of Chapter 4 of this thesis. Then, the slug frequency, corresponding to slug passage duration in time, was instigated by spectral analysis using the approach presented in [61] and in Section 4.3.2 of Chapter 4 of this thesis.

5.2.1 Experimental set-up

A continuous slug flow was generated by pumping de-ionized water and air to the T-junction inlets of the micro-optofluidic devices realized shown in Fig. 5.7 (b)-(c). The block scheme and the experimental set-up for the slug velocity flow characterization of the two micro-optofluidic slug velocity detectors are shown in Fig. 5.6 and Fig. 5.7 (a).

Two syringe pumps (neMESYS low-pressure module, Cetoni GmbH, Korbussen, Germany) were connected to the two channel inlets and different flow rates were imposed. The input light source was a laser system (NovaPro 660-125, RGB Lasersystems, Kelheim, Germany) that generates a light beam with a wavelength of 600 nm and a maximum output power of 1 mW. As displayed in the block scheme of Fig. 5.6, it was implemented as a simultaneous acquisition. The light intensity variation, split into two paths was acquired using two photodiodes with a gain of 70 *dB* (PDA100A, Thorlabs, Newton, NJ, USA) and the signal received was acquired by a PC oscilloscope (Picoscope 2204A, Pico Technology, Cambridgeshire, UK), with a sampling frequency of 1.5 KHz. For a visual inspection of the process, a digital USB microscope placed above the device, was used.

To validate the optical information by the two PDMS micro-optofluidic devices, a flow meter (SLF3S-1300F, Sensirion, Stäfa, Switzerland), with a sampling frequency of 200 Hz, was placed at the outlet of the devices, which was connected with the flow meter through a Tygon tube with an inner diameter of 1.3 mm.
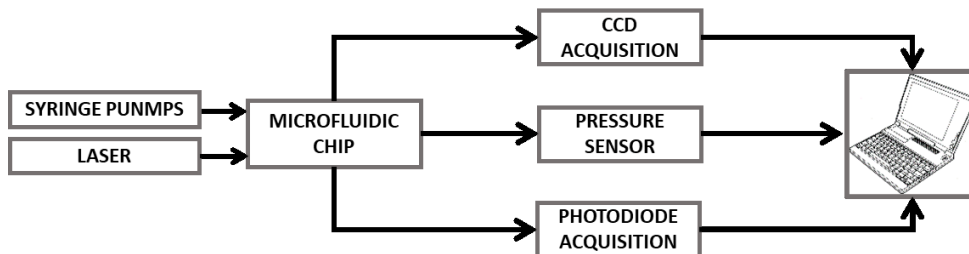
FIGURE 5.6: Block scheme of the experimental set-up.
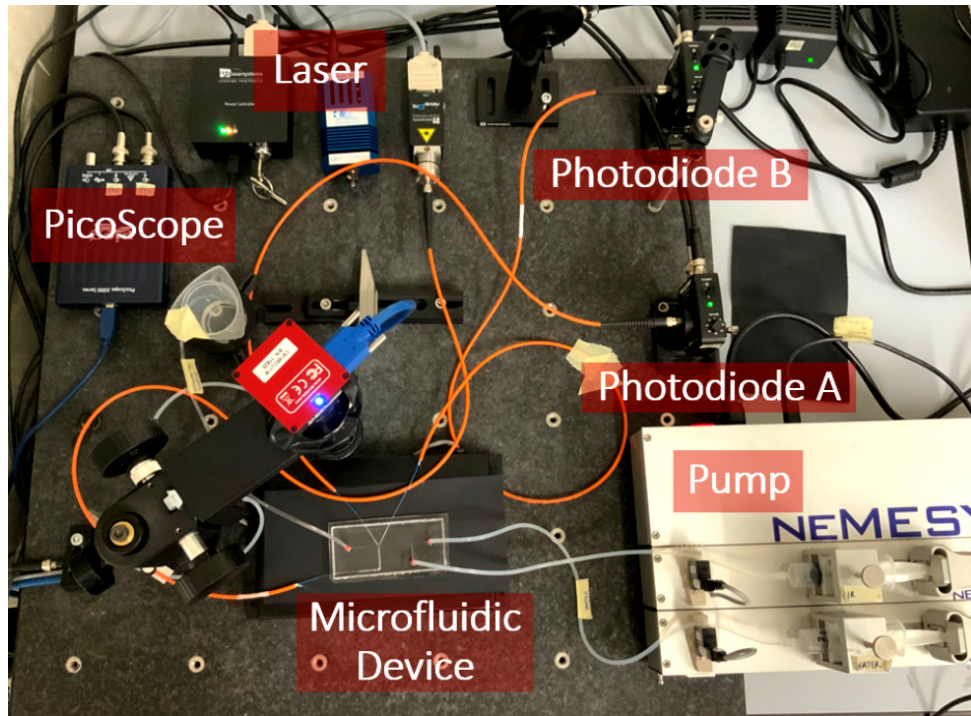
(a)
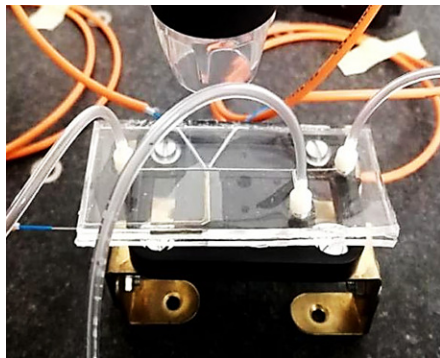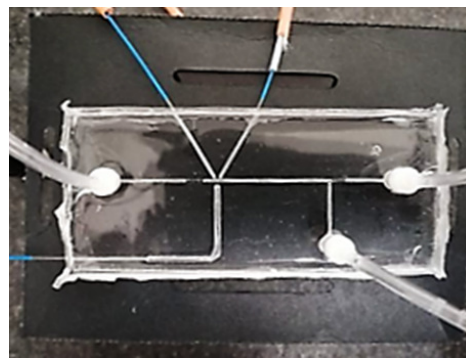
(b)   (c)

FIGURE 5.7: Pictures of (a) the experimental set-up for the slug velocity flow characterization, (b) the PDMS micro-optofluidic slug velocity detector integrating a gold PDMS-μSPT and (c) the PDMS micro-optofluidic slug velocity detector integrating a VeroClear-μSPT.

5.2.2   Experimental campaigns and data analysis

In the experimental campaign, a total of 25 experiments, 15 for *Device-1* and 10 for *Device-2* were carried out to test the correct functioning of the realized PDMS devices and to evaluate the variation between the two-phase flow velocities inside the micro-channel.

Flow's fluid dynamic evaluation was carried out by varying both the hydrodynamic pressure at the inlet of the devices and the power of the laser light used to visualize the process, as summarized in Table 5.1.

The data acquired were pre-processed by a low-pass filter with a 40 Hz cut-off frequency and a signal smoothing procedure. In the processing phase, the 50 signals acquired from both the photodiodes, connected at the output fibers insertions present

	Devices	Laser input [mW]	Flow rate [ml/min]					
Exp-1	**D1**	1	0.025	0.05	0.1	0.2	0.3	0.4
Exp-2	**D1**	5	-	0.05	0.1	0.2	-	-
Exp-3	**D1**	10	-	0.05	0.1	0.2	-	-
Exp-4	**D1**	25	-	0.05	0.1	0.2	-	-
Exp-5	**D2**	25	0.025	0.05	0.1	0.2	0.3	0.4
Exp-6	**D2**	50	-	0.05	0.1	0.2	-	-

TABLE 5.1: Experimental campaigns carried out, varying the power of the laser used to light the process and the hydrodynamic pressure $V_{air} = V_{water}$, for both the micro-optofluidic devices.

in the micro-optofluidic devices, were analyzed both in time and frequency domains to automatically detect the frequency and the velocity of the slug passages. The used methodology is widely described in Section 4.3 of Chapter 4. The optical monitoring system placed in the investigated area of the devices, composed of a laser light and two phododiodes integrated into the devices by optical fibers insertions, allows the capturing of the light split into two paths and the variation in the luminosity during the slug passage, due to the difference between the refraction index (n) of the PDMS device material ($n_{PDMS} = 1.41$), air ($n_{air} = 1$) and water ($n_{water} = 1.3$).

Thanks to this phenomenon, the air and liquid passages were detected in the optical signal at two brightness levels. The top level revealed the liquid presence, the low level revealed the air passage, and the two peaks revealed the air in the front and at the rear, as already shown in Fig. 3.4 (a). The flow monitoring system placed at the outlet of the devices, composed of a flow meter, measures the water flow rate, i.e. the velocity of the fluid.

Thanks to this system, the optical information was validated by the flow meter signal, which identifies the air and water passages on two levels. The top level reveals the water presence, the low level the air passage, a negative peak reveals the air slug front and a positive peak the air slug rear as already shown in Fig. 3.4 (b).

5.3 Results and discussion

5.3.1 Slug frequency measurements by spectral analysis

The spectral analysis, presented in Section 4.3.2 of Chapter 4 of this thesis, allows evaluating the slug frequency, corresponding to the slug passage duration in time, analyzing the optical signals acquired from the photodiodes integrated inside the devices. Being the otpical information acquired from the two photodiodes $\{PH_1; PH_2\}$ almost similar, only the information of one photodiode $\{PH_1\}$ was used.

In Fig. 5.8 (a)-(b) the raw and the filtered optical signal acquired in *Device-1* for Exp-3 with an input flow rate of 0.1 ml/min are shown. In particular, in the filtered signal a square wave in red was overlapped, which ranges between two values, to identify the passage period of water (T_w) and air slug (T_a). Computing the spectrum of the optical signal acquired, it was possible to evidence the frequency peak (f), as shown in Fig. 5.8 (c), related to the inter-distance of slug passage.

After studying the optical signal from the photodiode, the flow meter signal from the flow sensor is analyzed in order to validate the optical signal acquired in the test section of the device. In Fig. 5.9 (a)-(b) the raw and the filtered flow meter signal
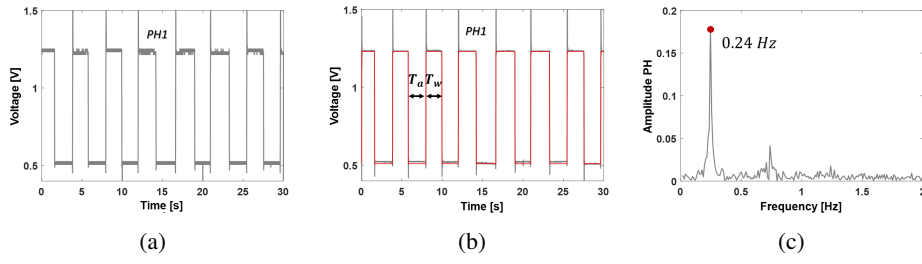
FIGURE 5.8: Optical acquisition by photodiode-based set-up in time and frequency domain for *Device-1* in Exp-3 with an input flow rate of 0.1 *ml/min*. (a) Raw and (b) filtered optical signals with a square wave (red line) overlapped to the filtered signal, which ranges between two values marking the passage period of water (T_w) and air slug (T_a); (c) spectrum of the optical signal.
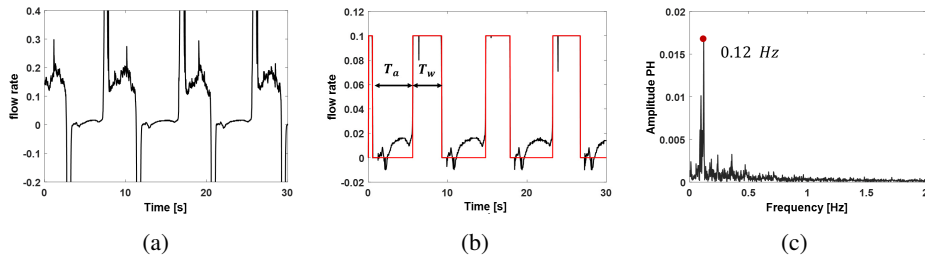
FIGURE 5.9: Flow meter acquisition by flow meter-based set-up in time and frequency domain for the *Device-1* in Exp-3 with an input flow rate of 0.1 *ml/min*. (a) Raw and (b) filtered flow meter signals with a square wave (red line) overlapped to the filtered signal, which ranges between two values marking the passage period of water (T_w) and air slug (T_a); (c) spectrum of flow meter signal.

acquired in *Device-1* for Exp-3 with an input flow rate of 0.1 *ml/min* are shown. In particular, in the filtered flow meter signal a square wave in red was overlapped, which ranges between the high level of water flow rate of 0.1 *ml/min* and 0 *ml/min* related to the air flow rate. Even if the flow rate of air is 0.1 *ml/min*, it is set to zero. Even in this case, by computing the spectrum of the flow meter signal acquired, it was possible to evidence the frequency peak (f), as shown in Fig. 5.9 (c), related to the inter-distance of slug passage.

The same trends were obtained for all the experiments carried out reported in Table 5.1 for *Device-1* and *Device-2*. After having obtained, by using the spectral analysis, the peaks values with the photodiode-based set-up and the flow meter-based set-up, it was possible to obtain the mean period of the slug flow, correlated with the inter-distance of slug passage, by using the equation in 5.1 where T is the inverse of the frequency peak (f) obtained from spectra and $< T_a >$ and $< T_w >$ are the mean period of water and air slug.

$$T = \frac{1}{f} = < T_a > + < T_w > \qquad (5.1)$$

In Fig. 5.10 (a)-(b) the mean period of slug flow detected by the photodiode-based set-up for *Device-1* and *Device-2*, respectively, are reported for all the experimental conditions. Meanwhile, in Fig. 5.11 (a)-(b) the mean period of slug flow detected by the flow meter-based set-up for *Device-1* and *Device-2*, respectively, are reported for all the experimental conditions.
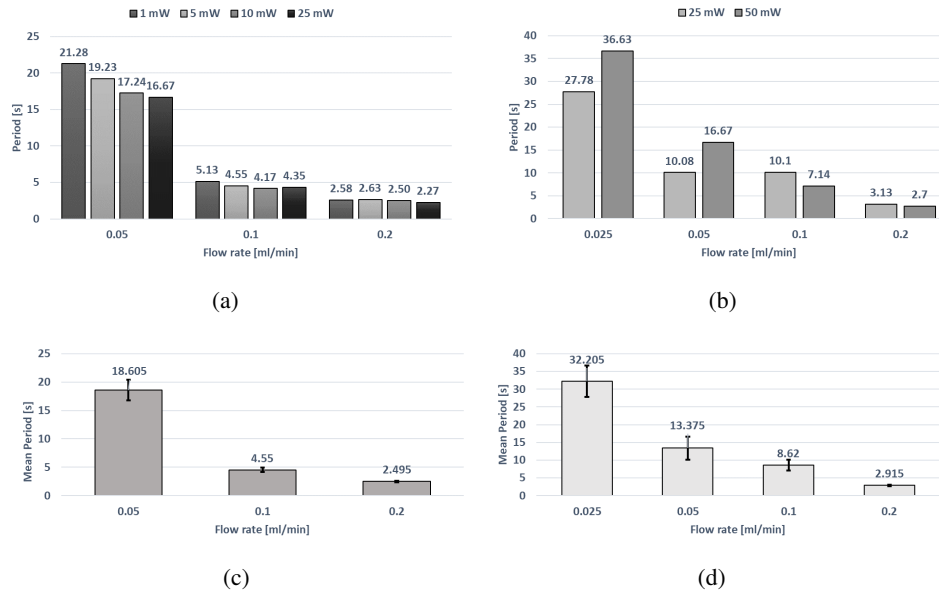
FIGURE 5.10: Mean period of slug flow detected by the photodiode-based set-up varying the laser light power for (a) *Device-1* and (b) *Device-2*. Mean period of the slug flow detected by the photodiode-based set-up averaged across the laser light power values for (c) *Device-1* and (d) *Device-2*.

Looking at these results, the slug passage, detected by the flow meter-based set-up, lasts twice than the slug passage detected by the photodiode-based set-up. This is due to the change of geometry and lengths along the path.

Other important results are that, even if the laser power is varying, the slug passage at an input flow rate is always more or less the same and increasing the flow rates the duration of the slug passages decreases becoming faster.

In Fig. 5.10 (c)-(d) and Fig. 5.11 (c)-(d) the mean period of the slug flow detected by the photodiode-based set-up and the flow meter-based set-up, respectively, was calculated by averaging the values of the same operating conditions of flow rate at the micro-channel inlet across the laser light power values for both devices. This confirms the robustness of the devices and of the optical and flow meter systems that allow the detection of the slug flow.

In addition, by computing a comparison with the system adopted in Chapter 4 of this thesis, where the same methodologies of analysis were adopted, there is a substantial difference between the two micro-channel adopted; in Chapter 4, a square-section serpentine channel with a side of 320 μm was used, while in this Chapter, a square-section rectilinear channel with a side of 400 μm was adopted. Thus, the dynamics of the slug flow within the straight micro-channel is different from that within the serpentine micro-channel and is more stable.

From this, it follows that, from the analysis in both the time domain and the frequency domain, no differences in the period of the slug passage of the two fluids under examination were found in the straight channel as was found in Chapter 4. The aspects and considerations just discussed apply equally to the calculation of slug flow velocity through the application of dual-slit methodology. As a possible future development, targeted experimental campaigns can be planned to investigate these aspects further.
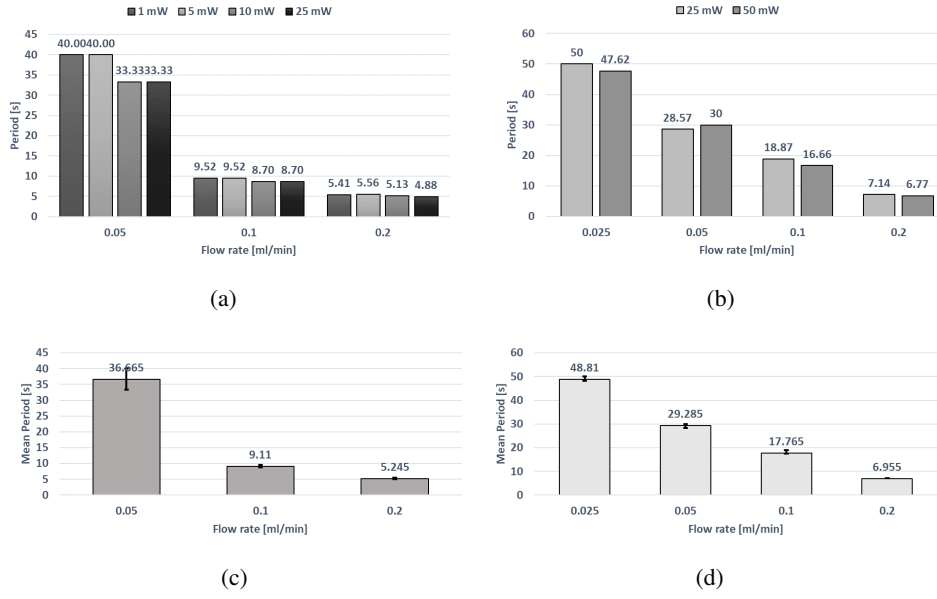
FIGURE 5.11: Mean period of slug flow detected by the flow meter-based set-up varying the laser light power for (a) *Device-1* and (b) *Device-2*. Mean period of the slug flow detected by the flow meter-based set-up averaged across the laser light power values for (c) *Device-1* and (d) *Device-2*.

5.3.2 Slug velocity measurements by dual-slit methodology

The dual-slit methodology, presented in Section 4.3.1 of Chapter 4 of this thesis, allows evaluating the slug velocity analyzing the optical signals acquired from the photodiodes $\{PH_1; PH_2\}$ integrated inside the devices.

In Fig. 5.12 (a)-(b) the raw and the filtered optical signals acquired by the two photodiodes $\{PH_1; PH_2\}$ in *Device-1* for Exp-3 with an input flow rate of 0.1 ml/min are shown. In particular, in the filtered signal a square wave in red was overlapped, which ranges between two values, to identify the passage period of water and air slug as done in Fig. 5.8 (b).

The cross-correlation function between the optical signals acquired by the two photodiodes $\{PH_1; PH_2\}$ was computed to evaluate the slug velocity as shown in Fig. 5.12 (c). The peak detected in the cross-correlation indicates the time delay of the two optical signals and can be correlated with the time needed by the slug flow to pass from one investigation point $\{PH_1\}$ to the next one $\{PH_2\}$. Being the distance (d_{ph}) between the two photodiodes of 1 mm, it is possible to compute the slug velocity by using the equation in 5.2 where n is the delay in samples between the two photodiodes and T_s the sampling period of 0.66 ms used during the acquisition. In Fig. 5.12 (c) the number of samples detected is 109 *samples* for an input flow rate of 0.1 ml/min and by applying the eq. 5.2 a slug velocity of 0.011 m/s is obtained.

$$v_{slug-exp} = \frac{d_{ph}}{n \cdot T_s} \tag{5.2}$$

$$v_{slug-anal} = \frac{Flow\ rate}{Area} \tag{5.3}$$

In Fig. 5.13 the slug velocity values for *Device-1* in Exp-1 and *Device-2* in Exp-5 are reported.
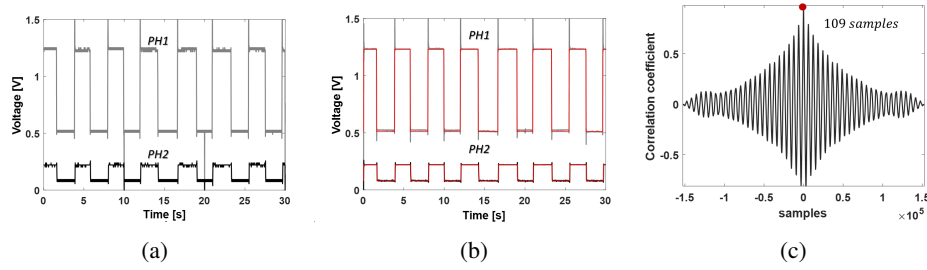
FIGURE 5.12: (a) Raw and (b) filtered optical signals acquired by the two photodiodes $\{PH_1; PH_2\}$ for *Device-1* in Exp-3 with an input flow rate 0.1 ml/min and (c) the cross-correlation between the signals acquired through the two photodiodes for the computation of the slug velocity.
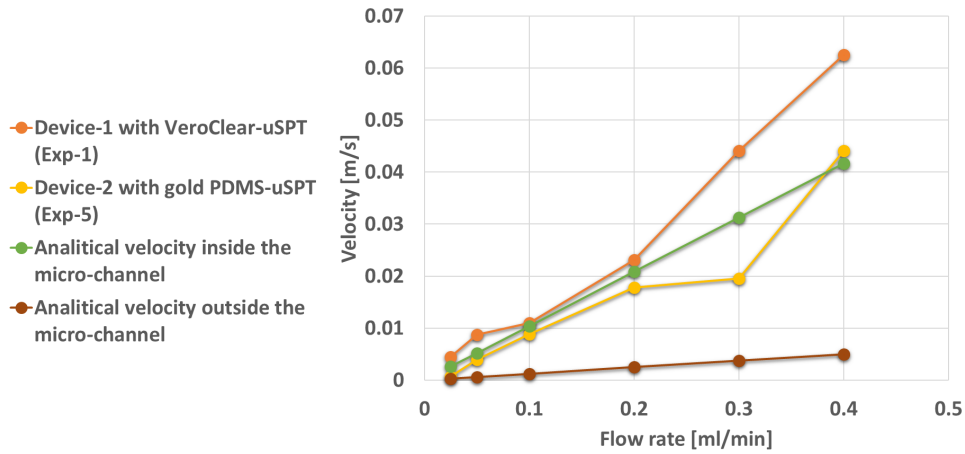
FIGURE 5.13: Slug velocity values obtained for *Device-1* in Exp-1 and *Device-2* in Exp-5 compared with the slug velocity values obtained analytically inside the micro-channel and outside the micro-channel for the input flow rates $\{0.025; 0.05; 0.1; 0.2; 0.3; 0.4\}$ ml/min.

	Devices	Trial No.	Flow rate		
			0.05 ml/min	0.1 ml/min	0.2 ml/min
			Slug Flow velocity [m/s]		
Exp-1	**D1**	1	0.0093	0.0117	0.0211
Exp-2	**D1**	2	0.008	0.0111	0.0224
Exp-3	**D1**	3	0.0075	0.0132	0.0214
Exp-4	**D1**	4	0.0065	0.0129	0.0197
Average			0.0078	0.0122	0.0211
STD			0.001	0.0008	0.0009
Exp-5	**D2**	1	0.0044	0.0073	0.0147
Exp-6	**D2**	2	0.0042	0.013	0.025
Average			0.0043	0.0101	0.0147
STD			0.0001	0.0028	0.0051

TABLE 5.2: Computation of the slug flow velocity accuracy by means of average value and standard deviation varying the hydrodynamic pressure $V_{air} = V_{water}$, for both the micro-optofluidic devices.

In order to validate the obtained slug velocity values, the slug velocity inside the micro-channel was evaluated analytically and to confirm the results achieved with the spectral analysis the slug velocity was evaluated analytically outside the device in a tube with a diameter of 1.3 *mm*. As shown in eq. 5.3 to compute analytically the slug velocity inside and outside the device, the input flow rates imposed were firstly converted from *ml/min* to m^3/s and secondly divided by the area of the micro-channel, with a squared section and a diameter of 400 μm and the area of the tube, with a circular section and a diameter of 1.3 *mm*, respectively.

In Fig. 5.13 the slug velocity values obtained analytically inside the micro-channel and outside the micro-channel for the input flow rates $\{0.025; 0.05; 0.1; 0.2; 0.3; 0.4\}$ *ml/min* are reported and compared with those obtained for *Device-1* in Exp-1 and *Device-2* in Exp-5. Looking at this plot, it is evident how the slug velocity values obtained experimentally follow analytically the slug velocity values evaluated inside the device and, the analytically slug velocity values evaluated outside the device confirm the results obtained with the spectral analysis by using the flow meter-based set-up.

Finally, in order to provide robustness to the implemented methodology and the realized PDMS devices, an analysis of the accuracy and resolution of the dual-slit methodology was carried out by computing the mean and the standard deviation for several trials considering $\{0.05; 0.1; 0.2\}$ *ml/min* as input flow rates. Table 5.2 shows the slug velocity values obtained at several input flow rates and repeated several times, and it is also shown the computation of the average and of the standard deviation for both devices. From this last result, it can be concluded that the methodology is robust and the obtained performance more than satisfactory.

Chapter 6

System for slug flows active control

Two-phase microfluidics has recently made contributions to several scientific disciplines, including chemistry, biology, and medicine [83]. Its main objective is to explore bi-phase flows that are produced in networks of micro-channels using two immiscible fluids or a mixture of fluid and micro-particles [3]. A wide range of flow regimes can be obtained as a result of the different phases that can take various forms in micro-channels [4].

In contrast to what occurs in macro metric hydrodynamics, rather less attention has been paid to biphasic flows in micro-systems. Although there are some experimental results published in the literature, there is still no solid foundation for reliably controlling the system flow [59].

Two-phase microfluidic processes can be actively or passively controlled. Passive control can produce specific flow patterns by exploiting the micro-channel geometrical characteristics and the physical properties of the fluids involved in the process (i.e. hydrophobicity [84], the frictional force between fluids and channel walls [85]). These methodologies avoid the need for new energy sources and reduce equipment complexity and cost without sacrificing efficiency.

Nevertheless, in some cases, it might be advantageous to quickly and precisely alter the flow patterns or deliver regulated fluid amounts in micro-channels. As a result, various techniques and tools have been developed and applied in recent years.

In [86], the magnetic field has been utilized to confine molecules and direct their movement in a condensed fluid phase. In [87], a mechanical pump has been developed for precision fluid handling, while pneumatic pressure has been employed in [88] to realize transportation, metering, and mixing of picoliter-sized liquid samples.

In [89], the mechanical pump configuration has been accompanied by an optical and signal-based process monitoring system for the active control of the two-phase process. Besides, the results of a closed control scheme and an open control loop have been compared. A real-time feed-forward compensator [75], which acts directly at the flow rate level of the mechanical pumps, enables the regulation of the required

frequency of slug flow.

Model Predictive Control (MPC), an approach capable of using the system's dynamic model to predict its behavior over a finite receding horizon, has already been used to manipulate colloidal anisotropic Brownian particles over defined trajectories in position and orientation [90].

In the context of two-phase flows, MPC has been employed to control the spatial dynamics of slug in a microfluidic network [65]. The output slug frequency has been obtained by directly regulating the elastomeric valves with the MPC action.

However, the authors assume that the input slug frequency has been maintained constant throughout the experimental validation and the output slug frequency has been obtained by directly controlling the elastomeric valves with the MPC action.

In this study, to avoid utilizing extra hardware in the micro-device, such as elastomeric valves, a slug flow of liquid has been generated in a 3D-printed micro-optofluidic device by regulating the desired output slug frequency through an MPC approach acting directly on the flow rate.

Given a desired output slug frequency, the MPC, which makes use of a data-driven identified model, regulates the flow rate of a syringe pump creating the desired alternation at the outlet of the device. A two-phase process is a highly nonlinear and unstable process. The application of MPC allows for controlling these processes effectively. Predictive efficiency, the possibility of easily adding design constraints and the management of control by model offer considerable advantages, in which other types of control are difficult.

However, the flow identification directly linked to the experimentation is crucial in helping to ease and solve computational fluid dynamics problems, since the properties of the fluids, the input flow conditions, the microfluidic device material, and the geometry of the channel can all have a significant impact on the system dynamics [74].

In addition, an experimental campaign showed that the whole framework, i.e. the pump, the micro-optofluidic device, the detection and control systems, which allow the fluid flow inside the microfluidic device to be monitored and controlled, was designed and could be integrated into a simple, inexpensive and portable system.

6.1   Model Predictive Control: theoretical background

Model Predictive Control (MPC) is an advanced method of designing and implementing feedback control systems and used to control a process while satisfying a set of constraints.

In [91], it is reported a perfect example that highlights the potential of this control technique, comparing it with real cases applicable to the human way of thinking. In particular, it is reported that the MPC approach is practically very similar to the way a player faces a chess game.

As soon as the game starts, a chess player tries to predict all possible future moves before making a move. It is impossible to extend these predictions until the end of the game, in two respects: the time required is limited and computationally complicated. Therefore, the player is limited to predicting a finite time horizon. Given his prediction, the player chooses the move he thinks is best (optimal). The ability to make a decision depends on two factors: a well-defined notion of what qualities make an optimal outcome and the decisions made previously.

Once the opposing player has made a move, the player repeats the prediction process based on the new situation. If the opponent has made a predicted move, the player

need only add another step to his previous prediction. If the opponent's move was unexpected, the player repeats the prediction taking into account the new state. This iterative process is repeated until the end of the game.

Prediction is only possible for a finite number of steps because the cost and complexity of prediction increase very rapidly with the number of steps. It is also necessary to decide on a move. This decision must be excellent and thus requires a performance estimate, a criterion that can be used to evaluate possible moves. The Model Predictive Control approach is essentially based on this way of thinking.

From a theoretical point of view, the basic idea of an MPC is to use a mathematical model of the system to be controlled to predict its behavior. It follows from this that the choice and the quality of the system model can drastically affect the success of the control action.

The overall goal of the MPC design is to compute a trajectory of a manipulated input variable u in the future to optimize the future behavior of the actual output of system y. The optimization is performed within a limited time window, providing information about the system at the beginning of the time window. The design of an MPC control system requires the analysis and evaluation of some particular parameters and functions needed for the final control. A classic block diagram of a system controlled by MPC is shown in Fig. 6.1.

The first parameter to evaluate and consider is the prediction horizon. It represents
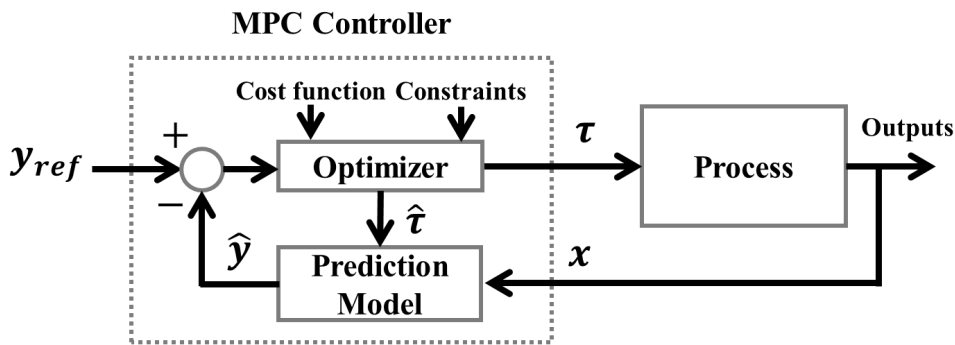
FIGURE 6.1: Classic block diagram of a system controlled by MPC.

the time window over which to predict the system model.

When the prediction is made through the model, the optimal trajectory of the future control signal along the prediction horizon is fully described. The control horizon defines which control signals, among all those determined within the prediction horizon, should be set as control inputs to the real system.

Typically, the actual control input to the real system involves using the first sample of the control signal, neglecting the rest of the trajectory, so that it can be reprogrammed in the next iteration. To predict the future evolution of the system and determine the control action, it is necessary to know the state of the system each time the prediction is to be made. This information must be taken from the actual system to bring the system model to its state.

As mentioned above, the MPC is an optimal controller and therefore requires the use of a criterion to make the optimal decision. The criterion is related to a function, called the objective function or cost function. The optimal control action is found by minimizing this cost function within the optimization window. In addition, a great advantage of the MPC approach is that constraints can be integrated very easily. These constraints can be generic, but they generally relate to how the control

action can interact with the system. Those just mentioned are the main features and parameters with which an MPC controller is designed.

This methodology has significant advantages in the control of systems; these controllers are based on dynamic models and are therefore able to satisfy multiple constraints simultaneously, taking into account time constraints.

Another key advantage of MPC over other optimal control methods is that its finite horizon allows a convenient trade-off between the online computational load to solve the minimum principle and the goodness-of-fit of the control action.

After having seen in a general way what MPC control is, it is possible to distinguish two macro areas in which this approach differs radically, linear and nonlinear MPC. It is easy to see how this choice is strongly conditioned by the type of system model available. As mentioned earlier, the basic MPC has advantages from a computational and robustness point of view, so when linearization of the system is possible, the linear approach can be used. However, when the approximation is excessive, the problem of uncertainty in the model begins to predominate, so in these cases, it is good to switch to a nonlinear MPC approach.

In the next section, the theoretical formulation for linear MPC control will be given, as it will be used later to control the frequency of slug passage within the micro-optofluidic device.

6.1.1 Linear MPC

A linear SISO (Single-Input Single-Output) system in the state space, described in eq. 6.1, where u is the input variable, y is the system output and x is the state variable vector with dimension equal to n, is considered.

$$\begin{cases} x(k+1) = A \cdot x(k) + B \cdot u(k) \\ y(k) = C \cdot x(k) + D \cdot u(k) \end{cases} \tag{6.1}$$

In the system considered, it is assumed that the input variable $u(k)$ does not affect the output of the system $y(k)$, so the matrix $D = 0$. The model in the proposed state-space form takes into account only the input variable at the time instant k.

However, it is possible to extend the model to enter some additional information about its past 'history'. For this purpose, it is necessary to introduce an integrator that takes into account the previous samples by making an extended model that considers the expressions written below, which represent the increment of the variables X and U.

$$\Delta x(k+1) = x(k+1) - x(k)$$

$$\Delta x(k) = x(k) - x(k-1)$$

$$\Delta u(k) = u(k) - u(k-1)$$

In this way, it is possible to formulate the eq. 6.1 of the state space in terms of memory by the eq. 6.2.

$$\Delta x(k+1) = A \cdot \Delta x(k) + B \cdot \Delta u(k) \tag{6.2}$$

The next step is to relate the variation of the state $\Delta x(k)$ with the output of the system $y(k)$.

To do this, it defines a new system in the state space having the state vector represented as follows:

$$x_{mpc}(k) = [\Delta x(k)^T \quad y(k)^T]$$

Similarly, with the state, the output variation is expressed as in eq. 6.3.

$$
\begin{aligned}
y(k+1) - y(k) &= C \cdot (x(k+1) - x(k)) = \\
&= C \cdot \Delta x(k+1) = \\
&= C \cdot A \cdot \Delta x(k) + C \cdot B \cdot \Delta u(k)
\end{aligned}
\tag{6.3}
$$

By combining the eqs. 6.2 and 6.3, it is possible to obtain the extended state space of eq. 6.4, where $o_m = [0 \quad 0 \quad \ldots \quad 0]$ with dimension n, equal to the dimension of the original state vector of the initial model.

$$
\begin{cases}
\overbrace{\begin{bmatrix} \Delta x(k+1) \\ y(k+1) \end{bmatrix}}^{x_{mpc}(k+1)} = \overbrace{\begin{bmatrix} A & o_m^T \\ C \cdot A & 1 \end{bmatrix}}^{A_{mpc}} \cdot \overbrace{\begin{bmatrix} \Delta x(k) \\ y(k) \end{bmatrix}}^{x_{mpc}(k)} + \overbrace{\begin{bmatrix} B \\ C \cdot B \end{bmatrix}}^{B_{mpc}} \cdot \Delta u(k) \\[3em]
y(k) = \underbrace{\begin{bmatrix} o_m^T & 1 \end{bmatrix}}_{C_{mpc}} \cdot \underbrace{\begin{bmatrix} \Delta x(k) \\ y(k) \end{bmatrix}}_{x_{mpc}(k)}
\end{cases}
\tag{6.4}
$$

$$
\begin{cases}
x_{mpc}(k+1) = A_{mpc} \cdot x_{mpc}(k) + B_{mpc} \cdot \Delta u(k) \\
y(k) = C_{mpc} \cdot x(k)
\end{cases}
\tag{6.5}
$$

The triplet $(A_{mpc}, B_{mpc}, C_{mpc})$ is called the augmented model, which will be used in the design of Model Predictive Control.

MPC algorithms use a dynamic model of the system under investigation, and the use of augmented models, in this particular case, is a promising means of extending these algorithms and adapting them to practical problems. Augmenting a model thus describes the act of adding additional dynamics to an existing model of the system. These additional dynamics can represent, for example, disturbances acting on the system, or they can be used to model the variation of parameters of the system's dynamic equations. The advantage of augmented models is that they do not conceptually change the underlying algorithm, thus preserving most or all of its properties. Now that the model has been defined, it is possible to move on to the actual design of predictive control. In particular, the aim is to predict and estimate the outputs of the process and the control signal starting from a generic instant k_i, using the newly identified extended model.

The first step is to define the prediction horizon N_p, the number of future control intervals the MPC controller must evaluate by prediction when optimizing its manipulated variables within the control interval, and the control horizon N_c, the number of

the manipulated variables moves to be optimized within the control interval.
After that, from the knowledge of $x_{mpc}(k_i)$, it is necessary to estimate the parameters
written below, where $x_{mpc}(k_i + m | k_i)$ represent the predicted state variable at instant
$k_i + m$ given the current real system information $x_{mpc}(k_i)$.

$$\Delta u(k_i), \quad \Delta u(k_i + 1), \quad \ldots, \quad \Delta u(k_i + N_c - 1)$$

$$x_{mpc}(k_i + 1 | k_i), \quad x_{mpc}(k_i + 2 | k_i), \quad \ldots, \quad x_{mpc}(k_i + N_p | k_i)$$

The future state variable can be calculated sequentially as follows:

$$x_{mpc}(k_i + 1 | k_i) = A_{mpc} \cdot x_{mpc}(k_i) + B_{mpc} \cdot \Delta u(k_i)$$

$$x_{mpc}(k_i + 2 | k_i) = A_{mpc} \cdot x_{mpc}(k_i + 1 | k_i) + B_{mpc} \cdot \Delta u(k_i + 1)$$

$$= A_{mpc}^2 \cdot x_{mpc}(k_i) + A_{mpc} \cdot B_{mpc} \cdot \Delta u(k_i) + B_{mpc} \cdot \Delta u(k_i + 1)$$

$$\vdots$$

$$x_{mpc}(k_i + N_p | k_i) = A_{mpc}^{N_p} \cdot x_{mpc}(k_i) + A_{mpc}^{N_p - 1} \cdot B \cdot \Delta u(k_i) + A_{mpc}^{N_p - 2} \cdot B \cdot \Delta u(k_i + 1)$$

$$+ \ldots + A_{mpc}^{N_p - N_c} \cdot B \cdot \Delta u(k_i + N_c - 1)$$

Doing the same procedure for the prediction of the output variable, it is possible to
have the following equations:

$$y(k_i + 1 | k_i) = C_{mpc} \cdot A_{mpc} \cdot x_{mpc}(k_i) + C_{mpc} \cdot B_{mpc} \cdot \Delta u(k_i)$$

$$y(k_i + 2 | k_i) = C_{mpc} \cdot A_{mpc}^2 \cdot x_{mpc}(k_i) + C_{mpc} \cdot A_{mpc} \cdot B_{mpc} \cdot \Delta u(k_i) +$$

$$+ C_{mpc} \cdot B_{mpc} \cdot \Delta u(k_i + 1)$$

$$y(k_i + 3 | k_i) = C_{mpc} \cdot A_{mpc}^3 \cdot x_{mpc}(k_i) + C_{mpc} \cdot A_{mpc}^2 \cdot B_{mpc} \cdot \Delta u(k_i) +$$

$$+ C_{mpc} \cdot A_{mpc} \cdot B_{mpc} \cdot \Delta u(k_i + 1) + C_{mpc} \cdot B_{mpc} \cdot \Delta u(k_i + 2)$$

$$\vdots$$

$$y(k_i + N_p | k_i) = C_{mpc} \cdot A_{mpc}^{N_p} \cdot x_{mpc}(k_i) + C_{mpc} \cdot A_{mpc}^{N_p - 1} \cdot B_{mpc} \cdot \Delta u(k_i) +$$

$$+ C_{mpc} \cdot A_{mpc}^{N_p - 2} \cdot B_{mpc} \cdot \Delta u(k_i + 1) + \ldots$$

$$+ C_{mpc} \cdot A_{mpc}^{N_p - N_c} \cdot B_{mpc} \cdot \Delta u(k_i + N_c - 1)$$

As can be seen, there is a certain recursiveness in relationships. Therefore, by defin-
ing the two matrices represented below, it is possible to write the output prediction
in a compact way, as shown in eq. 6.6.

$$F = [C_{mpc}A_{mpc} \quad C_{mpc}A_{mpc}^2 \quad C_{mpc}A_{mpc}^3 \quad \ldots C_{mpc}A_{mpc}^{N_p}]^T$$

$$\Phi = \begin{bmatrix} C_{mpc}B_{mpc} & 0 & 0 & \ldots & 0 \\ C_{mpc}A_{mpc}B_{mpc} & C_{mpc}B_{mpc} & 0 & \ldots & 0 \\ C_{mpc}A_{mpc}^2 B_{mpc} & C_{mpc}A_{mpc}B_{mpc} & C_{mpc}B_{mpc} & \ldots & 0 \\ \vdots & & & & \\ \vdots & & & & \\ C_{mpc}A_{mpc}^{N_p - 1}B_{mpc} & C_{mpc}A_{mpc}^{N_p - 2}B_{mpc} & C_{mpc}A_{mpc}^{N_p - 3}B_{mpc} & \ldots & C_{mpc}A_{mpc}^{N_p - N_c}B_{mpc} \end{bmatrix}$$

$$Y = F \cdot x_{mpc}(k_i) + \Phi \cdot \Delta U \tag{6.6}$$

$$Y = [y(k_i+1|k_i) \quad y(k_i+2|k_i) \quad y(k_i+3|k_i) \quad \dots \quad y(k_i+N_p|k_i)]^T$$

$$\Delta U = [\Delta u(k_i) \quad \Delta u(k_i+1) \quad \Delta u(k_i+2) \quad \dots \quad \Delta u(k_i+N_c-1)]^T$$

The equation 6.6 presents two unknowns, the vector of the predicted outputs Y and the vector of the input increment ΔU. To determine the vector of these outputs, it is first necessary to identify the vector ΔU. In this content comes into play the concept of optimization. The objective of predictive control is to drive the estimated predicted output as close as possible to a reference $r(k_i)$, within the predictive horizon N_p.

This problem is addressed through the concept of optimization. A cost function J is thus defined which reflects the objective of control. Assuming that the reference remains constant throughout the prediction horizon, it is defined as in eq. 6.7.

$$J = \overbrace{(R_s - Y)^T (R_s - Y)}^{I} + \overbrace{(\Delta U)^T R (\Delta U)}^{II} \tag{6.7}$$

$$R_s^T = \overbrace{\begin{bmatrix} 1 & 1 & 1 & \dots & 1 \end{bmatrix}}^{N_p} \cdot r(k_i) \qquad \text{and} \qquad R = \gamma \cdot I$$

The cost function J consists of two parts.

The first part is inherent to the purpose of the control, which is to minimize the deviation between the reference (kept constant during the predictive horizon) and the predicted output.

The second part instead of an optional term to the control is added to minimize the energy used by the control signal. The second term, therefore, corresponds to a calibration parameter, used to regulate the performance of the closed-loop system. To identify the optimal incremental input vector ΔU that minimizes the index J, equation 6.6 must be replaced by equation 6.7, obtaining the following result:

$$J = (R_s - Fx_{mpc}(k_i))^T (R_s - Fx_{mpc}(k_i)) - 2\Delta U^T \Phi^T (R_s - Fx_{mpc}(k_i)) + \Delta U^T (\Phi^T \Phi + R)\Delta U$$

Finally, deriving for ΔU and setting it equal to zero to identify the minimum ($\frac{\partial J}{\partial \Delta U} = 0$), the optimal incremental input vector is obtained, as shown in eq. 6.8.

$$\Delta U = (\Phi^T \Phi + R)^{-1} \Phi^T (R_s - Fx_{mpc}(k_i)) \tag{6.8}$$

Once a way to determine the optimal incremental input vector has been found, constraints can be added to individual variables.

Therefore, a minimization of the index J is desired, taking into account the constraints as follows:

$$\Delta u^{min} \leq \Delta u(k) \leq \Delta u^{max}$$

$$u^{min} \leq u(k) \leq u^{max}$$

$$y^{min} \leq y(k) \leq y^{max}$$

A SISO system was used in the problem just discussed, but it is possible to extend the same result to a generic multi-input multi-output (MIMO) system. However, the approach just proposed is precisely described in [92].

6.2 Experimental set-up

A continuous slug flow was generated by pumping fluids at different phases to the T-junction inlets of the micro-optofluidic slug velocity detector (see Fig. 6.2 (a)), described in details in Section 1.4 of Chapter 1.

The experimental set-up, shown in Fig. 6.2 (b), was used to collect data for modeling the slug flow passage through a data-driven approach.

Two syringe pumps (neMESYS low-pressure module, Cetoni GmbH, Korbussen, Germany) were connected to the two channel inlets and different flow rates were imposed. The input light source was a laser system (NovaPro 660-125, RGB Laser-systems, Kelheim, Germany) that generates a light beam with a wavelength of 600 nm and a maximum output power of 125 mW. The light intensity variation, split into two paths, was acquired by means of two photodiodes with a gain of 70 *dB* (PDA100A, Thorlabs, Newton, NJ, USA) and the signal received was acquired by a PC oscilloscope (Picoscope 2204A, Pico Technology, Cambridgeshire, UK), with a sampling frequency of 1.5 kHz. For a visual inspection of the process, a digital USB microscope was placed above the device.

| (a) | (b) |
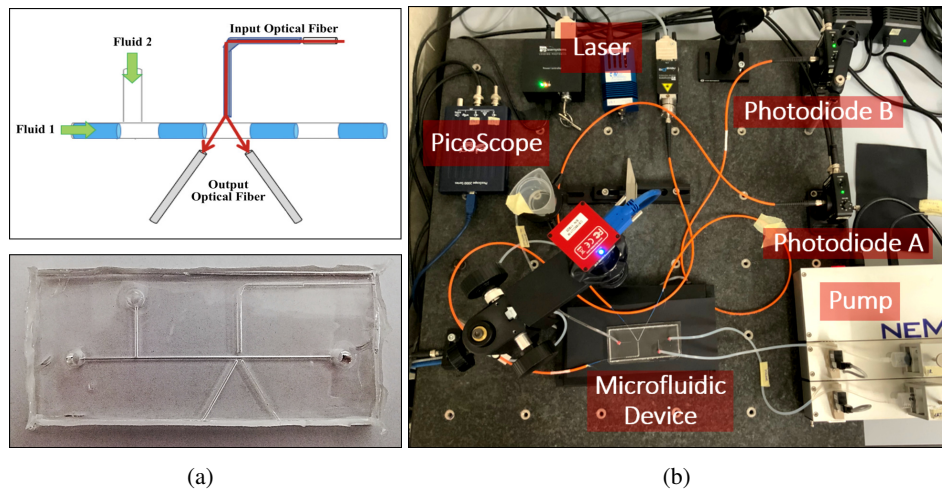
FIGURE 6.2: (a) Working principle and 3D printing realization of the micro-optofluidic slug velocity detector. (b) Picture of the experimental set-up.

6.3 Experimental campaigns and data analysis

In order to model the slug flow passage in the micro-channel and to evaluate the sensitivity of the micro-optofluidic slug velocity detector in real-time detection of slug flows, two experimental campaigns were carried out.

Two combinations of immiscible fluids were considered in their slug regime [61] as follows:

- Air-Water flow, labelled *Exp1-AW*;

- Hexadecane-Water flow, labelled *Exp2-AW*.

Each experimental campaign consists of 27 experiments that have been classified into three subsets. A total of 54 experiments were performed.

In the first subset (sub-set 1), equal flow rates are used for both fluids. In the second

(sub-set 2), the water flow rate is kept fixed and the air or hexadecane flow rate is varied. In the third and last (sub-set 3), the air or hexadecane flow rate is kept fixed and the water flow rate is varied.

For all experiments, the laser light was kept constant at the intensity power value of $1 \, mW$.

The experimental campaigns, *Exp1-AW* and *Exp2-AW* are described in detail in Tables 6.1 and 6.2.

The optical monitoring system placed in the investigated area of the micro-optofluidic slug velocity detector, composed of a laser light and the two photodiodes integrated into the devices by optical fibers insertions, allows to capture the light split into two paths and the variation in the luminosity during the slug passage, due to the difference between the refraction index (n) of the PDMS device material ($n_{PDMS} = 1.41$) and the fluids injected in the micro-channel: air ($n_{air} = 1$), water ($n_{water} = 1.33$) and hexadecane ($n_{hex} = 1.43$).

In Fig. 6.3 the optical signals acquired in the two experimental campaigns, *Exp1-AW* and *Exp2-HW*, in the experimental condition in which the flow rates of the two fluids are equal to $0.1 \, ml/min$, are shown. As it is possible to see they are correlated with the slug passage frames and in Fig. 6.3 (a) the top level revealed the water passage, with a voltage value of $1.4 \, V$, and the low level revealed the air passage, with a voltage value of $0.8 \, V$.

On the other hand, in Fig. 6.3 (b) the top level revealed the hexadecane passage, with a voltage value of about $2 \, V$, and the low level revealed the water passage, with a voltage value of $1.4 \, V$. Therefore, it can be concluded that the greater the refractive index value of the fluid fed into the micro-channel, the greater the voltage value read by the photodiode.

During the experimental campaigns, the data were acquired for about $60 \, s$ with a sampling frequency of $1.5 kHz$. Then, the data were pre-processed by a low-pass filter with a 40 Hz cut-off frequency and a signal smoothing procedure was applied. In the processing phase, the 54 signals acquired were analyzed both in time and frequency domains to automatically detect the frequency and the velocity of the slug passages.
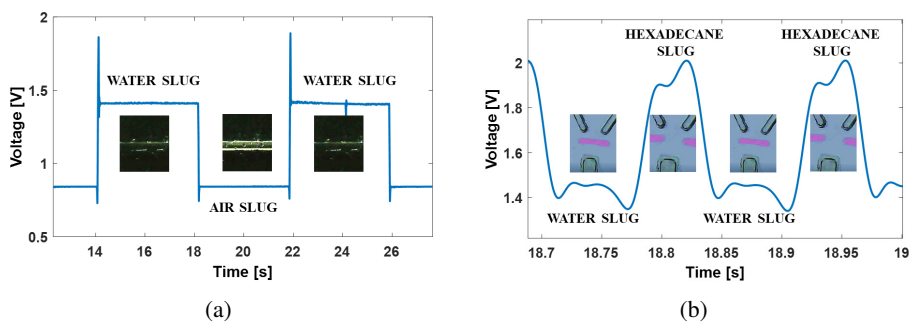
FIGURE 6.3: Optical signals acquired in the micro-optofluidic slug velocity detector correlated with the slug passage frames for (a) the *Exp1-AW* and (b) *Exp2-HW*.

6.4 Slug frequency and velocity measurements

In the experimental phase, the data were acquired for about $60 \, s$. After that, a processing phase is carried out in order to extrapolate some parameters related to the

Flow Rate [ml/min]

Sub-set 1 ($F_{air} = F_{water}$)		Sub-set 2 ($F_{air} \neq F_{water}$)		Sub-set 3 ($F_{air} \neq F_{water}$)	
F_{air}	F_{water}	F_{air}	F_{water}	F_{air}	F_{water}
0.05	0.05	0.07	0.1	0.1	0.07
0.06	0.06	0.08	0.1	0.1	0.08
0.07	0.07	0.09	0.1	0.1	0.09
0.08	0.08	0.1	0.1	0.1	0.1
0.09	0.09	0.2	0.1	0.1	0.2
0.1	0.1	0.3	0.1	0.1	0.3
0.2	0.2				
0.3	0.3				
0.4	0.4				
0.5	0.5				

TABLE 6.1: Experimental campaigns (*Exp1-AW*) carried out with the slug flow composed of air and water.

Flow Rate [ml/min]

Sub-set 1 ($F_{hex} = F_{water}$)		Sub-set 2 ($F_{hex} \neq F_{water}$)		Sub-set 3 ($F_{hex} \neq F_{water}$)	
F_{hex}	F_{water}	F_{hex}	F_{water}	F_{hex}	F_{water}
0.05	0.05	0.07	0.1	0.1	0.07
0.06	0.06	0.08	0.1	0.1	0.08
0.07	0.07	0.09	0.1	0.1	0.09
0.08	0.08	0.1	0.1	0.1	0.1
0.09	0.09	0.2	0.1	0.1	0.2
0.1	0.1	0.3	0.1	0.1	0.3
0.2	0.2				
0.3	0.3				
0.4	0.4				
0.5	0.5				

TABLE 6.2: Experimental campaigns (*Exp2-HW*) carried out with the slug flow composed of hexadecane and water.

slug passage inside the micro-channel.

In Fig. 6.4 (a) the optical signals acquired in the time domain from the two photodiodes, PH-A and PH-B, integrated into the micro-optofluidic device, in the experimental condition $F_{hex} = F_{water} = 0.1 \ ml/min$ are shown.

The two optical signals acquired present the same behavior, they are slightly shifted
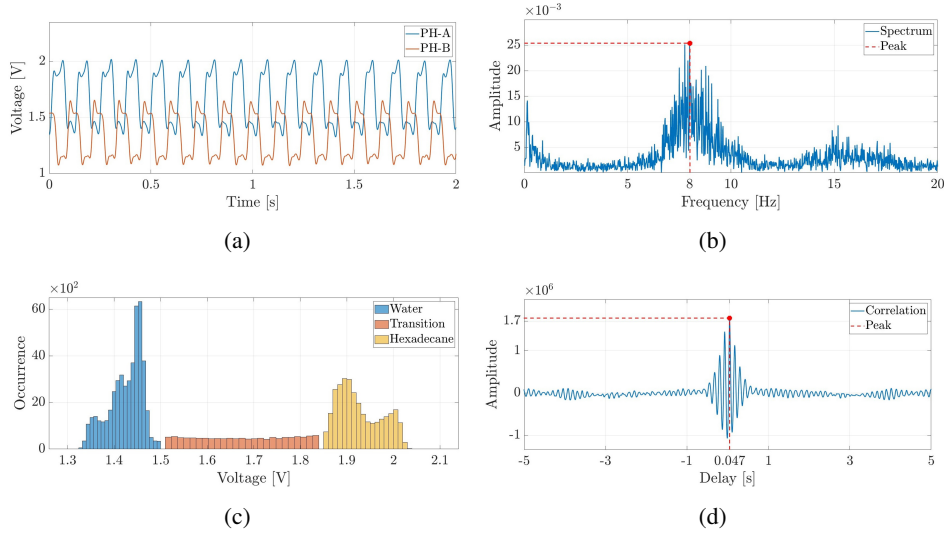
FIGURE 6.4: (a) Optical signals acquired through photodiodes in the experiment with $F_{hex} = F_{water} = 0.1 \ ml/min$. The corresponding (b) spectrum, (c) correlation and (d) distribution analysis.

horizontally being the two signals acquired in two different points of acquisition inside the micro-channel and shifted vertically due to the sensibility of the photodiodes. The same behavior is obtained for all the experimental conditions performed. The processing phase consists in analyzing the data in the time and in the frequency domain.

The first parameter is obtained in the frequency domain obtaining the spectrum from the optical signals acquired and identifying the peak frequency, as shown in Fig. 6.4 (b). The spectrum can be obtained from one optical signal, PH-A, being the two signals the same and related to the slug passage. The peak frequency is around $8Hz < f_{pk} < 8.38 \ Hz$, this means that the slugs are generated with the same frequency and the slug passage is every $T \simeq 1/18.19 \simeq 122ms$ in the micro-channel.

The second parameter is obtained in the time domain analyzing the samples distribution by counting how many times the optical signal is located at the high or low level in order to understand which of the fluids dominates the micro-channel, as shown in Fig. 6.4 (c). The two peaks identify the presence of water (in blue) and hexadecane (in yellow), instead, the samples in the middle (in orange) are related to the transition phase in passing from one fluid to the other. It is evident that the water tends to be more present in the micro-channel than in hexadecane.

The third parameter is the slug velocity obtained by computing the cross-correlation between the two optical signals acquired, PH-A and PH-B, as shown in Fig. 6.4 (d). The peak obtained identifies the delay between the two signals (τ). Therefore, knowing the distance between the two photodiodes (d), it is possible to determine the slug velocity thanks to the dual-slit methodology already presented in Section 4.3.1 of Chapter 4. In the case investigated, the estimated average slugs velocity is $v_{fl} = v_{hex} = v_{water} \simeq 0.021m/s$.

The last parameter extrapolated from the signals is the length of the slug. Knowing the sampling period (T_s), the velocity of hexadecane (v_{hex}) and water (v_{water}) slugs passage and counting the number of samples related to the water (N_{water}) and hexadecane (N_{hex}) voltage level, it is easily possible to determine the average length of the slugs as follows:

$$L_{hex} = \sum_{k=1}^{n_{hex}} v_{hex} \cdot T_s \cdot N_{hex,k} \simeq 1.2 \; mm$$

(6.9)

$$L_{water} = \sum_{k=1}^{n_{water}} v_{water} \cdot T_s \cdot N_{water,k} \simeq 1.56 \; mm$$

where n_{hex} and n_{water} are the number of hexadecane and water slugs within the time window of 60 s considered and $N_{water,k}$ and $N_{hex,k}$ represents the number of samples of the k-th slug. The results show how the length of the water slug is greater than that of hexadecane.

This further confirms the considerations made with the distribution analysis, that is the dominance of water inside the channel. Once analyzed all the optical signals
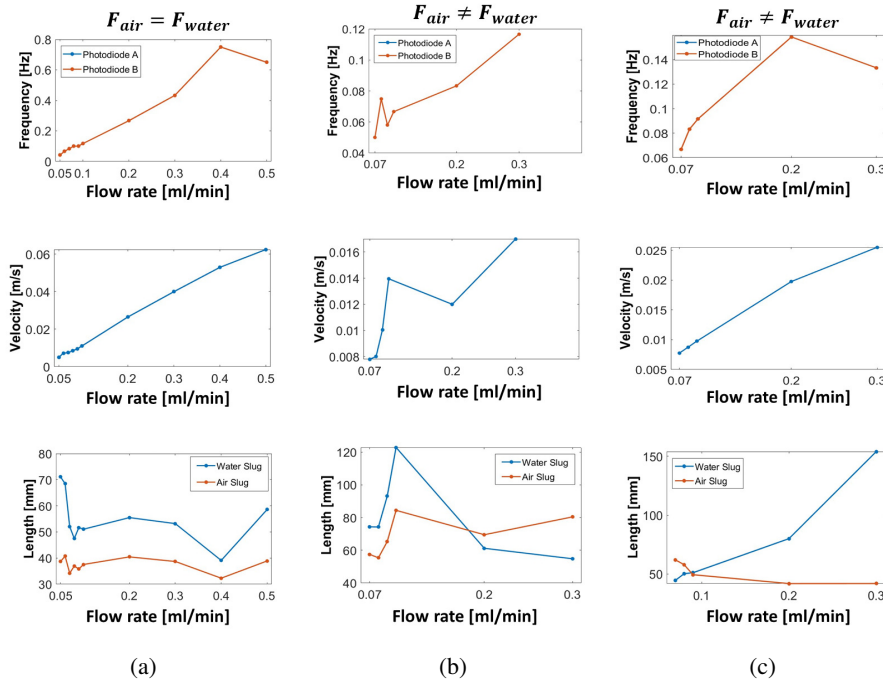
FIGURE 6.5: Frequency peaks (first line), velocities (second line) and slug lengths (third line) of the slugs passage for the *Exp1-AW* in the (a) sub-set 1, (b) sub-set 2 and (c) sub-set 3.

acquired with the methods presented above, it is possible to visualize the trend of the parameters to the variation of the flow rate, as shown in Fig. 6.5 for the experimental campaign *Exp1-AW* and in Fig. 6.6 for the experimental campaign *Exp2-HW*. In the first line has plotted the trend of the peak frequency, in the second line the trend of the slugs velocity and in the last line the average length of the slugs.

From the trend of peak frequency and velocity, for *Exp1-AW* and *Exp2-HW*, it is evident that the increase in flow rate increases both the velocity and the generation of slugs inside the micro-channel. Therefore, both the velocity and the peaks frequency are directly proportional to the flow rate, regardless of whether it is the fluid flow rate.

An interesting observation can be highlighted by the analysis of the length of the slugs. In *Exp1-AW*, when the two flow rates are equal or when the water flow rate is greater than that of air, the length of the water slug is always greater than that of air.
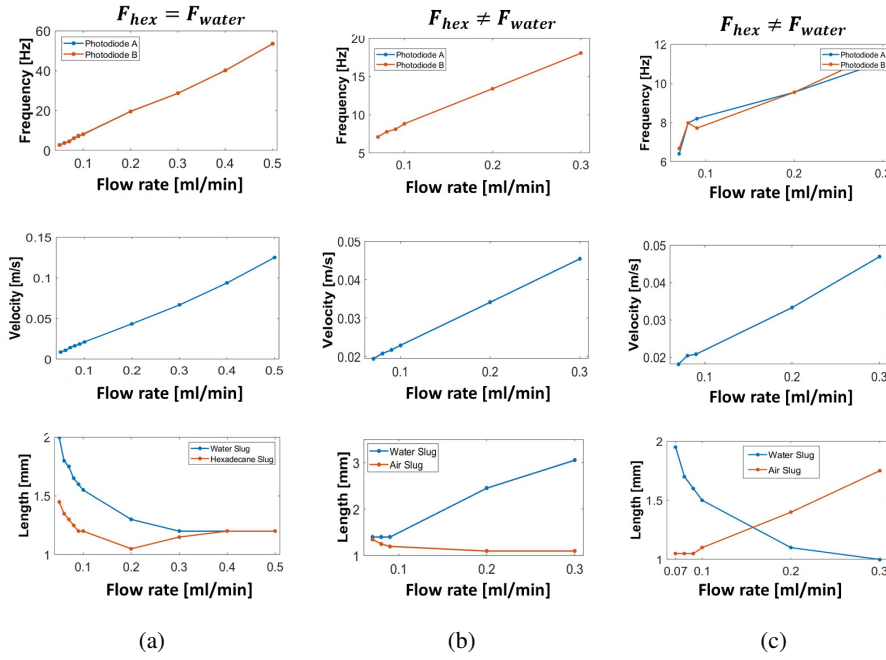
FIGURE 6.6: Frequency peaks (first line), velocities (second line) and slug lengths (third line) of the slugs passage for the *Exp2-HW* in the (a) sub-set 1, (b) sub-set 2 and (c) sub-set 3.

The length of the air slug is greater only when the air flow rate is quite high compared to that of water. This consideration highlights how in the Air-Water process water always tends to dominate the micro-channel.

In *Exp2-HW*, when the two flow rates are equal or when the water flow rate is greater than that of hexadecane, the length of the water slug is always greater than that of hexadecane. The length of the hexadecane slug is greater only when the hexadecane flow rate is quite high compared to that of water. This consideration highlights how in the Water-Hexadecane process water always tends to dominate the micro-channel. In addition, an increase in flow rate also cause an increasing of two important dimensionless parameters characteristics of the slug flow, the Reynolds (*Re*) and Capillary numbers *Ca*, obtained as follows:

$$Re = \frac{\rho U_{MAX} D_h}{\mu} \qquad (6.10)$$

$$D_h = \frac{2hw}{h+w}$$

$$Ca = \frac{\mu U_{MAX}}{\rho} \qquad (6.11)$$

where ρ and μ indicate the density and the viscosity of the fluids, U_{MAX} the maximum fluids' velocity and D_h the hydraulic diameter, where h and w are the height and the width of the micro-channel.

The Capillary number values are in the range of $[10^{-4}; 10^{-2}]$, being below the order of 10^{-2} the theoretical expectancy of the slug formation is validated for both the experimental campaigns. Instead, an increasing trend of the Reynolds number values underlines an increase of complexity in the flow for varying the input flow rates.

By comparing the two experimental campaigns, the process composed of hexadecane and water (*Exp2-HW*) is much faster than that composed of air and water (*Exp1-AW*). In addition, being faster it turns out to be much more stable.

6.5 Data-driven model identification

One of the most delicate aspects of the MPC approach is the choice and the quality of the system model which drastically implies the success of the control action. The data-driven identification process has been adopted to obtain the model of the system in question. Therefore, the identification process is concerned with deriving the model of a system by its observation, which is obtained as a set of input-output data measured directly in the real system.

In the section above, two experimental campaigns were carried out and being the *Exp2-HW* more stable of *Exp1-AW*, the sub-set 1 of *Exp2-HW* was taken into account to obtain the process model. In the experimental condition considered the two flow rates are equal.

Based on the analyses already performed, the characteristic curves for the slug passage frequency and slug velocity within the micro-optofluidic device are derived, as shown in the first and second line of Fig. 6.6 (a) and reported in a better form in Fig. 6.7 (a)-(b). Both characteristic curves illustrate how, as the flow rate increases, the slug frequency and velocity increase without altering the slug regime. Therefore, the relationship between slug frequency and imposed flow rates is nearly linear.

To assess the nonlinearity and complexity of the process, in Fig. 6.7 (c), the Reynolds number was evaluated using both experimental and nominal velocities, v_{sl} and v_n obtained as follows:

$$v_n = \frac{F}{A} \tag{6.12}$$

where F is the imposed flow rate expressed in $[m^3/s]$ and A is the area of the micro-channel expressed in $[m^2]$. The comparison indicates an increase in the flow's complexity and nonlinearity.

Moreover, although nominal and experimental values illustrate the same trends, when v_{fl} is considered, the process complexity and nonlinearity rise as the flow rates are incremented.

To obtain a complete model of the system, the study of the transient has to be performed. In this way, the slugs frequency $f_s l$ during the flow rates transition, i.e. during a flow rate step, can be determined.

For this purpose, additional experiments were conducted using the same experimental set-up described in Section 6.3 of this Chapter, with the difference that, in these experiments, the photodiodes acquisition was performed during the transition from one flow rate to another.

Fig. 6.8 shows an example of the transient analysis during a flow rate step from 0.07 ml/min to 0.08 ml/min, where the spectrum peak is evaluated in time windows of 2 s. In particular, in Fig. 6.8 (a) the temporal behavior of the acquired signal from one photodiode (PH-A) is shown, while in Fig. 6.8 (b) the behavior of the f_{sl} completed on the same signal is evaluated.

It is possible to notice in Fig. 6.8 (a) how the signal tends to shrink over time and increase the frequency of variability. This is also highlighted in Fig. 6.8 (b), in which the analysis examines the dynamics involved in changing f_{sl} during two steady-state values. The $\tilde{f}_{sl}$ represents the experimental steady-state value for an input flow rate of 0.08 ml/min, the value that the process must reach given the input step imposed.

Based on the data, it is inferred that the dynamics of the process are similar to a second-order system with a settling time of 5 s.

Therefore, in light of these considerations, the model can be derived analytically in the frequency and time domains. The transfer functions of second-order linear
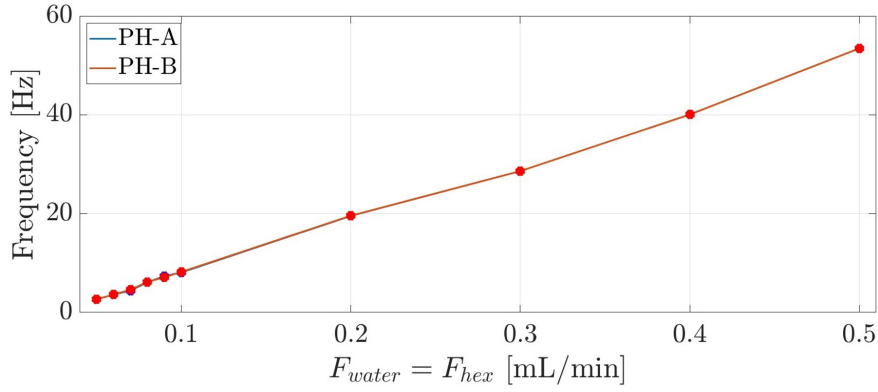
(a)
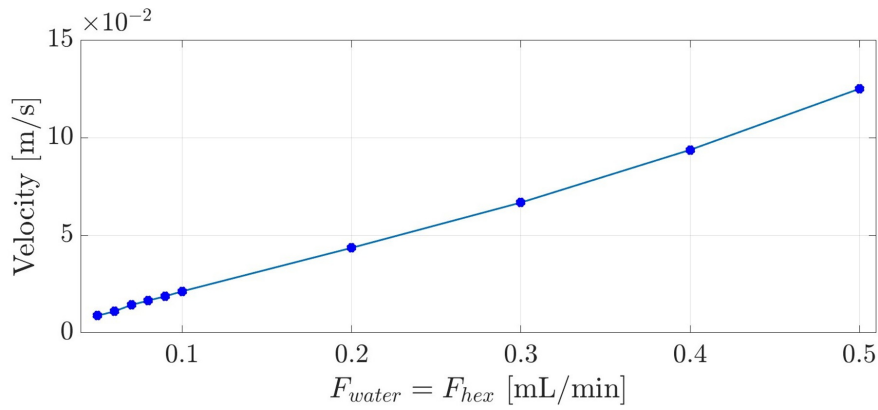
(b)
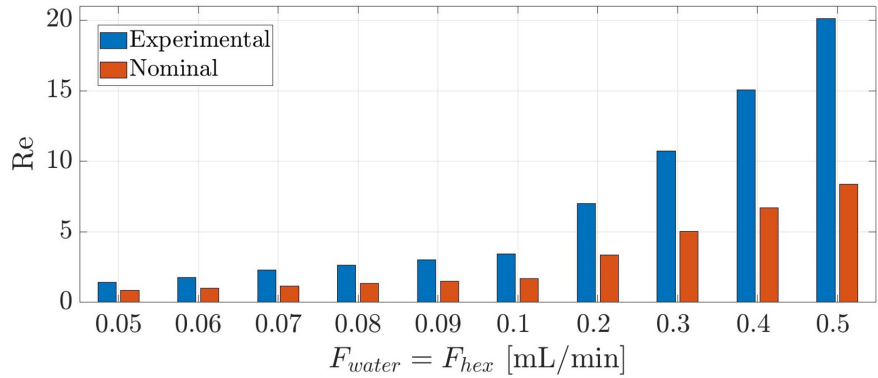
(c)

FIGURE 6.7: Experimental characterization of (a) the slug passage frequencies and (b) velocities. The slugs' frequency f_{sl} and the slugs' velocity v_{sl} detected and estimated per experiment plotted in function of the manipulation variables (F_{water}, F_{hex}). (c) Comparison between experimental and nominal Reynolds numbers, as a result of the variation of the inputs flow rates (F_{water}, F_{hex}).

systems are defined in the Laplace domain as follows:

$$P(s) = \frac{K_p \omega_n^2}{s^2 + 2\xi \omega_n s + \omega_n^2} \tag{6.13}$$

(a)

(b)
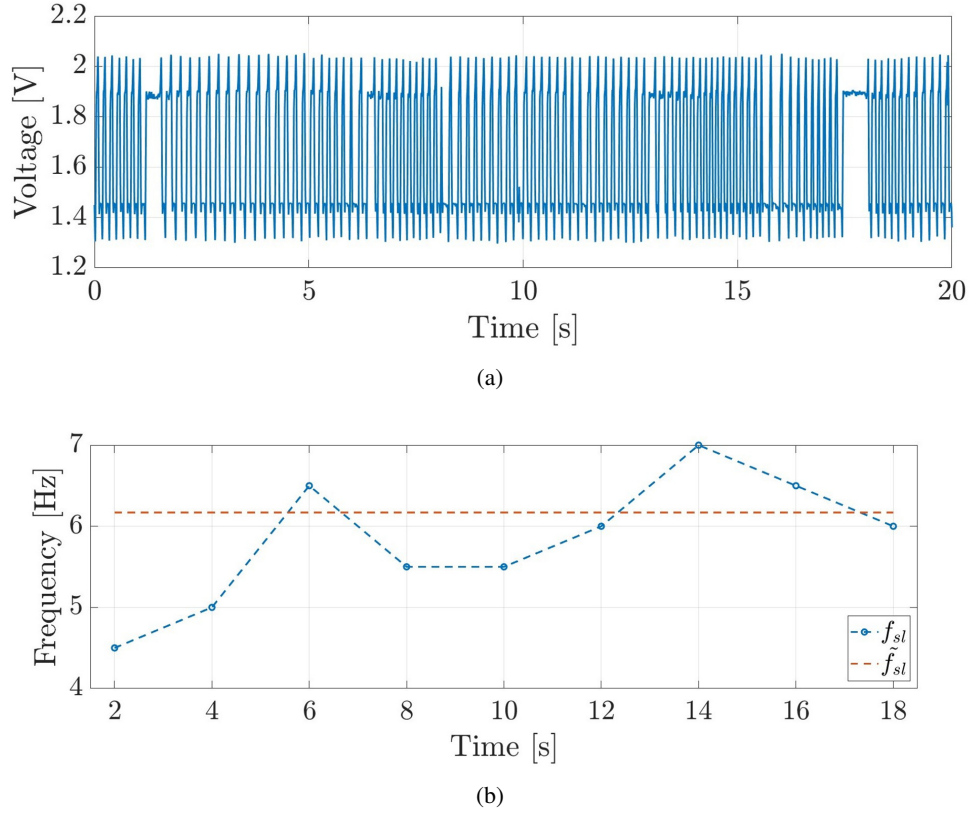
FIGURE 6.8: (a) Photodiode signal and (b) slugs frequency variation during a flow rate step from 0.07 *ml/min* to 0.08 *ml/min* in the sub-set 1 of the *Exp2-HW*. The spectrum peak was computed in time windows of 2 *s*.

where ω_n is the natural frequency, ξ is the damping coefficient and K_p is the process gain.

In our case, the transfer function relates the commanded flow rate F_m with the output slug frequency f_{sl}. Moreover, a Single-Input Single-Output (SISO) system is considered given that the two imposed flow rates are equivalent. The damping coefficient ξ has been chosen so that the system reaches the regime in the smoothest possible manner by fixing the overshoot percentage of the system at 4%, thus $\xi = 0.8$. The value of the natural frequency ω_n is related to the settling time t_s according to the following relationship:

$$\omega_n = \frac{4}{\xi t_s} \tag{6.14}$$

Therefore, considering $t_s = 5\ s$, $\omega_n = 1$. As regards the value of the gain process K_p, it is the change in the output y induced by a unit variation of the input u. Process gain is calculated by evaluating the change in $y(t)$ divided by the change in $u(t)$ at the initial and final steady-state conditions as shown in eq. 6.15.

$$K_p = \frac{\Delta y}{\Delta u} = \frac{y_{ss2} - y_{ss1}}{u_{ss2} - u_{ss1}} \tag{6.15}$$

Generally, K_p is unitary in such that at steady-state $y(t) = u(t)$. However, in this case, the relationship between the input flow rate and the output slug frequency is not unitary. Considering the range of the *sub-set 1* of the experimental campaign

Exp2-HW, the extreme values identified as follows:

$$u_{ss1} = 0.05 \qquad u_{ss2} = 0.5$$
$$y_{ss1} = 2.85 \qquad y_{ss2} = 53.44$$

replacing in eq. 6.15, $K_p = 112.42$ is obtained. Finally, replacing the obtained values in the transfer function 6.13 it is possible to obtain the following results:

$$P(s) = \frac{112.42}{s^2 + 1.6s + 1} \tag{6.16}$$

where the eigenvalues λ_1 and λ_2 are complex and conjugated, $\lambda_{1,2} = -0.8 \pm 0.6\ j$, which confirm the stability of the model.

Moreover, even though the data is consistent with the made assumptions of the model, a bias term $b_0 = 3\ Hz$ has been identified throughout the experimental campaign. As can be seen in Fig. 6.7 (a), the presented characteristic curve shows that a null input does not result in a null output. In the continuous-time domain, considering the general state space form as follows:

$$\dot{x}(t) = Ax(t) + Bu(t)$$
$$y(t) = Cx(t) + Du(t) \tag{6.17}$$

the matrices A, B, C and D were evaluated using the observability canonical form.

$$A = \begin{bmatrix} 0 & -1 \\ 1 & -1.6 \end{bmatrix} \qquad B = \begin{bmatrix} 112.42 \\ 0 \end{bmatrix} \tag{6.18}$$

$$C = \begin{bmatrix} 0 & 1 \end{bmatrix} \qquad D = \begin{bmatrix} 0 \end{bmatrix}$$

The system has two states, x_1 and x_2, of which x_1 is an internal state and x_2 represents the slug frequency f_{sl}. Using the observability canonical form, the state of the system x_2 is extracted and imposed equal to the output of the system $y(t)$. In this way, the output $y(t)$ corresponds exactly to the slug frequency f_{sl}. In the discrete-time domain, the eq. 6.17 became:

$$x(k+1) = A_d x(k) + B_d u(k)$$
$$y(k) = C_d x(k) + D_d u(k) \tag{6.19}$$

where the matrices A_d, B_d, C_d and D_d are the discrete version of the previous continuous matrices.

To evaluate the validity and fit of the model against the experimental values determined during the experimental campaign *Exp2-HW*, a comparison was made between the experimental characteristic curve and the analytically identified, as shown in Fig. 6.9 (a). As a result, the identified linear interpolation closely approximates the experimental steady-state values. Moreover, the model dynamics were evaluated by analyzing the step response with respect to the transition between specific input flow rates, i.e. $F_m \in [0.05, 0.06]$ ml/min in Fig. 6.9 (b), $F_m \in [0.1, 0.2]$ ml/min in Fig. 6.9 (c) and $F_m \in [0.4, 0.5]$ ml/min in Fig. 6.9 (d), recasting the reference frequency $\tilde{f}_{sl}$ appropriately.
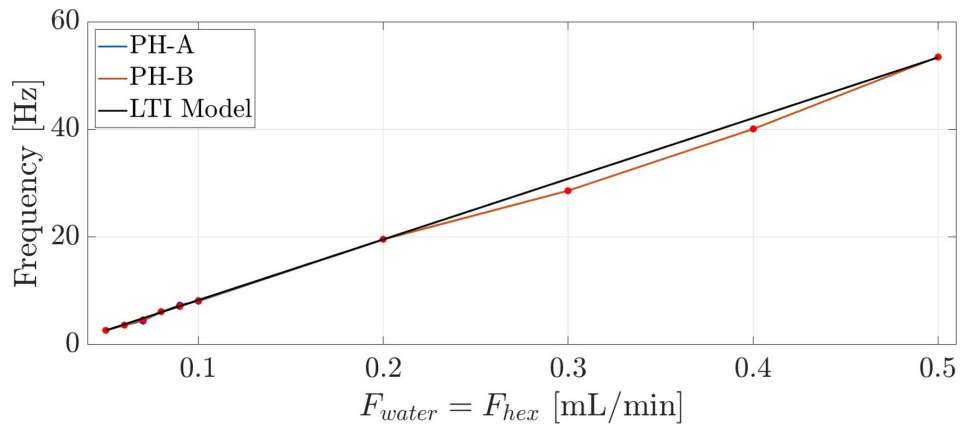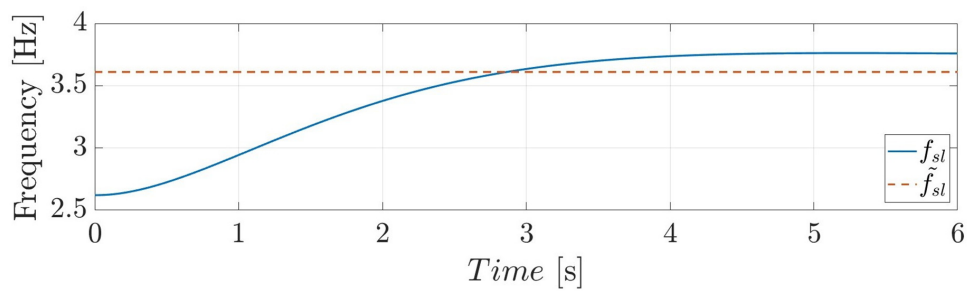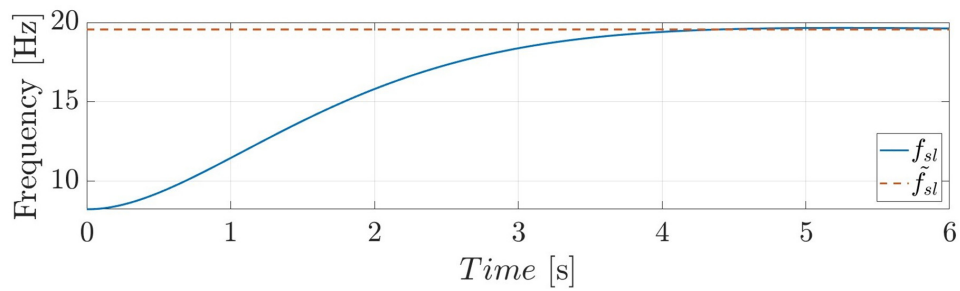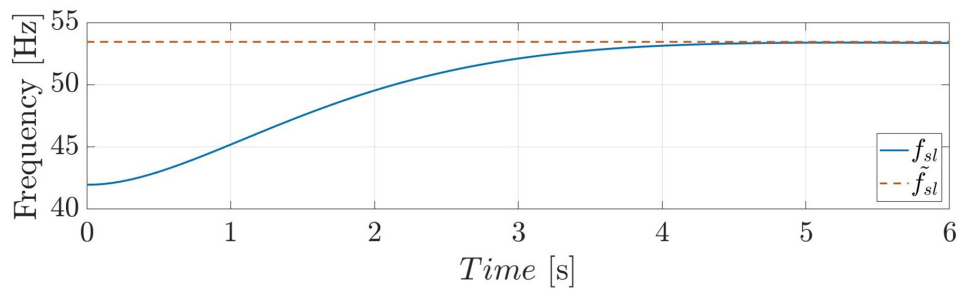
FIGURE 6.9: (a) Experimental steady state value $\tilde{f}_{sl}$ in comparison with the model steady state value f_{sl} (with bias term b_0 considered). Comparison of three specific step responses: (b) the input flow rate step between 0.05 ml/min and 0.06 ml/min, (c) the input flow rate step between 0.1 ml/min and 0.2 ml/min (d) and the input flow rate step between 0.4 ml/min and 0.5 ml/min.

6.6 MPC system realization

This section describes the proposed control architecture, schematically depicted in Fig. 6.10. The approach employs a state-of-the-art linear MPC [92] to regulate the slug frequency based on a desired one, i.e. f_{sl}^d. The MPC leverages the process linear approximation derived in Section 6.5 of this Chapter. As a result, it provides the control input $u_{fl} = F_m$ which influences the fluid actuation system and produces the fluids' alternation within the micro-optofluidic device, i.e. $u_{water} = F_{water}$ and $u_{hex} = F_{hex}$. The optical detection system closes the control loop by providing the actual f_{sl}.

The main objective of predictive control is to minimize as much as possible the error of the variable to be controlled with respect to the desired reference value within a prediction horizon, assuming that the reference signal remains constant within the optimization window.

This objective is translated into a design to find the best control parameter vector ΔU such that the error function between the reference and the predicted output is minimized. Considering the reference values vector at the sampling instant k as:

$$R_{f_{sl}}^T = \overbrace{[1\ 1\ 1\ \dots\ 1]}^{N_p} f_{sl}^d(k) \tag{6.20}$$

where N_p is the prediction horizon and the length of the optimization window, the cost function that reflects the control objective is:

$$J = (R_{f_{sl}} - Y)^T((R_{f_{sl}} - Y) + (\Delta U)^T \bar{R}(\Delta U) \tag{6.21}$$

where Y and ΔU are the vectors containing the predicted output and input variables respectively as follows:

$$Y = [y_{fl}(k+1)\ y_{fl}(k+2)\ \dots\ y_{fl}(k+N_p)]^T$$

$$\Delta U = [\Delta u_{fl}(k)\ \Delta u_{fl}(k+1)\ \dots\ \Delta u_{fl}(k+(N_c-1))]^T$$

with N_c being the control horizon dictating the number of parameters used to collect the entire control reference.

Besides, $\bar{R} = \gamma I$ is a diagonal matrix, where I is the identity matrix and $\gamma \in \mathbb{R}_{\geq 0}$ is a tuning parameter accounting for the desired closed-loop performances. Analyzing the cost function, the first term is inherent to minimize the error $e_{f_{sl}}$ between the desired reference value f_{sl}^d and the predicted output, while the second term is related to computational considerations.

The minimum condition for eq. 6.21 holds for

$$\frac{\partial J}{\Delta U} = 0. \tag{6.22}$$

and a closed form can be finally written. Further details are presented in [92]. Actuator limitations define the system's physical constraints. The fluid actuation system composed of syringe pumps can provide a fluid amount in a predefined range. Thus, a minimum and maximum flow rate can be defined in the optimization problem as follows:

$$u^{min} \leq u_{fl}(k) \leq u^{max} \tag{6.23}$$
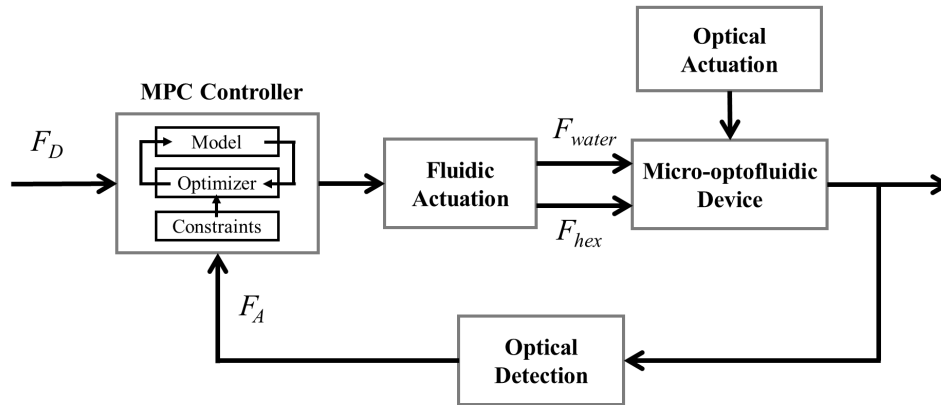
FIGURE 6.10: Block diagram of MPC control system for slug flow in the micro-optofluidic slug velocity detector.

6.6.1 Hardware implementation

Each of the blocks described in Fig. 6.10 is characterized by a specific device that performs the respective functions and operations. The picture of the experimental set-up used for the control and the devices used to implement the block diagram of Fig. 6.10 are illustrated in Fig. 6.11 (a)-(b), respectively.

The MPC control was implemented within the Raspberry Pi board using a Python code and is also responsible for defining the optimal flow rates (F_{water} and F_{hex}). The fluid actuation system is realized by the syringe pumps (Fusion 4000-X, Chemyx, Stafford, Virginia, USA), which act as mechanical actuators and are responsible for feeding the two fluids into the two inlets of the micro-optofluidic device with the respective flow rates (F_{water} and F_{hex}) defined by the control system.

The actuation system consists of a laser light (NovaPro 660-125, RGB Lasersystems, Kelheim, Germany) that emits a light beam at a fixed power of 5 mW that enters the micro-optofluidic device through a fiber insertion.

The addressing of the beam is enabled by the internal geometry of the device and the integrated optical component, the beam splitter. The optical detection system consists of a photodiode (PDA100A2, Thorlabs, Newton, NJ, USA) and an analog-to-digital converter (ADC CQRADS1115, CQRobot Ocean, London, UK). The photodiode acquires the light beam after the interaction with the fluids in the micro-channel through an optical fiber and is responsible for the transduction of the optical signal into an electrical signal. The gain of the photodiode is the same as that used during the experimental campaign, i.e. 70 dB. The digitized signal is then sent to the control system, the Raspberry pi board.

The MPC control, the data analysis and the user interface are handled entirely by the Raspberry pi board in Python programming language. The code consists of a start menu with several available options to start or stop the desired fluid flow rates, to display the behavior of the inputs (F_{water} and F_{hex}) and output (f_{sl}^c, the current slug frequency) and to perform the MPC control to achieve the desired slug frequency reference f_{sl}^d. The operating principle of the MPC control is represented by the flowchart in Fig. 6.12. Due to the process characterization, the range of manipulated variables (F_{water} and F_{hex}) of interest is relative to the flow rate range between 0.05 ml/min and 0.5 ml/min. For this reason, in the first step, the two inputs are initialized at 0.05 ml/min. The MPC control loop can be designed to control the process infinitely. However, our interest is in reaching the desired reference value.

Therefore, the MPC control action will be maintained until the error between the desired reference value f_{sl}^d and the current process output f_{sl}^c is less than a certain tolerance.

Thereafter, the control action is interrupted and the last process input values, i.e. the last imposed optimum flow rates, are maintained. In particular, as shown in Fig. 6.13, a tolerance of 10% was established for the reference range from 2.65 Hz to 12 Hz, 5% for the range from 12 Hz to 30 Hz and 2% for the range from 30 Hz to 53.44 Hz.
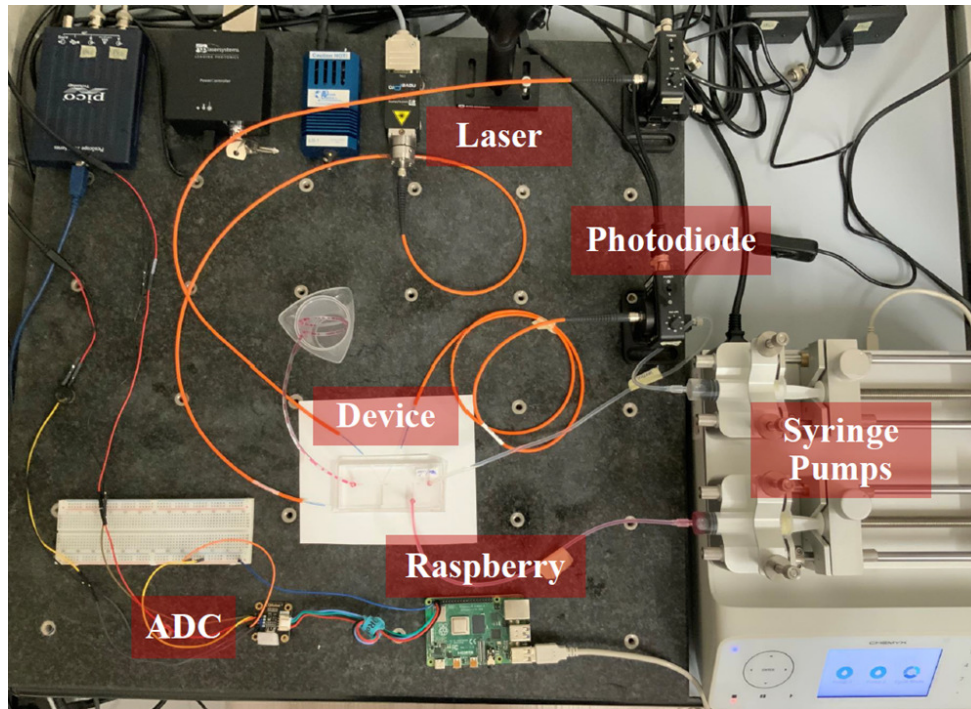
(a)
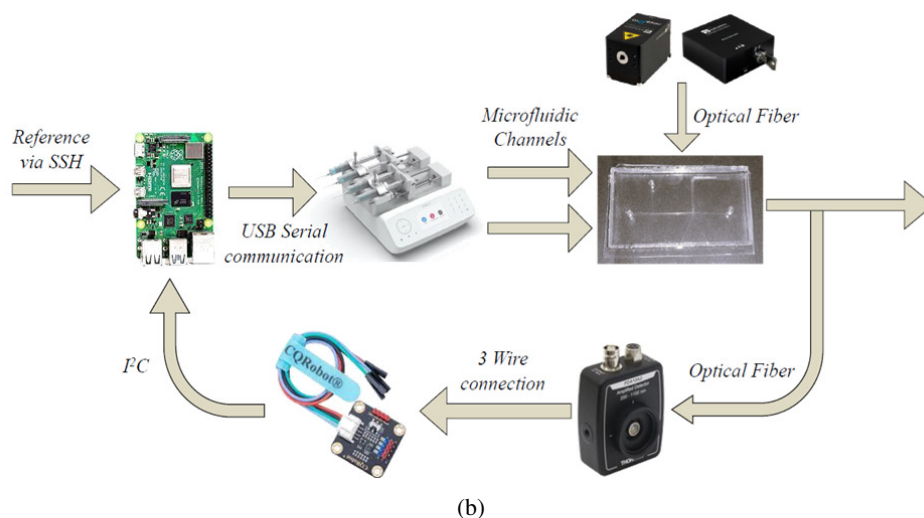
(b)

FIGURE 6.11: (a) A picture of the experimental control set-up and (b) its control scheme describing the system layout and how the various devices communicate and interact.
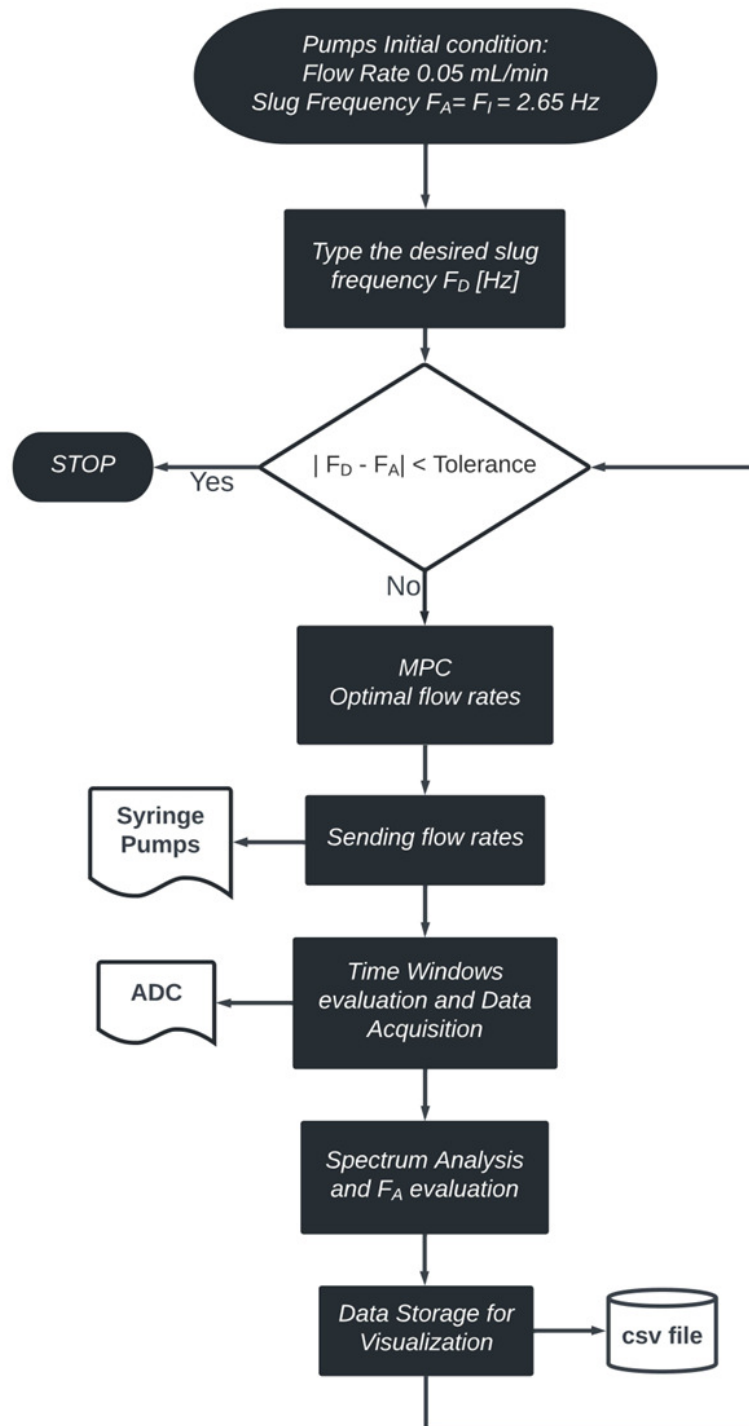
FIGURE 6.12: Flowchart of the implemented code in Python for MPC control of slug flow.
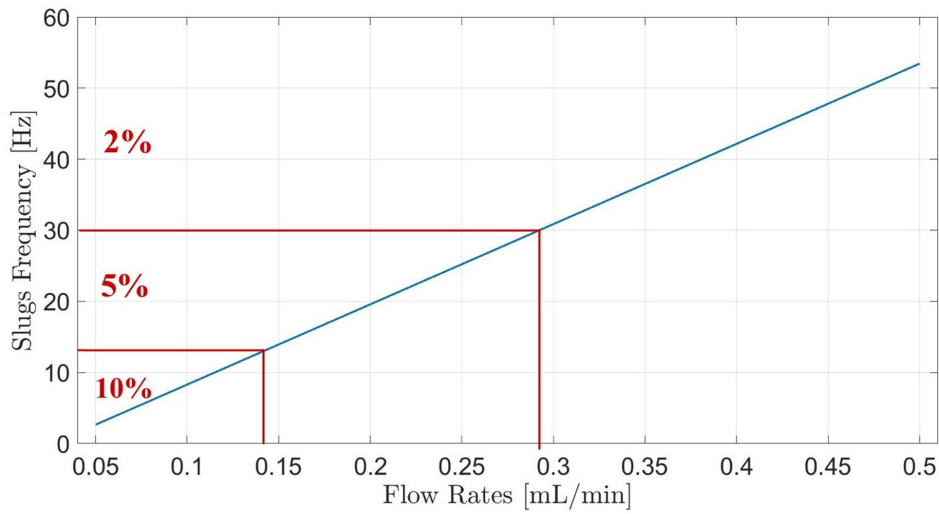
FIGURE 6.13: Distribution of the frequency range of slug passage into three different tolerance bands.

6.6.2 Algorithm implementation

At each iteration, the MPC control code acts as follows:

- the optimal input flow rate ΔU_{opt} is determined via the optimization eq. 6.21 with a control horizon N_c of 3 s;

- the first value optimal input flow rate ΔU_{opt} is taken and checked to see if it meets the set constraint;

- the control system (Raspberry pi board) communicates the optimal flow rates to the syringe pumps which are immediately fixed, $F_{water} = F_{hex} = u_{opt}$;

- the photodiode signal is acquired with a sampling rate of 600 Hz. Due to the hardware configuration, the control system must inevitably take a few moments to acquire the signal required to determine the current slugs frequency f_{sl}^c. This information cannot be extracted instantaneously from the photodiode. To limit the loss of time due to signal acquisition, a fixed time window of 0.5 s has been defined;

- the spectrum of the signal acquired is determined and the current slugs frequency f_{sl}^c is evaluated;

- all control and process data are stored in a CSV file;

- the error $e_{f_{sl}}$ between the desired reference value f_{sl}^d and the current process slugs frequency f_{sl}^c is determined.

The data stored in the CSV file is updated for each iteration of the control system and is used by another code, the real-time visualization code, which is started in parallel with the main code.

This code provides the process count and control actions, displays the control inputs (F_{water} and F_{hex}), the process output f_{sl}^c, the error trend $e_{f_{sl}}$ and the signal acquired from the photodiodes.

6.7 Results and discussion

6.7.1 Single and Multi-frequency MPC control

Several experiments were conducted to evaluate the effectiveness of the presented control architecture. In particular, two specific scenarios were carried out. In the first scenario, a single desired reference value f_{sl}^d was set to evaluate the controller's performance in transient and steady-state. The second involves experiments in which several successive references were set. These tests were useful to determine the applicability of the proposed methodology in real devices for monitoring purposes.

- *Single frequency tracking*: A series of experiments was conducted with $f_{sl}^d \in [5; 10; 15; 20; 25; 30; 40; 50]$ Hz.

As examples, the cases in which $f_{sl}^d = [10; 25; 40]$ Hz are shown in Fig. 6.14(a)-(b)-(c), respectively. In particular, in the first column of Fig. 6.14 is reported the comparison between the control input flow rate and the actual flow rate, in the middle the comparison between the f_{sl}^c and f_{sl}^d and in the last one the slug frequency error $e_{f_{sl}}$ during the control action.

It can be seen from the plots in the third column of Fig. 6.14, that the error of the
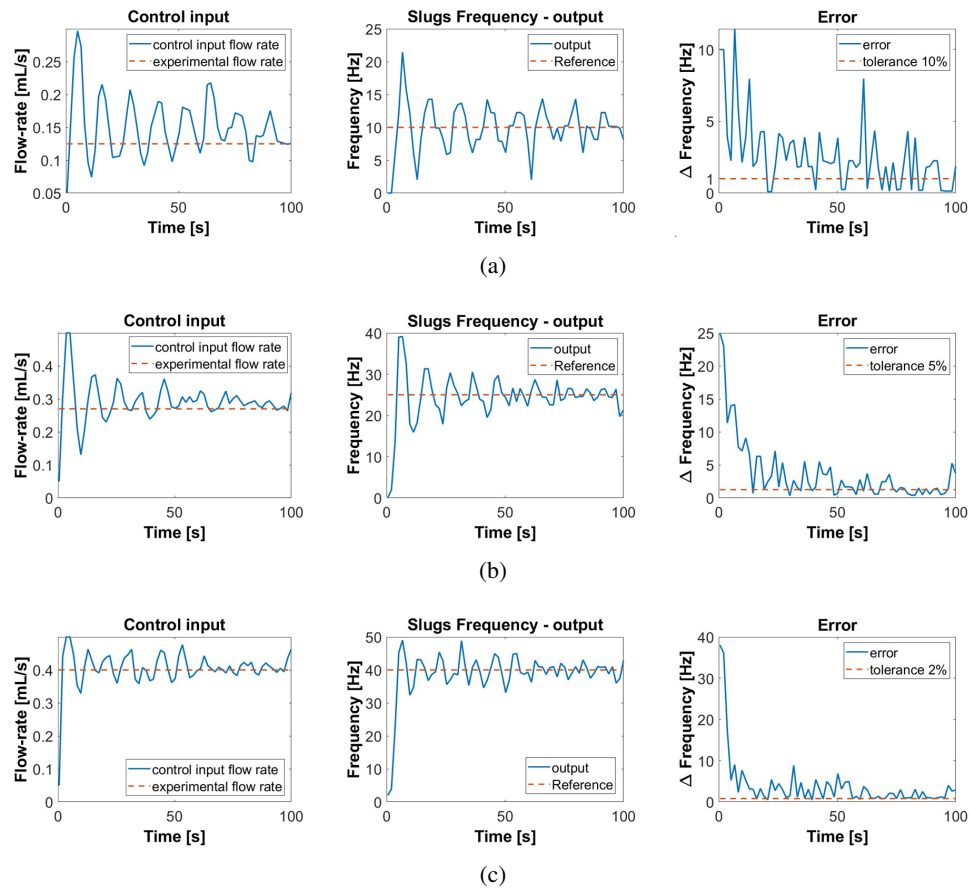
FIGURE 6.14: Single-frequency reference test for slug passage at (a) 10 Hz, (b) 25 Hz and (c) 40 Hz. In the first column the control input flow rates, in the middle column the frequency of slugs passage and in the last column the error behavior during the control action.

slug passage frequency by setting low frequencies, such as 5 *Hz*, at the input of the microfluidic channel is to around 100 *s*, but by increasing the frequency values set at the input of the microfluidic channel to 40 *Hz*, the error tends to zero in less than 5 *s*.
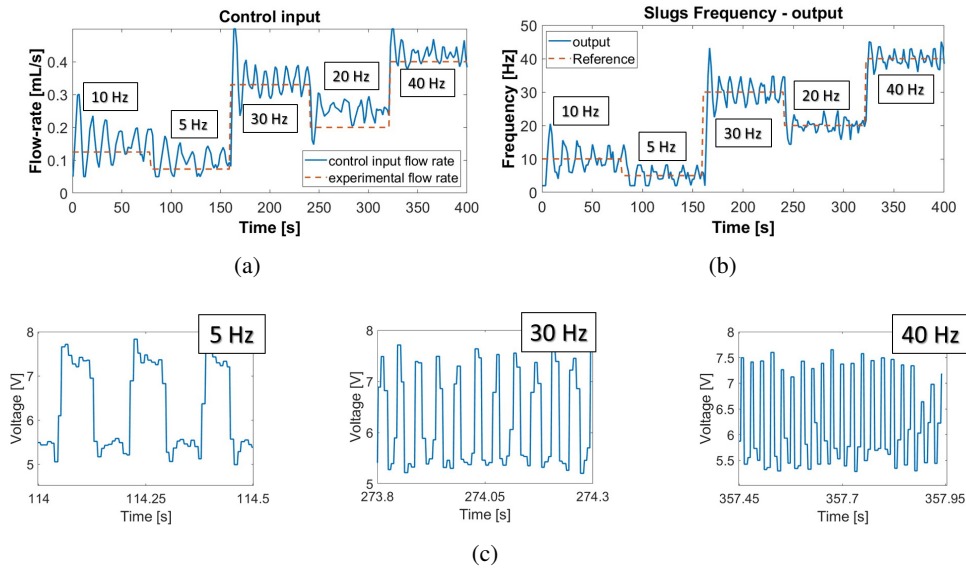
FIGURE 6.15: Multi-frequency reference test for slugs passage by setting the slugs passage frequency reference values to $\{10; 5; 30; 20; 40\}$ *Hz*. (a) Control input flow rates, (b) behavior of the slugs passage frequency and (c) examples of optical signals acquired with the photodiode for 5 Hz, 30 Hz and 40 Hz during the control action.

Thus it can be seen that as the slug passage frequency imposed at the microfluidic channel input increases, the error reduces drastically.

Indeed, in previous studies, and in particular in [93], [94], it has been seen that robust two-phase microfluidic process models can be obtained by working mainly at high slug passage frequencies $[30-80]$ *Hz*. From the following study, it can be concluded that in terms of real-time applications using a control monitoring period of 60 *s*, the controller performance obtained at slow dynamics can be considered discrete, but very good in the case of fast dynamics. Possible future developments could include trying to optimize the MPC's model better by using a nonlinear model that can guarantee excellent performance at both low and high slug passage frequencies, or using two separate models based on the dynamics of the microfluidic process.

 - *Multi-frequency tracking*: In this scenario, the MPC control was provided with a series of successive slug frequency reference values $f_{sl}^d \in [10; 5; 30; 20; 40]$ *Hz*. The purpose of the experiment is to show the ability of the system to follow different reference values, updated every 80 *s*. The set values were chosen in such a way that the MPC control is strongly stressed by exchanging high and low-frequency reference values.

Fig. 6.15 shows the results of the experiments. In particular, Fig. 6.15 (s) shows the control input flow rates expected and obtained, Fig. 6.15 (b) the behavior of the desired and actual slugs passage frequency and Fig. 6.15 (c) some examples of optical signals acquired with the photodiode for 5 *Hz*, 30 *Hz* and 40 *Hz* during the control action. As expected, an initial increase is observed for each imposed reference value, leading to a non-negligible inaccuracy in the slug frequency, followed by a reduction in the error.

In light of the performance obtained, the mean values of the slug frequency $\mu_{f_{sl}}$ and the standard deviation $\sigma_{f_{sl}}$ at steady-state were calculated and presented in Table 6.3. The mean and standard deviations are calculated from $t = 30$ *s*.

The results show that $\mu_{f_{sl}} \sim f_{sl}^d$ for each experiment conducted. In contrast, the standard deviation $\sigma_{f_{sl}}$ is between 2 and 3 *Hz*. Oscillations around the reference values

f_{sl}^d [Hz]	$\mu_{f_{sl}}$ [Hz]	$\sigma_{f_{sl}}$ [Hz]	u_{fl}^{exp} [ml/min]	$\mu_{u_{fl}}$ [ml/min]	$\omega_{u_{fl}}$ [ml/min]
5	5.12	1.98	0.073	0.099	0.023
10	10.08	2.49	0.125	0.147	0.030
15	15.06	2.70	0.160	0.197	0.032
20	19.89	1.94	0.200	0.247	0.020
25	24.76	2.61	0.270	0.287	0.026
30	30.03	2.84	0.330	0.329	0.029
40	40.02	2.98	0.400	0.409	0.028
50	49.57	2.88	0.480	0.472	0.025

TABLE 6.3: MPC control performance at steady-state for each experiment carried out. In the left part of the table, the performance related to the output of the control system is present. Instead, in the right part of the table, the performance related to the input of the control system is present.

are the cause of this variability. However, as long as the process remains bounded within the tolerance range, this behavior is considered acceptable.

Chapter 7

Device for slug flows passive control

Currently, the hydrodynamic of two-phase flows in a micro-channel plays an important role in micro–nano technology, enabling the design of point-of-care devices in the biomedical field and micro-electrical–mechanical systems in chemical processes [2], [3], [95].

An open issue in this context is the design of control systems easily adaptable to different operative conditions and able to guarantee process reproducibility and reliability [65], [96]. The studies presented in the literature are strictly related to specific experimental conditions and far from being a well-established framework that can drive flow control. Recently, some case studies have been presented in the literature using a system-on-a-chip (SoC) approach that embeds model predictive control strategies [97]. The SoC offers a high level of control and modularity, but its functionalities are strongly dependent on both integrated control logic and knowledge of the process model [64].

In this work, a chemical approach based on the treatment of the micro-channel surface is presented as a control strategy that is easily adaptable for embedded micro-devices. The interaction between fluids and the micro-channel surface was studied to investigate the possibility of slowing down or accelerating the two-phase flows, generated by the interlaced sequence of two immiscible fluids at a microfluidic T-junction: at the T-junction, two immiscible liquids produce droplets whose movement is associated with periodic variation of the refractive index (RI) [98]. This approach was tested using a micro-optofluidic device (mofd), presented in Section 1.2 of this thesis, in which the micro-channel and the micro-optical components for real-time flow detection are integrated.

Two-phase flows in the micro-channel are determined by the wetting properties of the channel surface and, from this perspective, functionalization strategies are fundamental to tailor fluid dynamics at the micrometric scale. Among the materials used to fabricate micro-channels, polydimethyl-siloxane (PDMS) is a long-lasting material largely used in microfluidic device fabrication due to fast prototyping by

soft-lithography [44] and recently also 3D printing [99], due to its material properties, namely, biocompatibility, transparency and easy Complementary Metal-Oxide Semiconductors (CMOS) integration. Accordingly, compared with other microfluidic devices made of rigid materials, such as glass, silicon or ceramics, PDMS-based reactors guarantee easier manufacturing processes at low cost.

In recent decades, micro-optical components were also created using polydimethylsiloxane (PDMS), and integrated with the microfluidic device, opening the opportunity of moving from the equipment used to perform the standard optical sensing procedures to their miniaturization into a single low-cost portable device [6], [100], [101].

Optical approaches to detect and control two-phase flows in micro-channels offer the advantages of a wide range of measurement options being minimally invasive. In recent studies, optical signals were used to classify and identify the two-phase flow inside the micro-channel [61], to characterize the flow nonlinearity [5], [16], and for a real-time velocity detection [102].

The idea proposed in this work is to investigate the possibility of integrating a passive flow control within a micro-optofluidic device by PDMS surface treatment, thereby avoiding external devices, as used in the active control, and overcoming the need for specific micro-channel geometry, as required, in the passive control.

Examples of active control are based on mechanical pumping, pneumatic pressure or electro-magnetic field [103]. A passive control, mainly used in capillary micro-channels [84], [85] can be implemented to generate a specific flow pattern, thus exploiting the geometrical properties of the micro-channel and the physical properties of the fluids involved in the process, such as the hydrophobicity or the surface tension between the fluids and the walls of the channels. This approach does not require additional energy sources and does not increase the complexity and cost of the external equipment.

One of the main concerns relating to PDMS properties affecting microfluidic device performance is its hydrophobicity and low chemical resistance to many nonpolar organic solvents, and, to address these drawbacks, surface modification strategies are often adoptedusing a wide selection of functionalization approaches [104]. In particular, surface coating with inorganic structures might contribute to improving PDMS robustness although surface behavior modification must be expected [105]–[108]. The combination of inorganic nanomaterials with PDMS in microfluidic devices involves nanostructured ZnO, a semiconductor material that is non-toxic and biodegradable, and considered a versatile nanoplatform in many fields, including biosensing and bioimaging [109], [110] and photocatalytic applications for water treatments [111].

Other authors deposited ZnO nanostructures on a PDMS micro-channel with the aim of exploiting micro or nanoscale surface roughness to tailor flow resistance inside the channel and control water mobility inside closed channels. However, most of the presented approaches use PDMS microfluidic devices with a silicon, quartz or glass base, thus requiring a photolithographic procedure to open the channel [112], [113].

In this work, a selective deposition of ZnO nanostructured coating was performed inside the PDMS channel, without altering the overall optical transparency, to modify the morphology and chemical composition of the surface. The proposed methodology differs from similar approaches reported in the literature where ZnO growth by CBD was achieved on silicon or quartz substrates preliminarily deposited with thin ZnO or other material deposited as a seed layer [114], [115]. In this work, we
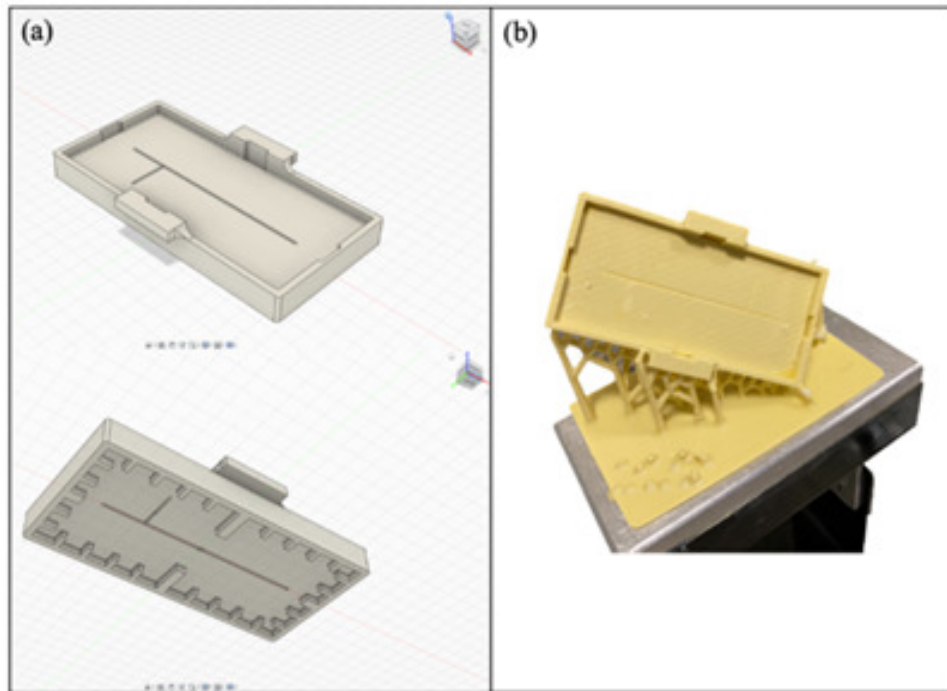
FIGURE 7.1: (a) Customized mask for the PDMS device design using Autodesk®
Fusion 360; (b) 3D printed mask.

grow ZnO nanostructures directly on PDMS micro-channels with an exclusive so-
lution approach. This strategy has the advantage of being economical and does not
require any additional lithographic step, thus resulting as suitable for disposable use
to overcome any issues related to ZnO durability.

Chemical bath deposition (CBD) was integrated into the process flow used to fabri-
cate the PDMS-based micro-optofluidic devices (mofd): in particular, ZnO nanorods
were grown by CBD on a PDMS mofd by using a 3D printed mask to selectively
limit the growth inside the micro-channel.

To test the capability of these PDMS-ZnO-based devices, optical signals acquired in
a specific test section of the micro-channel were analyzed and compared with un-
modified PDMS devices. The fluid dynamic study allowed us to unveil the key roles
of surface roughness and chemistry on water/air and glycerol/air mobility.

7.1 Methods for device surfaces characterization

Materials

Zinc acetate dihydrated ($Zn(CH_3COO)_2 2H_2O$) and ethylene diamine ($NH_2CH_2CH_2NH_2$)
were purchased from Sigma Aldrich (St. Louis, MO, USA). The PDMS was the Syl-
gard 184 elastomer kit from Dow Corning. The commercial UV DLP Hard White
resin was purchased from Photocentric Ltd. (Peterborough, UK) and is a liquid,
high-temperature resistant, photo-polymeric resin based on a proprietary mixture of
acrylate monomers.

Zinc Oxide Chemical Bath Deposition on PDMS

The PDMS devices were dipped for 1 h in an aqueous solution of zinc acetate dehy-
drate ($Zn(CH_3COO)_2 \cdot 2H_2O, 99.999\%, 0.1$ M) and then heated overnight at $110\,^{\circ}C$.
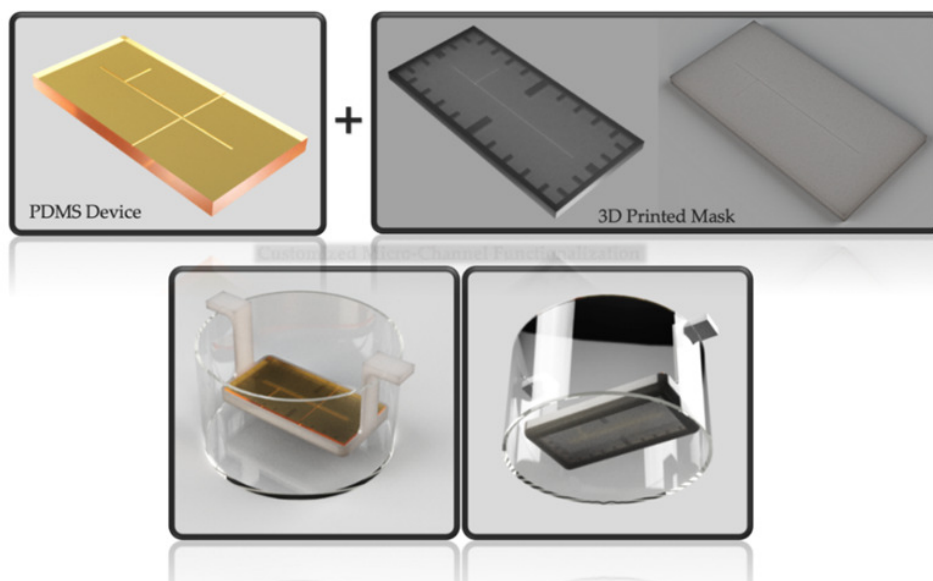
FIGURE 7.2: Rendering of the mask–device assembly suspended by a 3D printed support in the bath to grow ZnO inside the device's channel.

The ZnO seed-coated PDMS substrates were immersed in a nutrient bath containing an aqueous solution of zinc acetate dehydrate (0.05 M) and ethylenediamine (EDA, 0.05 M). After stirring at 90 $^{\circ}C$ for 3 h, the sample was rinsed with deionized water (DI) and dried at room temperature [116], [117].

To promote the ZnO growth exclusively in the PDMS device's micro-channel, first, a customized mask was designed using the 3D modeling software Autodesk® Fusion 360 (Autodesk Inc., San Rafael, CA, USA) (Fig. 7.1 (a)). Next, it was 3D printed using an LCD 3D printer (LC Ceramic Precision, Photocentric Ltd., Peterborough, UK) with the Hard White resin as the material. The obtained final part is shown in Fig. 7.1 (b). The mask–device assembly required immersion, keeping its surface at a fixed height where ZnO nanocrystals could grow. The 3D printed support shown in Fig. 7.2 was designed to place the device at a predetermined height during the ZnO growth.

Contact Angle Measurements

Pristine and chemically modified PDMS surfaces were characterized by static water contact angle (θ) measurements, at room temperature, in air, using a Lite Optical Tensiometer TL100 (KSV, Helsinki, Finland) with an accuracy of $\pm 3^{\circ}$. Briefly, 5 μl of Milli-Q water (resistivity 18.2 $M\Omega$ at 25 $^{\circ}C$) drops were applied on the PDMS device surface with a calibrated micro-syringe, and measurements of θ were made on both sides of the two-dimensional projection of the droplet. Five different sets of measurements were performed on different surface portions of every sample to obtain statistically reliable results.

X-rays Photoelectron Spectroscopy

X-ray photoelectron spectra (XPS) were measured for pristine and chemically modified PDMS devices at a 45° take-off angle, relative to the surface sample holder, with
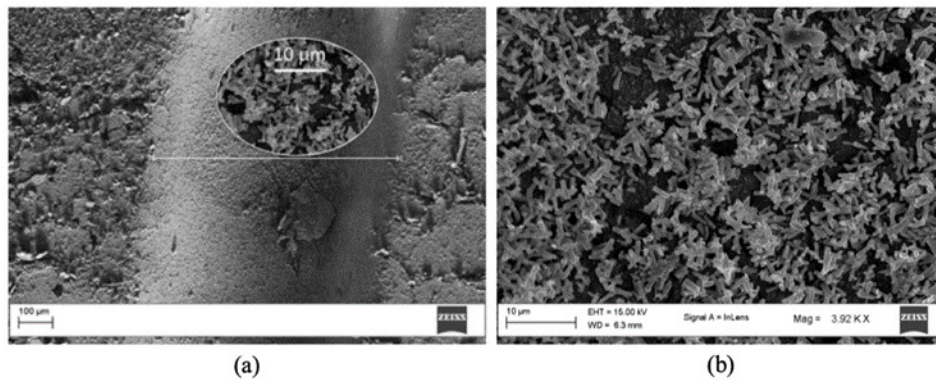
FIGURE 7.3: (a) SEM image of the channel region of the PDMS mofd after ZnO growth; (b) high-resolution image of ZnO nanostructures inside the channel.

a PHI 5600 Multi Technique System (Physical Electronics GmbH, Feldkirchen, Germany, base pressure of the main chamber $1x10^{-8}$ *Pa*) [118], [119]. Samples placed on a molybdenum specimen holder were excited with the Al-Kα X-ray radiation using a pass energy of 5.85 eV.

The instrumental energy resolution was $\leq$ 0.5 eV. Structures due to the Al-Kα X-ray satellites were subtracted from the spectra prior to data processing. XPS peak intensities were obtained after a Shirley background removal. Spectra calibration was achieved by fixing the Ag3d5/2 peak of a clean sample at 368.3 eV; this method turned the C1s main peak at 285.0 eV. Atomic concentration analysis was performed by considering the relevant atomic sensitivity factors.

Atomic Force Microscopy Measurements

The morphology of the pristine and chemically modified PDMS devices was observed by atomic force microscopy (AFM) using an NT-MDT Integra System instrument (Moscow, Russia). The noise level before and after each measurement was 0.01 *nm*. AFM characterizations were performed in a high-amplitude mode (tapping mode, resonance frequency 150 *Hz*) to avoid any possible modification of the grafted layer on the surfaces, caused by the interactions with the tip, whose nominal curvature radius was 10 *nm*. Surface roughness (RMS, Ra) was measured from 2020 and 55 μm^2 scans and was the average of at least three images scanned at different locations on the sample surface.

Scanning Electron Microscopy Measurements

Images were acquired using a field emission scanning electron microscope (FESEM, VP-Supra 550 FE-SEM (Zeiss, Oberkochen, Germany)) at accelerating voltages of 15 kV. Samples were sputtered with a thin gold layer to reduce the surface charging up.

7.1.1 PDMS and ZnO-PDMS surface analysis

Fluid flow in the micro-channel and fluid interaction with micro-channel surfaces are critical for mofd performance. The wettability of the micro-channel surface governs the dynamic of fluids through a balance of cohesive forces within the liquid and adhesive forces between the liquid and its surroundings.
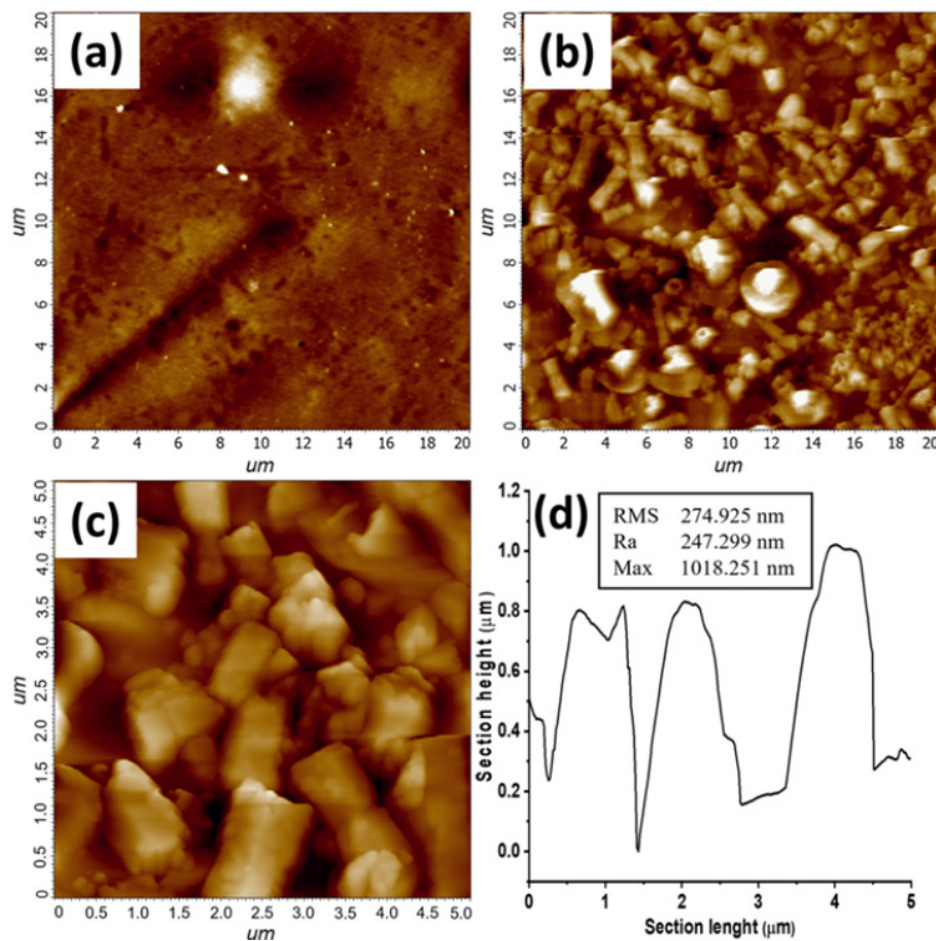
FIGURE 7.4: (a) AFM images of the PDMS-ZnO surface: scale bar $20x20\mu m^2$, and (b) $5x5\mu m^2$; (c) $20x20\mu m^2$ AFM image of bare PDMS surface; (d) section analysis and topographical information.

Accordingly, a control of hydrophobicity allows for an improved versatility of these systems. In particular, the possibility of modulating the surface hydrophobicity by growing ZnO nanostructured layers inside the device's channels opens the way to fluid dynamic control at a local scale and thus, to the development of novel microfluidic devices [120]. Therefore, coating the main micro-channel of the PDMS device with a nanostructured layer of ZnO rods is expected to influence the dynamics of a two-phase fluid, due to both liquid–solid chemical affinity and morphological factors relating to the roughness control.

In this work, two PDMS-based mofd were compared: a bare reference (PDMS) with uncoated surfaces and a ZnO-treated sample (ZnO-PDMS) with micro-channel coated surfaces. Chemical bath deposition performed at $90°C$ in aqueous nutrient solution was considered as a suitable technique to grow ZnO nanostructured layers composed of nanorods inside the PDMS channels, as shown in Fig. 7.3.

The low-resolution SEM image (Fig. 7.3 (a)) clearly shows the channel region of the PDMS component, while Fig. 7.3 (b) provides detail of the ZnO nanorods' dense coverage of the entire channel area.

ZnO nanorods were well visible in the AFM measurements (Fig. 7.4) which revealed the hexagonal structure typical of the wurtzitic phase. It was noteworthy that a bimodal growth of ZnO nanostructures was detected on the PDMS surface (Fig.

(a)   (b)

(c)
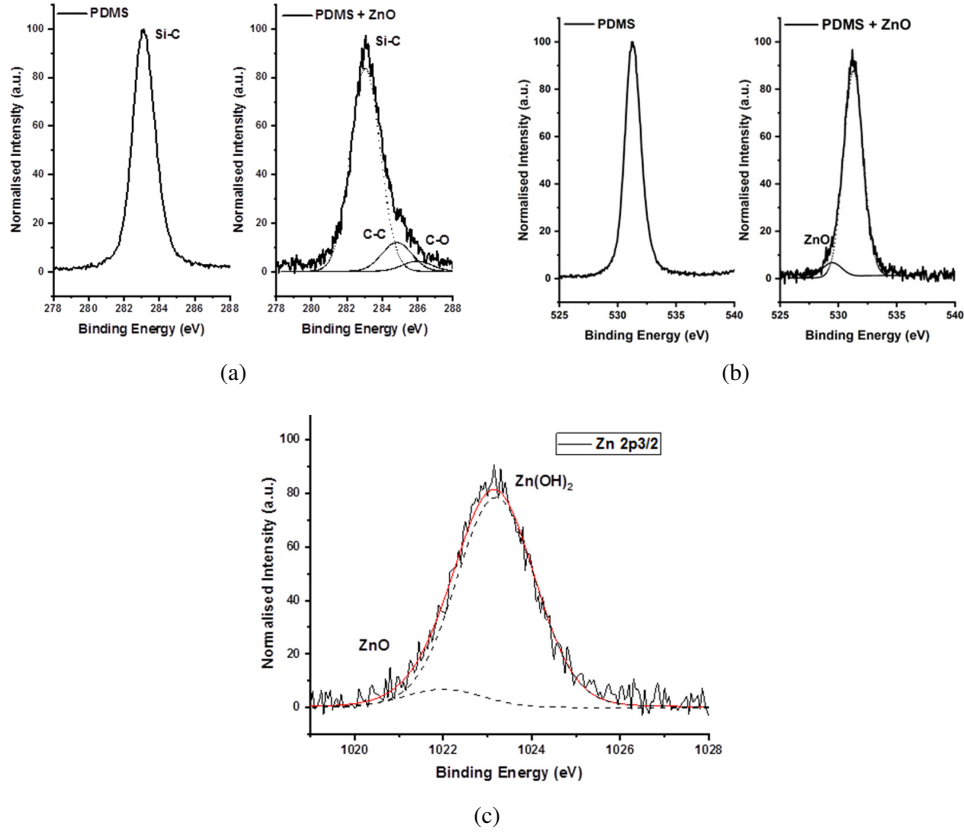
FIGURE 7.5: PDMS reference (dotted lines) and PDMS-ZnO treated slub (solid lines) spectral comparison of (a) C1s, (b) O1s, and (c) $Zn_2p_3/2$ X-ray photoelectron peaks.

Sample	C [%]	O [%]	Si [%]	Zn [%]	N [%]
PDMS	51.5	28.6	19.9	0	0
ZnO-PDMS	52.5	29.4	7.3	4.4	6.4

TABLE 7.1:   XPS atomic concentration analysis for two representatives PDMS and ZnO-PDMS mofd devices.

7.4 (a)-(b)): large hexagonal and misoriented micro-rods on top of a layer of smaller c-axis oriented nanorods.

The surface morphology of bare PDMS is shown for comparison in Fig. 7.4 (c). Related topographical information, expressed in terms of roughness (root mean square (RMS) and mean heights (Ra)) and maximal heights of the structures [121], are reported in Fig. 7.4 (d). Mean lateral particle dimensions, estimated by ImageJ software, were $1.6\mu m$, with a minimum value of 670 nm and a maximum value of $2.5\mu m$.

 The presence of ZnO inside the micro-channel on the PDMS surface was also confirmed by XPS analysis. Table 7.1 shows the XPS atomic concentration analysis for two representatives PDMS and ZnO-PDMS devices.

By comparing the C1s XP spectra before and after the CBD growth (Fig. 7.5 (a)), a band broadening was well evident and additional components to the main Si-C (at 283.7 eV) were evident at high binding energy and were associated with C-O bonds (286.2 eV) and C = O bonds (288 eV). The O1s peak after the ZnO growth was characterized by a tail at 529.6 eV associated with O_2^- and OH^- ions in the defective sublattice of ZnO (Fig. 7.5 (b)).
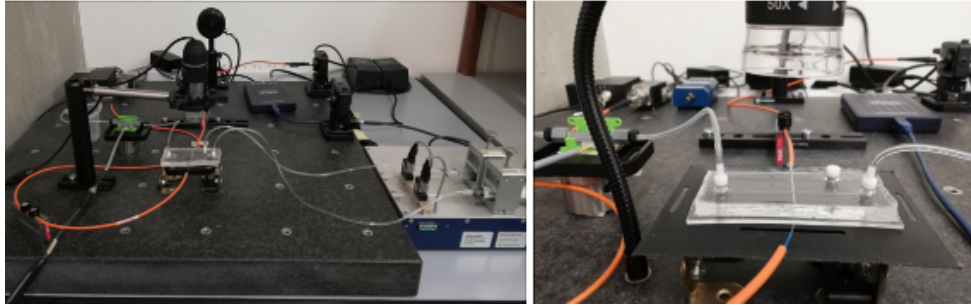
FIGURE 7.6: Pictures of the experimental set-up used for the two-phase flow detection.

It was noteworthy to observe that the shape of the Zn2p3/2 peak revealed two components (Fig. 7.5 (c)), one associated with ZnO at 1022 eV [122] and a second at 1023.2 eV associated with a zinc hydroxide phase, $\varepsilon - ZnO(OH)_2$, formed during the CBD growth in the alkaline solution [123], [124].

7.2 Experimental set-up

An interlacing sequence of air and water was generated by pumping liquid and air at the inlet of the T-junction of the PDMS micro-optofluidic device. The experimental set-up for the flow monitoring in the designed investigation area of the micro-optofluidic device is shown in Fig. 7.6.

Two syringe pumps (neMESYS low-pressure module, Cetoni GmbH, Korbussen, Germany) were connected to the two channel inlets and different flow rates were imposed. The input light source was a laser system (NovaPro 660-125, RGB Lasersystems, Kelheim, Germany) that generates a light beam with a wavelength of 600 *nm*. The light intensity variation was acquired using a photodiode with a gain of 40 *dB* (PDA100A, Thorlabs, Newton, NJ, USA) and the signal received was acquired by a PC oscilloscope (Picoscope 2204A, Pico Technology, Cambridgeshire, UK), with a sampling frequency of 1.5 *KHz*. A digital USB microscope was placed above the device to simultaneously conduct image recording of the process.

7.3 Signals acquisition and processing

In the experimental campaign, a total of 24 experiments, 12 per mof-device (PDMS-mofd and the ZnO-PDMS-mofd), were carried out to evaluate the variation between the two-phase flow velocities inside the micro-channel.

The experiments were performed using a different device for each experimental condition, thus demonstrating the reproducibility of the functionalization strategy.

To evidence how the chemical treatment affects the flow dynamics, the fluids considered were air, water and a mixture of glycerol–water (50%w/w): investigated two-phase flows were (i) air–water (FLOW1) and (ii) air–glycerol–water (FLOW2). The data acquired were pre-processed by a low-pass filter with a 40 Hz cut-off frequency and a signal smoothing procedure. In the processing phase, the 24 signals acquired were analyzed both in time and frequency domains to automatically detect the frequency of the air–liquid passages. The developed methodology was widely used in previous works [16].

By optical fiber insertion, it was possible to capture the variation in the luminosity during the two-phase passage, due to the difference between the refraction index

	Laser Light Power [*mW*]	$V_{air} = V_{water}$ **Flow rate [*ml/min*]**
EXP1	5	0.1, 0.2, 0.3
EXP2	10	0.1, 0.2, 0.3

TABLE 7.2: Experimental campaigns carried out, varying the power of the laser used to light the process and the hydrodynamic pressure, for both the PDMS mofd and ZnO-PDMS mofd for both fluid combinations of air–water (FLOW1) and air–glycerol–water (FLOW2).

(n) of the chip material PDMS ($n_{PDMS} = 1.41$), air ($n_{air} = 1$), water ($n_{water} = 1.3$) and mixture ($n_{(Glycerol\text{-}Water)} = 1.39$). Thanks to this phenomenon, the air and liquid passages were detected in the optical signal at two brightness levels. The top-level revealed the liquid presence, the low-level revealed the air passage, and the two peaks revealed the air in the front and at the rear.

7.4 Results and discussion

7.4.1 Slug frequency measurements

Flow's fluid dynamic evaluation was carried out by varying both the hydrodynamic pressure at the inlet of the chip and the power of the laser light used to visualize the process, as summarized in Table 7.2.

The hydrodynamic pressure was set using three input flow rate values (f), keeping the same velocity for air (V_{air}) and liquid (V_{lq}). The power of the laser was set using two levels of intensity (P). After turning on the laser, the same power intensity was maintained for 60 *s* for each hydrodynamic condition (f).

Fig. 7.7 shows the optical signal and related CCD video frames acquired during an air–water passage in the test section of the micro-optofluidic device.

Figs. 7.8 and 7.9 show the trends and spectra of the optical signals acquired using a photodetector, respectively, in the PDMS mofd and ZnO-PDMS mofd using FLOW1 (air–water) in the EXP1 combinations.

The parameters T_w and T_a, indicated in Figs. 7.8 (a) and 7.9 (a), identify the duration of the liquid and air passage, respectively. The value of the frequency peak (fp), reported in Figs. 7.8 (b) and 7.9 (b), is related to the inter-distance of air–water (or glycerol/water) passage.

This frequency peak was used to calculate the average period (T_{period}) of the flow passage:

$$T_{period} = \frac{1}{f_p} = <Tw> + <Ta> \tag{7.1}$$

By visual inspection, it was evident how the performances of the two devices were different: the number of FLOW1 passages in 30 *s* in the PDMS mofd was fewer than in the ZnO-PDMS mofd. A similar behavior was observed when FLOW1 was tested in the EXP1 conditions.

The period of the air–liquid passage (T_period) in the area investigated using both PDMS and ZnO-PDMS mofd devices are reported in Fig. 7.10.

The two bar graphs reported in Figs. 7.10 (a)-(b) summarize the obtained results for the two fluid combinations (FLOW1 and FLOW2) in EXP1 and EXP2 conditions. To note, the T_{period} of FLOW2 was always lower (faster flow) than FLOW1 (slower flow), disregarding the micro-channel treatments and the experimental conditions, as expected when considering the glycerol–water solution viscosity and density.

It is noteworthy that, in Fig. 9.8 (a), the T_{period} obtained for FLOW1 in the same experimental conditions (i.e., laser power and input flow-rate) was lower in the ZnO-PDMS mofd (faster flow) than in the PDMS-mofd (slower flow). This means that the ZnO surface functionalization led to an increase in the velocity of FLOW1. This finding accords with the contact angle (CA) measurements of the PDMS surface after ZnO coating: in particular, the contact angle increased from 108° to 133°, and
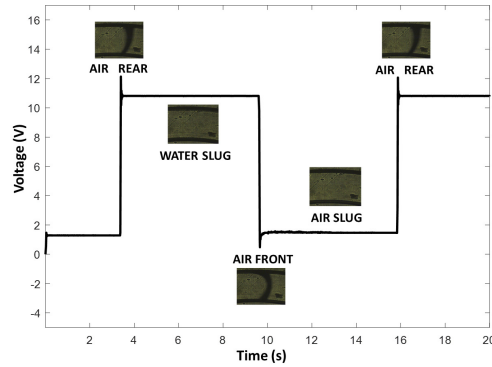
FIGURE 7.7: Optical signal acquired in the PDMS mofd correlated to the FLOW1 passage in the EXP2 conditions (flow rate 0.1 ml/min).
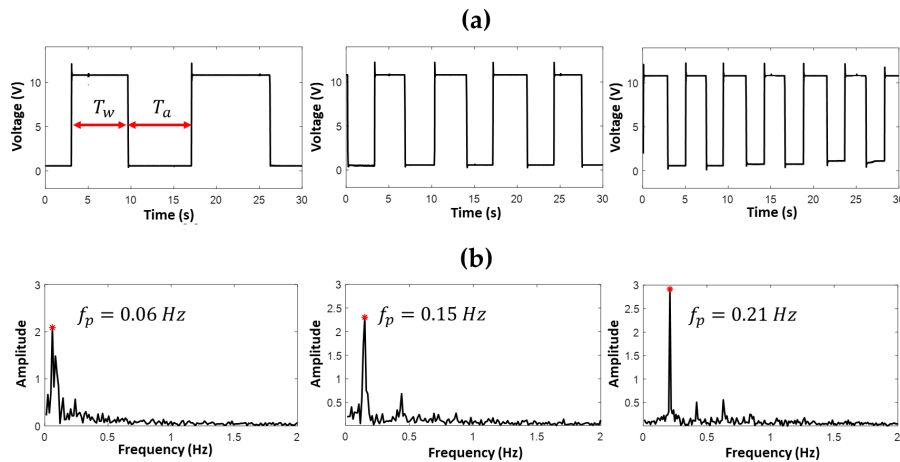
FIGURE 7.8: Optical acquisition for FLOW1 in PDMS mofd using EXP1 combinations, flow rate $V_{air} = V_{water} = (0.1, 0.2, 0.3)$ ml/min: (a) the slug passage signals, and (b) the spectra.

such hydrophobicity enhancement was related to the increase of surface roughness due to the presence of ZnO micro-structures [125], causing enhanced water flow inside the channel [107].

Conversely, Fig. 7.10 (b) reports the period of the air–liquid passage (T_{period}) related to FLOW2, in the same experimental conditions: the T_{period} is greater in the ZnO-PDMS mofd (slower flow) than the PDMS mofd (faster flow). Glycerol–water solution has a polarity lower than water and, in addition, is a trihydric alcohol able to form an extended hydrogen-bonded network. Accordingly, the observed behavior of FLOW2 in a ZnO-PDMS device can be attributed to the interaction of glycerol with the ZnO rods present in the micro-channel and related network of H-bond formation between the surface atomic moieties of the deposited oxide [126].
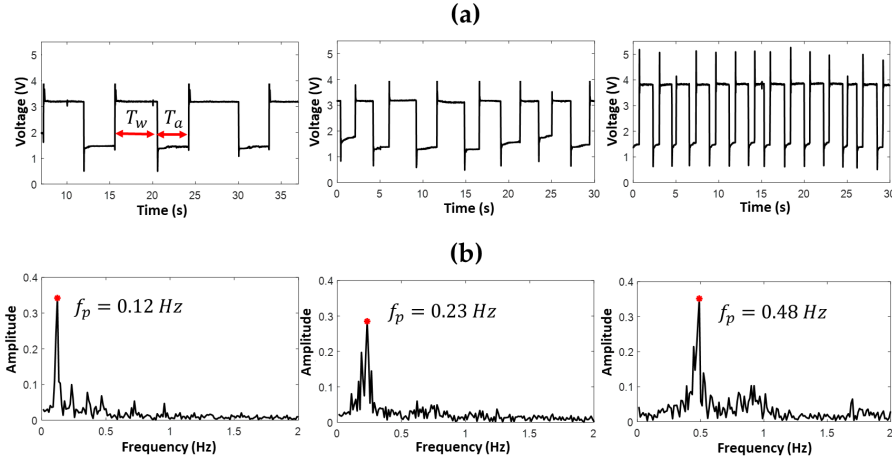
FIGURE 7.9: Optical acquisition for FLOW1 in ZnO-PDMS mofd using EXP1 combinations flow rate $V_{air} = V_{water}(0.1, 0.2, 0.3)$ ml/min: (a) the slug passage signals, and (b) the spectra.
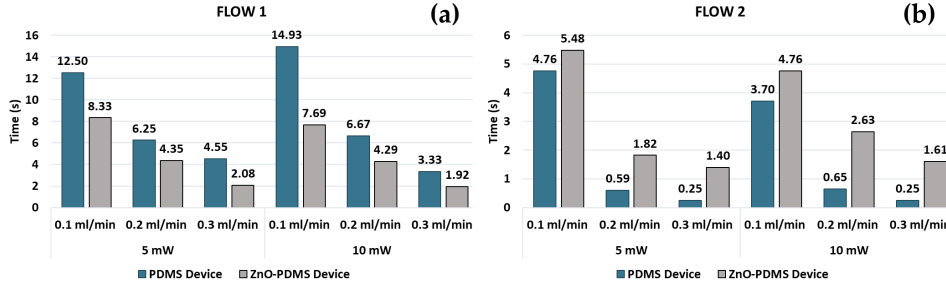
FIGURE 7.10: T_{period} measured in EXP1 and EXP2 conditions for (a) FLOW1, and (b) FLOW2, in PDMS mofd and ZnO-PDMS mofd.

In order to quantify the difference in the performance of the two devices, the percentage of change for each experimental condition was computed as follows:

$$\Delta\% = \left(\left(\frac{X_f}{X_i} \right) \cdot 100 \right) - 100 \tag{7.2}$$

where X_f is the value of T_{period} measured for the PDMS-mofd device and X_i is for the T_{period} in the ZnO-PDMS mofd device.

Fig. 7.11 reports the percentage ($\Delta\%$) values obtained.

On one hand, as expected, the $\Delta\%$ obtained for FLOW1 was positive, underlining that the passage of FLOW1 was faster in the ZnO-PDMS mofd than in the PDMS mofd. On the other hand, the $\Delta\%$ obtained for FLOW2 was negative due to the slower flow passage in the ZnO-PDMS mofd than the PDMS-mofd.

Additionally, it was observed that this percentage variation was highly sensitive to the experimental conditions (input flow rate and laser power). In particular, for FLOW2, the increase in the $\Delta\%$ values following the increase in the input flow rates for both laser power conditions was much more regular than for FLOW1. That could be foreseen coherently with the higher level of instability of the air flow and the stabilization effect of the glycerol correlated to its density value ($\rho = 1261$ kg/m^3) with respect to water ($\rho = 1000$ kg/m^3).

These results evidence the possibility of increasing the level of control of the flow
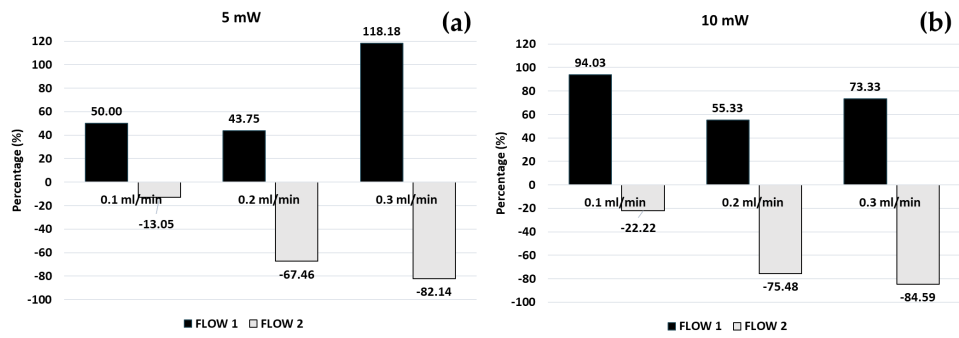
FIGURE 7.11: The percentage of change ($\Delta\%$) of T_{period} measured in the flow passage using the PDMS mofd and ZnO-PDMS mofd per experimental condition (EXP1 and EXP2) for (a) FLOW1 and (b) FLOW2.

inside the micro-channel by combining the external forces (pressure strength and laser power) with a low-cost chemical treatment of the micro-channel surface.

We continue to study the role of ZnO degradation on device performance as we are aware of drawbacks associated with ZnO solubility that can affect material functionality [123].

Part II

METHODS AND DEVICES FOR PARTICLE FLOWS INVESTIGATION

Chapter 8

Methods for micro-particles investigation

Up to now, the most sophisticated laboratory equipment ensuring a complete analysis of particles in suspension is a Flow Cytometer [127]. It is routinely used in diagnostic and research fields to detect physical and chemical features of cells [128] and to count them.

A microfluidic-based system able to detect variations in number, concentration, and shape of particles as well as their hydrodynamic properties would considerably improve the identification of various physiological and pathological conditions. The composition of a biological fluid can be various due to its intrinsic properties or to alteration induced by pathology. It is an example the blood, which is composed of cells with distinguishable traits like size, shape, surface characteristics, compactness, and plasma composition [129]. All these listed items affect the differentiated migration dynamics of specific blood particles/cells. Some pathologies, such as atherosclerosis or thrombosis, can be associated directly with blood disorders altering the cells' movement, whereas others, like anemia or leukemia, affect the cells' proliferation and indirectly the flow [130], [131].

For over a century, manual cell counting using a cytometer and microscope has been the prevalent technique in laboratories, despite requiring bulky equipment and being a time-consuming approach. As an alternative to manual counting, automated cell counters based on the Coulter Counter principle have been developed and become commercially available [132]. The limits in their use are to require bulky and costly equipment and a large number of samples and reagents. Advances in microfluidics have shown promising results in the development of low-cost and portable Lab-on-a-Chip devices with higher throughput, sensitivity, and accuracy [96], [133], [134]. In the miniaturization efforts, different technological issues have arisen in relation to the biological or chemical application contexts [83], [135]–[137] and to the detection approaches [138]–[141]. It is significant to mention the recent advancement in the use of microfluidics for the study of physiological processes as in the case of organs-on-chip [142], [143], and in biology as for the cellular analysis [144], [145] and cell-to-cell interactions [146].

The application of flow visualization in biological systems is becoming increasingly common in studies ranging from intracellular transport to the movements of whole organisms. In cell biology, the standard method for measuring cell-scale flows and/or displacements has been particle image velocimetry (PIV) [147], [148]. More and more researchers have recently been looking to live-cell imaging to provide a quantitative understanding of cellular mechanisms. In [149], it was developed a quantitative phase velocimetry (QPV) approach, by using the principle of PIV to track the entire flow of bulk material through a single cell, in [150], a live scanning particle image velocimetry (LS-PIV) was implemented to quantify peak blood velocities in live mice harboring brain arteriovenous malformation. They detect the blood velocities and exaggerated pulsatility along the abnormal vascular network in these animals. In [151], a free and open-source solution for performing efficient and robust quantification of collective cellular migration in the increasingly popular 3D dynamic data sets in life sciences are developed. In [152], the PIV approach was used for analyzing the dynamics of in vivo models of collective migration. That evidence the relevance of the topics and the challenging open issues around that and the effort in finding a straightforward methodology for velocity cell detection.

In this work, the micro-particles velocities were computed by taking into account the digital particle image velocimetry (DPIV) method based on image analysis and the micro-particles number was obtained by a custom counting algorithm. In the following chapters, these two methods will be discussed in detail.

8.1 Digital Particle Image Velocimetry

Particle image velocimetry (PIV) is an optical, non-invasive technique used to visualize 3D flow fields. In PIV, small tracer particles are added to the flow and from the positions of these particles at two instances of time, it is possible to determine the flow velocity field.

PIV was introduced in the late 1970s and since then has become an essential measurement technique in fluid mechanics laboratories in both research institutes and industry. For a considerable time, the common mode of operation was the analysis of PIV photographs, but nowadays, with the increasing power of computers and the widespread use of CCD cameras, the primary technique used is Digital Particle Image Velocimetry (DPIV). DPIV is the digital counterpart of the PIV techniques: digitally recorded video images are analyzed computationally, removing the directional ambiguity generally associated with PIV, by implementing local spatial cross-correlation between two consecutive images.

So, digital particle image velocimetry is an optical method for quantitative and qualitative flow visualization, used to obtain instantaneous velocity measurements and related properties in fluids.

8.1.1 DPIV methodology

In DPIV, the fluid velocity is inferred from the motion of tracer particles. These small particles are added to the flow and the motion of this fluid is analyzed by illuminating the reflective particles contained in the fluid. The illuminated particles within this light-sheet plane are recorded by a camera (see Fig. 8.1).

 The recording of two consecutive images enables the determination of the particle displacement. The first image *(A)* is captured at the time instant t while the second *(B)* at $t + \Delta t$. The displacement can be calculated for groups of particles by evaluating the cross-correlation of many small sub-images (interrogation areas). The
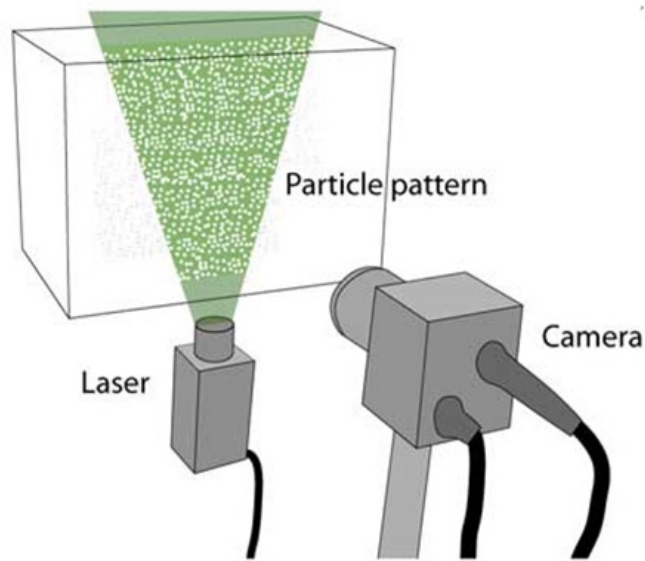
FIGURE 8.1: Working principle of DPIV: A laser sheet illuminates the particles contained in the fluid. A high-speed camera records the displacement of the particle pattern. Reprinted from [153].

correlation yields the most probable displacement for a group of particles traveling on a straight line between image *A* and *B* [153].

Taking into account the displacement Δs and the time interval Δt between the image *A* and the image *B*, it is possible to calculate the velocity vector of the particles. The algorithm used for the analysis of PIV images is the cross-correlation, which evaluates the average displacement of all the particles in each reference evaluation area. The discrete cross-correlation function is defined as in eq. 8.1, where *C* is the resulting correlation matrix, while *A* and *B* are the interrogation areas of the two consecutive images.

$$C(m,n) = \sum_i \sum_j A(i,j)B(i-m,j-n) \tag{8.1}$$

The most probable displacement of the particles from *A* to *B* is determined by the maximum peak location in *C* [154].

Two approaches can be used to solve this equation: the first is to compute the matrix *C* in the spatial domain and it is called "direct cross-correlation" (DCC), while the second is to compute the correlation matrix in the frequency domain and it is called "discrete Fourier transform" (DFT).

In the experiments carried out in this thesis, the second approach will be adopted, which uses a fast Fourier transform to calculate the DFT. In this method, interrogation areas of the same size are used; every particle displacement induces some loss of information, noticed by the increasing amount of background noise in the correlation matrix. A displacement of more than 32 pixels can cause incorrect measurements. The drawback of the DFT is the decreased accuracy, but this disadvantage can be solved by using several passes of the DFT in the same dataset: the result of the first analysis pass is used to offset the interrogation area in the following passes, in order to minimize the loss of information due to the particle displacement [153]. Usually, for the first pass, a bigger interrogation area is used, while the interrogation areas of the following passes are smaller. In conclusion, two types of DFT approaches can be
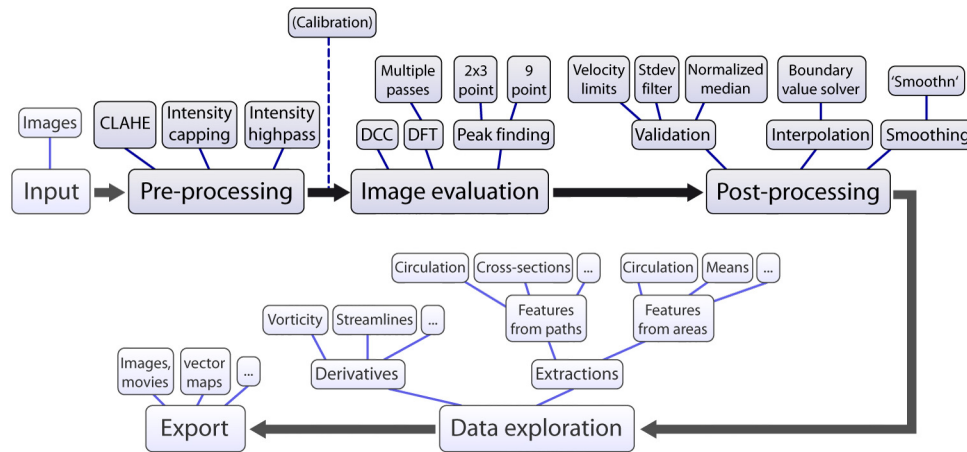
FIGURE 8.2: DPIV analyses in PIVlab and JPIV. Overview of the workflow and the implemented features. Reprinted from [153].

applied, the single-pass DFT approach and the multi-pass DFT approach; the latter method is the most performing.

8.1.2 DPIV platform

The DPIV analysis can be done by using different platforms. In general, each PIV software follows the same scheme as that of Fig. 8.2.

The first step of the process is the acquisition of the data: the images are produced and prepared to be analyzed. Then, the image has to be pre-processed: image pre-processing is a technique to improve the image data that suppress undesired disturbances and noises; it does not increase image information content. This data improvement facilitates the third phase, the image evaluation, which can be implemented through the platform JPIV and PIVlab. The final step is image post-processing, useful to have the best possible types of data, such as smoothing, validation, interpolation, etc...

JPIV is an open source and independent platform for 2D Particle Image Velocimetry (PIV) [155]. It is not intended for image acquisition and image pre-processing, but it is used for many applications such as image and vector field display, flow estimation, vector field statistics and vector field filtering.

PIVlab is an open-source software programmed in MATLAB [153] ; it is a program that can derive velocity information from image data using the PIV method. It does not only calculate the velocity distribution within particle image pairs but can also use to derive, display and export multiple parameters of the flow pattern. One of the main features is that it is a completely GUI-based PIV tool, so most of the functions are accessible from the GUI through a simple graphical user interface. However, it is possible to access PIV analysis functions from the MATLAB command line, in order to include it in a custom platform to perform a faster and fully automatic analysis.

8.1.3 DPIV implementation and post-processing

The data acquired in a video format are processed by the DPIV-based automatic algorithm to have instantaneous velocity measurements and visualizations. Time-varying velocities vector maps, showing the displacements of the micro-particles in time in an investigated area, are obtained and then considered to investigate the
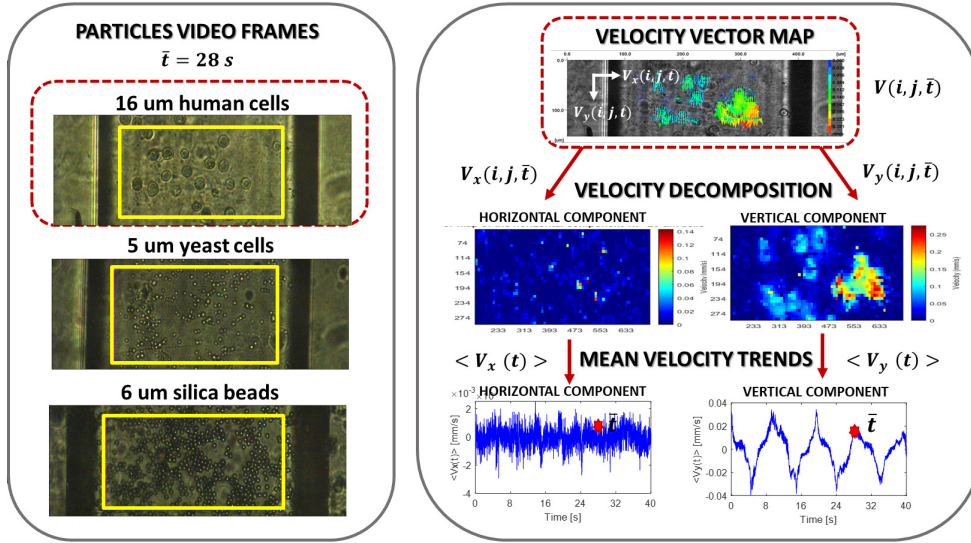
FIGURE 8.3: The algorithm steps of the procedure for the video processing based on DPIV analysis. On the left column, the extraction of the video frames. On the right column for the human cells, in sequence the instantaneous velocity vector maps $V(i,j,\bar{t})$, its decomposition in the horizontal and vertical velocity components $\{V_x(i,j,\bar{t}), V_y(i,j,\bar{t})\}$, and the mean velocity trends $\langle V_x(t)\rangle$ and $\langle V_y(t)\rangle$.

micro-particles flow patterns and to correlate the dynamics of the flow velocity in the time and frequency with the experimental conditions carried out. Thanks to this approach, the complexity of the standard Flow Cytometer equipment is shifted in the algorithm implementation.

Initially, each video is decomposed into frames and a specific region of interest (ROI) is set. The ROI is the portion of the monitored area that is considered for the hydro-dynamic cell flow investigation.

In Fig. 8.3, the algorithm steps from the extraction of the video frames to the computation of the micro-particle velocity trends are presented. On the left three frames, one per cell type, are reported respectively for the yeast cells (5 μm), the human cells (16 μm) and the silica beads (6 μm). The ROI selected is highlighted in yellow. On the right, for the human cells, a frame at a time instant $\bar{t}$ of the time-varying velocity vector map $V(i,j,\bar{t})$, obtained by the DPIV processing performed by the software JPIV is obtained.

In this way, it is possible to know only the spatial velocity distribution, where the vectors indicate the direction of the movement and, the color-coding and the vector length represent the magnitude of the displacement.

Implementing the DPIV processing by the PIVlab function in the MATLAB environment it is possible to obtain the velocity spatial distribution on the horizontal and vertical directions $V_x(i,j,\bar{t})$ and $V_y(i,j,\bar{t})$, respectively, as shown in the second line of the right column of Fig. 8.3.

Then always in MATLAB, it is possible to proceed with a post-processing phase. The velocity spatial distribution on the horizontal and vertical directions are spatially averaged, in order to obtain the mean velocity values $\langle V_x(\bar{t})\rangle$ and $\langle V_y(\bar{t})\rangle$. This procedure repeated automatically for all the frames of the time-varying vector map gives two signals representing the mean velocity trends on x and y directions *versus* time, respectively $\langle V_x(t)\rangle$ and $\langle V_y(t)\rangle$.

In addition, looking at the movement of the micro-particles along the micro-channel

and based on the image orientation, the dominant velocity component is the vertical one. The micro-particle flows flowed from the top to the bottom of the investigated area and vice-versa with an oscillating input flow. In particular, the trend of the vertical velocity component ($\langle V_y(t) \rangle$) shows the periodicity of the oscillating input flow imposed and no-periodicity can be detected in the trend of the horizontal velocity component ($\langle V_x(t) \rangle$).

Working in the Matlab environments it is possible to automatically run the analysis on different videos and post-processing the results in time and frequency domains. Additionally thanks to the flexibility of the used platform, the algorithm will be optimized to be suitable for real-time detection in embedded systems.

8.1.4 DPIV validation and optimization

As mentioned above, the DPIV analysis implements the cross-correlation between the interrogations areas of consecutive pairs of images as the most probable displacement of the micro-particles inside the area considered. The approach used in this thesis for the image correlation analysis is the discrete Fourier transform (DFT) in the frequency domain where the Fourier transform is applied to the interrogation areas of both images; then the product, in the complex domain, of these transforms is computed and anti-transformed, using the inverse FFT [153]. On one hand, the DFT requires a smaller computational effort than the other method available [156] but, on the other hand, having a fixed dimension for the interrogation areas a loss of information related to the displacement of particles could be determined. To overcome this accuracy decrease, the multi-pass DFT can be used by choosing a bigger interrogation area in the first pass, and smaller areas in the successive steps.

In the beginning in order to validate the methodology implemented, just described above, by considering as example human cells with a diameter of 16 μm, the velocity was computed analytically and compared with the results obtained with the platform DPIV-based realized in MATLAB. Fig. 8.4 reports a sequence of 2 frames in which the obtained analytical results (see Fig. 8.4 (a)) and by DPIV analysis (see Fig. 8.4 (b)-(c)) have been compared.

In particular, the velocities of three particles, selected in red in the left image of Fig. 8.4 (a), were computed analytically by considering their positions, as reported in the computation for v_{p1}, v_{p2} and v_{p3} on the right image of Fig. 8.4 (a). By computing the DPIV analysis on the frames selected, it is possible to obtain the velocity map related to the particles' displacement along the main flow direction (V_y, vertical direction) as shown in the left image of Fig. 8.4 (b), where the three tags are for the particles selected. On the right image of Fig. 8.4 (b), it is reported the average velocity trend obtained for the complete duration of the considered experiment, and the red star points out the time instant ($t = 10\ s$) of the two frames selected. In this case, a DPIV analysis with three passes (by using as interrogation windows: Area1 = 64 pixels, Area 2 = 32 pixels and Area3 = 16 pixels) was carried out. From this result, it is possible to conclude the validity of the methodology implemented being the results obtained analytically and numerically (implemented DPIV algorithm) equivalent.

After validating the DPIV methodology, in order to optimize, as much as possible the DPIV analysis, a comparison between the DPIV analysis performed by a single pass (a single interrogation area) and three passes (three different interrogation areas) was executed. The use of a small interrogation area, in combination with the algorithm "PIVlab-postproc" (including the local median filter and the standard deviation filter) used in the post-processing phase, does not produce artifacts but allows for reducing the noise (so the outlier effects). That brings for a more precise computation of the

$$v_{p1} = \frac{8\,[pixel\,displacement] * 4.65e-6\,[pixel\,dimension]}{10\,[magnification] * \left(\frac{1}{60}\right)[frame\,per\,second]} = 0.22\,\frac{mm}{s}$$

$$v_{p2} = \frac{17\,[pixel\,displacement] * 4.65e-6\,[pixel\,dimension]}{10\,[magnification] * \left(\frac{1}{60}\right)[frame\,per\,second]} = 0.16\,\frac{mm}{s}$$

$$v_{p3} = \frac{15\,[px\,displacement] * 4.65e-6\,[pixel\,dimension]}{10\,[magnification] * \left(\frac{1}{60}\right)[frame\,per\,second]} = 0.14\,\frac{mm}{s}$$
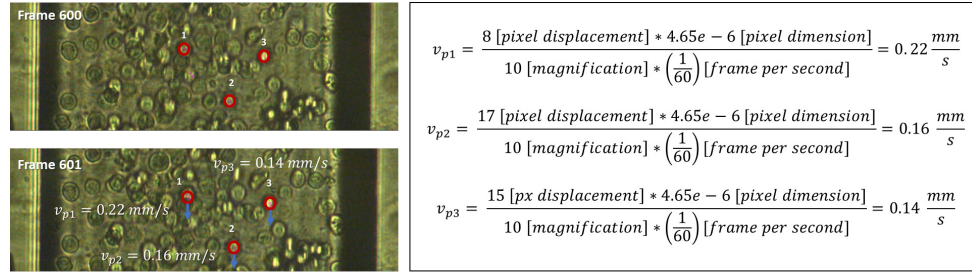
(a)
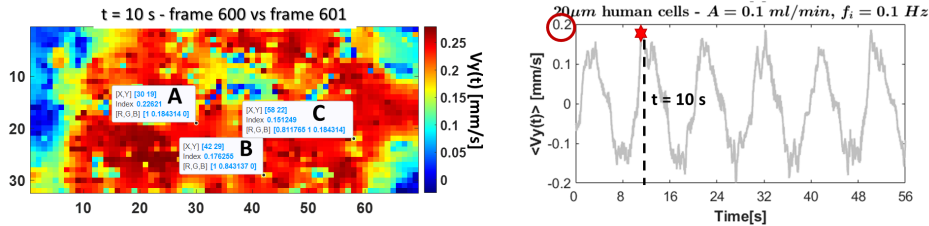
(b)
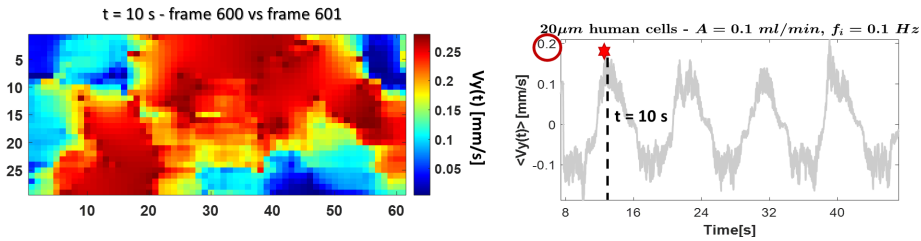
(c)

FIGURE 8.4: (a) Extracting two subsequent frames 600-601 from the video related to an experiment with the human cells (HeLa Cells - 16 μm) and the analytical velocity computation of three selected particles (in red). (b) On the left, the velocity map V_y along the vertical direction and on the right, the average velocity trend obtained for the complete duration of the considered experiment. Results obtained considering a DPIV analysis with three passes by using the following interrogation windows: Area1 = 64 pixels, Area 2 = 32 pixels and Area3 = 16 pixels. (c) Same plots of (d) by using a DPIV analysis with a single pass by using an interrogation window of 64 pixels.

velocity in small regions. The blue points in the colormap of Fig. 8.4 (b)-(c), set to 0, are those where no particle movement is detected or with no particles.

First of all, it is possible to quantify the losses in terms of accuracy by comparing the maximum value obtained from the vector map (left image of Fig. 8.4 (b)-(c)), which corresponds to the maximum read in the color bar (0.25 mm/s) with the maximum value obtained from the velocity signal <Vy(t)> (right image of Fig. 8.4 (b)-(c)), which turns out to be 0.2 mm/s. It is worth noting a lack of $\sim$ 0.05 mm/s.

Returning to the comparison between single-pass and multi-pass, DPIV analysis was initially performed using a fixed large interrogation window. Specifically, the DPIV algorithm was set up with a single pass and a 64-pixel interrogation window (named s1 setting) and the flow of human cells (see Fig. 8.4 (c)) and yeast cells (see Fig. 8.5 (c)) in the same experimental condition were analyzed. The cells were injected in a micro-channel with an oscillating input flow having an amplitude of A = 0.1 ml/min and a frequency of f=0.1 Hz. These results were compared with those obtained by performing DPIV analysis with three passes and interrogation windows

of 64-32-16 pixels (named s2 setting) (see Fig. 8.4 (b) and Fig. 8.5 (b)).

In particular, in Figs. 8.5 (b)-(c) the velocity vector maps obtained in the time instants $t1 = 15\ s$, $t2 = 17\ s$ and $t3 = 20\ s$ were considered, and the same time instants are marked in red in the two average velocity signals $< Vy(t) >$, computed by the results of the DPIV in both settings (s1 and s2). In both cases the validity of the approach is evident, the color maps change color ($t1 = 15\ s$, $t2 = 17\ s$ and $t3 = 20\ s$) in correspondence of the varying of the velocity value and the displacement direction change. Looking at the color maps in Fig. 8.5 (b)-(c) it is worth noticing a higher precision in the cells displacements detection in the DPIV-s2 with respect to the DPV-s1.

Both approaches are valid, but the use of a larger interrogation window reduces the calculation time and the results are less accurate. As the accuracy of the results is more important, we can conclude that a multi-step DPIV analysis is more advantageous.
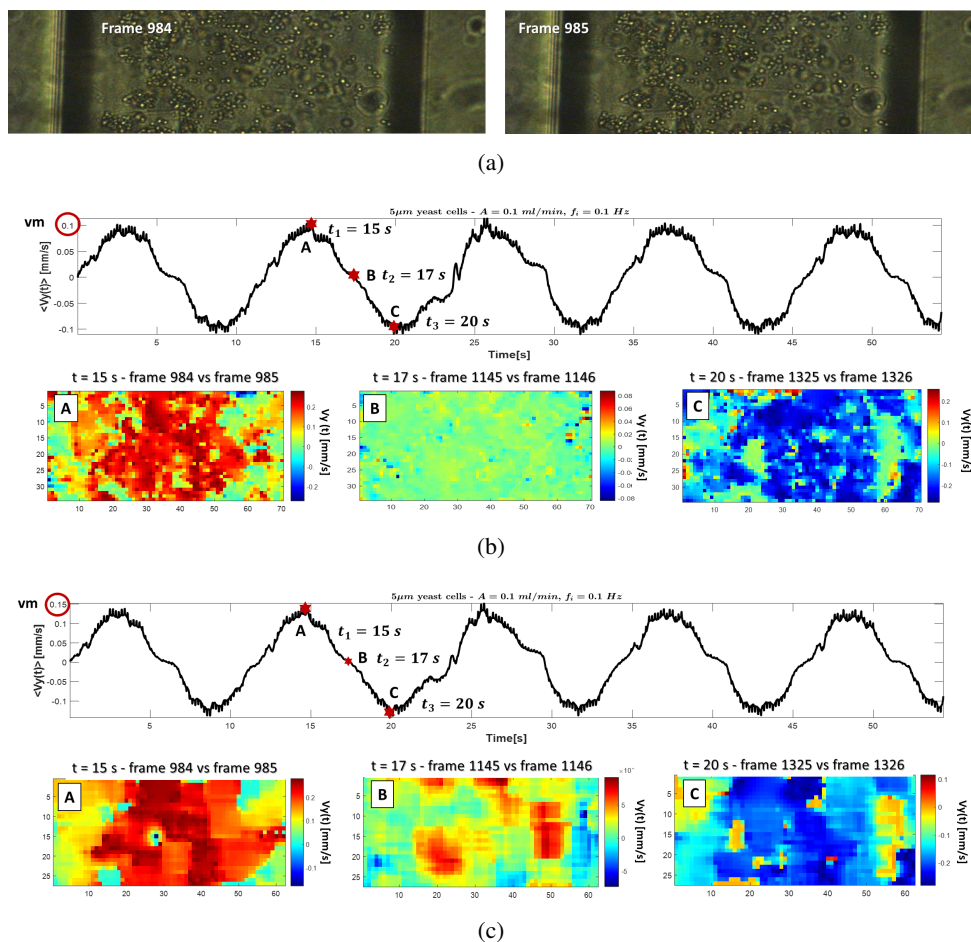
FIGURE 8.5: (a) Extracting two subsequent frames 984-985 from the video related to an experiment with the yeast cells having a diameter of 5 μm to perform the velocity vector map in the time instant $t1 = 15\ s$. Comparison between the DPIV analysis with (b) three passes and the interrogation windows of 64-32-16 pixels and the DPIV analysis with a (c) single pass and an interrogation window of 64 pixels.

8.2 Particle counting

In diagnostic and research life science laboratories, cell counting is a common task for any cell-based assay. The less expensive procedure is to count the cells using a reusable hemocytometer by visualizing them with a bright field optical microscope [157]. To reduce the systematic and random error of the manual count and to improve the statistic values, these approaches have been automated with micro-particles imaging analysis acquisition based on enhanced technologies and paired with a sophisticated micro-particles counting algorithm.

Initially, a standard platform called *ImageJ* [158], which is widely used in this field for counting single-particle images, was taken into account to understand the basic steps to be performed.

In Fig. 8.6 the flow chart of the basic steps implemented to count the particles
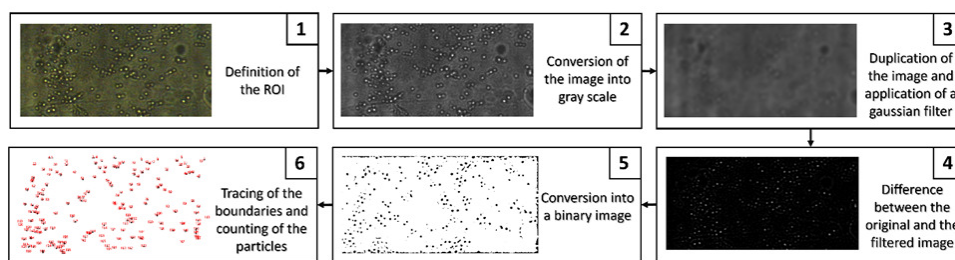
FIGURE 8.6: The flow chart of the algorithm implemented to count the particles in ImageJ.
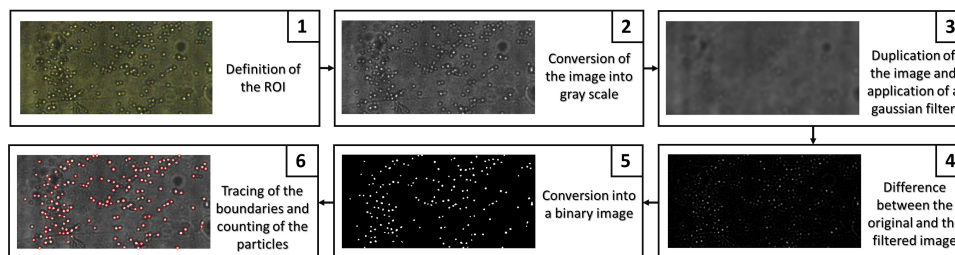
FIGURE 8.7: The flow chart of the algorithm implemented to count the particles in the MATLAB environment.

in ImageJ is shown considering as an example synthetic micro-particles with a diameter of 5 μm. In order to realize a single platform capable of integrating both the DPIV analysis and the particle counting, the basic steps implemented in ImageJ were transposed into the MATLAB environment. The steps performed in both cases are similar.

In Fig. 8.7 the flow chart of the micro-particle counting algorithm implemented in the MATLAB environment is shown considering the same synthetic micro-particles with a diameter of 5 μm used for the ImageJ software.

The images, to be analyzed, are loaded automatically into the platform and the first step is the definition of the region of interest (ROI) in the images, which will be taken into account for the duration of the analysis. After the ROI definition, each image is converted into grayscale by using the function 'rgb2gray'. In addition, to adjust the images' intensity values to the grayscale images, the function 'imadjust' is applied. Then, a Gaussian filter is applied to the new images, by using the function 'imgaussfilt', to smooth the images and reduce the noise. The arguments of this last

function are the images to be filtered and sigma, which is the standard deviation of the Gaussian distribution, defines the filter size. The difference between the original and the filtered images contains the noise removed in the filtering phase. However, the locations of the micro-particles are still visible in these noise images as regions of increased variability. At this point, the new images must be converted into binary images, by using the function 'imbinarize', which creates binary images by selecting a threshold value. All the values above the threshold will be replaced with 1 and all the others with 0. The threshold is not a fixed value but changes for every image, and it can be calculated through the function 'graythresh', which computes a global threshold from a grayscale image. Finally, the function 'bwboundaries' was used to trace the exterior boundaries of objects in the binary images. The arguments of this function are the binary images and the option 'noholes', since the boundaries of holes inside other objects will not be included. The function returns a cell array with the boundaries pixel locations, a label matrix where the objects are labeled and the number of micro-particles found. After that, a check on the detected micro-particles is carried out, to eliminate possible artifacts. With the function 'regionprops', it is possible to measure some micro-particle properties such as the area, the center and the circularity. Therefore, it is possible to verify if the detected particles have an appropriate area, consistent with the micro-particle size investigated, defining the minimum and maximum dimensions of the searched objects, to count among the found micro-particles only those that have an appropriate size. There is another threshold parameter that needs to be set based on the shape of the objects. After defining this parameter, the exterior boundaries of particles are traced and the number of particles is found.

The procedure proposed provides a continuous counting in time of the micro-particle number in the investigated area, avoiding any manual and individual selecting of the frames to be studied. It analyzes automatically the video, frame by frame, counts the number of particles per frame and collects this information in a signal as shown in Fig. 8.8.
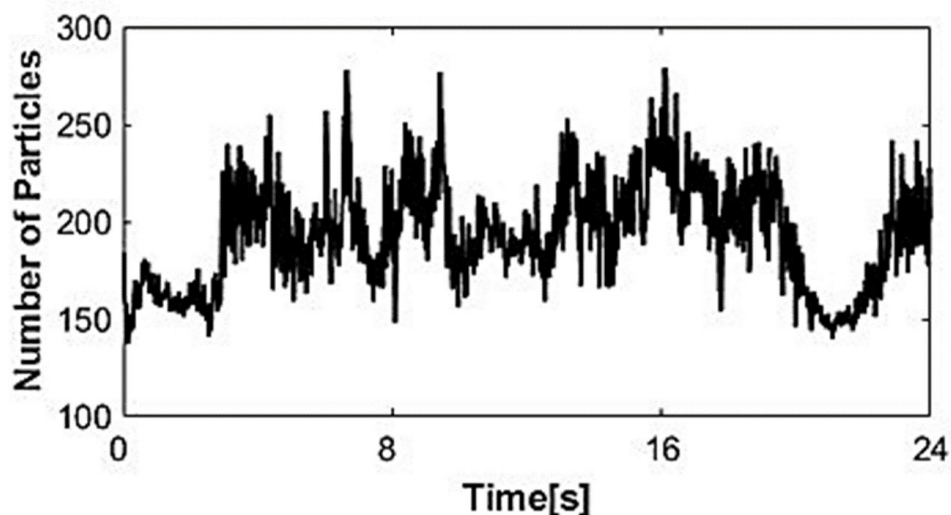
FIGURE 8.8: Signal reconstructed by the algorithm for the micro-particles counting for the synthetic micro-particles with a diameter of 5 *μm* flowing in a micro-channel of 400 *μm* imposing an input flow rate of 0.1 *ml/min*.

Chapter 9

Hydrodynamic study of unsteady biological flows

In this chapter, a counting Digital Particle Image Velocimetry(DPIV)-based method to investigate the collective behavior of particles, in micro-channels or chambers, in response to hydrodynamic stimuli is presented.

The algorithm proposed to offer the advantage to extract automatically the information on the number of particles, flowing in an investigated area in time, and their velocities. The experiments carried out for its validation evidence the difference in the particles' hydrodynamic responses to external stimuli and the possibility to associate them with the particles' physical properties.

The simplified optical set-up and the algorithm flexibility, make this methodology suitable for real-time detection in embedded systems for the study of cell interaction, as in the Lab-on-a-Chip.

This work aims to develop an approach for the investigation of micro-particles moving in micro-channels or chambers. To do that, a wide experimental campaign was carried out, using micro-particles of different nature, as living cells and silica beads, and with different physical properties, such as density and size (from 5 μm to 16 μm). An external oscillating flow was imposed at the inlet of a micro-channel and the process was continuously monitored in a test area simultaneously by using a CCD camera and a photo-detector. The videos and the signals acquired were analyzed to determine information correlated to the changes in time of the micro-particle number and their velocities.

In the last decades, image processing based method [159]–[162] and microfluidics based systems for particle counting and detection have been developed to overcome the barriers associated with conventional methods [163], [164], but the use of real-time image processing is still very challenging [165] due to hardware and software requirements.

In order to overcome these issues for the development of a real-time approach, in this work, the possibility to detect the flows by the use of photo-detector signals as an alternative to the camera acquisition has been also investigated. The optical detection by signals was proved to be useful for characterizing the flow non-linearity [5],
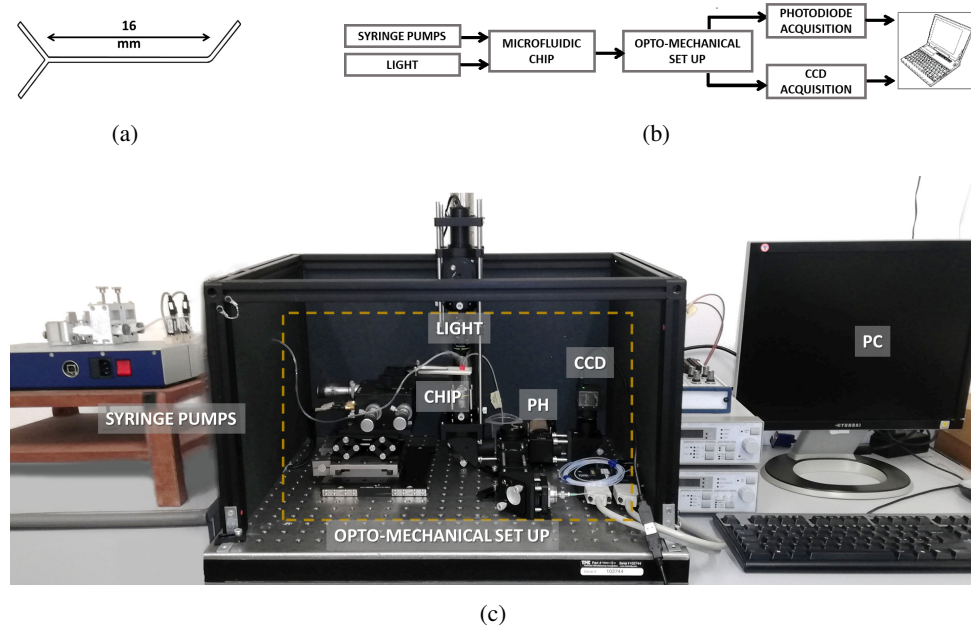
FIGURE 9.1: (a) The Y-junction squared rectilinear micro-channel with a diameter of 320 μm. The opto-mechanical experimental set-up: (b) description by a flowchart and (c) a picture.

[16], it was possible the development of a real-time velocity detection system for the slug flow analysis in a micro-channel [102] and the realization of a micro-optofluidic flow detector for the investigation of biological and chemical samples on chip [8].

In this chapter, the signals, collected by the photo-detector, were compared with the velocity trends obtained by the DPIV-based algorithm as a proof of concept for a further simplification and speed-up of the data acquisition and analysis, based on a simpler optical detection than the video recording needed for the on-chip implementation.

9.1 Experimental set-up

The experimental set-up is composed of a syringe pump, a microfluidic chip and an opto-mechanical system. The syringe pump (neMESYS low-pressure module, Cetoni GmbH, Korbussen, Germany) was used to inject a fluid mixed with microparticles in a Y-junction squared rectilinear micro-channel in cyclo-olefin copolymer (SMS0104, Thinxxs, Zweibrücken, Germany), with a length of 16 mm and a diameter of 320 μm, its geometry is shown in Fig. 9.1 (a).

The microfluidic process was analyzed in an investigated area at a distance of 8 mm from the inlet, illuminated by a white light. A photo-detector (SM05PD1A, Thorlabs, Newton, NJ, USA) connected to an acquisition board (BNC-2110, National Instruments, Austin, TX, USA) and a CCD camera (DCU224, Thorlabs, Newton, NJ, USA), included both in the opto-mechanical system (Thorlabs, Newton, NJ, USA) allow a simultaneous process monitoring.

A magnification of 10x (PLN, Olympus, Tokyo, Japan) and a distance of 3.5 mm between the focal plane and the objective has been considered. The data were recorded for about 75 seconds, with a video frame rate of 60 frames per second, around 4.500

Micro-particles	Mass [kg]	Radius [m]	Volume [m^3]	Density [$\frac{Kg}{m^3}$]
Yeast cells	$7.37e^{-14}$	$2.5e^{-6}$	$6.54e^{-17}$	1126
Human cells	$2.23e^{-12}$	$8.0e^{-6}$	$2.14e^{-15}$	1040
Silica beads	$1.36e^{-13}$	$3.0e^{-6}$	$1.13e^{-16}$	1200

TABLE 9.1: The physical properties of the micro-particles.

Micro-particles	Frequency f_i [Hz]	Amplitude A [ml/min]
Yeast cells	0.1	$0, 0.03, 0.04, 0.05, 0.07, 0.1, 0.15, 0.2$
	0.2	$0.05, 0.07, 0.1, 0.2$
Human cells	0.1	$0.04, 0.05, 0.07, 0.1, 0.15$
Silica beads	0.1	$0.04, 0.05, 0.07, 0.1, 0.15$

TABLE 9.2: The experimental campaigns.

frames per experiment, and a sampling frequency of 1 kHz for the photo-detector acquisition. A detailed description of the opto-mechanical set-up is reported in the paper [61]. A flow chart and a picture of the experimental set-up are shown in Fig. 9.1 (b) and Fig. 9.1 (c).

9.2 Experimental campaigns

The microfluidic chip was fed by an oscillating flow. The biological fluids employed for the experiments were obtained by diluting some micro-particles in a saline solution, the phosphate buffered saline (PBS). The micro-particles diluted with the PBS were of two types: live cells and artificial beads. The live cells, of eukaryotic origins, were: the yeast cells of *Saccharomyces cerevisiae* and the human epithelial *HeLa cells*. The relevant difference between these two types of cells concerns their dimension: the yeast cells have a diameter of 5 μm while the human cells have a diameter of 16 μm. The artificial beads were silica beads with a diameter of 6 μm. The number concentration of particles, diluted in 10 ml of PBS fluid, were $1x10^5$ for the silica beads, $1x10^7$ for human cells and $1x10^8$ for the yeast cells. The physical properties of the particles, such as mass, radius, volume and density, are summarized in Table 9.1.

Initially, a single-phase PBS flow, in absence of micro-particles, was recorded to quantify the effect of the fluid background in the images and the signals. The PBS flow was injected at the inlet with an oscillating flow at a frequency of $f_i = 0.1$ Hz and an amplitude of $A = 0.1$ ml/min. The following 22 experiments conducted are summarized per type of cells in Table 9.2.

The micro-particle flow was fed into the micro-channel using an oscillating flow at a frequency of $f_i \in \{0.1; 0.2\}$ Hz and an amplitude strength varying in the range $A \in \{0; 0.2\}$ ml/min. For the three categories of cells, five equal experimental conditions were considered with $f_i = 0.1$ Hz and $A \in \{0.04; 0.05; 0.07; 0.1; 0.15\}$ ml/min. Then, for the yeast cells, the campaign was extended considering three other experiments with $f_i = 0.1$ Hz and $A \in \{0; 0.03; 0.2\}$ ml/min and four experiments with $f_i = 0.2$ Hz and $A \in \{0.05; 0.07; 0.1; 0.2\}$ ml/min.

9.3 Results and discussion

To evaluate the hydrodynamic response of the micro-particle flow in different flow strength conditions, an automatic procedure to analyze the 22 collected videos was implemented by two algorithms. The first algorithm, based on the Digital Particle Image Velocimetry (DPIV) analysis, was successfully applied in [77], [166] to track the red blood cell flows. In this work, it was improved to compute automatically the vector maps of cell migration velocity in the investigated area, and subsequently, decompose and average those to have the velocity distribution trends along with the horizontal and vertical directions. The mean velocity trends obtained were then correlated with the signals of the photo-detector.

As expected, the velocity values obtained are affected by the number of cells present instantaneously in the micro-channel area. The cell distribution along the micro-channel is unpredictable and cannot be controlled by knowing the cell concentration in the fluid or the external flow. This aspect becomes more relevant due to the difference in the micro-particles' physical properties. For that in the second algorithm, an *ad-hoc* procedure for counting in time the number of micro-particles in the investigated area was implemented.

The two algorithms were used to analyze the data collected in the experimental campaigns, allowing the investigation of how the hydrodynamic response of the micro-particles could be correlated with their physical properties and characterize their collective behavior. To compare the results obtained for different cell types, the velocity signals $\langle V_y(t) \rangle$ per experiment, computed by the DPIV-based algorithm, were considered. The different numbers of particles in the area can affect significantly the value of the velocity, so the velocity signals were normalized concerning the average number of particles and computed by the algorithm implemented.

The computational time required for the analysis of 1000 video frames (using a PC with Intel® Core™ i7-6500U CPU @ 2.50GHz 2.59GHz, RAM 8 Gb, operative system 64 bit) was 1 hour for the DPIV-based algorithm and 2 minutes for the counting algorithm.

To evaluate the micro-particle hydrodynamic responses, after the normalization phase, the dynamics of the signals were analyzed in the time and the frequency domains, as described in the following.

9.3.1 Micro-particle migration velocity

Using the DPIV algorithm presented in Section 8.1, it was possible to compute the micro-particle migration velocity. The ROI was set equal for the experiments using the same cells. The DPIV analysis was conducted by a three-passes discrete Fourier transform (DFT) in the frequency domain as implemented by the PIVlab tool [153]. The three interrogation areas in pixel were chosen as follows: $Area1 = 64$, $Area2 = 32$ and $Area3 = 16$. The step size has been set to half of the last interrogation area, then $Step = 8$.

Looking at the movement of the micro-particles along the micro-channel and based on the image orientation, the dominant velocity component is the vertical one. For this reason, the following analysis is related to the $\langle V_y(t) \rangle$. In Fig. 9.2, the velocity trends $\langle V_y(t) \rangle$ in a time interval of 56 s for each type of micro-particles for the experimental condition $\{f_i = 0.1 \text{ Hz}, A = 0.1 \text{ ml/min}\}$ have been plotted. The oscillating trend of the velocity highlights the effects induced by the oscillating input flow. In particular, in Fig. 9.2, considering the same experimental condition, the amplitude of the velocity trend for the beads is lower than that found in the human and yeast
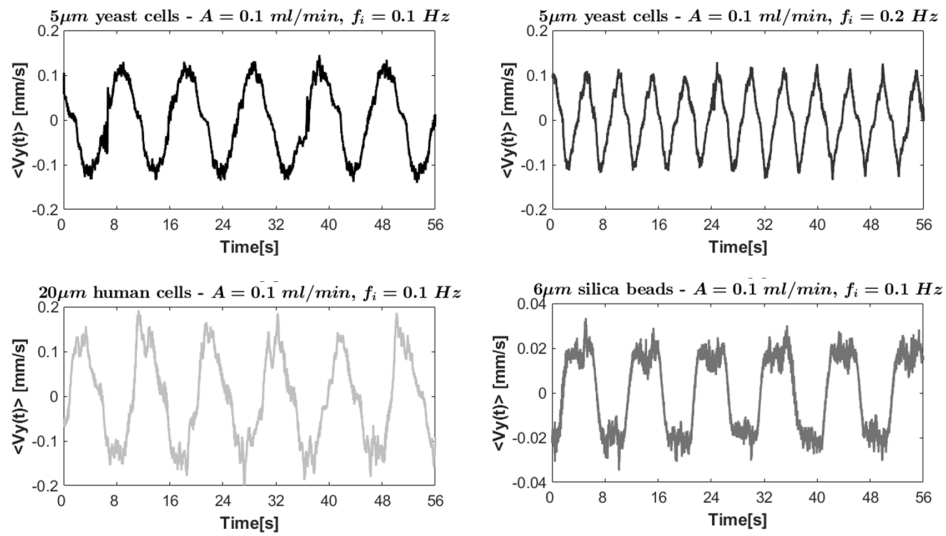
FIGURE 9.2: For all the micro-particles, the velocity trends $\langle V_y(t) \rangle$ obtained in the experimental condition with $\{A = 0.1 \text{ ml/min}, f_i = 0.1 \text{ Hz}\}$.

cells due to the higher value of density concerning the fluid. Being heavier, they tend to lay down on the bottom of the micro-channel and offer greater resistance to the dragging force.

In order to overcome the hardware and software requirements for the development of a real-time approach, the possibility to detect the flows by the use of a photo-detector, which converts the optical signal into an electrical one, as an alternative to camera acquisition has been investigated. In the experimental set-up implemented, it detects and measures the light variations due to the passage of the micro-particles inside the micro-channel. Then, it can convert them into voltage variations.

The signals collected by the photo-detector, after being filtered and down-sampled, have been compared with the velocity trends obtained by the DPIV-based algorithm as a proof of concept for further simplification and speed-up of the data acquisition and analysis. In Fig. 9.3, on the left column, the velocity trends and the photo-detector signals are superimposed for the yeast cells in the two experimental conditions with $\{A = 0.1 \text{ ml/min}, f_i = 0.1; 0.2 \text{ Hz}\}$. Both signals were normalized. It is worth noticing a synchronous oscillating behavior with a phase shift due to the rounding of the down-sampling. That is confirmed by the spectral analysis on the right column shown in Fig. 9.3. The two frequencies of the external oscillating flow imposed at the inlet are undoubtedly detected and driving the changes in the cell flows.

9.3.2 Micro-particle counting

Using the algorithm presented in Section 8.2, the detection of micro-particle results is simple, fast and accurate. For its validation, the results obtained were compared with the one of a standard platform *ImageJ* [158], widely used in this field for particle counting single images. The steps performed in both cases are similar.

Three frames per experiment (the first, the last and one in the middle) were selected and the number of micro-particles was counted. Considering the experiments with the yeast cells and the silica beads the variation detected was of the order of the 10%. In Fig. 9.4 (a), as an example, a frame with the micro-particles detected by the two
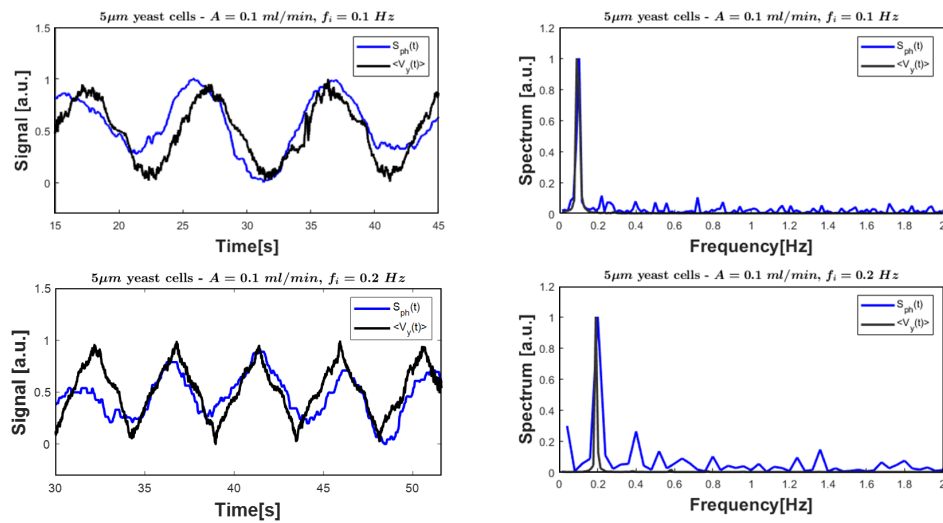
FIGURE 9.3: The time course and spectral analysis of the velocity trends extracted by the DPIV-based algorithm and the photo-detector signals for the experiments $\{A = 0.1 -$ ml/min, $f_i = \{0.1; 0.2\}$ Hz$\}$ with the yeast cells.
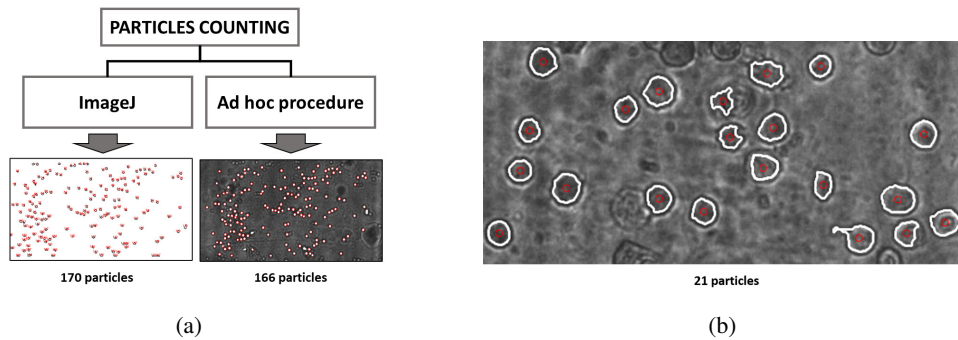
FIGURE 9.4: (a) Frames with detected yeast cells, in red circles, by using the platform ImageJ and the procedure implemented in the MATLAB environment. (b) A frame with human cells detected (16 μm), marked in red circles, by using the procedure presented.

approaches are shown.

The mean number of micro-particles, counted by the implemented algorithm for each experiment, is reported in Table 9.3 for all the micro-particles investigated per experiment.

Additionally, the micro-particle counting becomes more difficult by the standard platform, when the color inside the particle is similar to the background and the boundary of the particles can not be defined appropriately, as in the case of human cells (16 μm). This aspect was overcome by the proposed algorithm, as shown in the analyzed frame reported in Fig. 9.4 (b).

It is worth underlining that this proposed algorithm, not only is easily adaptable to different operative conditions with a higher level of precision, but it is able also to analyze a video automatically, allowing to obtain the changes of the number of particles in time for all the experiment duration.

In Fig. 9.5, for yeast cells in the experiment $\{A = 0.15$ ml/min, $f_i = 0.1$ Hz$\}$ in a time interval of about 24 s, the velocity trends $\langle V_y(t) \rangle$ and the signals reconstructed by counting instantaneously the number of particles over time is plotted.

Particles	Freq. [Hz]	Ampl. [ml/min]							
		0	**0.03**	**0.04**	**0.05**	**0.07**	**0.1**	**0.15**	**0.2**
Yeast cells	**0.1**	192	165	160	164	178	198	224	211
	0.2	-	-	-	216	233	227	-	231
Silica Beads	**0.1**	-	-	336	351	318	381	326	-
Human cells	**0.1**	-	-	15	20	12	45	14	-

TABLE 9.3: The average number of particles $\langle N_p(t) \rangle$ counted through the developed algorithm per experiment.
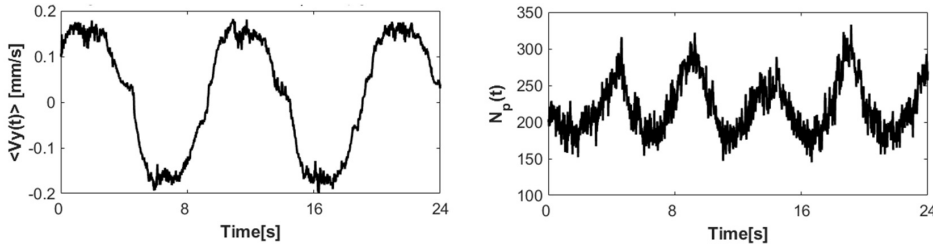
FIGURE 9.5: The velocity trends $\langle V_y(t) \rangle$ and the signal reconstructed by the algorithm for the micro-particle counting for the yeast cells in the experimental condition $\{A = 0.15 \text{ ml/min}, f_i = 0.1 \text{ Hz}\}$.

9.3.3 Micro-particle hydrodynamic response in time

The micro-particle hydrodynamic response in the time domain was evaluated by computing the range of the velocity signal $\langle V_y(t) \rangle$, as in eq. 9.1.

$$Range\langle V_y(t) \rangle = max(\langle V_y(t) \rangle) - min(\langle V_y(t) \rangle) \tag{9.1}$$

Fig. 9.6 shows in the y-axis the values of the velocity range ($Range\langle V_y(t) \rangle$) per experiment normalized with respect to the average number of micro-particles ($\langle N_p(t) \rangle$) computed in the investigated area per experiment. Each point in the curve has been obtained as an average of the velocity values obtained under dynamical conditions maintained for 75 s. The stability of the signal ranges, shown in Fig. 9.2, confirms the robustness of the analysis in time and its reproducibility.

In Fig. 9.6 (a) the three curves are respectively for the micro-particles considered (silica beads, yeast cells and human cells) and each point per curve is correlated to a driving force by varying the amplitude of the external oscillating input flow strength A with a constant frequency $f_i = 0.1$ Hz. It is noticeable that the normalized parameter ($Range\langle V_y(t) \rangle / \langle N_p(t) \rangle$) increases as the amplitude of the flow increases. A parabolic interpolation of the points was performed per particle type, as shown in Fig. 9.6 (b). The parameter R^2, reported in the picture with the fitting equations, is always greater than 0.90 confirming the quality of the fitting. It is evident that the normalized parameter ($Range\langle V_y(t) \rangle / \langle N_p(t) \rangle$) is sensitive to the dimensions of the micro-particles, indeed the values of the human cells (16 μm) are one order magnitude greater and increase faster than yeast cells (5 μm) and silica beads (6 μm). That leads to an immediate classification between the two classes of live cells. Additionally, it is worth evidence of a significant difference in the parabolic interpolation obtained for the yeast cells (live cells) and silica beads (synthetic particles), in spite of having the same dimension. That evidences the possibility of a differentiation correlated to other physical properties such as the particles' density and surface tissues.
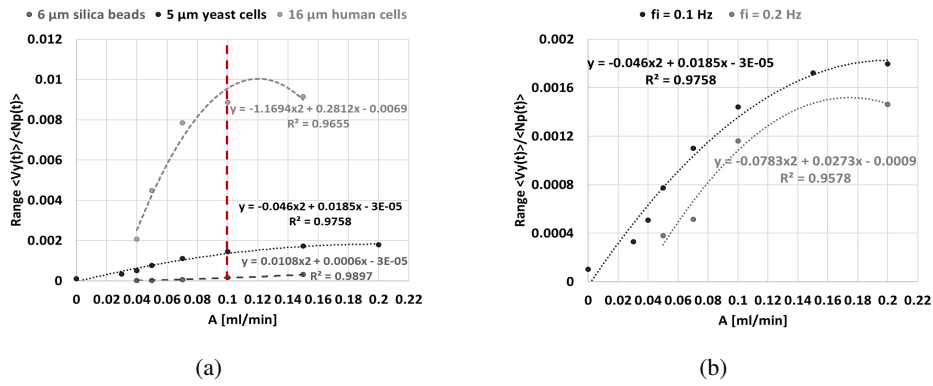
FIGURE 9.6: The normalized parameter ($Range\langle V_y(t)\rangle/\langle N_p(t)\rangle$) varying the oscillating input flow strength at the inlet A: (a) for the three micro-particle types at $f_i = 0.1$ Hz; (b) for the yeast cells at the input frequencies $f_i n \in \{0.1; 0.2\}$ Hz.

To investigate the effect that can be induced in the process by changing the frequency f_i of the external oscillating input flow strength, the graph of Fig. 9.6 (b), reports the normalized parameter ($Range\langle V_y(t)\rangle/\langle N_p(t)\rangle$) for the experiments with yeast cells (5 μm). In particular, the two curves are respectively for the driving force frequencies $f_i \in \{0.1; 0.2\}$ Hz and each point per curve is correlated to a driving force setting by varying the amplitude of the external oscillating input flow strength A. Also in this case, a good interpolation with a parabolic function was obtained: the normalized parameter ($Range\langle V_y(t)\rangle/\langle N_p(t)\rangle$) rises as the amplitude of the external oscillating input flow increases. The curves shift detected can be associated with the input frequency f_i: the lower the input frequency, the greater the signal range. This can be correlated to the inertial of the micro-particle flow, a slower input flow can be propagated more efficiently.

To summarize, the curves in Figs. 9.6 (a)-(b), far apart from each other, it is worth noticing the possibility to detect respectively the difference in density of the three micro-particles and the effect determined by the driving force frequency.

9.3.4 Micro-particle hydrodynamic response in frequency

The first experiment investigated in the frequency domain was the $\langle V_y(t)\rangle$ for the single-phase PBS solution. It was fed at the inlet of the channel with an oscillating input flow with a frequency of $f_i = 0.1$ Hz and an amplitude of $A = 0.1$ ml/min. The frequency peaks identified were $f_{pk} \in \{6; 7.5\}$ Hz. They were correlated to the PBS background flow, assumed as process artifacts and neglected in the following data analysis.

In the spectral analysis of $\langle V_y(t)\rangle$, two ranges were studied separately: the low frequency $f \in \{0; 2\}$ Hz and the high frequency $f \in \{2; 30\}$ Hz. As an example, Fig. 9.7 shows the spectra for the experiments with yeast cells, for $f_i = 0.1$ Hz and $A = \{0.04, 0.05, 0.07, 0.1, 0.15\}$ ml/min: at the top the low-frequency spectra and at the bottom the high-frequency spectra.

In the spectra at the low-frequency range in Fig. 9.7, the dominant peak detected is at $f_{pk} = 0.1$ Hz, consistently with the frequency of the oscillating input flow considered $f_i = 0.1$ Hz. The amplitude of the peak at $f_{pk} = 0.1$ Hz increases with the rise of the flow strength A. In the high-frequency range in Fig. 9.7, different behavior can be observed. More dominant peaks are evident for lower values of the input
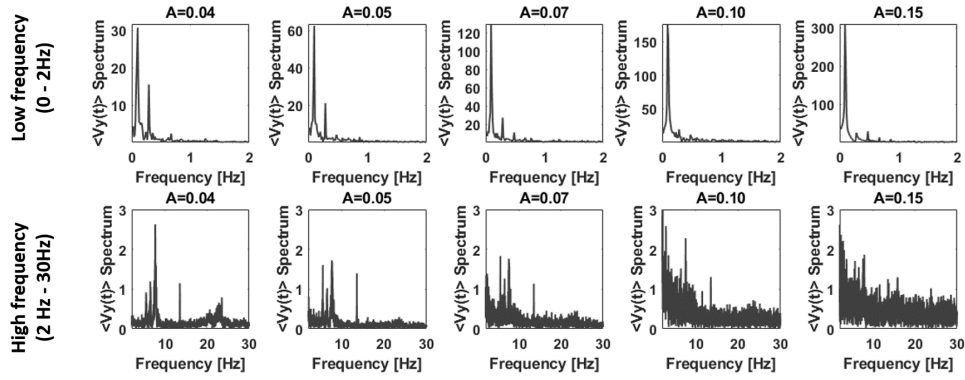
FIGURE 9.7: The $\langle V_y(t) \rangle$ spectra for the experiments with yeast cells in the input strength conditions $f_i = 0.1$ Hz and $A = \{0.04; 0.05; 0.07; 0.1; 0.15\}$ ml/min. At the top the spectra in the low-frequency range ($f \in 0\{;2\}$ Hz), and at the bottom the spectra in the high-frequency range ($f \in \{2; 30\}$ Hz).
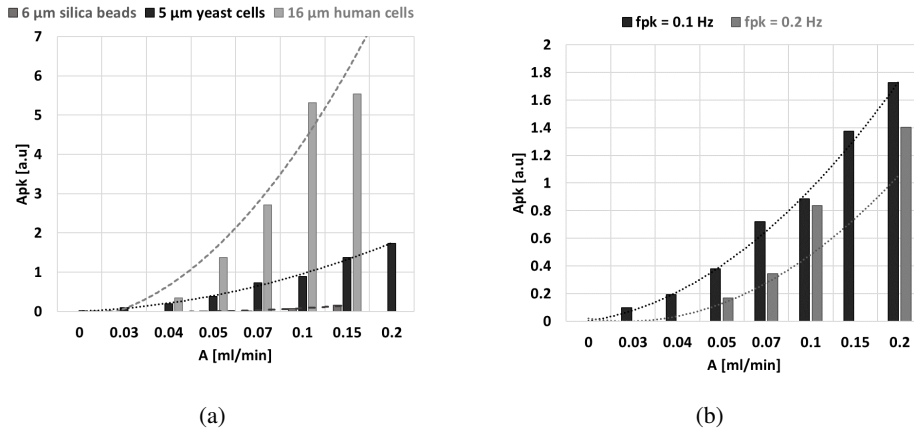
FIGURE 9.8: The spectral analysis of $\langle V_y(t) \rangle$ varying the oscillating input flow strength A. (a) For the three cell types, the amplitude of the peaks $f_{pk} = 0.1$ Hz for the experiment with the oscillating input flow frequency at $f_i = 0.1$ Hz. (b) For the yeast cells the amplitude of the peaks $f_{pk} = 0.1$ Hz and $f_{pk} = 0.2$ Hz, respectively for the experiments with the oscillating input flow frequency $f_i = 0.1$ Hz and $f_i = 0.2$ Hz.

flow strength such as $A = \{0.04, 0.05\}$ *ml/min*; the situation changes at its increase $A \geq 0.1$ ml/min, where no peak is distinguishable and a broadband behavior can be noticed.

Considering all together the behaviors in the low and high-frequency ranges, it is possible to conclude that for high external flow, the frequency induced by the pump is driving the hydrodynamic process, no other dynamics are relevant. Instead for low external flow, the oscillation induced at the input coexists with the other dynamics identified in the high-frequency range that can be associated with the oscillations and interactions of the collective particles.

Extending this study to other experiments with human cells and silica beads, similar behaviors were identified. In the experiments with the yeast cells where the oscillating input flow was set at $f_i = 0.2$ Hz, the dominant peaks in the low frequency were detected at $f_{pk} = 0.2$ Hz.

In Fig. 9.8 (a) for the experiments with oscillating input frequency $f_i = 0.1$ Hz,

the amplitude of peak $f_{pk} = 0.1$ Hz normalized with respect to the average number of micro-particles ($\langle N_p(t)\rangle$) is reported per cell types varying A. In Fig. 9.8 (b) for the yeast cells the amplitude of peaks $f_{pk} \in \{0.1; 0.2\}$ Hz normalized with respect to the average number of micro-particles ($\langle N_p(t)\rangle$) for the experiments with $f_i \in \{0.1; 0.2\}$ Hz are compared.

In all the experiments the normalized peak amplitude f_{pk} increases with external oscillating flow A and the values have been interpolated through parabolic functions. The amplitude of the normalized peaks for the experiments with human cells are bigger than those related to the other type of micro-particles; very small amplitudes with silica beads were observed. That enforces the results of the analysis in the time domain and underlines the role played by the micro-particles' physical properties in the hydrodynamic process.

In Fig. 9.9, the two most relevant peaks detected in the spectral analysis in the high-
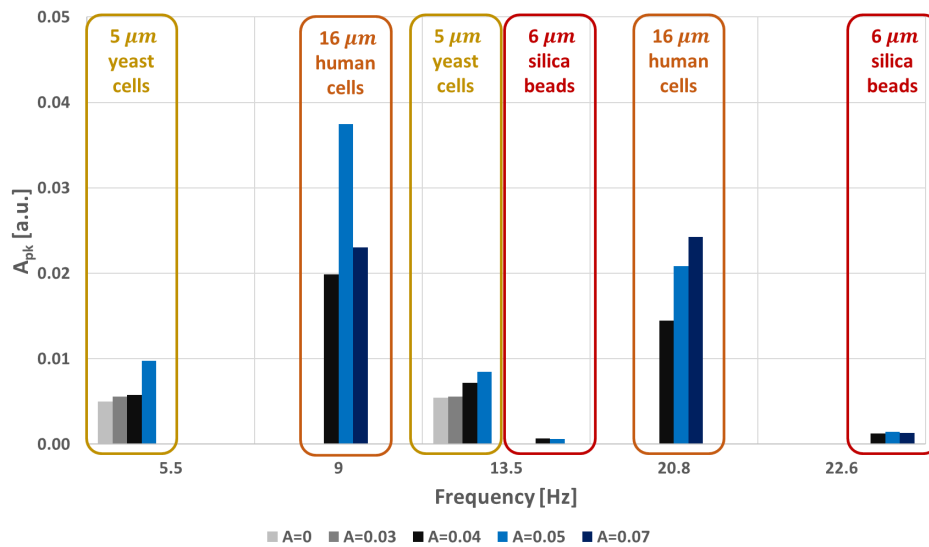
FIGURE 9.9: Global comparison among the amplitude of two relevant peaks detected in the high-frequency range of the spectral analysis per cell type, for the experiments with the oscillating input flow at $f_i = 0.1$ Hz and varying the strength A.

frequency range per cell type in the experiments with oscillating input $f_i = 0.1$ Hz are reported: no-frequencies in common for all cells type were found. For yeast cells the two peaks were at $f_{pk} \in \{5.5; 13.5\}$ Hz, for human cells at $f_{pk} \in \{9; 20.8\}$ Hz, and for silica beads $f_{pk} \in \{13.5; 22.6\}$ Hz. The amplitude of the peaks related to the silica beads is the lowest and does not seem to be sensitive to the input strength A. Instead, for the lives cells (yeast cells and human cells), the amplitude of the frequency peaks is affected significantly by the input strength A. In addition, in the spectral analysis in the high-frequency range for the yeast cells in the experiments with oscillating input at $f_i = 0.2$ Hz, the two most relevant peaks detected f_{pk} were the same as for oscillating input at $f_i = 0.1$ Hz.

That enforces and consolidates the previous consideration that the high-frequency components can be associated with the characteristics of the micro-particles' physical properties (such as dimension and density) and their interactions.

Chapter 10

Particles inertial focusing in micro-channels

The capability to precisely control the movement of particles at the microscale is essential in the development of innovative microfluidic systems for the analysis of bio-chemical samples [66]. In microfluidics, both active and passive techniques can be used to separate fluids and particles in a sample. Active techniques depend on external force fields. Passive techniques only rely on hydrodynamic forces intrinsic to the process and/or the geometry of the channel itself.

Among passive approaches, inertial focusing has gained considerable attention since its first use in microfluidics, as it offers precise particle control through the use of purely hydrodynamic interactions at high velocities to which traditional microfluidic principles are no longer applicable [167], [168]. On the basis of this phenomenon, discovered experimentally in 1961 by Segré and Silberberg [169], cells and particles immersed in a fluid migrate through streamlines and deterministically ordered to equilibrium positions near the channel walls. This behavior is due to inertial forces, which are typically neglected in microfluidic flows.

Generally, the flow of a fluid in the micro-channel, for low Reynolds number values, is laminar, which reflects the dominance of the viscous effect over inertial forces. In the case of a micro-flow of fluid and particles, it is not possible to neglect the inertial effects, and thus to linearise the Navier-Stokes equation [78]. Therefore, in order to model these phenomena, it is necessary to supplement the analysis of a laminar fluid flow in the micro-channel with a modeling of the processes that determine the displacements of the particles.

In the following, the theoretical basis of inertial focusing, and the model of a straight and curvilinear channel using fluid dynamics computation approaches will be explained, followed by related experiments and preliminary results.

10.1 Theoretical background

The physical principle of inertial focusing is related to the velocity profile of the fluid in which the particles are immersed, which induces equilibrium positions dependent

on the particle size across the channel cross-section. It is a technique widely used for the manipulation of biological samples, acquisition of the possible circulation of tumor cells, small prokaryotic cells, etc...

Contrary to the common perception that, in microfluidics, flow inertia is negligible, inertial microfluidic forces work in an intermediate range ($\sim 1 < Re_c < \sim 100$) between the Stokes regime and the turbulent regime ($Re_c \sim 2000$), where both inertia and fluid viscosity are finite. Therefore, the first check to be made concerns the Reynolds number of the channel (Re_c) defined as in eq. 10.1.ρ and μ indicate the density and the viscosity of the fluid, U_{MAX} the maximum fluid velocity, D_h the hydraulic diameter defined in eq. 10.2 in which h and w are the height and width of the channel cross-section, respectively.

$$Re_c = \rho U_{MAX} \frac{D_h}{\mu} \tag{10.1}$$

$$D_h = \frac{2hw}{h+w} \tag{10.2}$$

Thus, the finite inertia of the fluid in which the particles are immersed, in the condition verified with regard to the Reynolds number of the channel, leads to two inertial effects that are the basis of inertial microfluidics, namely: inertial motion and secondary flow.

The first, i.e. inertial motion, is a phenomenon in which randomly dispersed particles entering a straight channel move laterally to different equilibrium positions after a fairly consistent length, and which depends on fluid viscosity, fluid density, hydraulic diameter, fluid velocity and particle size. The key to the theoretical development of inertial focusing was the inclusion of inertial terms in the Navier-Stokes equations.

In 1965 Saffman [170] proposed a theoretical force independent of particle rotation due simply to the difference in fluid velocity on both sides of the particle in a linear shear flow.

An important contribution was made by Vasseur and Cox, who found a direct force along the channel walls proportional to the change in shear ratio [171]. Shear Gradient Lift Force and Gradient Lift Force are the dominant contributions and are often referred to as Inertial Lift (Saffmann).

In 1974, Ho and Leal [172] combined the two forces and calculated the net lift force (FL) on a particle much smaller than the channel ($a/DH << 1$, where a is the diameter of the particle and D_h is the hydraulic diameter of the channel) in a two-dimensional Poiseulle flow and for very small Reynolds numbers ($Re << 1$).

In 2004, Matas et al. [173] proposed a review with the most interesting findings on the phenomenon. Di Carlo et al. [174] introduced some corrections concerning FL, extending Segrè and Silberberg's analysis to channels with a rectangular cross-section (Reynolds number of the particle Re_p greater than or equal to 1) where Re_p is defined in eq. 10.3.

$$Re_p = \frac{Re_c \cdot a^2}{Dh^2} \tag{10.3}$$

Hood et al. [175] and Chao Liu et al. [176] proposed mathematical models for FL based on the work of Ho and Leal [172]. Specifically, the authors find an equation from the numerical results recorded, which allows the FL to be estimated. This equation is composed of 4 terms: the first two are related to radial motion (the shear

gradient lift and the wall-induced forces), the third term is the Saffman forces induced due to the delay of the particles near the walls, the last term is a correction of the shear gradient lift related to the channel proportions.

Straight micro-channels

In straight channels, the phenomenon of inertial motion, i.e. the motion and equilibrium of the particles, is linked to two simultaneous inertial effects:

- The shear gradient lift force (FLS), due to the curvature of the fluid velocity profile and its interaction with the particles, directs the particles away from the center of the channel;

- The wall lift force (FLW), resulting from the interaction of the flow field between the suspended particles and those adjacent to the channel walls, directs the particles away from them.

Inertial equilibrium positions arise from the balance between the FLS and the FLW. Fig. 10.1 (a)-(b)-(c) shows the equilibrium positions obtained from the inertial focusing phenomenon in the case of a channel with a circular, square and rectangular cross-section. Although this is a complex phenomenon that
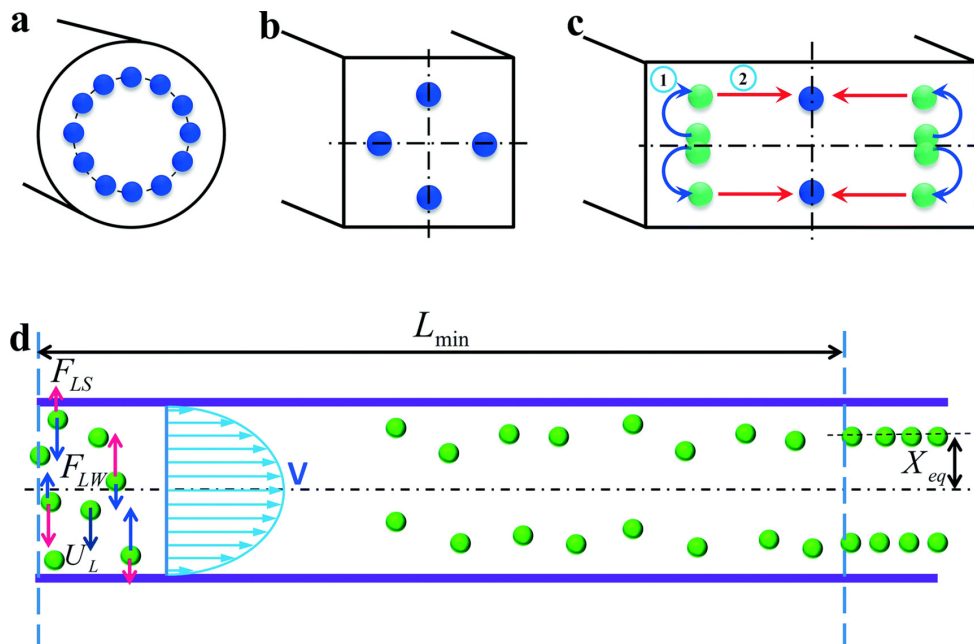
FIGURE 10.1: Inertial equilibrium positions in a straight channel with different cross-sections: (a) circular, (b) square and (c) rectangular cross-sections with a low aspect ratio (AR=0.5). (d) The lateral migration speed U_L and minimum channel length for particle focusing L_{min}. Reprinted from [167].

is still under discussion, there are indisputable results on which many authors agree regarding the inertial focusing of particles in straight channels:

- The dominant forces (FLS and FLW) cancel each other out on an equilibrium perimeter;

- This equilibrium perimeter changes depending on the channel; in channels with circular cross-sections and for small particles ($a/D_h << 1$),

this equilibrium perimeter corresponds to approximately ~0.6 times the radius of the cross-section towards the center. As Re_c increases, it gets closer to the walls, and for larger particles, it is slightly closer to the center;

- In channels with square/rectangular cross-sections, the interaction with the walls not only repels the particles but also makes them move laterally at four/two equilibrium points (due to certain conditions). Movement at the perimeter occurs faster than lateral migration, making the latter the limiting factor in alignment;

- FL is strongly dependent on particle size; large particles will migrate faster than smaller ones under the same conditions;

Straight channels have the limitation of slow lateral motion and several equilibrium positions, from four to two, so secondary flows can be generated to overcome this problem. In conclusion, inertial focusing in straight channels depends on two main parameters:

- The particle confinement ratio $\lambda = a/D_h$, where a, is the particle size and D_h the hydraulic diameter;

- The Reynolds number of the particle (Re_p) related to the Reynolds number of the channel (Re_c).

Several studies have shown that in order to have inertial focusing it must be verified that $\lambda = a/D_h > 0.07$ and $Re_p >= 1$ [174].
For straight channels, it is also possible to define the minimum length for inertial focusing to occur in order to obtain the inertial equilibrium positions (see Fig. 10.1 (d)). If $Re_p << 1$, the particles are subject to the dominant viscous drag and follow the fluid flow lines. However, as Re_p increases in the order of 1, inertial lift forces become dominant and lateral migration of particles through fluid lines becomes obvious, which justifies the fact that inertial focusing occurs for Re_p greater than or equal to 1 and that λ must be greater than 0.07.

Curvilinear micro-channels

Equilibrium positions can be further controlled using curved channels, where a secondary flow called Dean flow is introduced. The force of this secondary flow is characterized by the inertia of the fluid and the curvature of the channel and is represented by a dimensionless number called Dean number defined in eq. 10.4. δ is the curvature ratio defined in eq. 10.5 and r is the radius of curvature of the channel.

$$De = Re_c \cdot \delta^{1/2} \tag{10.4}$$

$$\delta = \frac{D_h}{2r} \tag{10.5}$$

This secondary flow causes an additional drag force on the particles, thus adjusting the number and equilibrium positions dictated by the inertial focus. Secondary flow usually appears in a curved channel or a straight channel

with disturbing obstacles. In a curved channel, secondary flow is induced by a pressure gradient in the radial direction due to difficulty in adjusting the fluid momentum in the center and the region close to the channel wall within the curvature. The fluid elements near the center line of the channel have a higher momentum than those near the wall, and thus push the flow outwards and cause the stagnant fluid elements near the channel wall to move inwards along the circumference, forming two counter-rotating flows, called Dean vortex (see Fig. 10.2) [177].

In general, a straight channel has the advantage of simplicity and ease of use. However, since the lift force (FL) is inversely proportional to the square of the hydraulic diameter $FL \propto 1/D_h^2$, the cross-sectional dimensions of the channels are limited enough to be able to provide sufficient lateral lift forces. The introduction of a secondary flow linked to a channel geometry with a curvature or by placing an obstacle, would not only help the phenomenon but also change the final equilibrium positions.

Dean vortexes can modify inertial equilibrium positions by imposing an additional viscous drag force on particles perpendicular to the main flow. Differential focusing of particles of different sizes, in accordance with the ratio of inertial lift force to secondary flow resistance (FL/FD), allows for complete separation of the particles.
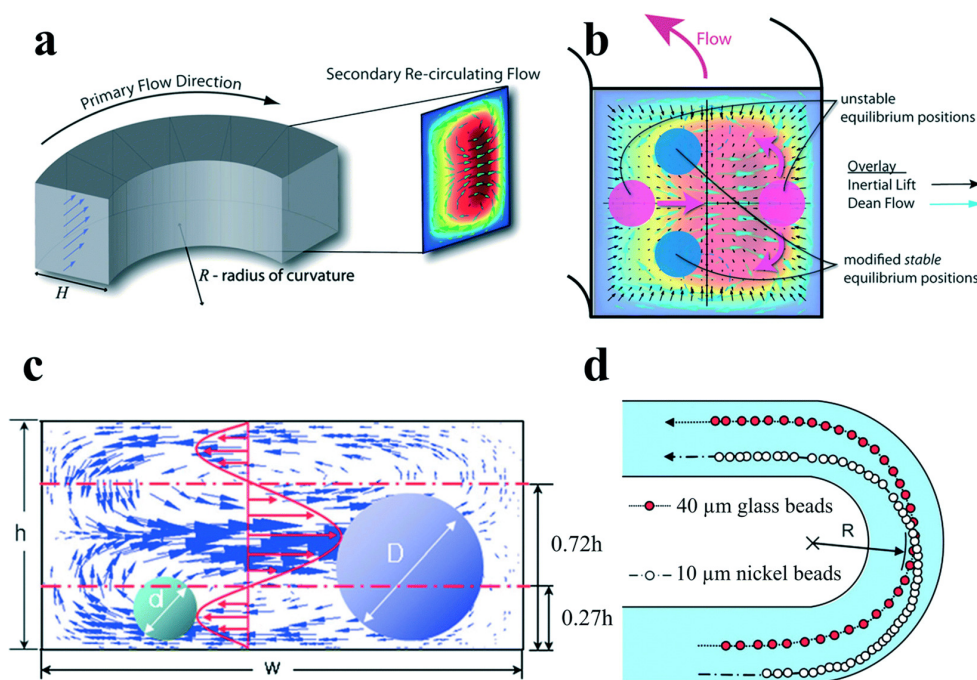
FIGURE 10.2: (a) Dean flow with two counter-rotating vortices is created in curved channels. Reprinted from [178]. (b) The superposition of inertial lift force and Dean flow in a curved channel modifies the number and position of the inertial equilibrium positions. Reprinted from [178]. (c)-(d) Size-based separation by the different directions of secondary flow drag force exerted by the velocity distribution. Reprinted from [179].

10.2 Multi-physics modeling in straight micro-channel

This evidence in the literature was confirmed by simulations in COMSOL Multiphysics 5.5 to analyze and compare inertial focusing behavior and particle trajectories. In particular, the Computational Fluid-dynamics (CFD) module and the Particle Tracking module were used. The model in COMSOL was implemented using the same methodology as in [180]. The simulation is divided into two parts:

- The CFD module allows a stationary study to calculate the velocity and pressure of the fluid inside the channel.

- The Particle Tracking module allows a time-dependent study to track the movement of particles within the channel.

To create the model in COMSOL, the first step is to select the physics, in particular fluid physics. The second step consists of defining the study geometry by CAD directly in COMSOL, as shown in Fig. 10.3. Finally, the third step consists of defining the properties of the fluid to be placed inside the channel, including density and dynamic viscosity. The Navier-Stokes equations were
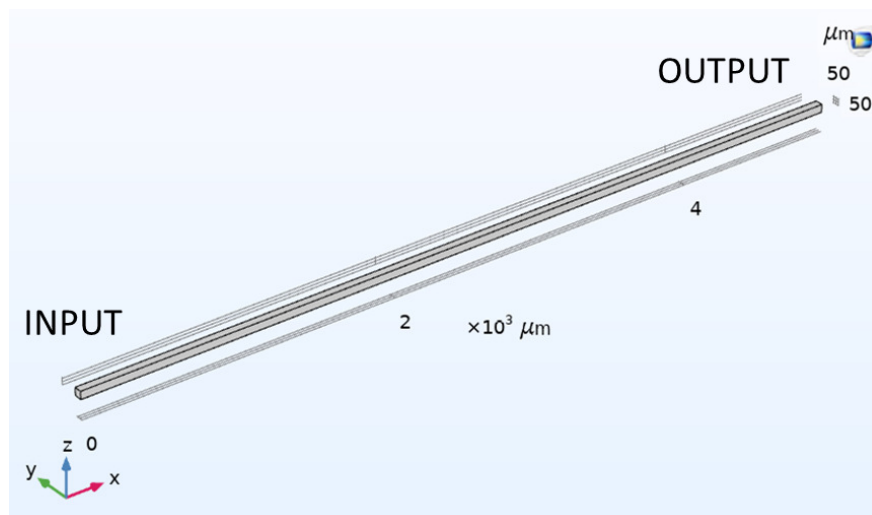
FIGURE 10.3: CAD of a straight channel with a square cross-section 50x50 μm and length 5 *mm* modeled in COMSOL.

solved by a laminar flow model assuming incompressible and single-phase flows. Fig. 10.4 shows the COMSOL implementation of laminar flow within the straight channel.

In addition to the physical equations of the process, the following parameters must also be defined in the laminar flow model:

- The inlet surface and the velocity at which the fluid is fed into the channel;

- The outlet surface of the fluid from the channel, defining zero static pressure as a boundary condition;

- The surfaces constituting the walls of the channel, setting zero slip of the fluid along the walls as a boundary condition.
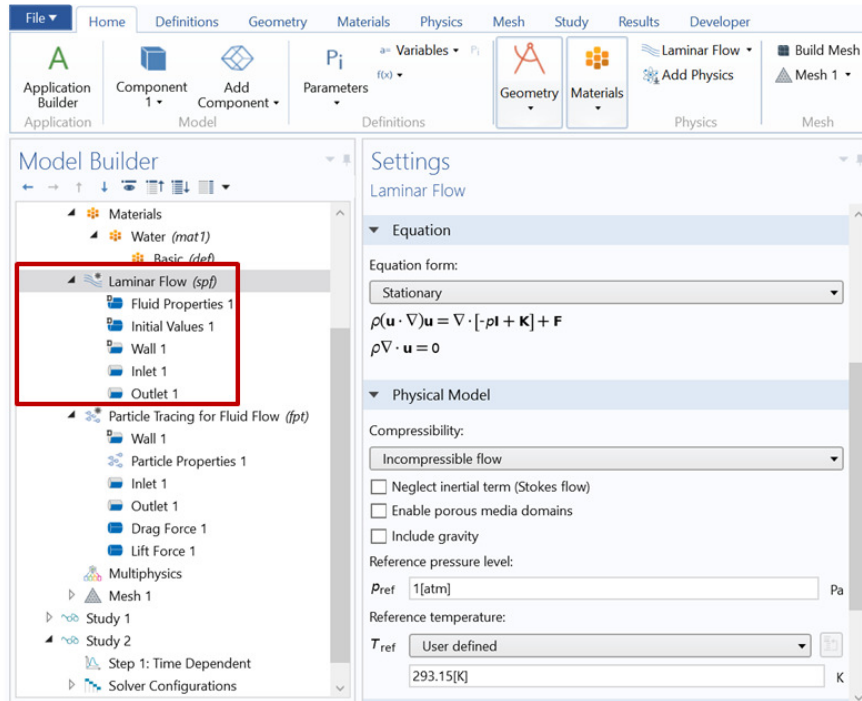
FIGURE 10.4: Setting of the laminar flow model in COMSOL.
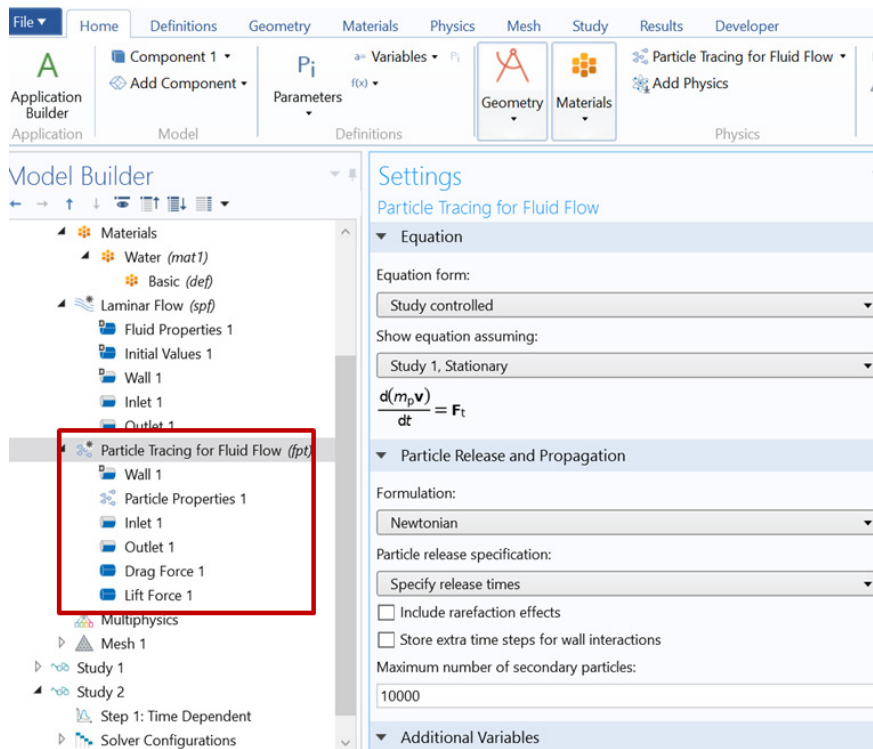
FIGURE 10.5: Implementation of particle momentum, drag force and lift force in COMSOL.

After simulating the laminar flow model, the parameters of the particle tracking model are defined.

A number of parameters must also be defined for this model, including the inlet and outlet surfaces of the particles, but especially the forces that come
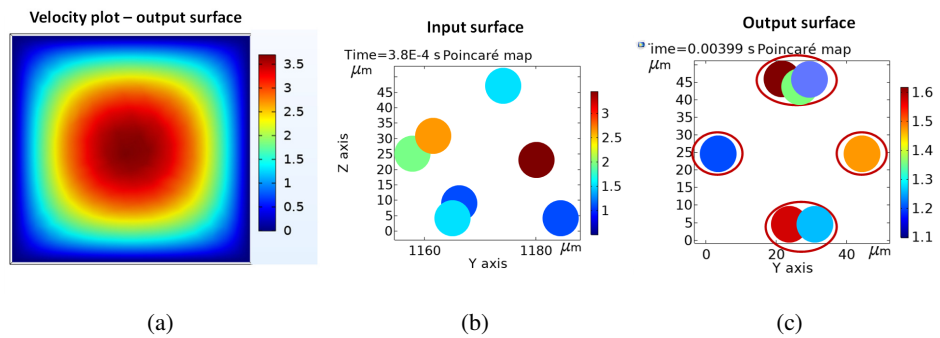
FIGURE 10.6: (a) COMSOL simulations of 10 μm particles suspended in water: speed distribution in the channel, spatial particle distribution in the inlet section and spatial particle distribution in the outlet section for a 50x50 μm straight channel.

into play, including:

- The momentum of the particles given by Newton's second law;

- The drag force given by Stokes' law, which includes a correction factor for the drag force for particles near walls;

- The lift force.

In Fig. 10.5, the implementation of Newton's force, drag force and lift force in COMSOL is shown.

The particles were added by defining their diameter and density; the different particle sizes only influence the magnitude of the force affecting the particles. In order to ensure proper motion of the fluid and particles within the channel, the models were modeled and simulated using a physics-controlled fine mesh.

Each model was solved with the GMRES iterative solver. For straight channels with a square cross-section (w/h=1), the necessary conditions for inertial focusing were simulated and verified. In particular, for a channel with a 50x50 μm square cross-section, 10 μm particles suspended in water were considered, as they have almost similar densities. The density and viscosity values of the two fluids under consideration lead to the possibility of achieving a $Re_p > 1$ value with low fluid velocity values. This is confirmed in Fig. 10.6 where it is possible to note in simulation a phenomenon of inertial focusing of the particles, i.e. the four equilibrium positions, setting a fluid velocity of 1.8 m/s.

10.3   Multi-physics modeling in curvilinear micro-channel

The same model implemented for a straight channel in COMSOL, presented in the previous section, is used for modeling a curvilinear channel, with the difference that the CAD of the straight channel is replaced by the CAD of a curvilinear channel.

The geometry of the implemented CAD is shown in the Fig. 10.7 (a). The micro-channel has a square cross-section of 80x80 μm and a radius of curvature of 3.6 mm. A flow of 8 μm spherical particles ($\rho = 1060 \ kg/m^3$)

suspended in glycerol solution ($\mu = 0.002$ *Pa.s.*) will be simulated. Particularly in the inlet surface, named s_{in}, the particles have been arranged at the four equilibrium points as shown in Fig. 10.7 (b). The aim is to understand in simulation whether the trajectories and equilibrium positions of the particles once reached at the end of a straight section undergo any changes once they enter a curved section. Before the particle flow was simulated, the

(a)   (b)
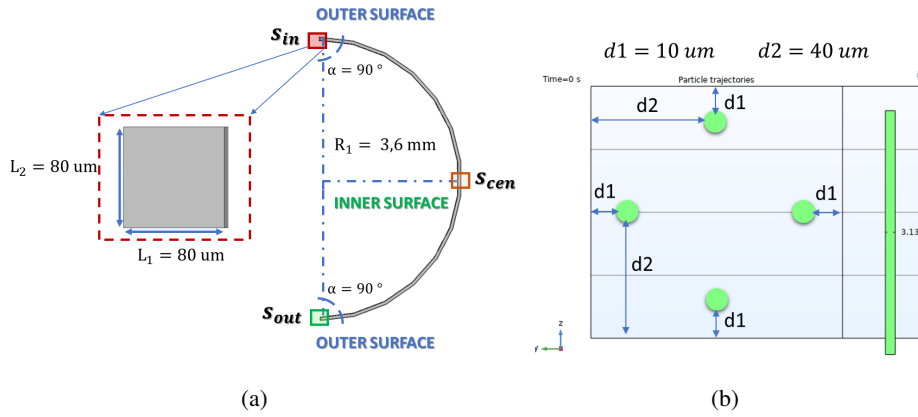
FIGURE 10.7: (a) CAD of a curvilinear channel with a square cross-section 80x80 μm and a radius of curvature of 3.6 *mm* modeled in COMSOL. (b) Distributed particles of 8 μm at the four equilibrium points in the input surface of the channel, named s_{in}.

N° simulation	De	Re_c	v $[m/s]$
SIM-1	1.04	10	0.125
SIM-2	9.48	90	1.125
SIM-3	17.91	170	2.125
SIM-4	26.35	250	3.125
SIM-5	40	380	4.75
SIM-6	90	860	10.75
SIM-7	200	1900	23.75

TABLE 10.1: Simulations performed in COMSOL with the relative parameters taken into account.

effect of increasing the Dean number on the secondary flow was examined in the simulation. A laminar Poiseuille velocity profile was used as the inlet boundary condition and the Dean number was varied by increasing the inlet fluid velocity.

The parameters of the simulations performed in COMSOL are shown in Table 10.1.

In Fig. 10.8, the axial velocity profile and the secondary flow patterns, represented with radial velocity vectors, in the middle surface of the curvature, named s_{cen}, can be observed by varying the Dean numbers ($1 < De < 200$). For a Dean number $De = 1$, it is possible to see a fully developed laminar profile.

Double-rotation symmetrical vortices are visible in the secondary flow model, but they are centered within the channel. The effects of Dean's drag force are available, but they are not large enough to move toward the outer wall. So its effect on suspended particles becomes almost negligible, in agreement with

the results obtained in [181] where at low Dean numbers, a minimal effect of Dean drag on particles is present.

As Dean's number increases, the velocity profile shifts more and more towards the outer wall and the symmetrical vortices of the secondary flow move towards the upper and lower outer walls [182]. By increasing the intensity of the radial pressure gradient, the fluid near the inner walls in the plane of symmetry is then drawn outwards. After seeing the velocity profiles and the
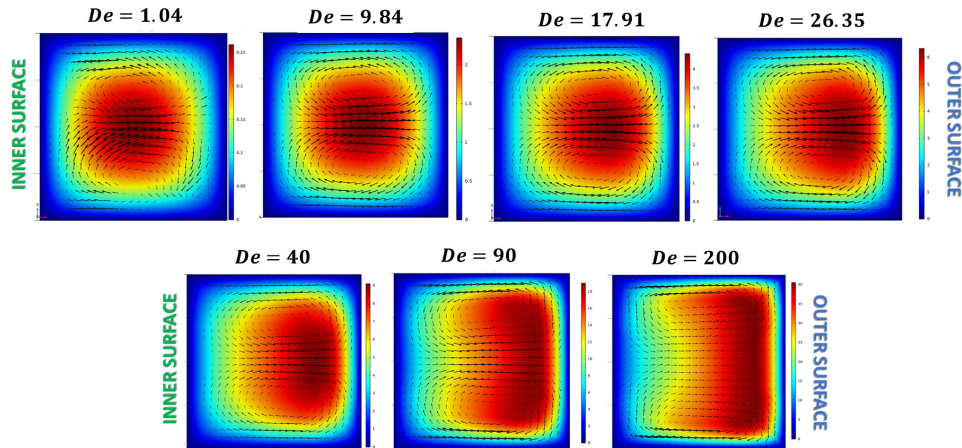
FIGURE 10.8: Contour profile of axial velocity and radial velocity vectors in the middle of the curvature in the surface named s_{cen}. From the top left to the bottom right De = 1.04, 9.84, 17.91, 26.35, 40, 90, 200.

secondary flow as the dean number varies, the particle flows were simulated by varying the Dean number in the range $\{1.04; 26.35\}$.

Starting from the initial condition of the particles shown in Fig. 10.7, two tests were carried out in simulation to evaluate the spatial distribution of the particles in the output surface named s_{out}. Two different meshes were used in COMSOL, as can be seen in Fig. 10.9, where a mesh was defined as normal and finer. As can be seen, the channel under investigation is defined in space by means of a mesh composed of edges, vertices and faces. By varying the type of mesh, the numerical simulation carried out can present a higher level of accuracy, but longer computational times. In Fig. 10.10 the results
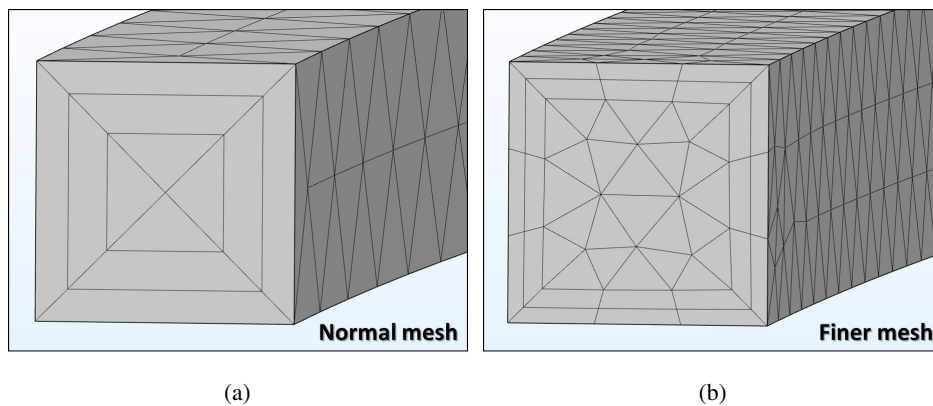
FIGURE 10.9: Comparison in COMSOL between setting a normal mesh (a) and a finer mesh (b) to the curvilinear channel under consideration.

obtained from the two types of test in the case in which the mesh is normal and in which it is finer, varying the Dean number in the range $\{1.04; 26.34\}$ are shown. in particular, the output section has been divided into three subsections named A1, A2 and A3.

The first result that can be seen is that there is no clear difference between the two types of mesh used. In the case under consideration, the results are equivalent. The second result that can be seen is that the four imposed equilibrium positions in the input surface (s_{in}) are not maintained in the output surface (s_{out}). The particles obtain a different spatial arrangement, tending more towards the center of the channel in the subsection named A2. In conclusion, the four equilibrium positions of the particles are not maintained once a curvilinear channel is crossed, and this geometry can be exploited to spin the particles toward a desired position within the channel.
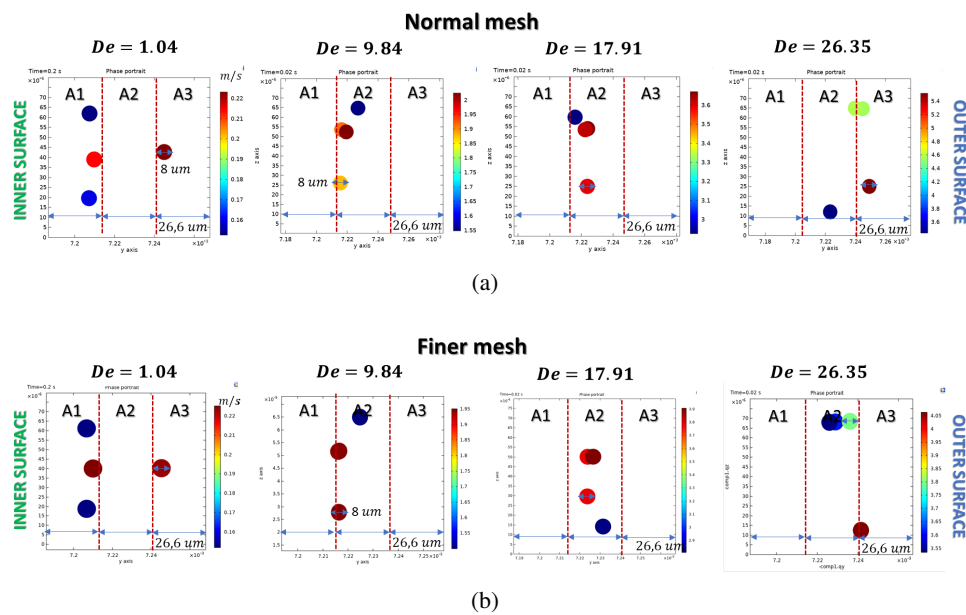
FIGURE 10.10: Spatial particle distribution at the end of the curvature in the named surface s_{out}. From the left to the right De = 1.04, 9.84, 17.91, 26.35.

10.4 Experimental set-up

After seeing the behavior of a particle fluid in simulation, the experimental part is carried on. The experimental set-up used, shown in Fig. 10.11 (a), consists of three main parts: the fluidic system, the optics and the mechanical system.

The fluidic system consists of the microfluidic channel and the syringe pumps (PHD 2000 Infusion, Harvard Apparatus, Holliston, Massachusetts, USA) that allow suspended particles in solution to be fed into the micro-channel.

The micro-channel is rectilinear and made of borosilicate (VitroTubes, Vitro-Com, Mountain Lakes, NJ, USA) having a square cross-section of $80x80\ \mu m$ and a length of 8 cm. The micro-channel is bonded to glass slides and tubes of 1 mm diameter at the inlet and outlet, as shown in Fig. 10.11 (b).

The optical part consists of a high-intensity illuminator (Fiber-Lite MI-150,
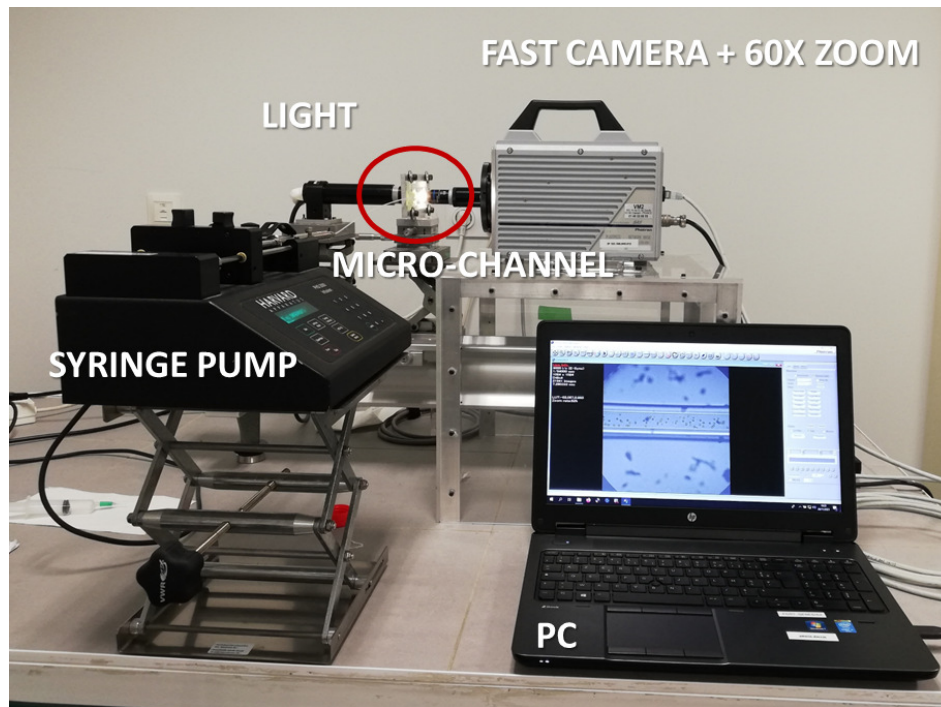
(a)
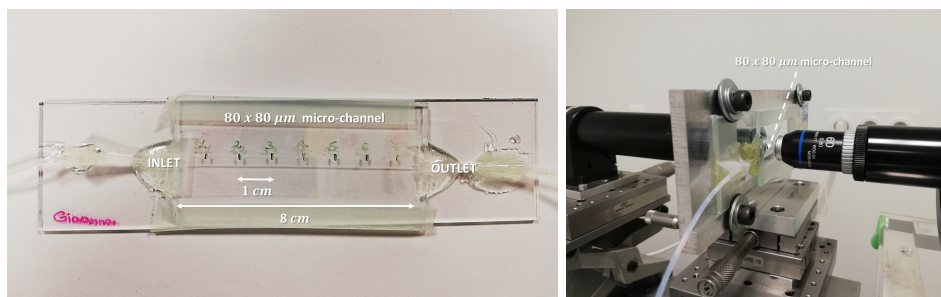
(b)   (c)

FIGURE 10.11: (a) Picture of the experimental set-up, (b) realized system including the micro-channel 80x80 μm and (b) zoom of the micro-channel in a vertical position in the experimental set-up.

Dolan Jenner industries, Boxborough, MA, USA), and a high-resolution CCD camera (SA5, Photron, Tokyo, Japan), equipped with a lens (x40) and allows a wide range of frame rates, between 50 and 120000 fps. To further increase optical magnification, an optical tube was interposed between the lens and the camera. The camera is then connected to a computer on which a software is installed to visualize the process and capture process video.

The mechanical part consists of a height-adjustable aluminum system with several adjustment systems that allow the platform where the micro-channel is placed to be moved upright along the three axes (x, y and z) and to stabilize the whole system (see Fig. 10.11 (c)).

N° video	Flow rate [$\mu l/min$]	Velocity [m/s]	*Re*	*fps*	Height acquisition
T1	40	0.104	8.33	3000	center
T3	40	0.104	8.33	3000	top
T6	40	0.104	8.33	3000	bottom
T8	70	0.182	14.6	3000	center
T12	120	0.313	25	6000	center

TABLE 10.2: Video of the experiments analyzed by using peanuts particles of 5.1x3.4 μm in the straight micro-channel 80x80 μm.

10.5 Experimental campaigns

The experimental campaign performed with the experimental set-up just described is summarized in Table 10.2. The neutral buoyancy suspension contains polystyrene particles ($\rho_p = 1050 \ kg/m^3$) and suspension fluid. The particles have the shape of peanuts having a total length of 5.1 μm and a diameter of 3.4 μm.

The suspension fluid is a mixture of 80.27% distilled water and 19.73% glycerol (in volume fraction). The result of this combination is considered an incompressible Newtonian fluid that has a density ρ_f equal to that of particlesρ_p, and a dynamic viscosity $\mu 0.0015 cP$ at room temperature [153]. The concentration of particles in the suspension fluid is 2%. The syringe pump (syringe capacity 8 *ml* and diameter 9.525 *mm*) generates laminar flow at a volumetric flow rate of 40, 70 and 120 $\mu l/min$, corresponding to Reynolds number values of 8.33, 14.6 and 25.

The video acquisitions were made on three different height levels within the micro-channel, which as shown in the Sketch of Fig. 10.12 named top, center and bottom and Fig. 10.14 (b).

10.6 Results and discussion

10.6.1 DPIV particles velocity detection

In [183], [184], inertial lateral migration of particles in monodisperse or bidisperse suspensions in micro-channel flows was investigated under different conditions by varying the Reynolds number, the particles' size ratios and concentrations. Particular attention was done to the measurements of particle distributions inside the micro-channels and several particle equilibrium positions were found.

The purpose presupposed in this section is to identify the velocity values, along the horizontal and vertical directions of particle flow within the micro-channel through the video acquisitions made under the experimental conditions of Table 10.2 by applying the algorithm presented in Chapter 8.

The analysis was performed in the MATLAB environment, and the first step is to preprocess the acquired video frames. It is, therefore, necessary to straighten the image so that the channel appears straight and not tilted, brighten the image if it is too dark, and define the region of interest to be placed under analysis, as shown in Fig. 10.12.

Before starting with the analysis, velocity profiles for the three investigated

(a)   (b)
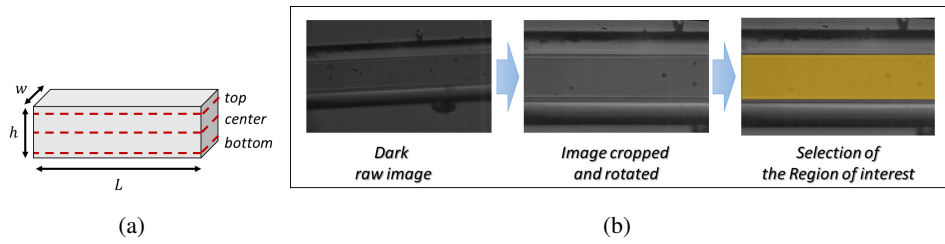
FIGURE 10.12: (a) Sketch of a micro-channel indicating the three areas of video acquisition and analysis (top, center and bottom). (b) Steps performed on the video frames acquired in order to proceed with the analysis.
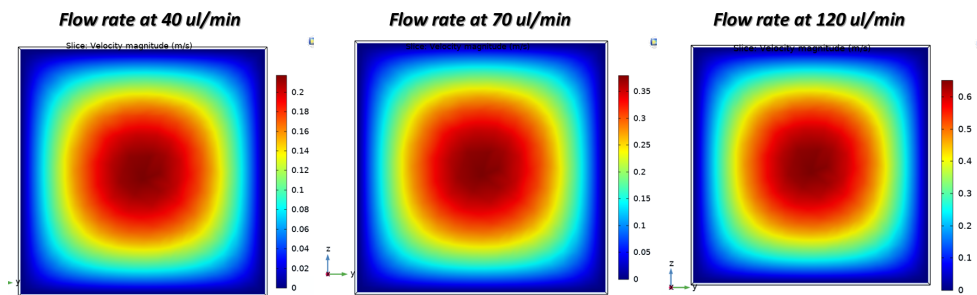
FIGURE 10.13: Radial velocity vectors obtained in COMSOL in the straight micro-channel 80x80 μm in the experimental conditions T1,T8 and T12 having a flow rate of $\{40, 70, 120\}$ ul/min, respectively.

(a)   (b)

(c)
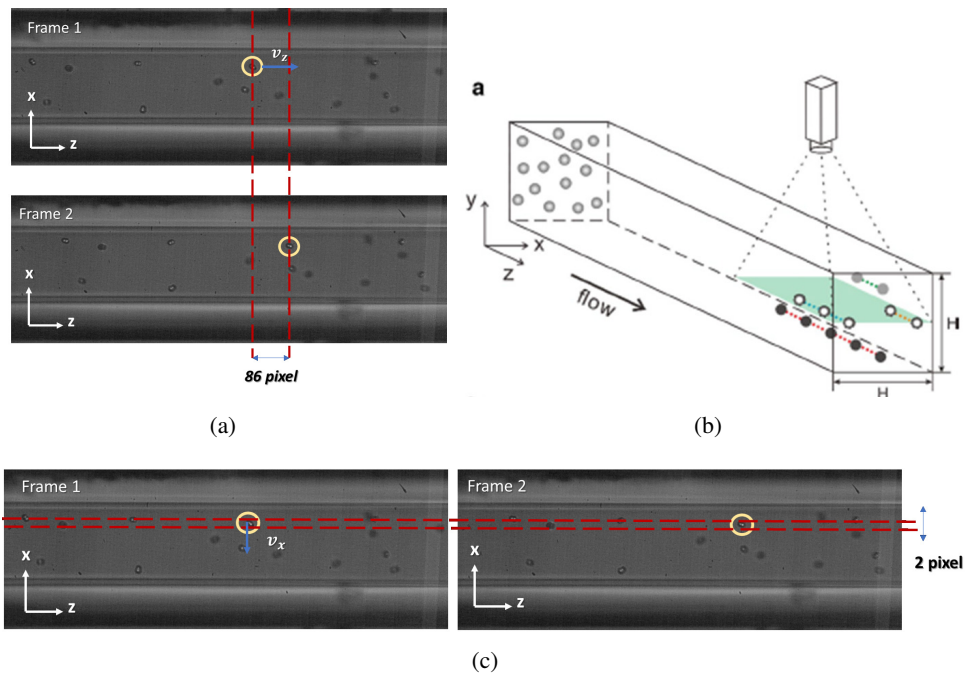
FIGURE 10.14: (a) Comparison of two frames to obtain the horizontal displacement of a particle selected in yellow. (b) Schematic diagram of the experimental set-up. Reprinted from [185]. (c) Comparison between two frames to obtain the vertical displacement of a particle selected in yellow.

flow rates of $\{40; 70; 120\}$ $\mu l/min$ were first verified through COMSOL simulations, as can be seen in Fig. 10.13, in order to compare them with the results obtained.

Another test was to analytically calculate horizontal and vertical velocity values considering a sample particle, in the experimental condition T1, in order to demonstrate the validity of the method used. In Fig. 10.14 (a) two frames were considered and a horizontal displacement of 86 pixels of a particle was obtained. By applying the formula present at eq. 10.6, it is possible to obtain a horizontal velocity (v_z) of 0.109 m/s which is in line with the results obtained in the simulation.

The same procedure was applied to obtain the vertical displacement of the same particle taken into consideration. A vertical displacement of 2 pixels was detected and a vertical velocity (v_x) of 0.0026 m/s, as shown in eq.10.7 and Fig. 10.14 (c).

$$v_z = \frac{number\,of\,pixel\,detected \cdot pixel\,dimension}{magnification \cdot \left(\frac{1}{fps}\right)} = \frac{86[pixel] \cdot 17[pixel]}{40 \cdot \left(\frac{1}{3000}\right)}$$

(10.6)

$$v_x = \frac{number\,of\,pixel\,detected \cdot pixel\,dimension}{magnification \cdot \left(\frac{1}{fps}\right)} = \frac{2[pixel] \cdot 17[pixel]}{40 \cdot \left(\frac{1}{3000}\right)}$$

(10.7)

The results obtained by applying the DPIV analysis, presented in Chapter 8 of this thesis, are presented in Figs. 10.15, 10.16 and 10.17.

In particular, in Fig. 10.15 the horizontal velocities obtained in the experimental conditions T1, T3 and T6 are visualized. The same flow rate of 40 $\mu l/min$ was imposed and three different areas of analysis were taken into account, named top, center and bottom. It is possible to observe that the velocities are in line with the simulation carried out in COMSOL and several velocity values in the range $\{0.1; 0.12\}$ are obtained. This depends on the position of the particles inside the micro-channel because based on that they are affected by the velocity profile imposed.

Regarding the results of Fig. 10.16, the horizontal velocities obtained in the experimental conditions T1, T8 and T12 are shown. The flow rate was imposed at $\{40; 70; 120\}$ $\mu l/min$, respectively, and the center area of analysis was taken into account. In these graphs, it is evident how the particle velocities increase as the flow rate increases, and the same values obtained in the simulation (Fig. 10.13) are present.

In Fig. 10.17 there is a comparison between the horizontal and vertical velocity, detected in the experimental conditions T1 and T8, versus the micro-channel width. In this representation, it is possible to see that the particles tend to stay near the walls of the micro-channel.

An important detectable result is that the vertical velocity value detected under both experimental conditions is two orders of magnitude lower than the horizontal velocity value. Moreover, it can be seen that the horizontal velocity is kept constant, while the vertical velocity tends to oscillate. This is due to the imposed flow rate that tries to push the particles from the left to the right and thus has a horizontal velocity value that is always positive, but a

vertical velocity value that is either positive or negative.
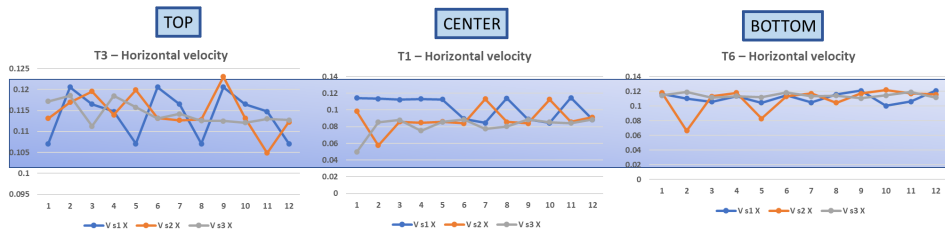
FIGURE 10.15: The obtained horizontal velocities for three selected particles in experiments T1, T3 and T6 in the three analysis areas (top, center and bottom) with a flow rate of 40 $\mu l/min$.
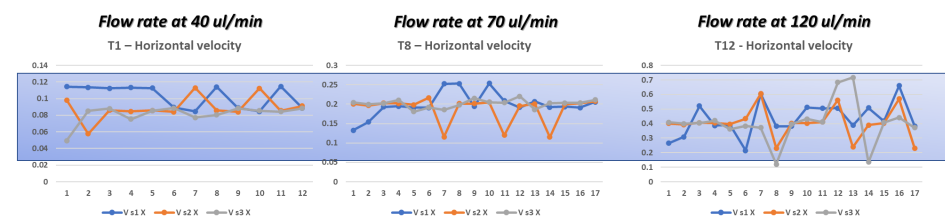
FIGURE 10.16: The obtained horizontal velocities for three selected particles in experiments T1,T8 and T12 in the central micro-channel analysis section with flow rates $\{40, 70, 120\}$ $\mu l/min$, respectively.

(a)

(b)
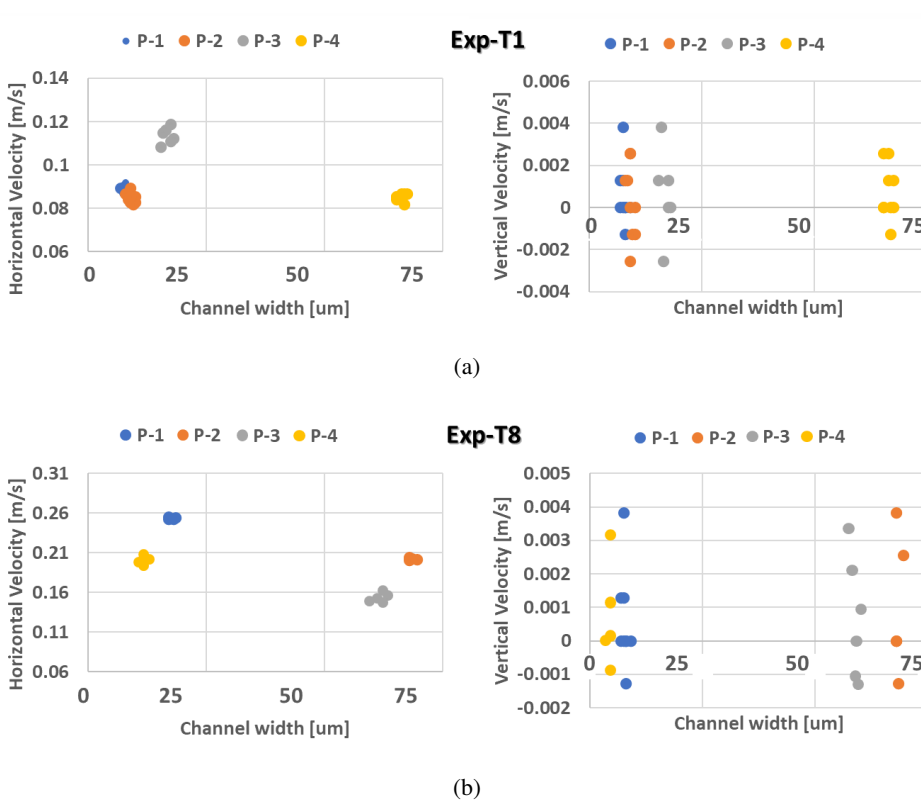
FIGURE 10.17: Comparison of horizontal and vertical velocities versus channel size for 4 selected particles in Exp-T1 and Exp-T8.

Chapter 11

Micro-optofluidic chamber characterization

In this section, the micro-optofluidic chamber, designed and realized in Section 1.5 of Chapter 1, was characterized to detect fluids of various natures and solutions at several concentrations.

11.1 Experimental set-up

A continuous single-phase flow was generated by pumping fluids of different natures and solutions at several concentrations to the inlet of the micro-optofluidic system realized. The block scheme, the experimental set-up implemented for the characterization, the micro-optofluidic system and a zoom of the chamber are shown in Fig. 11.1 and in Fig. 11.2 (a)-(b)-(c).
A piezo pump (mp6, Bartels mikrotecknik, Dortmund, Germany) controlled by a driven board (Quad-Key, Bartels mikrotecknik, Dortmund, Germany) is connected to the channel outlet and a constant in-taking flow rate of $0.01\ ml/min$ was imposed. A tygon tube with a diameter of 1.3 mm allows the connection of the channel inlet with the flacon filled with fluid. The fluids are fed into the device not by direct pumping but through a process of aspiration at the outlet. In this way, only the flacon with the solution at the inlet has to be changed.
The input light source, used with the micro-optofluidic chamber, was a halogen light (KL 1500 LCD, SCHOTT, Southbridge, USA) which allows varying light temperatures with different operating modes and electronic and mechanical light control. As displayed in the block scheme of Fig. 11.1, it was implemented a simultaneous acquisition with two different instruments, spectrometer and a photodiode. The light intensity variation was acquired by means of the photodiode with a gain of 40 dB (PDA100A, Thorlabs, Newton,
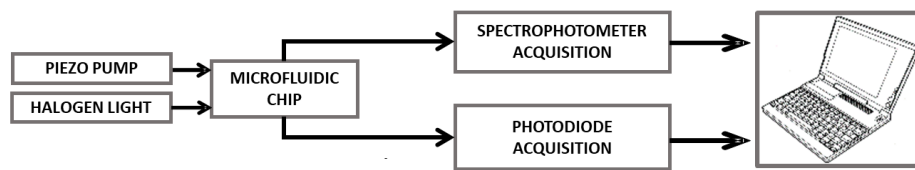
FIGURE 11.1: Block scheme of the experimental set-up implemented for the micro-optofluidic chamber characterization.

NJ, USA) and the signal received was acquired by a PC oscilloscope (Pico-scope 2204A, Pico Technology, Cambridgeshire, UK), with a sampling frequency of 1.5 kHz. The light intensity variation was acquired also by means of the spectrometer (USB2000, Ocean Optics, Dunedin, Florida, USA) for measuring the intensity of light relative to wavelength. Both pieces of information are sent to the PC.

11.2   Experimental campaigns

In order to characterize the micro-optofluidic chamber three different kinds of fluids were considered for a total of 11 experiments and summarized in Table 11.1. The first two kinds of fluids belong to the one-phase flow and the third one to the two-phase flow.

The first topology includes fluids at different densities and refractive index as shown in the histograms of Fig. 11.3, the second one includes colored water in different shades and finally, the third one a solution of saline buffered saline (PBS) in which some micro-particles (beads), with a diameter of 6 *um* and realized in Polymethyl methacrylate (PMMA), were diluted at different concentrations.

Fluids	Colored Water	Beads
Air	Yellow	PBS with 1% beads concentration
Water	Red	PBS with 10% beads concentration
PBS	Green	-
Water and 16% glycerol	Blue	-
Water and 33% glycerol	-	-

TABLE 11.1: Investigated fluids and solutions to characterize the micro-optofluidic chamber.

11.3   Results and discussion

11.3.1   Hydrodynamic study for fluids and particles suspension

After the simultaneous acquisition of the signals through the set-up shown in Fig. 11.2 (a), a signal processing phase was implemented. A low-pass filter with a 40 Hz cut-off frequency was applied. Fig. 11.4 reports the results obtained with the two acquisition systems integrated into the micro-optofluidic
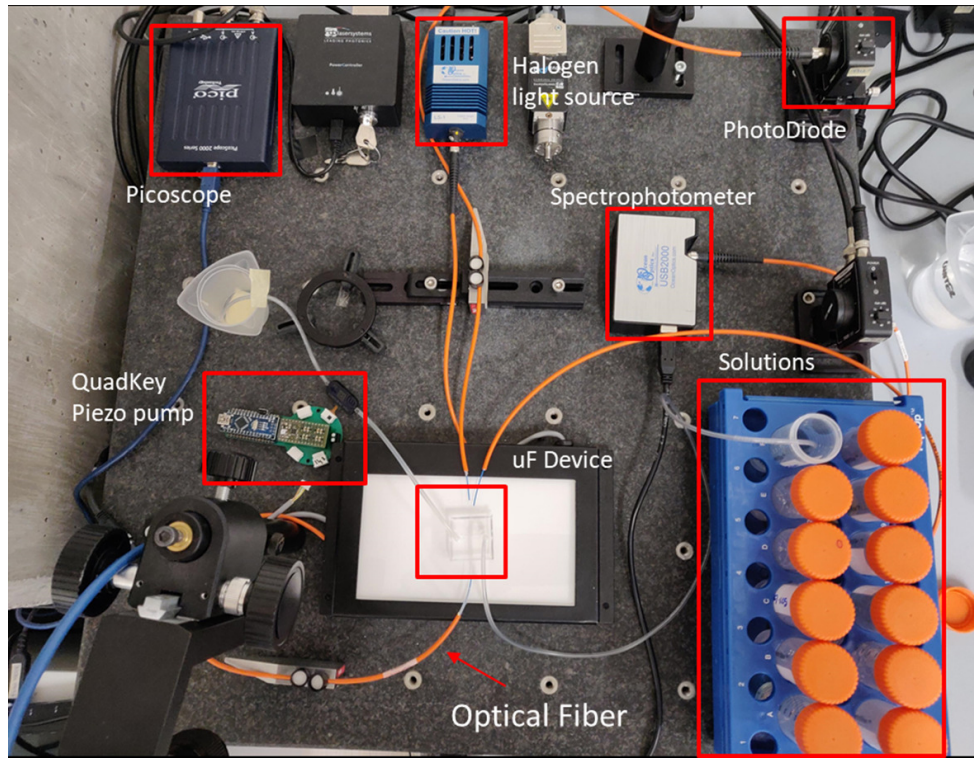
(a)
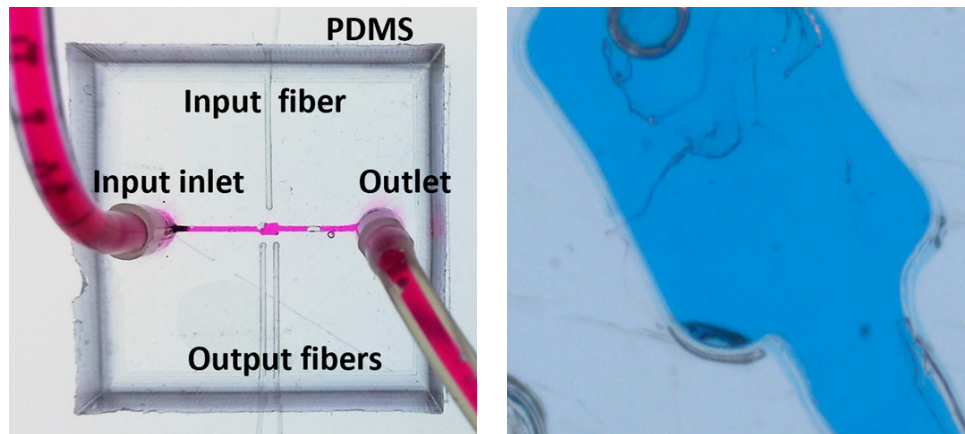
(b)

(c)

FIGURE 11.2: (a) The picture of the experimental set-up, (b) the micro-optofluidic chamber and (c) the zoom of the chamber filled with blue-colored water.
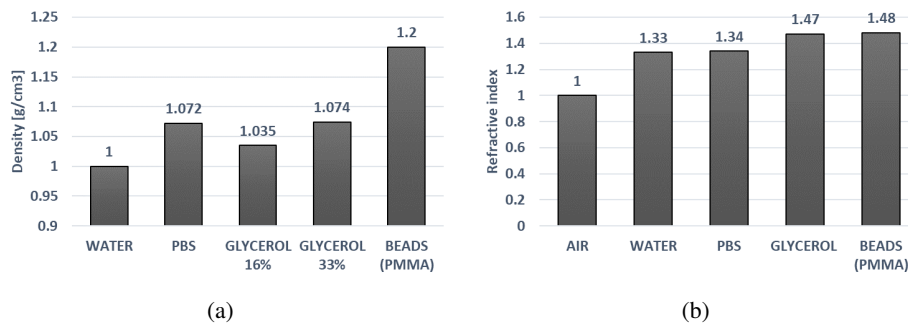
FIGURE 11.3: Values of (a) density and (b) refractive index for the fluids and beads investigated.

chamber.

In particular, Fig. 11.4 (a)-(b) shows the trends and the percentage of the transmission measurements obtained with the spectrometer acquisition during the passage of blue-colored water in the chamber (orange line) and the water imposed as reference (blue line). The signals obtained are independent of time; they are a static acquisition of the process carried out within the first 5 s of fluid flow inside the chamber. In this case, by looking at these two plots, the transmission peak is about 500 *nm* which is the theoretical wavelength of blue.

Thanks to spectrometer acquisition, it is possible to identify at which wavelength fluids are most sensitive and vice-versa. Regarding the photodiode acquisition, time-dependent and acquired for about 60 *s*, in Fig. 11.4 (b) it is shown the optical signal acquired during the passage of blue-colored water in the chamber and a constant voltage of 0.1033 *V* is detected. Being the micro-optofluidic chamber designed to exploit the phenomenon of light absorption, based on the fluids injected the voltage reading from the photodiode will vary.

A different behavior is detected with the micro-particles suspended in PBS at several concentrations. In Fig. 11.5 (a) two pictures show the chamber filled with two different beads concentration and in Fig. 11.5 (b) the corresponding obtained results by using the photodiode acquisition. The first result obtained is that the voltage values read in the two cases are different and correlated with the percentage of concentration. The higher the concentration of the micro-particles, the lower the read voltage. This is because the light interacting with them cannot reach the reading fiber on the opposite side being the concentration of the micro-particles dense.

The second result is that with the time increasing, there are not constant voltage values during the acquisition and this is due to the density of the micro-particles diluted in the PBS solution. Being the density of micro-particles greater than the PBS solution they tend to plummet to the bottom. Fig. 11.5 (c) shows a visual representation time-dependent of the sedimentation process when the chamber is filled with micro-particles suspended in PBS solution. During measurement, the sedimentation of some micro-particles allows light to pass through and thus increase the voltage value read by the photodiode.
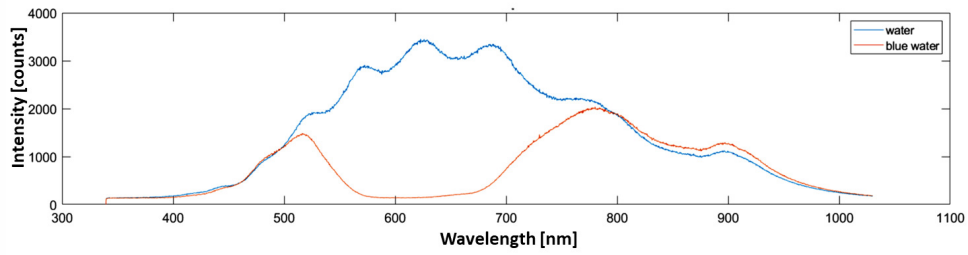
(a)
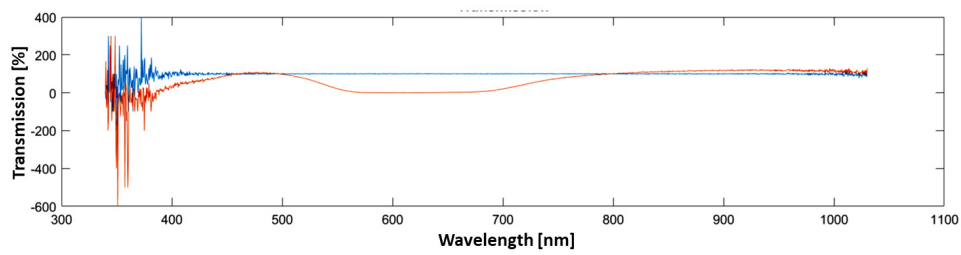
(b)
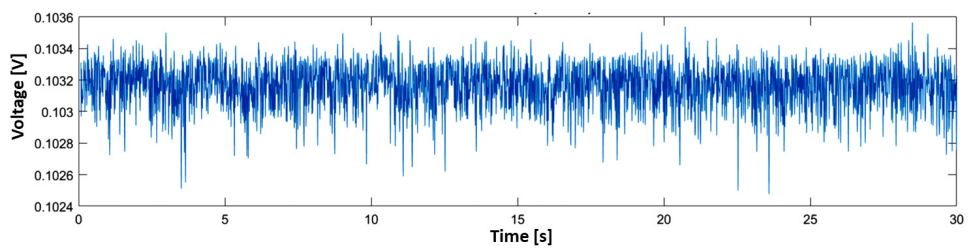
(c)

FIGURE 11.4: (a) Trends and (b) percentage of the transmission measurements obtained with the spectrometer acquisition during the passage of blue-colored water in the chamber with water as a reference. (c) Trends obtained in the time domain with the photodiode acquisition during the passage of blue-colored water in the chamber.

(a)   (b)

(c)
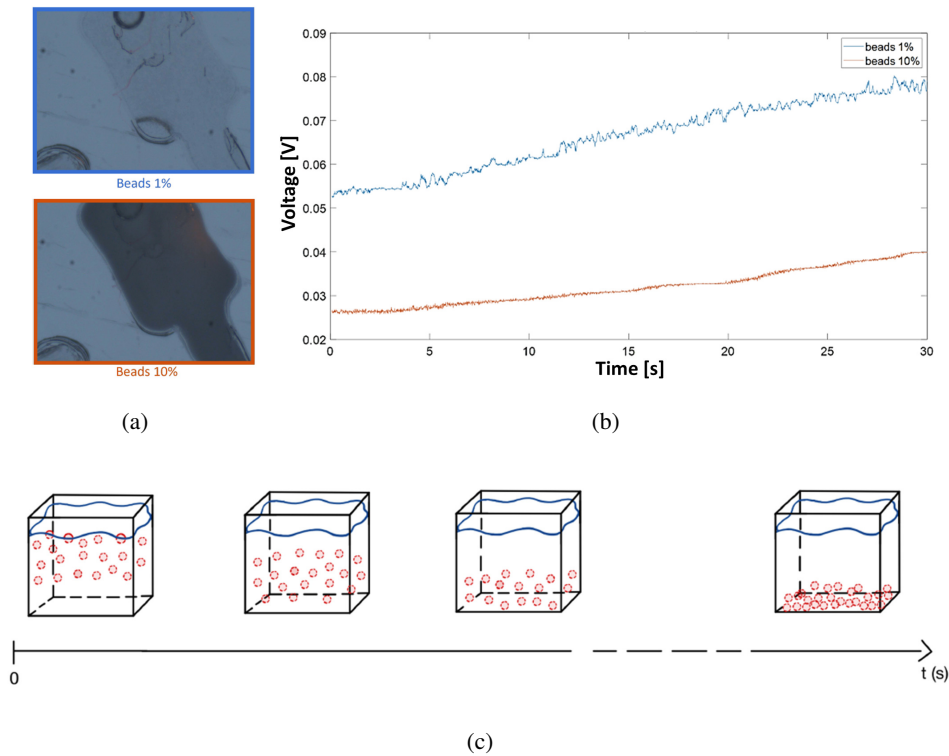
FIGURE 11.5: (a) Pictures of the chamber filled with two different beads concentration, (b) trends in the time domain obtained with the photodiode acquisition with the corresponding beads concentrations and (c) a visual representation of the sedimentation process inside the chamber filled with beads.

The same problem arises with transmission acquisition with the spectrometer, but since it is time-invariant as a static acquisition at a known instant of time in order to be able to compare the values obtained with those of the photodiode, the voltage value to be considered is the average voltage value calculated in the first five seconds, being the transmission measurement performed in the same time window.

Furthermore, a way to overcome the sedimentation phenomenon is to make the density of the solution in which the particles are suspended approximately equal to the density of the micro-particles.

In Fig. 11.6 the results of the measurements acquired with the two instruments, the spectrometer in the first column and the photodiode in the second column, are summarized. In particular, Fig. 11.6 (a)-(b) shows the measurements obtained for the various colored water, Fig. 11.6 (c)-(d) for the fluids of different nature and Fig. 11.6 (e)-(f) for the micro-particles suspended in PBS solution at different concentration.

As can be seen, the micro-optofluidic chamber allows for the differentiation of the different fluids studied. In particular, the maximum transmission values in the visible electromagnetic spectrum (Fig. 11.6 (a)) and the average voltage values of the signals acquired by the photodiode (Fig. 11.6 (b)) show the same trend. It should also be noted that the wavelength obtained for each color belongs to the corresponding red (625-740 nm), blue (435-500 nm), green (520-565 nm) and yellow (565-590 nm) wavelength bands.

The same applies to the results in Fig. 11.6 (c)-(d), where the average transmission values and the average voltage values for the different fluids are shown. Although, when comparing some of them, such as PBS and aqueous solution with glycerol, the results do not appear to be perfectly equivalent, this is not surprising as the two used instruments show different aspects of the test fluids, but seem to follow the same refractive index trend shown in Fig. 11.3 (b). Regarding the results of Fig. 11.6 (e)-(f), the different instruments are able to detect the presence of beads in the solutions and clearly differentiate the two different concentrations of beads.
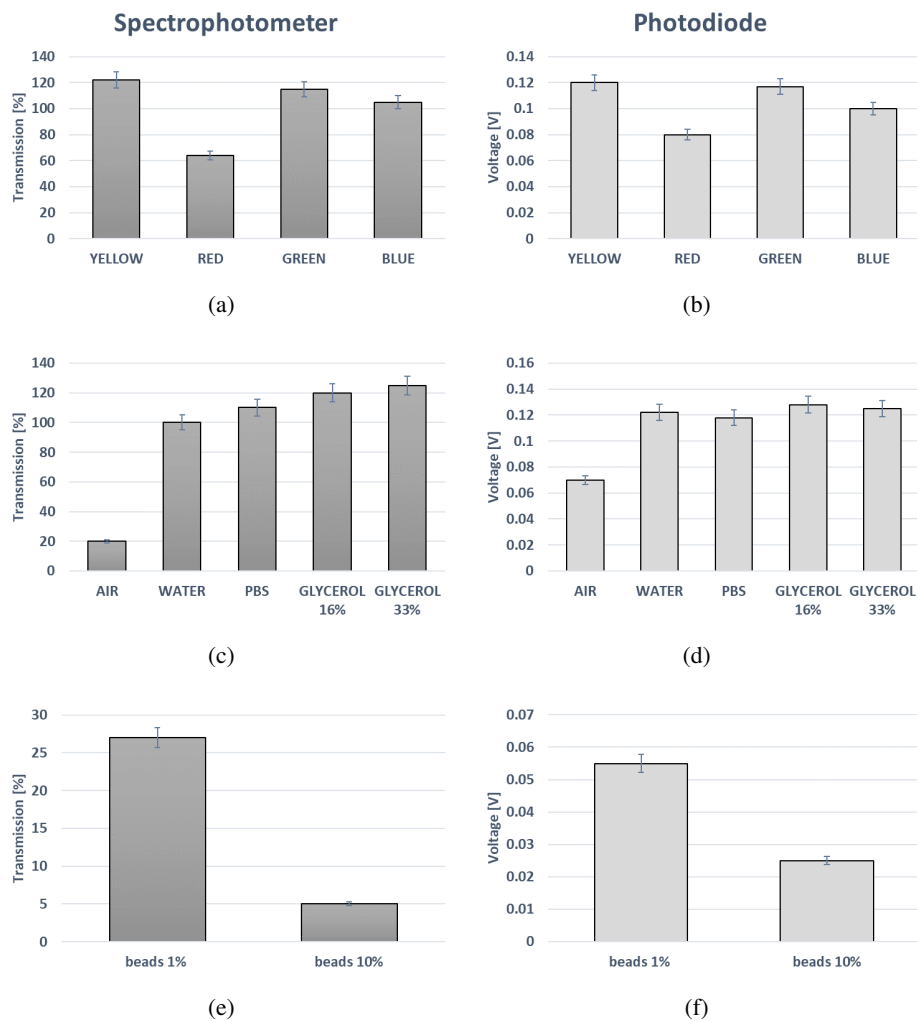
FIGURE 11.6: (a)-(c)-(d) Percentage values of transmission obtained by spectrometer acquisition and (b)-(d)-(e) voltage values obtained by photodiode acquisition for all the fluids investigated in the micro-optofluidic chamber.

Chapter 12

Micro-optofluidic devices for hydrodynamic investigation

A two-phase flow consists of two immiscible fluids, one dispersed in the other, that are circulating in the same micro-system (for instance gas-liquid, immiscible liquid-liquid or liquid and micro-particles) [4], [59].

Nowadays, the study of two-phase flows in micro-channels has an important role in micro-nano technology, enabling the design of lab-on-chip devices in the bio-medical field, as well as the study of chemical processes [2], [3].

In literature, different methods have been adopted to detect and control two-phase flows in micro-channels; in particular, the optical and sensor approaches offer the advantages of a wide range of measurement options being minimally invasive [6].

In recent studies carried out, optical signals were used to characterize the flow non-linearity [5], [16] and some parameters have been introduced to classify and identify the slug flows inside the micro-channel [60], [61].

In addition, based on optical signals detected, it was possible the development of a real-time velocity detection platform for the slug flow analysis in a micro-channel [102]. In this context, it is an open issue to switch from the equipment used to perform the standard optical sensing procedures to their miniaturization into a single low-cost portable device [62], [63].

In this chapter, three micro-optofluidic devices presented in Chapter 1 (the micro-optofluidic switch, the micro-optofluidic slug detector and the micro-optofluidic chamber), were tested to differentiate and evaluate cells and DNA suspension concentration. They were realized in Poly-dimethylsiloxane (PDMS) using a master-slave protocol based on the 3D printing techniques. These devices were designed to be compact, integrating the micro-optic and microfluidic components.

Two experimental campaigns were carried out and the optical signals acquired in a specific test section of the micro-channel were used to test the devices' capabilities.
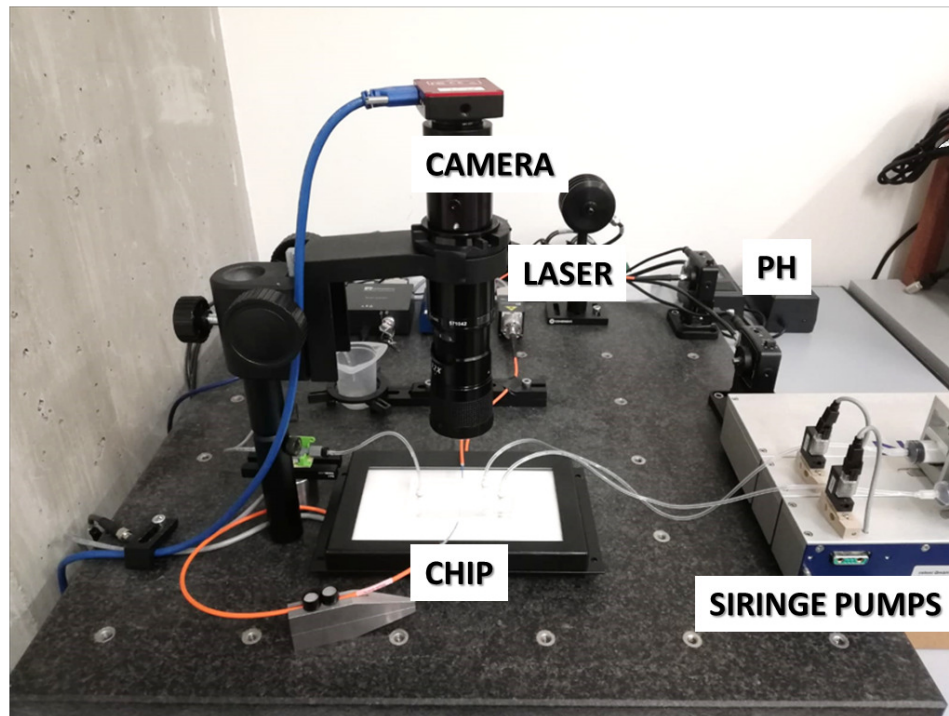
FIGURE 12.1: The experimental set-up used to differentiate and evaluate cells and DNA suspension concentration.

12.1 Experimental set-up

A continuous flow was generated and pumped at one inlet of the micro-optofluidic systems realized and, in two devices, the other inlet was plugged. The experimental set-up to differentiate and evaluate cells and DNA suspension concentration is shown in Fig. 12.1.

One syringe pump (neMESYS low-pressure module, Cetoni GmbH, Korbussen, Germany) was connected to one channel inlet and a constant flow rate of $0.1 \, ml/min$ was imposed. The input light source, used with the micro-optofluidic switch and the micro-optofluidic slug detector, was a laser system (NovaPro 660-125, RGB Lasersystems, Kelheim, Germany), that generates a light beam with a wavelength of 600 nm and an output power of 1 mW. The input light source, used with the micro-optofluidic chamber, was a halogen light (KL 1500 LCD, SCHOTT, Southbridge, USA) which allows varying light temperatures with different operating modes and electronic and mechanical light control. The light intensity variation was acquired by means of a photodiode with a gain of 40 dB (PDA 100A, Thorlabs, Newton, NJ, USA) and the signal received was acquired by a PC oscilloscope (Picoscope 2204A, Pico Technology, Cambridgeshire, UK), with a sampling frequency of 1.5 KHz. For a visual inspection of the process a digital camera (Zelux CS165CU1/M, Thorlabs, Newton, NJ, USA) with a variable magnification system (MVL12X12Z, Thorlabs, Newton, NJ, USA), placed above the device, was used.

12.2 Fibers calibration in micro-optofluidic devices

The innovation of the micro-optofluidic devices presented in this paper consists of the integration of the optical part with the microfluidic part. Specifically, the optical part consists of the insertion of optical fibers in special areas defined in the design phase that turn out to be independent of the microfluidic part, as it is shown in Chapter 1 in Figs. 1.3, 1.7, 1.17.
With one optical fiber, the light source is placed inside the device to illuminate the microfluidic process, and with the other optical fiber, placed in the same direction but opposite allows the acquisition of optical information through a photodiode. Since the insertion of the optical fibers is operator-dependent, a calibration must be performed before the experiments begin. As shown in Fig. 12.2 the calibration consists of evaluating the distance between the two optical fibers at each start of the experimental campaign. $F1$ indicates the fiber connected with the light source and $F2$ the fiber connected with the photodiode.
In Fig. 12.2 (a) it was measured between the two fibers $F1 - F2$ a distance of $d = 4.56$ *mm* for the micro-optofluidic switch, in Fig. 12.2 (b) $d = 4$ *mm* for the micro-optofluidic slug detector and in Fig. 12.2 (c) $d = 2.74$ *mm* for the micro-optofluidic chamber.
The smaller the distance between the two fibers the larger the signal read, the larger the distance the smaller the signal read.

12.3 Experimental campaigns

In order to differentiate DNA and cell fluids and to evaluate the cell suspension concentrations, two experimental campaigns were carried out: *Exp-1* and *Exp-2*. *Exp-1* was performed with the micro-optofluidic switch and the micro-optofluidic slug detector. Meanwhile, *Exp-2* was performed with all three devices. Both experiments were performed on two days, one month apart.
The first campaign (*Exp-1*) consists of 5 experiments where the following fluids were injected into the channel inlet of the microfluidic devices:

- De-ionized water (one phase flow used for calibration)

- DNA genomic A, with a concentration of $6 \cdot 10^{-}5$ *ug/ul* (Day-1) and $2.5 \cdot 10^{-}5$ *ug/ul* (Day-2), diluted in 10 *ml* of de-ionized water;

- DNA genomic B, with a concentration of $3 \cdot 10^{-}5$ *ug/ul* (Day-1) and $1.5 \cdot 10^{-}5$ *ug/ul* (Day-2), diluted in 10 *ml* of de-ionized water;

- a cell culture media, Dulbecco's Modified Eagle Medium (DMEM) (one phase flow used for calibration);

- DMEM with 10% of Fetal Bovine Serum (FBS);
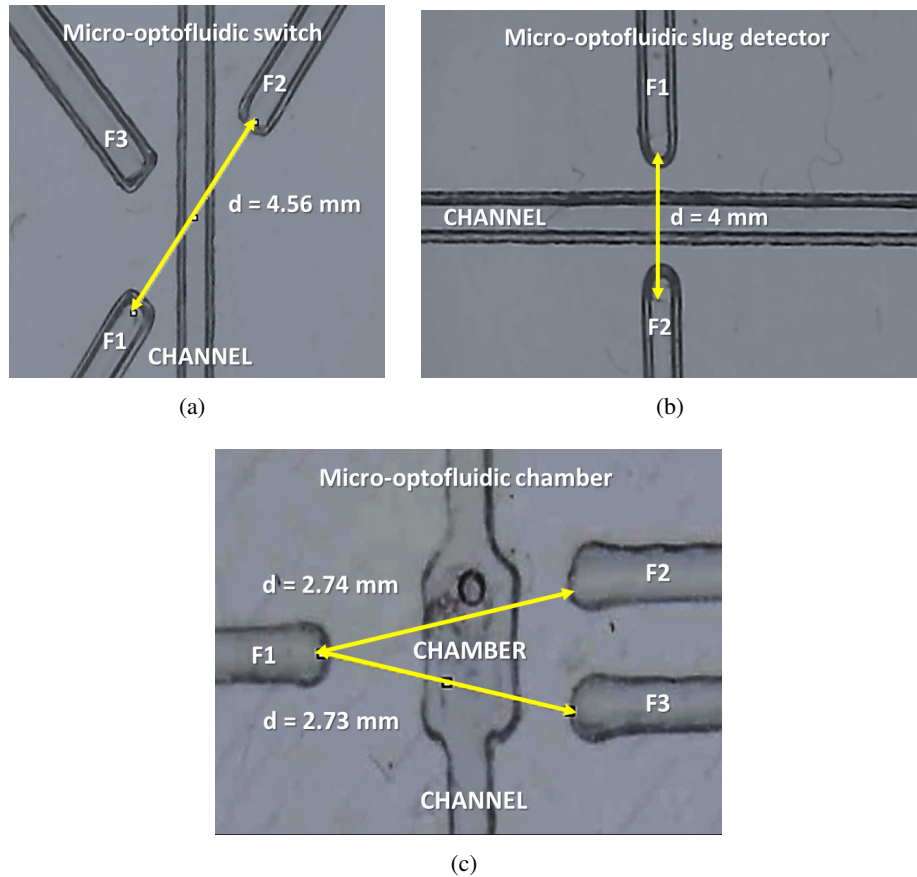
FIGURE 12.2: Fiber calibration, showing a zoom of the investigated area for the investigated micro-optofluidic devices. (a) The distance $d = 4.56$ *mm* between F1-F2 in the *micro-optofluidic switch*; (b) The distance $d = 4$ *mm* between F1-F2 in the *micro-optofluidic slug detector*; (c) The distance $d = 2.7$ *mm* between F1-F2 in the *micro-optofluidic chamber*.

The second experimental campaign (*Exp-2*) consists of 4 experiments in which the fluid is composed of live cells of 5 μm, named yeast cells of Saccharomyces cerevisiae belonging to the eukaryotic family, diluted in a saline solution, a phosphate-buffered saline (PBS). The following fluids were injected into the channel inlet:

- the phosphate buffered saline (one phase flow used for calibration);

- Yeast cells with a number concentration of 10^6;

- Yeast cells with a number concentration of 10^7;

- Yeast cells with a number concentration of 10^8.

Continuous acquisitions of 1 *min* were obtained for each experiment. The mean and the standard deviation were calculated considering the time window of 2 *s*.

12.4 Results and discussion

12.4.1 Hydrodynamic study for cells and DNA suspension

The two experimental campaigns performed were carried out to evidence the potentiality of the three devices realized by the authors to differentiate several fluids and to evaluate cells and DNA suspension concentration.

In Fig. 12.3 (a) the voltage values acquired during *Exp-1* in the *micro-optofluidic switch* are reported. In *Day-1* the fiber distance F1-F2 is of about $d = 4.72$ *mm* and in *Day-2* $d = 4.68$ *mm*. It is evident, how the fiber distance affects the voltage values acquired. The greater the distance, the smaller the voltage value read. However, the trend obtained in both acquisitions is the same. The voltage is low when the water de-ionized, used as a reference, is present and increases with different fluids. When water with DNA flows in the microfluidic channel, the voltage value increases with respect to the water value. Being the DNA_A number of concentration double with respect to the DNA_B number of concentration, in both days of acquisition, the voltage value related to the DNA_A is greater than DNA_B.

Regarding the DMEM, a cell culture media and the DMEM+FBS, a cell culture media with the addition of a common natural media for cell culture or tissue culture rich in nutrients, also in this case a slight difference in voltage is evident. In this case, seems that the increase of components in the fluid increases the read voltage value. The same behavior and trend it is evident for the *micro-optofluidic slug detector*, the voltage values are shown in Fig. 12.3 (b).

It can be seen from these results that the *micro-optofluidic switch* operates better by being designed with greater sensitivity to the refractive index of water.

In Fig. 12.4 (a)-(b)-(c) the voltage values acquired during *Exp-2* in the *micro-optofluidic switch*, the *micro-optofluidic slug detector* and the *micro-optofluidic chamber* are reported. In both cases, the PBS, the phosphate-buffered saline, has been considered as a reference.

In Figs. 12.4 (a)-(c), for the *micro-optofluidic switch* and the *micro-optofluidic chamber* it is possible to see that the voltage value acquired, even if the fiber distance is different, decrease when the cell concentration increase. In this device, the higher the concentration of these cells, the more difficulty light has in passing through them and reaching the photodiode.

An opposite result is presented in fig. 12.4 (b) regarding the *micro-optofluidic slug detector*. In this case, the higher the concentration of these cells, the more light hits them and creates a scattering effect that increases the light that then reaches the photodiode. From these results, it can be seen that the three devices can be used also for the evaluation of cell suspension concentration.

Micro-optofluidic switch

(a)

Micro-optofluidic slug detector

(b)
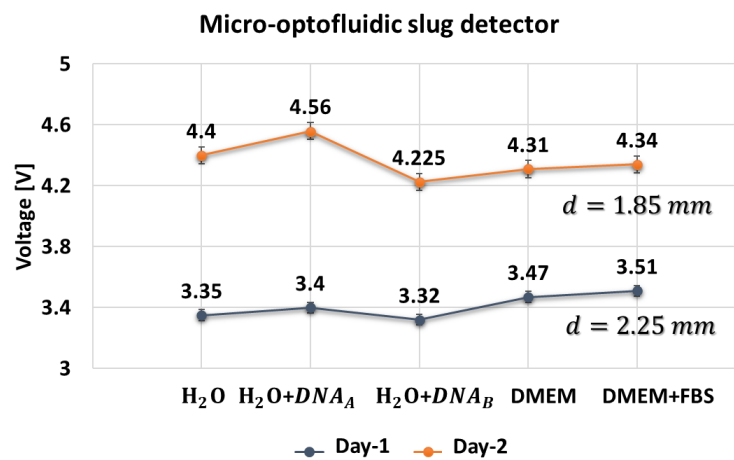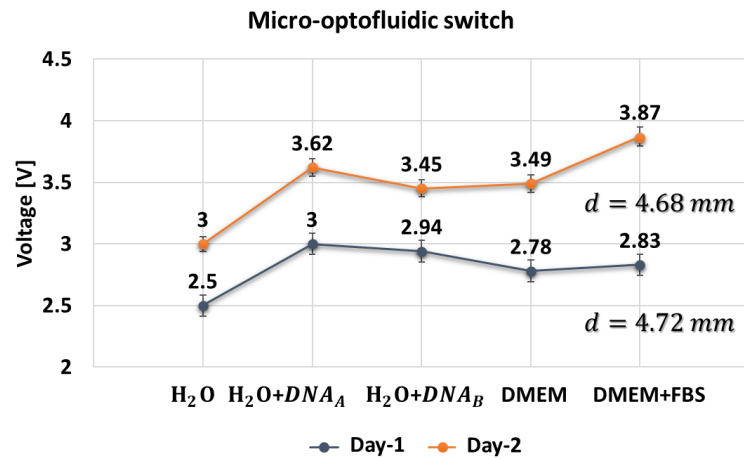
FIGURE 12.3: The voltage signal acquired by the photodiode for the detection and the evaluation of DNA suspension in de-ionized water and other fluids on (a) the *micro-optofluidic switch* and on (b) the *micro-optofluidic slug detector*.

(a)

(b)

(c)
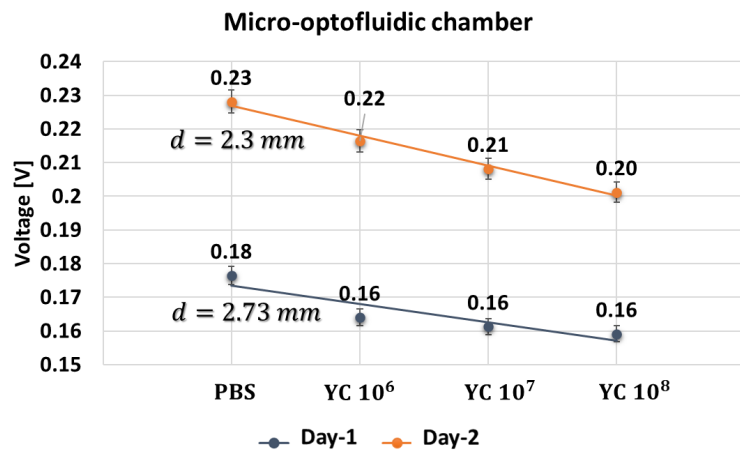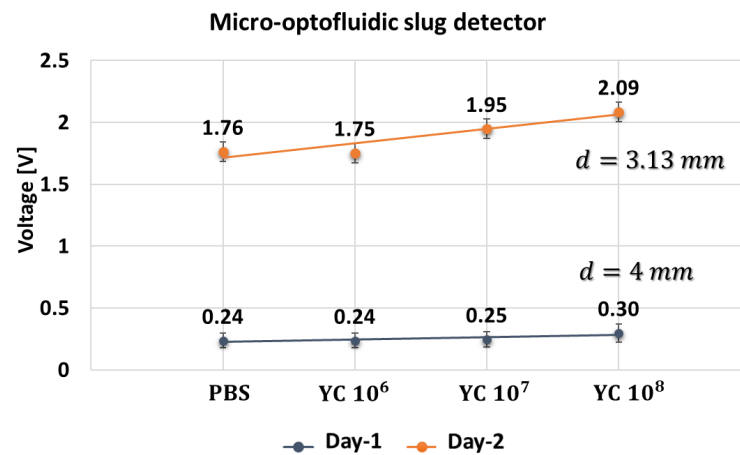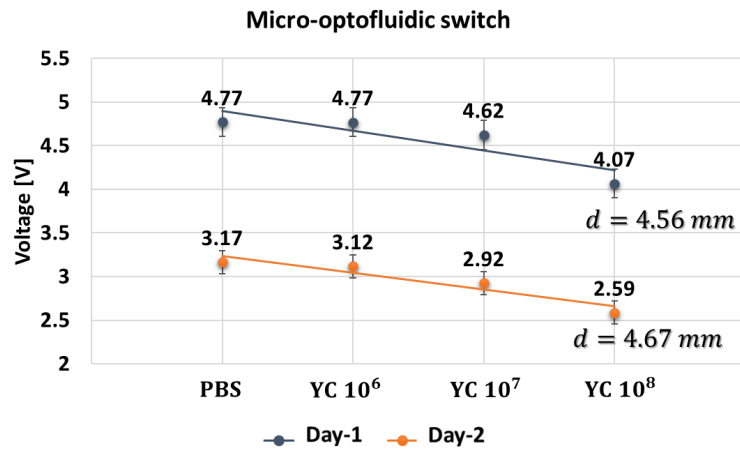
FIGURE 12.4: The voltage signal acquired by the photodiode for the detection and evaluation of the yeast cells concentrations in PBS suspension considered $\{YC\ 10^6,$ $YC\ 10^7,\ YC\ 10^8\}$ on (a) the *micro-optofluidic switch*, (b) the *micro-optofluidic slug detector* and (c) the *the micro-optofluidic chamber*.

Conclusions

In this thesis, slug flows and suspended micro-particles/cells into a fluid inside a micro-channel were considered to develop methodologies and technologies that can be easily integrated into a system for the real-time detection, and control of microfluidic processes on a chip.
The objective of the research was double. From one side, to design and fabricate using low-cost technologies, micro-optofluidic (MoF) devices, capable to replicate and miniaturize standard equipment used for biological and chemical analysis on samples. On the other side, to define methods and implement platforms for the real-time detection and control of two-phase microfluidic processes suitable for the integration with the MoF devices for a system-on-chip realization.
From the technological point of view, two 3D printing-based fabrication approaches were presented, stereolithography based on an HTL resin and a master-slave approach based on PDMS. In the first chapter, four MoF devices designed and fabricated, using these technologies, were shown.
In the first part of this thesis (**Part I**), systems and devices for slug flow detection and control were presented and in the second part (**Part II**), methods and devices for micro-particles suspension investigation. A summary of each chapter with possible future developments is provided below.

 - In **Part I**-*Chapter 2*, the two MoF flow devices made of HTL-resin by the Projection Micro Stereolithography (PμSL) and in PDMS by an ad-hoc developed mater-slave 3D printing approach were characterized and compared. The materials used differ in terms of roughness and contact angle with the fluid investigated within the micro-channel, but from the analyses performed, no flow instability within the micro-channel would be associated with the surface, making both fabrication techniques suitable for MoF devices' realization. The performance of the two devices as slug flow detectors was analyzed in the optimal operating conditions (power of the light and input flow rates). The results of the comparative analysis revealed their advantages and disadvantages. The advantages of PμSL are its suitability for printing complex MoF devices with high precision and in a single step. However, the use of HTL resin with lower transparency than PDMS results in lower

sensing performance. Therefore, future research efforts should be directed toward developing resin grades for 3D printing that exhibit the same optical properties as PDMS. In addition, further studies should consider the multi-material strategy in order to create plastic optical fibers fully integrated into the 3D-printed MoF device.

- In **Part I**-*Chapter 3*, the two PDMS MoF devices, the slug detector and the slug switch, realized by the 3D printing master-slave protocol, were compared for slug flow detection. Despite they are based on two different optical working principles, light absorption and light total internal reflection, respectively, both can be easily adopted under different experimental conditions and incorporated into portable systems for real-time applications. An optical monitoring system allocated in the test section of the devices was used to test the performance of the two MoF devices in PDMS. To check the optical detection of the slug flow in terms of slug passage duration, a flow meter was placed at the output of the devices. On one side, it was shown that the MoF slug switch is much more sensitive than the MoF slug detector. On the other hand, for the MoF slug switch, to have optimal performance, its geometry needs to be revised due to the fluids refraction index taking into account (in the presented experiments water-air). The MoF slug detector does not need optimization of the design, using different fluids and a possible improvement, to be tested to increase its sensitivity to light variation, could be to enlarge the length of the input optical fiber in the area of interest.

- In **Part I**-*Chapter 4*, a real-time velocity detection system, for the slug flow analysis in a micro-channel based on optical signals monitoring was presented. Due to the process's nonlinearity, an irregular behavior is expected, so the possibility to use simple low-cost procedures for its monitoring represents an important step in the development of a microfluidic system-on-chip. The attention was focused on the slug flows (air and water) in serpentine micro-channels with a diameter of 320 μm and 640 μm. The process was monitored through a photodiode set-up. Two approaches based on the post-processing of the optical signal in the time and frequency domain were established for the slug flow characterization in an investigated area inside the micro-channel. The first one based on the dual-slit methodology computes the average of the slugs' velocity and the latter the average slug frequency passage. A fulfilling slug flow characterization was obtained by a wide experimental campaign for different input flow rates. For each experiment, it was possible to distinguish the average of the water and air slugs' velocity and frequency and the correlation between these two parameters. This data analysis approach was then implemented in a Platform for the real-time detection of the slug flow. The platform performances were successfully validated experimentally. The results obtained represent an important step in the development of non-invasive, low-cost portable systems for micro-flow analysis which could also be suitable for easy on-chip integration. This approach was used in the design of the MoF slug velocity detector presented in *Chapter 5* and partially integrated into the MPC system for the slug control in *Chapter 6*.

- In **Part I**-*Chapter 5*, a MoF slug velocity detector was designed, realized and characterized. It consists of a standard T-junction and a micro-optical component capable of splitting light into two paths. With this device, it was possible to reduce the optical components of a standard experimental set-up for process monitoring. The optical signals acquired in its characterization were post-processed by the methods discussed in *Chapter 4* to determine the slug frequency and the slug velocity. As discussed, the approach for the realization of the micro-optical components using 3D printing is very promising.

- In **Part I**-*Chapter 6*, an active approach to control the slug flow inside the micro-channel was presented. A linear model predictive control (MPC) integrated system for slug flow in a micro-channel was designed, implemented and realized. In particular, the MoF slug velocity detector presented in *Chapter 5*, was integrated into a system and thanks to a micro-controller, it was possible to set the slug flow inside the micro-channel. To realize that, it was defined as a linear model having as output the frequency of the slug flow and it was implemented in the micro-controller the procedure for the real-time analysis of the optical information acquired by the process. The integrated platform was successfully tested. In future improvements, the MPC will be extended to wide experimental conditions by the definition of a data-driven nonlinear model of the process, which could significantly extend the use of the system to a variety of experimental applications. In terms of hardware set-up, it could be advantageous to find a solution to speed up the optical signal processing.

- In **Part I**-*Chapter 7*, a passive approach to control the slug flow inside the micro-channel was investigated. The surface of the micro-channel in the standard PDMS MoF device was modified with a ZnO nanorod coating. The slug flow detection was performed by the approach defined in *Chapter 4*. Different fluids were used for the comparison of the devices. The experiments confirmed the possibility to control the fluids due to their different interaction with the wall of the micro-channels. The results evidence the possibility to speed up or slow down the process, thus by passive control based on chemical functionalization of the PDMS surface and the fluids' selection.

- In **Part II**-*Chapter 8*, the approach developed for the investigation of micro-particle suspensions in micro-channel was based on two algorithms: a Digital Particle Image Velocimetry (DPIV)-based algorithm and a custom counting algorithm. The data analysis was implemented to run automatically and adaptable to different experimental conditions. The DPIV procedure was customized based on the dimension of the Region of Interest (ROI) investigated and the particle sizes. The custom particle counting algorithm gives the instantaneous micro-particles number to investigate the process in unsteady dynamical conditions: the value of the computed velocity will be independent of the particle number. Additionally, a post-processing algorithm was implemented to evaluate the trend of the particle average velocity in an area of interest. Having information on the process under investigation, both by images and signals, was a great advantage in the development of the integrated particle detection platform. The DPIV-customized algorithm was run

on a portable computer and in real-time was possible to manage the optical data acquisition and analysis.

- In **Part II**-*Chapter 9*, the customized DPIV-based method was used to investigate the biological fluids in micro-channels in response to hydrodynamic stimuli. The biological fluids were composed of three types of micro-particles, of different natures and sizes: the yeast cells (5 μm), the human cells (16 μm) and the silica beads (6 μm). They were injected in a micro-channel with different oscillating flows and the process was monitored in an investigated area by using an optical set-up. The velocity signals evidence of the particle hydrodynamic responses to external stimuli and the possibility to associate them with the micro-particles physical properties. In order to study their collective behavior, a particular emphasis was given to the analysis in the frequency domain, both in the low and high range, as a fundamental step for the investigation of the possible resonance effect in cell assembly. Additionally, the signals collected by the photodiode were compared with the velocity trends obtained by the DPIV-based algorithm as a proof of concept for further simplification and speed-up of the data acquisition and analysis based on a simpler optical detection than the video recording. This could open the way to a greater simplification of the real-time process analysis.

- In **Part II**-*Chapter 10*, a theoretical background of inertial focusing, an effective means of passively controlling the equilibrium positions of high-speed particles in microfluidic channels was presented. Multi-physical modeling of the phenomenon was carried out and presented on both rectilinear and curvilinear channels, with related results obtained in simulation. To validate the models, an experimental campaign was carried out, using a rectilinear and curvilinear micro-channel. The experimentally acquired video data were analyzed by the DPIV-based algorithm. Possible future developments include a detailed analysis of the migration in the curvilinear channel to confirm the results obtained through numerical simulation and further refinement and optimization of the DPIV-based algorithm to calculate the velocities of particle migration to the equilibrium positions inside the micro-channel.

- In **Part II**-*Chapter 11*, the MoF chamber was characterized and its suitability to be integrated into a system to study the hydrodynamic response of fluids of different natures and suspended particles at different concentrations was investigated. The MoF chamber shows good sensitivity in differentiating fluids of different densities and particles at different concentrations. Future developments will take into account an oval-shaped geometry optimization and an experimental campaign to evaluate its use in order to study cell interaction.

- In **Part II**-*Chapter 12*, the three PDMS MoF T-junction devices were tested to differentiate and evaluate cells and DNA suspension concentration. The experimental results confirm their use in biological fluid characterization and their sensitivity to the particle concentration, particularly using the MoF slug switch. A possible future improvement will be to permanently integrate the fibers into the devices in order to remove the operator-dependent error

and to test them using other biological fluids. The experimentation represents proof of suitability for their use in a chemical and biological context, with the advantage of their portability and relatively low-cost and ease of fabrication.

Bibliography

[1] L. G. Bleris, J. Garcia, M. V. Kothare, and M. G. Arnold, "Towards embedded model predictive control for system-on-a-chip applications," *Journal of Process Control*, vol. 16, no. 3, pp. 255–264, 2006.

[2] S. Mashaghi, A. Abbaspourrad, D. A. Weitz, and A. M. van Oijen, "Droplet microfluidics: A tool for biology, chemistry and nanotechnology," *TrAC Trends in Analytical Chemistry*, vol. 82, pp. 118–125, 2016.

[3] G. M. Whitesides, "The origins and the future of microfluidics," *nature*, vol. 442, no. 7101, pp. 368–373, 2006.

[4] P. Tabeling, *Introduction to microfluidics*. Oxford University Press on Demand, 2005.

[5] F. Schembri, F. Sapuppo, and M. Bucolo, "Experimental classification of nonlinear dynamics in microfluidic bubbles' flow," *Nonlinear Dynamics*, vol. 67, no. 4, pp. 2807–2819, 2012.

[6] P. Minzioni, R. Osellame, C. Sada, *et al.*, "Roadmap for optofluidics," *Journal of Optics*, vol. 19, no. 9, p. 093 003, 2017.

[7] F. Cairone, S. Gagliano, D. C. Carbone, G. Recca, and M. Bucolo, "Micro-optofluidic switch realized by 3d printing technology," *Microfluidics and nanofluidics*, vol. 20, no. 4, pp. 1–10, 2016.

[8] F. Cairone, S. Davi, G. Stella, *et al.*, "3d-printed micro-optofluidic device for chemical fluids and cells detection," *Biomedical Microdevices*, vol. 22, no. 2, pp. 1–10, 2020.

[9] F. Cairone, F. Gallo Afflitto, G. Stella, *et al.*, "Micro-optical waveguides realization by low-cost technologies," in *Micro*, MDPI, vol. 2, 2022, pp. 123–136.

[10] S. M. Scott and Z. Ali, "Fabrication methods for microfluidic devices: An overview," *Micromachines*, vol. 12, no. 3, p. 319, 2021.

[11] W. Zhou, J. Le, Y. Chen, Y. Cai, Z. Hong, and Y. Chai, "Recent advances in microfluidic devices for bacteria and fungus research," *TrAC Trends in Analytical Chemistry*, vol. 112, pp. 175–195, 2019.

[12] J. McDonald, D. Duffy, J. Anderson, *et al.*, "Method for fabrication of microfluidic systems in glass," *Electrophoresis*, vol. 21, pp. 27–40, 2000.

[13] G. S. Fiorini and D. T. Chiu, "Disposable microfluidic devices: Fabrication, function, and application," *BioTechniques*, vol. 38, no. 3, pp. 429–446, 2005.

[14] N Convery and N Gadegaard, *Years of microfluidics. micro nano eng 2: 76–91*, 30.

[15] B. K. Gale, A. R. Jafek, C. J. Lambert, *et al.*, "A review of current methods in microfluidic device fabrication and future commercialization prospects," *Inventions*, vol. 3, no. 3, p. 60, 2018.

[16] F. Schembri and M. Bucolo, "Periodic input flows tuning nonlinear two-phase dynamics in a snake microchannel," *Microfluidics and nanofluidics*, vol. 11, no. 2, pp. 189–197, 2011.

[17] D. J. Harrison, K. Fluri, K. Seiler, Z. Fan, C. S. Effenhauser, and A. Manz, "Micromachining a miniaturized capillary electrophoresis-based chemical analysis system on a chip," *Science*, vol. 261, no. 5123, pp. 895–897, 1993.

[18] S. C. Jacobson, R. Hergenröder, L. B. Koutny, and J. M. Ramsey, "Open channel electrochromatography on a microchip," *Analytical Chemistry*, vol. 66, no. 14, pp. 2369–2373, 1994.

[19] S. C. Jacobson, A. W. Moore, and J. M. Ramsey, "Fused quartz substrates for microchip electrophoresis," *Analytical Chemistry*, vol. 67, no. 13, pp. 2059–2063, 1995.

[20] C. M. Matzke, R. J. Kottenstette, S. A. Casalnuovo, *et al.*, "Microfabricated silicon gas chromatographic microchannels: Fabrication and performance," in *Micromachining and Microfabrication Process Technology IV*, SPIE, vol. 3511, 1998, pp. 262–268.

[21] A. W. Moore, S. C. Jacobson, and J. M. Ramsey, "Microchip separations of neutral species via micellar electrokinetic capillary chromatography," *Analytical Chemistry*, vol. 67, no. 22, pp. 4184–4189, 1995.

[22] A Tony, A Rasouli, A Farahinia, *et al.*, "Toward a soft microfluidic system: Concept and preliminary developments," in *2021 27th International Conference on Mechatronics and Machine Vision in Practice (M2VIP)*, IEEE, 2021, pp. 755–759.

[23] H. Becker and C. Gärtner, "Polymer microfabrication methods for microfluidic analytical applications," *ELECTROPHORESIS: An International Journal*, vol. 21, no. 1, pp. 12–26, 2000.

[24] T.-C. Chao and A. Ros, "Microfluidic single-cell analysis of intracellular compounds," *Journal of the Royal Society Interface*, vol. 5, no. suppl_2, S139–S150, 2008.

[25] E. Eriksson, K. Sott, F. Lundqvist, *et al.*, "A microfluidic device for reversible environmental changes around single cells using optical tweezers for cell selection and positioning," *Lab on a Chip*, vol. 10, no. 5, pp. 617–625, 2010.

[26] B. Zheng, L. S. Roach, and R. F. Ismagilov, "Screening of protein crystallization conditions on a microfluidic chip using nanoliter-size droplets," *Journal of the American chemical society*, vol. 125, no. 37, pp. 11 170–11 171, 2003.

[27] D. T. Chiu, N. L. Jeon, S. Huang, *et al.*, "Patterned deposition of cells and proteins onto surfaces by using three-dimensional microfluidic systems," *Proceedings of the National Academy of Sciences*, vol. 97, no. 6, pp. 2408–2413, 2000.

[28] A. Benedetto, G. Accetta, Y. Fujita, and G. Charras, "Spatiotemporal control of gene expression using microfluidics," *Lab on a Chip*, vol. 14, no. 7, pp. 1336–1347, 2014.

[29] D. L. Huber, R. P. Manginell, M. A. Samara, B.-I. Kim, and B. C. Bunker, "Programmed adsorption and release of proteins in a microfluidic device," *Science*, vol. 301, no. 5631, pp. 352–354, 2003.

[30] A. D. Stroock and G. M. Whitesides, "Controlling flows in microchannels with patterned surface charge and topography," *Accounts of chemical research*, vol. 36, no. 8, pp. 597–604, 2003.

[31] Y. Xia and G. M. Whitesides, "Soft lithography," *Angewandte Chemie International Edition*, vol. 37, no. 5, pp. 550–575, 1998.

[32] D. Hoelzle, M. Lake, C. Narciso, *et al.*, "Microfluidic device design, fabrication, and testing protocols," 2015.

[33] M. P. Wolf, G. B. Salieb-Beugelaar, and P. Hunziker, "Pdms with designer functionalities—properties, modifications strategies, and applications," *Progress in Polymer Science*, vol. 83, pp. 97–134, 2018.

[34] A. Borók, K. Laboda, and A. Bonyár, "Pdms bonding technologies for microfluidic applications: A review," *Biosensors*, vol. 11, no. 8, p. 292, 2021.

[35] D. Han and H. Lee, "Recent advances in multi-material additive manufacturing: Methods and applications," *Current Opinion in Chemical Engineering*, vol. 28, pp. 158–166, 2020.

[36] S. N. Bhatia and D. E. Ingber, "Microfluidic organs-on-chips," *Nature biotechnology*, vol. 32, no. 8, pp. 760–772, 2014.

[37] Q. Yang, Q. Lian, and F. Xu, "Perspective: Fabrication of integrated organ-on-a-chip via bioprinting," *Biomicrofluidics*, vol. 11, no. 3, p. 031 301, 2017.

[38] D. J. Beebe, G. A. Mensing, G. M. Walker, *et al.*, "Physics and applications of microfluidics in biology," *Annual review of biomedical engineering*, vol. 4, no. 1, pp. 261–286, 2002.

[39] Q. Alkhalaf, S. Pande, and R. R. Palkar, "Review of polydimethylsiloxane (pdms) as a material for additive manufacturing," *Innovative Design, Analysis and Development Practices in Aerospace and Automotive Engineering*, pp. 265–275, 2021.

[40] K. Thakare, L. Jerpseth, Z. Pei, A. Elwany, F. Quek, and H. Qin, "Bioprinting of organ-on-chip systems: A literature review from a manufacturing perspective," *Journal of Manufacturing and Materials Processing*, vol. 5, no. 3, p. 91, 2021.

[41] C. M. B. Ho, S. H. Ng, K. H. H. Li, and Y.-J. Yoon, "3d printed microfluidics for biological applications," *Lab on a Chip*, vol. 15, no. 18, pp. 3627–3637, 2015.

[42] G Stella, N Skariya, S Gagliano, G Cicala, and M Bucolo, *Micro-optofluidic systems for slug detection*, 2021.

[43] A Shrivastava, *Introduction to plastics engineering. introd to plast eng: 1–16*, 2018.

[44] J. C. McDonald and G. M. Whitesides, "Poly (dimethylsiloxane) as a material for fabricating microfluidic devices," *Accounts of chemical research*, vol. 35, no. 7, pp. 491–499, 2002.

[45] N. Gorji, R O'connor, and D Brabazon, "Xps, sem, afm, and nano-indentation characterization for powder recycling within additive manufacturing process," in *IOP Conference Series: Materials Science and Engineering*, IOP Publishing, vol. 1182, 2021, p. 012 025.

[46] C. Sendner, D. Horinek, L. Bocquet, and R. R. Netz, "Interfacial water at hydrophobic and hydrophilic surfaces: Slip, viscosity, and diffusion," *Langmuir*, vol. 25, no. 18, pp. 10 768–10 781, 2009.

[47] C.-H. Choi, K. J. A. Westin, and K. S. Breuer, "To slip or not to slip: Water flows in hydrophilic and hydrophobic microchannels," in *ASME International Mechanical Engineering Congress and Exposition*, vol. 36487, 2002, pp. 557–564.

[48] G. Zhou and S.-C. Yao, "Effect of surface roughness on laminar liquid flow in micro-channels," *Applied Thermal Engineering*, vol. 31, no. 2-3, pp. 228–234, 2011.

[49] T. L. Alford, L. C. Feldman, and J. W. Mayer, *Fundamentals of nanoscale film analysis*. Springer Science & Business Media, 2007.

[50] Y. Hwang, O. H. Paydar, and R. N. Candler, "3d printed molds for non-planar pdms microfluidic channels," *Sensors and Actuators A: Physical*, vol. 226, pp. 137–142, 2015.

[51] M. Villegas, Z. Cetinic, A. Shakeri, and T. F. Didar, "Fabricating smooth pdms microfluidic channels from low-resolution 3d printed molds using an omniphobic lubricant-infused coating," *Analytica chimica acta*, vol. 1000, pp. 248–255, 2018.

[52] N. Vaidya and O. Solgaard, "3d printed optics with nanometer scale surface roughness," *Microsystems & nanoengineering*, vol. 4, no. 1, pp. 1–8, 2018.

[53] W. Qu, G. M. Mala, and D. Li, "Pressure-driven water flows in trapezoidal silicon microchannels," *International Journal of Heat and Mass Transfer*, vol. 43, no. 3, pp. 353–364, 2000.

[54] D. Pfund, D. Rector, A. Shekarriz, A. Popescu, and J. Welty, "Pressure drop measurements in a microchannel," *AIChE Journal*, vol. 46, no. 8, pp. 1496–1507, 2000.

[55] C. A. Warr, H. S. Hinnen, S. Avery, R. J. Cate, G. P. Nordin, and W. G. Pitt, "3d-printed microfluidic droplet generator with hydrophilic and hydrophobic polymers," *Micromachines*, vol. 12, no. 1, p. 91, 2021.

[56] F. Eduati, R. Utharala, D. Madhavan, *et al.*, "A microfluidics platform for combinatorial drug screening on cancer biopsies," *Nature communications*, vol. 9, no. 1, pp. 1–13, 2018.

[57] R. Song, M. S. Abbasi, and J. Lee, "Fabrication of 3d printed modular microfluidic system for generating and manipulating complex emulsion droplets," *Microfluidics and Nanofluidics*, vol. 23, no. 7, pp. 1–11, 2019.

[58] Y.-S. Sun, "Comparison of chip inlet geometry in microfluidic devices for cell studies," *Molecules*, vol. 21, no. 6, p. 778, 2016.

[59] A. Serizawa, Z. Feng, and Z. Kawara, "Two-phase flow in microchannels," *Experimental Thermal and Fluid Science*, vol. 26, no. 6-7, pp. 703–714, 2002.

[60] F. Cairone and M. Bucolo, "Data-driven identification of two-phase microfluidic flows," in *2016 24th Mediterranean Conference on Control and Automation (MED)*, IEEE, 2016, pp. 797–802.

[61] F. Cairone, S. Gagliano, and M. Bucolo, "Experimental study on the slug flow in a serpentine microchannel," *Experimental Thermal and Fluid Science*, vol. 76, pp. 34–44, 2016.

[62] Y. Fainman, D. Psaltis, and C. Yang, *Optofluidics: fundamentals, devices, and applications*. McGraw-Hill Education, 2010.

[63] M. Brammer and T. Mappes, "Modular platforms for optofluidic systems," *Optofluidics*, vol. 1, no. 2013, pp. 1–10, 2013.

[64] L. G. Bleris, P. D. Vouzis, J. G. Garcia, M. G. Arnold, and M. V. Kothare, "Pathways for optimization-based drug delivery," *Control Engineering Practice*, vol. 15, no. 10, pp. 1280–1291, 2007.

[65] J. Maddala and R. Rengaswamy, "Droplet digital signal generation in microfluidic networks using model predictive control," *Journal of Process Control*, vol. 23, no. 2, pp. 132–139, 2013.

[66] M. Bucolo, J Guo, M. Intaglietta, and W. Coltro, *Guest editorial special issue on microfluidics engineering for point-of-care diagnostics*, 2017.

[67] B. Kuswandi, J. Huskens, W. Verboom, *et al.*, "Optical sensing systems for microfluidic devices: A review," *Analytica chimica acta*, vol. 601, no. 2, pp. 141–155, 2007.

[68] D.-G. Seol, T. Bhaumik, C. Bergmann, S. A. Socolofsky, *et al.*, "Particle image velocimetry measurements of the mean flow characteristics in a bubble plume," *Journal of engineering mechanics*, vol. 133, no. 6, p. 665, 2007.

[69] Y. MURAI and F. YAMAMOTO, "Simultaneous piv/ptv measurements of bubble and particle phases in gas-liquid two-phase flow based on image separation and reconstruction," *Journal of Hydrodynamics, Ser. B*, vol. 16, no. 6, pp. 756–766, 2004.

[70] T. Kraus, A. Günther, N. de Mas, M. A. Schmidt, and K. F. Jensen, "An integrated multiphase flow sensor for microchannels," *Experiments in Fluids*, vol. 36, no. 6, pp. 819–832, 2004.

[71] F. Sapuppo, A. Llobera, F. Schembri, M. Intaglietta, V. J. Cadarso, and M. Bucolo, "A polymeric micro-optical interface for flow monitoring in biomicrofluidics," *Biomicrofluidics*, vol. 4, no. 2, p. 024 108, 2010.

[72] A. Mahvash and A. Ross, "Application of chmms to two-phase flow pattern identification," *Engineering Applications of Artificial Intelligence*, vol. 21, no. 8, pp. 1144–1152, 2008.

[73] ——, "Two-phase flow pattern identification using continuous hidden markov model," *International journal of multiphase flow*, vol. 34, no. 3, pp. 303–311, 2008.

[74] F. Cairone, P. Anandan, and M. Bucolo, "Nonlinear systems synchronization for modeling two-phase microfluidics flows," *Nonlinear Dynamics*, vol. 92, no. 1, pp. 75–84, 2018.

[75] S. Gagliano, F. Cairone, A. Amenta, and M. Bucolo, "A real time feed forward control of slug flow in microchannels," *Energies*, vol. 12, no. 13, p. 2556, 2019.

[76] F. Sapuppo, M. Bucolo, M. Intaglietta, P. C. Johnson, L. Fortuna, and P. Arena, "An improved instrument for real-time measurement of blood flow velocity in microvessels," *IEEE Transactions on Instrumentation and Measurement*, vol. 56, no. 6, pp. 2663–2671, 2007.

[77] F Cairone, D Ortiz, P. Cabrales, M Intaglietta, and M Bucolo, "Emergent behaviors in rbcs flows in micro-channels using digital particle image velocimetry," *Microvascular research*, vol. 116, pp. 77–86, 2018.

[78] H Bruus, *Theoretical microfluidics. volume 18 oxford university press*, 2008.

[79] E Aurell, G. Boffetta, A Crisanti, G Paladin, and A Vulpiani, "Predictability in the large: An extension of the concept of lyapunov exponent," *Journal of Physics A: Mathematical and General*, vol. 30, no. 1, p. 1, 1997.

[80] A Bonasera, M Bucolo, L Fortuna, M Frasca, and A Rizzo, "Experimental evaluation of the d-infinite parameter to characterize chaotic dynamics," in *AIP Conference Proceedings*, American Institute of Physics, vol. 676, 2003, pp. 355–362.

[81] J. M. T. Thompson, H. B. Stewart, and R. Turner, "Nonlinear dynamics and chaos," *Computers in Physics*, vol. 4, no. 5, pp. 562–563, 1990.

[82] M. T. Rosenstein, J. J. Collins, and C. J. De Luca, "A practical method for calculating largest lyapunov exponents from small data sets," *Physica D: Nonlinear Phenomena*, vol. 65, no. 1-2, pp. 117–134, 1993.

[83] D. Janasek, J. Franzke, and A. Manz, "Scaling and the design of miniaturized chemical-analysis systems," *Nature*, vol. 442, no. 7101, pp. 374–380, 2006.

[84] J. W. Suk and J.-H. Cho, "Capillary flow control using hydrophobic patterns," *Journal of micromechanics and microengineering*, vol. 17, no. 4, N11, 2007.

[85] D. Juncker, H. Schmid, U. Drechsler, *et al.*, "Autonomous microfluidic capillary system," *Analytical chemistry*, vol. 74, no. 24, pp. 6139–6144, 2002.

[86] K. M. Grant, J. W. Hemmert, and H. S. White, "Magnetic field-controlled microfluidic transport," *Journal of the American Chemical Society*, vol. 124, no. 3, pp. 462–467, 2002.

[87] R. Z. Gao, M. Hébert, J. Huissoon, and C. L. Ren, "μPump: An open-source pressure pump for precision fluid handling in microfluidics," *HardwareX*, vol. 7, e00096, 2020.

[88] K. Hosokawa, T. Fujii, and I. Endo, "Handling of picoliter liquid samples in a poly (dimethylsiloxane)-based microfluidic device," *Analytical chemistry*, vol. 71, no. 20, pp. 4781–4785, 1999.

[89] F. Cairone and M. Bucolo, "Design of control systems for two-phase microfluidic processes," in *2016 24th Mediterranean Conference on Control and Automation (MED)*, IEEE, 2016, pp. 973–978.

[90] D. Kumar, A. Shenoy, S. Li, and C. M. Schroeder, "Orientation control and nonlinear trajectory tracking of colloidal particles using microfluidics," *Physical Review Fluids*, vol. 4, no. 11, p. 114 203, 2019.

[91] S. V. Raković and W. S. Levine, *Handbook of model predictive control*. Springer, 2018.

[92] L. Wang, *Model predictive control system design and implementation using MATLAB®*. Springer Science & Business Media, 2009.

[93] F. Cairone, G. Stella, S. Gagliano, and M. Bucolo, "Data-driven modelling of fast slug flows in micro-channels," in *15th European Workshop on Advanced Control and Diagnosis*, Springer, 2022, pp. 405–422.

[94] G. Stella, S. Gagliano, and M. Bucolo, "Narx models of two-phase microchannels flow in comparison," in *2022 30th Mediterranean Conference on Control and Automation (MED)*, IEEE, 2022, pp. 343–348.

[95] D. T. Chiu, A. J. Demello, D. Di Carlo, *et al.*, "Small but perfectly formed? successes, challenges, and opportunities for microfluidics in the chemical and biological sciences," *Chem*, vol. 2, no. 2, pp. 201–223, 2017.

[96] S. Gupta, K. Ramesh, S. Ahmed, and V. Kakkar, "Lab-on-chip technology: A review on design trends and future scope in biomedical applications," *Int. J. Bio-Sci. Bio-Technol*, vol. 8, pp. 311–322, 2016.

[97] M. L. Sin, J. Gao, J. C. Liao, and P. K. Wong, "System integration-a major step toward lab on a chip," *Journal of biological engineering*, vol. 5, no. 1, pp. 1–22, 2011.

[98] Z. Shen, Y. Zou, and X. Chen, "Characterization of microdroplets using optofluidic signals," *Lab on a Chip*, vol. 12, no. 19, pp. 3816–3820, 2012.

[99] A. K. Au, W. Huynh, L. F. Horowitz, and A. Folch, "3d-printed microfluidics," *Angewandte Chemie International Edition*, vol. 55, no. 12, pp. 3862–3881, 2016.

[100] Q Kou, I Yesilyurt, V Studer, M Belotti, E Cambril, and Y Chen, "On-chip optical components and microfluidic systems," *Microelectronic engineering*, vol. 73, pp. 876–880, 2004.

[101] J. Seo and L. P. Lee, "Disposable integrated microfluidics with self-aligned planar microlenses," *Sensors and actuators B: Chemical*, vol. 99, no. 2-3, pp. 615–622, 2004.

[102] S. Gagliano, G. Stella, and M. Bucolo, "Real-time detection of slug velocity in microchannels," *Micromachines*, vol. 11, no. 3, p. 241, 2020.

[103] P. C. Li, *Microfluidic lab-on-a-chip for chemical and biological analysis and discovery*. CRC press, 2005.

[104] J. Zhou, A. V. Ellis, and N. H. Voelcker, "Recent developments in pdms surface modification for microfluidic devices," *Electrophoresis*, vol. 31, no. 1, pp. 2–16, 2010.

[105] G. T. Roman and C. T. Culbertson, "Surface engineering of poly (dimethylsiloxane) microfluidic devices using transition metal sol- gel chemistry," *Langmuir*, vol. 22, no. 9, pp. 4445–4451, 2006.

[106] B.-Y. Kim, L.-Y. Hong, Y.-M. Chung, D.-P. Kim, and C.-S. Lee, "Solvent-resistant pdms microfluidic devices with hybrid inorganic/organic polymer coatings," *Advanced Functional Materials*, vol. 19, no. 23, pp. 3796–3803, 2009.

[107] M. Hen, E. Edri, O. Guy, *et al.*, "Microfluidic devices containing zno nanorods with tunable surface chemistry and wetting-independent water mobility," *Langmuir*, vol. 35, no. 9, pp. 3265–3271, 2019.

[108] S. Habouti, C. Kunstmann-Olsen, J. D. Hoyland, H.-G. Rubahn, and M. Es-Souni, "In situ zno–pva nanocomposite coated microfluidic chips for biosensing," *Applied Physics A*, vol. 115, no. 2, pp. 645–649, 2014.

[109] Z. Chen, S.-B. Cheng, P. Cao, *et al.*, "Detection of exosomes by zno nanowires coated three-dimensional scaffold chip device," *Biosensors and Bioelectronics*, vol. 122, pp. 211–216, 2018.

[110] Z. Wang, M. R. Bockstaller, and K. Matyjaszewski, "Synthesis and applications of zno/polymer nanohybrids," *ACS Materials Letters*, vol. 3, no. 5, pp. 599–621, 2021.

[111] I. Azzouz, Y. G. Habba, M. Capochichi-Gnambodoe, *et al.*, "Zinc oxide nano-enabled microfluidic reactor for water purification and its applicability to volatile organic compounds," *Microsystems & Nanoengineering*, vol. 4, no. 1, pp. 1–7, 2018.

[112] D. Sooriyaarachchi, S. Maharubin, and G. Z. Tan, "Zno nanowire-anchored microfluidic device with herringbone structure fabricated by maskless photolithography," *Biomedical Engineering and Computational Biology*, vol. 11, p. 1 179 597 220 941 431, 2020.

[113] N. Hao, M. Zhang, and J. X. Zhang, "Microfluidics for zno micro-/nanomaterials development: Rational design, controllable synthesis, and on-chip bioapplications," *Biomaterials science*, vol. 8, no. 7, pp. 1783–1801, 2020.

[114] J. Kim, J. W. Hong, D. P. Kim, J. H. Shin, and I. Park, "Nanowire-integrated microfluidic devices for facile and reagent-free mechanical cell lysis," *Lab on a Chip*, vol. 12, no. 16, pp. 2914–2921, 2012.

[115] V. Vohra, T. Anzai, S. Inaba, W. Porzio, and L. Barba, "Transfer-printing of active layers to achieve high quality interfaces in sequentially deposited multilayer inverted polymer solar cells fabricated in air," *Science and Technology of advanced MaTerialS*, vol. 17, no. 1, pp. 530–540, 2016.

[116] M. E. Fragalà, Y. Aleeva, and G. Malandrino, "Zno nanorod arrays fabrication via chemical bath deposition: Ligand concentration effect study," *Superlattices and Microstructures*, vol. 48, no. 4, pp. 408–415, 2010.

[117] M. Salmeri, G. Ognibene, L. Saitta, *et al.*, "Optimization of zno nanorods growth on polyetheresulfone electrospun mats to promote antibacterial properties," *Molecules*, vol. 25, no. 7, p. 1696, 2020.

[118] J. Matthew, *Surface analysis by auger and x-ray photoelectron spectroscopy. d. briggs and jt grant (eds). impublications, chichester, uk and surfacespectra, manchester, uk, 2003. 900 pp., isbn 1-901019-04-7, 900 pp*, 2004.

[119] A. Gulino, "Structural and electronic characterization of self-assembled molecular nanoarchitectures by x-ray photoelectron spectroscopy," *Analytical and bioanalytical chemistry*, vol. 405, no. 5, pp. 1479–1495, 2013.

[120] S. Dai, Y. Zhu, Y. Gu, and Z. Du, "Biomimetic fabrication and photoelectric properties of superhydrophobic zno nanostructures on flexible pdms substrates replicated from rose petal," *Applied Physics A*, vol. 125, no. 2, pp. 1–11, 2019.

[121] H. K. Webb, V. K. Truong, J. Hasan, C. Fluke, R. J. Crawford, and E. P. Ivanova, "Roughness parameters for standard description of surface nanoarchitecture," *Scanning*, vol. 34, no. 4, pp. 257–263, 2012.

[122] Y Du, M.-S. Zhang, J Hong, Y Shen, Q Chen, and Z Yin, "Structural and optical properties of nanophase zinc oxide," *Applied Physics A*, vol. 76, no. 2, pp. 171–176, 2003.

[123] M. Wang, L. Jiang, E. J. Kim, and S. H. Hahn, "Electronic structure and optical properties of zn (oh) 2: Lda+ u calculations and intense yellow luminescence," *RSC advances*, vol. 5, no. 106, pp. 87 496–87 503, 2015.

[124] G Ognibene, D. Cristaldi, R Fiorenza, *et al.*, "Photoactivity of hierarchically nanostructured zno–pes fibre mats for water treatments," *RSC advances*, vol. 6, no. 49, pp. 42 778–42 785, 2016.

[125] P. Y. Dave, K. H. Patel, K. V. Chauhan, A. K. Chawla, and S. K. Rawal, "Examination of zinc oxide films prepared by magnetron sputtering," *Procedia Technology*, vol. 23, pp. 328–335, 2016.

[126] A. F. Cristino, I. A. Matias, D. E. Bastos, R. Galhano dos Santos, A. P. Ribeiro, and L. M. Martins, "Glycerol role in nano oxides synthesis and catalysis," *Catalysts*, vol. 10, no. 12, p. 1406, 2020.

[127] A. Cossarizza, H.-D. Chang, A. Radbruch, *et al.*, "Guidelines for the use of flow cytometry and cell sorting in immunological studies," *European journal of immunology*, vol. 47, no. 10, pp. 1584–1797, 2017.

[128] H. Cong, F.-C. Loo, J. Chen, Y. Wang, S.-K. Kong, and H.-P. Ho, "Target trapping and in situ single-cell genetic marker detection with a focused optical beam," *Biosensors and Bioelectronics*, vol. 133, pp. 236–242, 2019.

[129] P. K. Dagur and J. P. McCoy Jr, "Collection, storage, and preparation of human blood cells," *Current protocols in cytometry*, vol. 73, no. 1, pp. 5–1, 2015.

[130] S. Losserand, G. Coupier, and T. Podgorski, "Migration velocity of red blood cells in microchannels," *Microvascular research*, vol. 124, pp. 30–36, 2019.

[131] A. Arboix, C. Jiménez, J. Massons, O. Parra, and C. Besses, "Hematological disorders: A commonly unrecognized cause of acute stroke," *Expert review of hematology*, vol. 9, no. 9, pp. 891–901, 2016.

[132] A. Vembadi, A. Menachery, and M. A. Qasaimeh, "Cell cytometry: Review and perspective on biotechnological advances," *Frontiers in bioengineering and biotechnology*, vol. 7, p. 147, 2019.

[133] A. M. Streets and Y. Huang, "Chip in a lab: Microfluidics for next generation life science research," *Biomicrofluidics*, vol. 7, no. 1, p. 011 302, 2013.

[134] D. Mark, S. Haeberle, G. Roth, F. v. Stetten, and R. Zengerle, "Microfluidic lab-on-a-chip platforms: Requirements, characteristics and applications," *Microfluidics based microsystems*, pp. 305–376, 2010.

[135] M. Salve, K. Amreen, P. K. Pattnaik, and S. Goel, "Integrated microfluidic device with carbon-thread microelectrodes for electrochemical dna elemental analysis," *IEEE Transactions on NanoBioscience*, 2021.

[136] H.-Y. Tan and Y.-C. Toh, "What can microfluidics do for human microbiome research?" *Biomicrofluidics*, vol. 14, no. 5, p. 051 303, 2020.

[137] D. B. Weibel and G. M. Whitesides, "Applications of microfluidics in chemical biology," *Current opinion in chemical biology*, vol. 10, no. 6, pp. 584–591, 2006.

[138] G. Ochoa-Vazquez, B. Kharisov, A. Arizmendi-Morquecho, *et al.*, "Microfluidics and surface-enhanced raman spectroscopy: A perfect match for new analytical tools," *IEEE Transactions on NanoBioscience*, vol. 18, no. 4, pp. 558–566, 2019.

[139] G. Aubry and H. Lu, "A perspective on optical developments in microfluidic platforms for caenorhabditis elegans research," *Biomicrofluidics*, vol. 8, no. 1, p. 011 301, 2014.

[140] L. Novak, P. Neuzil, J. Pipper, Y. Zhang, and S. Lee, "An integrated fluorescence detection system for lab-on-a-chip applications," *Lab on a Chip*, vol. 7, no. 1, pp. 27–29, 2007.

[141] I. Grabowska, M. Sajnoga, M. Juchniewicz, M. Chudy, A. Dybko, and Z. Brzozka, "Microfluidic system with electrochemical and optical detection," *Microelectronic engineering*, vol. 84, no. 5-8, pp. 1741–1743, 2007.

[142] N. Azizipour, R. Avazpour, D. H. Rosenzweig, M. Sawan, and A. Ajji, "Evolution of biochip technology: A review from lab-on-a-chip to organ-on-a-chip," *Micromachines*, vol. 11, no. 6, p. 599, 2020.

[143] K. D. Seo, B. K. Kwak, S. Sanchez, and D. S. Kim, "Microfluidic-assisted fabrication of flexible and location traceable organo-motor," *IEEE Transactions on Nanobioscience*, vol. 14, no. 3, pp. 298–304, 2015.

[144] P. Chen, S. Li, Y. Guo, X. Zeng, and B.-F. Liu, "A review on microfluidics manipulation of the extracellular chemical microenvironment and its emerging application to cell analysis," *Analytica Chimica Acta*, vol. 1125, pp. 94–113, 2020.

[145] J. Sibbitts, K. A. Sellens, S. Jia, S. A. Klasner, and C. T. Culbertson, "Cellular analysis using microfluidics," *Analytical chemistry*, vol. 90, no. 1, 2017.

[146] M. Rothbauer, H. Zirath, and P. Ertl, "Recent advances in microfluidic technologies for cell-to-cell interaction studies," *Lab on a Chip*, vol. 18, no. 2, pp. 249–270, 2018.

[147] A. G. Koutsiaris, D. S. Mathioulakis, and S. Tsangaris, "Microscope piv for velocity-field measurement of particle suspensions flowing inside glass capillaries," *Measurement Science and Technology*, vol. 10, no. 11, p. 1037, 1999.

[148] C. D. Meinhart, S. T. Wereley, and J. G. Santiago, "Piv measurements of a microchannel flow," *Experiments in fluids*, vol. 27, no. 5, pp. 414–419, 1999.

[149] S. Pradeep and T. A. Zangle, "Quantitative phase velocimetry measures bulk intracellular transport of cell mass during the cell cycle," *Scientific reports*, vol. 12, no. 1, pp. 1–14, 2022.

[150] T. N. Kim, P. W. Goodwill, Y. Chen, *et al.*, "Line-scanning particle image velocimetry: An optical approach for quantifying a wide range of blood flow speeds in live animals," *PloS one*, vol. 7, no. 6, e38590, 2012.

[151] M. Pereyra, A. Drusko, F. Krämer, F. Strobl, E. H. Stelzer, and F. Matthäus, "Quickpiv: Efficient 3d particle image velocimetry software applied to quantifying cellular migration during embryogenesis," *BMC bioinformatics*, vol. 22, no. 1, pp. 1–20, 2021.

[152] M. F. Sampedro, G. L. Miño, C. D. Galetto, and V. Sigot, "Spatio-temporal analysis of collective migration in vivo by particle image velocimetry," *Physical Biology*, vol. 18, no. 6, p. 066 008, 2021.

[153] W. Thielicke and E. Stamhuis, "Pivlab–towards user-friendly, affordable and accurate digital particle image velocimetry in matlab," *Journal of open research software*, vol. 2, no. 1, 2014.

[154] H Huang, D Dabiri, and M. Gharib, "On errors of digital particle image velocimetry," *Measurement Science and Technology*, vol. 8, no. 12, p. 1427, 1997.

[155] P. Vennemann, "Jpiv documentation," 2020.

[156] M. Raffel, C. E. Willert, J. Kompenhans, *et al.*, *Particle image velocimetry: a practical guide*. Springer, 1998, vol. 2.

[157] M. R. Green and J. Sambrook, "Estimation of cell number by hemocytometry counting," *Cold Spring Harbor Protocols*, vol. 2019, no. 11, pdb–prot097980, 2019.

[158] C. A. Schneider, W. S. Rasband, and K. W. Eliceiri, "Nih image to imagej: 25 years of image analysis," *Nature methods*, vol. 9, no. 7, pp. 671–675, 2012.

[159] S. Sunardi, A. Yudhana, and S. Saifullah, "Identity analysis of egg based on digital and thermal imaging: Image processing and counting object concept," *International Journal of Electrical and Computer Engineering*, vol. 7, no. 1, p. 200, 2017.

[160] T. Liu, W. Wu, W. Chen, C. Sun, X. Zhu, and W. Guo, "Automated image-processing for counting seedlings in a wheat field," *Precision agriculture*, vol. 17, no. 4, pp. 392–406, 2016.

[161] N Ab Azar, A Babakhani, A Broumandnia, and K Sepanloo, "A novel method for detecting and counting overlapping tracks in ssntd by image processing techniques," *Radiation Measurements*, vol. 91, pp. 36–43, 2016.

[162] Y. Toh, T. Ng, and B. Liew, "Automated fish counting using image processing," in *2009 international conference on computational intelligence and software engineering*, IEEE, 2009, pp. 1–5.

[163] H. Zhang, C. H. Chon, X. Pan, and D. Li, "Methods for counting particles in microfluidic applications," *Microfluidics and nanofluidics*, vol. 7, no. 6, pp. 739–749, 2009.

[164] D. Huh, W. Gu, Y. Kamotani, J. B. Grotberg, and S. Takayama, "Microfluidics for flow cytometric analysis of cells and particles," *Physiological measurement*, vol. 26, no. 3, R73, 2005.

[165] T. Hou, H. Chang, H. Jiang, *et al.*, "Smartphone based microfluidic lab-on-chip device for real-time detection, counting and sizing of living algae," *Measurement*, vol. 187, p. 110 304, 2022.

[166] F. Cairone, D. Mirabella, P. J. Cabrales, M. Intaglietta, and M. Bucolo, "Quantitative analysis of spatial irregularities in rbcs flows," *Chaos, Solitons & Fractals*, vol. 115, pp. 349–355, 2018.

[167] J. Zhou and I. Papautsky, "Fundamentals of inertial focusing in microchannels," *Lab on a Chip*, vol. 13, no. 6, pp. 1121–1132, 2013.

[168] J. M. Martel and M. Toner, "Inertial focusing in microfluidics," *Annual review of biomedical engineering*, vol. 16, p. 371, 2014.

[169] G Segre and A Silberberg, "Radial particle displacements in poiseuille flow of suspensions," *Nature*, vol. 189, no. 4760, pp. 209–210, 1961.

[170] P. G. Saffman, "The lift on a small sphere in a slow shear flow," *Journal of fluid mechanics*, vol. 22, no. 2, pp. 385–400, 1965.

[171] P Vasseur and R. Cox, "The lateral migration of spherical particles sedimenting in a stagnant bounded fluid," *Journal of fluid mechanics*, vol. 80, no. 3, pp. 561–591, 1977.

[172] B. Ho and L. Leal, "Inertial migration of rigid spheres in two-dimensional unidirectional flows," *Journal of fluid mechanics*, vol. 65, no. 2, pp. 365–400, 1974.

[173] J.-P. Matas, V. Glezer, É. Guazzelli, and J. F. Morris, "Trains of particles in finite-reynolds-number pipe flow," *Physics of Fluids*, vol. 16, no. 11, pp. 4192–4195, 2004.

[174] D. Di Carlo, D. Irimia, R. G. Tompkins, and M. Toner, "Continuous inertial focusing, ordering, and separation of particles in microchannels," *Proceedings of the National Academy of Sciences*, vol. 104, no. 48, pp. 18 892–18 897, 2007.

[175] K. Hood, S. Lee, and M. Roper, "Inertial migration of a rigid sphere in three-dimensional poiseuille flow," *Journal of Fluid Mechanics*, vol. 765, pp. 452–479, 2015.

[176] C. Liu, G. Hu, X. Jiang, and J. Sun, "Inertial focusing of spherical particles in rectangular microchannels over a wide range of reynolds numbers," *Lab on a Chip*, vol. 15, no. 4, pp. 1168–1177, 2015.

[177] J. Zhang, S. Yan, D. Yuan, *et al.*, "Fundamentals and applications of inertial microfluidics: A review," *Lab on a Chip*, vol. 16, no. 1, pp. 10–34, 2016.

[178] D. Di Carlo, "Inertial microfluidics," *Lab on a Chip*, vol. 9, no. 21, pp. 3038–3046, 2009.

[179] D. H. Yoon, J. B. Ha, Y. K. Bahk, T. Arakawa, S. Shoji, and J. S. Go, "Size-selective separation of micro beads by utilizing secondary flow in a curved rectangular microchannel," *Lab on a Chip*, vol. 9, no. 1, pp. 87–90, 2009.

[180] Y. Ying and Y. Lin, "Inertial focusing and separation of particles in similar curved channels," *Scientific reports*, vol. 9, no. 1, pp. 1–12, 2019.

[181] J. M. Martel and M. Toner, "Particle focusing in curved microfluidic channels," *Scientific Reports*, vol. 3, no. 1, pp. 1–8, 2013.

[182] J.-C. Chu, J.-T. Teng, and R. Greif, "Experimental and numerical study on the flow characteristics in curved rectangular microchannels," *Applied Thermal Engineering*, vol. 30, no. 13, pp. 1558–1566, 2010.

[183] Y. Gao, P. Magaud, C. Lafforgue, S. Colin, and L. Baldas, "Inertial lateral migration and self-assembly of particles in bidisperse suspensions in microchannel flows," *Microfluidics and Nanofluidics*, vol. 23, no. 7, pp. 1–14, 2019.

[184] M. Abbas, P. Magaud, Y. Gao, and S. Geoffroy, "Migration of finite sized particles in a laminar square channel flow from low to high reynolds numbers," *Physics of Fluids*, vol. 26, no. 12, p. 123 301, 2014.

[185] Y. Gao, P. Magaud, L. Baldas, C. Lafforgue, M. Abbas, and S. Colin, "Self-ordered particle trains in inertial microchannel flows," *Microfluidics and Nanofluidics*, vol. 21, no. 10, pp. 1–10, 2017.